Laminar fMRI of long-range connections: Methods and contrast mechanisms

Viktor Pfaffenrot

Laminar fMRI of long-range connections: Methods and contrast mechanisms

Viktor Pfaffenrot

Erwin L. Hahn Institute for Magnetic Resonance Imaging

The research presented in this thesis was carried out at the Erwin L. Hahn Institute for Magnetic Resonance Imaging, Essen, Germany and the Maastricht University using the 7T MRI facility at Scannexus B.V., Maastricht, The Netherlands.

© Viktor Pfaffenrot, 2022.
All rights reserved. No part of this thesis may be reproduced or transmitted in any form or by any means, electronic or mechanical, including photocopy, recording or otherwise without permission of the author.

Cover design Pascal Guthardt, 2022

Print Datext Druck Center, Essen, Germany

ISBN 978-3-00-073549-3

Laminar fMRI of long-range connections: Methods and contrast mechanisms

Proefschrift ter verkrijging van de graad van doctor
aan de Radboud Universiteit Nijmegen
op gezag van de rector magnificus prof. dr. J.H.J.M. van Krieken,
volgens besluit van het college voor promoties
in het openbaar te verdedigen op

dinsdag 20 december 2022
om 12.30 uur precies

door

Viktor Pfaffenrot
geboren op 6 juli 1990
te Pawlodar, Kazachstan

Promoter:

Prof. dr. D.G. Norris

Copromotor:

Dr. P.J. Koopmans (Universität Duisburg-Essen, Duitsland)

Manuscriptcommissie:

Prof. dr. ir. T.W.J. Scheenen

Dr. W. van der Zwaag (Spinoza Centre for Neuroimaging)

Prof. dr. B.A. Poser (Maastricht University)

Laminar fMRI of long-range connections: Methods and contrast mechanisms

Dissertation to obtain the degree of doctor
from Radboud University Nijmegen
on the authority of the Rector Magnificus prof. dr. J.H.J.M. van Krieken,
according to the decision of the Doctorate Board
to be defended in public on

Thursday, December 20, 2022
at 12.30 pm

by

Viktor Pfaffenrot
born on July 6, 1990
in Pawlodar, Kazakhstan

Supervisor:

Prof. dr. D.G. Norris

Co-supervisor:

Dr. P.J. Koopmans (University of Duisburg-Essen, Germany)

Manuscript Committee:

Prof. dr. ir. T.W.J. Scheenen

Dr. W. van der Zwaag (Spinoza Centre for Neuroimaging)

Prof. dr. B.A. Poser (Maastricht University)

To my family

Contents

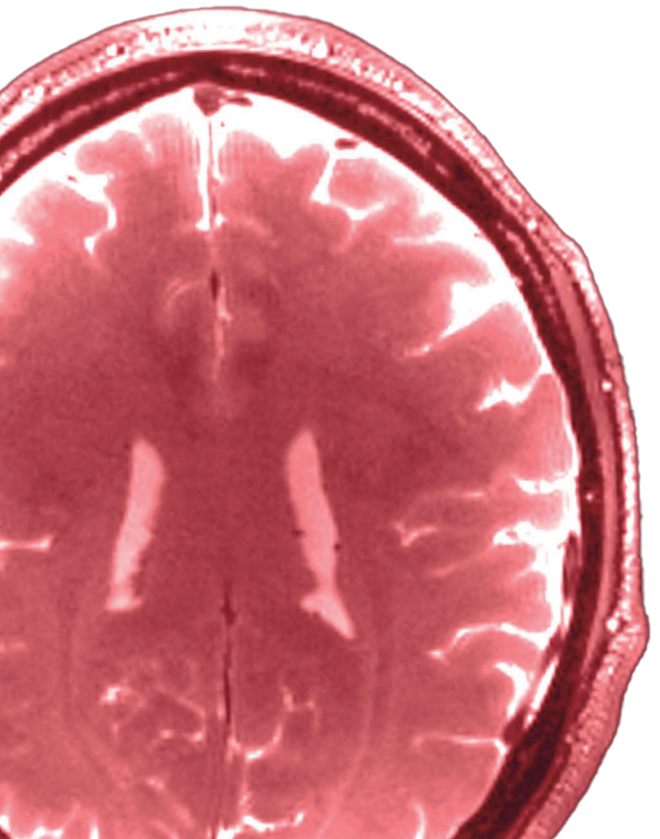

1

Introduction

"The brain immediately confronts us with its great complexity. The human brain weighs only three to four pounds but contains about 100 billion neurons "

— Gerald Fischbach

The human brain is the most complex organ of the body and has fascinated neuroscientists (like Gerald Fischbach) and scientists from other disciplines alike since decades. What makes the brain so complex is its organization at multiple, yet tightly connected, levels spanning different spatial scales, from conglomerates of small molecules and synapses over circuits of spatially organized neurons to networks forming entire maps and systems (Fig. 1.1).

The development of Magnetic Resonance Imaging (MRI) in the early 80's and the discovery that the contrast in an MR image changes with varying blood oxygenation in the 90's[1,2] opened up a promising possibility for scientists to examine the brain and its function non-invasively in vivo. With the tools of functional MRI (fMRI) at hand, neuroscience has been able to characterize maps and networks of sensory inputs like visual[3] or somatosensor[4] and higher cognitive processes like learning[5,6], working memory[7] or social interaction[8] in health and disease.

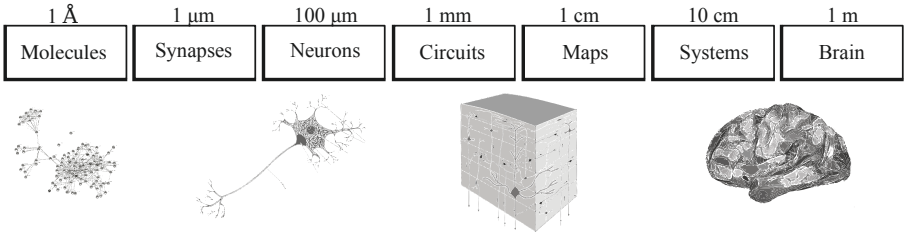

Fig. 1.1 Levels of brain organization. The organization of the brain spans multiple levels of spatial scales. They reach from molecules, synapses and neurons (microscale), over local circuits of cortical layers and columns (mesoscale) to maps, systems and the whole brain (macroscale) (adapted from [9–11]).

But there are still blank spots on the map. Albeit its relatively high spatial resolution, classical fMRI examines the brain at a macroscale, i.e. at the level of relatively course whole brain networks to local maps on the order of 1 cm while other modalities, like optical imaging, can map single cell connectivity on the order of 50 μm[12]. However, since these invasive microscopic techniques can only be used in animal models, fMRI is currently the only modality that promises to probe activation non-invasively from multiple distinct brain areas while still providing a sufficiently high spatial resolution to elucidate local functions. More importantly, not only the presence but also the directionality of information flow can be revealed with fMRI opening up a new dimension in studying brain networks. This can be achieved by means of measuring at the mesoscale, i.e. at the level of cortical layers, to bridge the gap between the high-resolution, local microscale and the more global macroscale.

The neurons in gray matter (GM) are organized in layers[13], and these layers have different roles in signal transduction and reception[14,15]. The structure of the neocortex is typically six-layered as shown on the example of the primary visual cortex (V1) in Fig. 1.2A. This particular brain area exhibits a prominent layer IV which can be further subdivided into layers IVa-c. This layer is also referred to as the granular layer due to its high density of granular cells whereas layers above and below the granular layer are referred to as supra- and infragranular layers, respectively. While other regions differ from the six-layered organization of the neocortex, they also exhibit a laminar structure as exemplified by Fig. 1.2B showing the laminae of the cornu amonis (CA) region of the hippocampus.

Studying brain connectivity in cats on a laminar level, Douglas et al.[16] have pioneered the idea of a model for information flow: the "canonical microcircuit", i.e. a fundamental computational unit repeated, with some variations, throughout the neocortex (Fig. 1.2C). This model predicts that feed-

forward connections, i.e. connections afferent from brain areas earlier in the processing pipeline, terminate in the granular layer. Through a cascade of intrinsic connections, feedforward (or bottom-up) signals leave supragranular layers. On the other hand, feedback connections, i.e. signals from areas higher in the hierarchy, terminate in non-granular layers and avoid layer IV. This differentiation between bottom-up and top-down connections hold the key to understand the directionality of information flow.

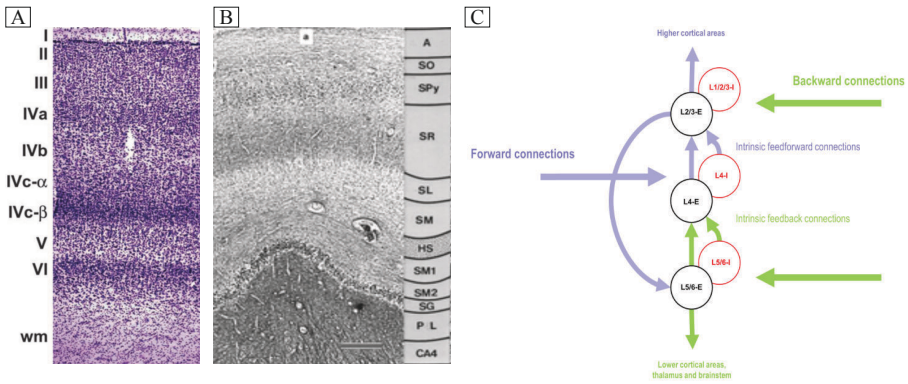

Fig. 1.2 Laminar structure of the brian. (A) Nissl stain of the macaque primary visual cortex (V1) showing the laminar cytoarchitecture. (B) Laminar organization of the hippocampal cornu amonis (CA) region. (C) Diagram of the canonical microcircuit showing intrinsic and extrinsic connections. Extrinsic feedforward signals terminate in the granular layer while feedback afferent connections terminate nongranularly (adapted from [15, 17, 18]).

As it will be explained later in Chapter 2 in more detail, fMRI cannot probe signals at the level of cortical layers directly. This is, on the one hand, due to the limited spatio-temporal resolution of fMRI. The resolution required to image single layers (on the order of 100 μm[19]) has a detrimental effect on image acquisition speed and image signal-to-noise ratio (SNR). Secondly, fMRI is intrinsically slow because it relies on changes in the magnetic properties of local vasculature which responds on the order of seconds with respect to neuronal activation occurring on a timescale of tens of milliseconds[20]. Al-

though this sluggishness can be circumvent by relying on spatial rather than temporal means to unreveal directionality as described above, one downside of fMRI being driven by neuronal vasculature is that its architecture differs from that of the neurons. In Fig. 1.3, stainings of the vasculature of macaque and human V1 (Fig. 1.3A,B) and human hippocampus (Fig. 1.3C) show that the density of microvessels, i.e. small capillaries and venules, closely matches the laminar cytoarchitecture (Fig. 1.2A). However, the vascular network also consists of macroscopic vessels showing a less consistent distribution. Depending on the specific MR contrast flavour used in the acquisition of fMRI data, the laminar fMRI response will be sensitive toward different parts of the vascular system.

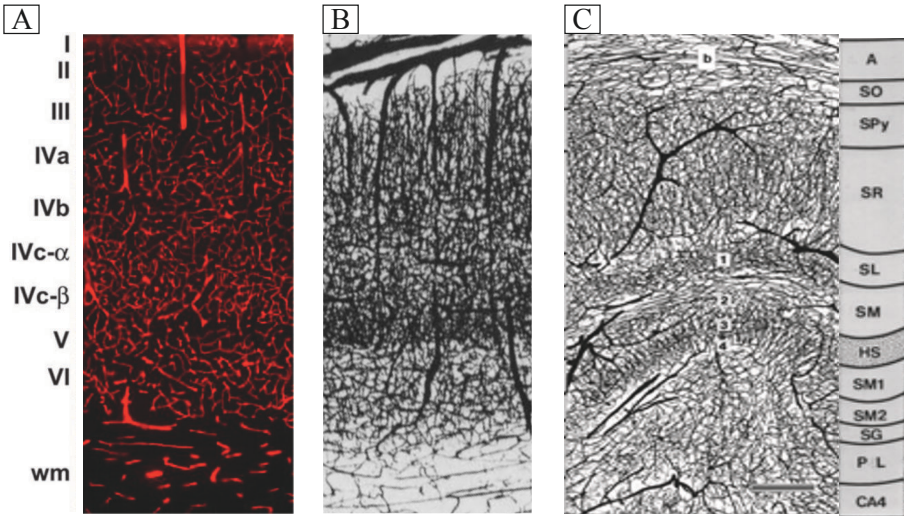

Fig. 1.3 Vascular structure. (A) Cy-3 anticollagen type IV stain of macaque V1 (same piece of cortex as shown in Fig. 1.2A). (B) Indian ink stain of human V1. (C) Ink stain of hippocampal CA region (same as in Fig. 1.2B). Labels of cell layers are shown for reference (adapted from [17, 18, 21]).

1.1 Objective of the thesis

The main purpose of this thesis is to explore possibilities to acquire clean laminar fMRI signals from multiple, widely separated areas of the human brain. To this end, two main problems need to be addressed:

(1) Obtaining high spatio-temporal resolution *and* large brain coverage at the same time.
(2) Achieving high *intrinsic* resolution irrespective of the scanner resolution.

The fact that many brain areas are organized in networks which are more widely distributed over the brain poses a challenge on the acquisition of sub-millimeter laminar data. Meeting the criteria of a large field-of-view (FOV), high spatial resolutions and acceptable scan times is not easily fulfilled as the image acquisition process in MRI is sequential rather than parallel. Therefore, the first objective of this thesis was to investigate an approach where, instead of imaging the entire FOV, only the areas of interest are excited using tailored 2D radiofrequency (RF) pulses. This zoomed multi-FOV imaging reduces the burden on the image acquisition and allows for higher acceleration of the scanning process ultimately leading to more time-efficient acquisitions of long-range connections at high spatial resolutions.

The second problem is to obtain a high intrinsic resolution, i.e. the resolution given by the MR contrast mechanism itself. As touched upon in the previous section, laminar fMRI measures signal changes associated with changes in the cortical vasculature. The most widely used gradient echo (GRE) blood oxygenation level dependent (BOLD) contrast is known to suffer from a sensitivity bias toward signal changes in and around large unspecific venous vessels. Therefore, even with a nominal high spatial resolution, the intrinsic blurring in GRE-BOLD prohibits the acquisition of spatially distinct laminar signals. Hence, the second objective of this thesis is to investigate and to improve the intrinsic resolution in laminar fMRI by using different contrast

mechanisms based on spin echoes (SE) and changes in cerebral blood volume (CBV).

To acquire laminar fRMI data of widely separated areas, two requirements must be fulfilled: First, the baseline SNR must be high to account for the loss in SNR due to the high spatial resolution. This can be achieved by using scanners operating at ultra-high fields (UHF), i.e. main magnetic field strengths of $B_0 \geq 7$ T, which provide the desired higher baseline SNR but also increased functional contrast-to-noise ratio (fCNR) and increased parallel imaging (PI) capabilities to speed up the acquisition of large image matrices. Despite these advantages, operating at UHF also comes with technical and physical obstacles. Due to the shorter radiofrequency (RF) wavelength at UHF, transmit field (B_1^+) inhomogeneities arise at the spatial scale of the human head which need to be compensated by introducing new RF hardware and excitation methods, i.e. parallel transmission (pTx). However, these technical efforts also open up opportunities for laminar fMRI. Parallel transmission can be used to accelerate the 2D RF pulses used for zoomed multi-FOV imaging increasing the temporal efficiency of laminar fMRI. The second requirement is the availability of large-FOV RF coils. Neuroscientists in e.g. the field of pain research, are interested in studying neuronal input as early as the upper spinal cord. This implies that the used RF coil needs to provide sufficient receive and transmit sensitivity over the entire brain, a prerequisite not easily fulfilled with standard RF hardware at 7 T.

These objectives led to the following structure of the thesis. After introducing the basics of (functional) MRI focusing on MR physics, MRI at 7 T and the biophysics of laminar fMRI in **Chapter 2**, **Chapter 3** describes a study performed at "conventional" spatial resolution to explore large FOV RF hardware and multi-channel pTx to acquire whole brain MRI with the focus on fMRI of the cerebellum and the motor cortex. These two widely separated areas robustly respond to the same functional stimulation although the for-

mer is typically not very well covered with conventional RF hardware at 7 T. **Chapter 4** directly builds up on the large FOV and pTx capability provided by the RF coil and describes prospects for the zoomed multi-FOV imaging approach to acquire widely separated brain areas at sub-millimeter resolution while simultaneously reducing SNR penalty through noise amplification in parallel imaging.

In **Chapter 5**, an extensive numerical and empirical study performed at 7 T is presented, investigating the capability of a T_2-prepared sequence to acquire laminar fMRI data with the SE-BOLD contrast. This contrast promises a higher sensitivity toward signal changes near the locus of neuronal activity, i.e. this contrast exhibits a higher intrinsic resolution compared to GRE-BOLD. The study characterizes the sequence' specificity as well as the influence of possible confounding contributions to the shape of T_2-weighted laminar fMRI profiles. As an alternative to BOLD, contrasts based on changes of CBV have been proposed to capitalize on observations that the CBV response is more confined to the network of small arterioles and capillaries. One approach to sensitize the MR signal toward changes in CBV is to selectively reduce GM signal by means of the magnetization transfer (MT) phenomenon. Exploiting the flexibility of the sequence used in Chapter 5, an MT-prepared sequence is designed in **Chapter 6**. Through numerical simulations, the MT-contrast is optimized for laminar fMRI at 7 T and used in experiments to investigate the influence of the MT-preparation on laminar data.

Finally, **Chapter 7** concludes the thesis with a summary and a general discussion of the main results, outlines prospects for further investigations and highlights the synergy between the methods presented in the previous chapters.

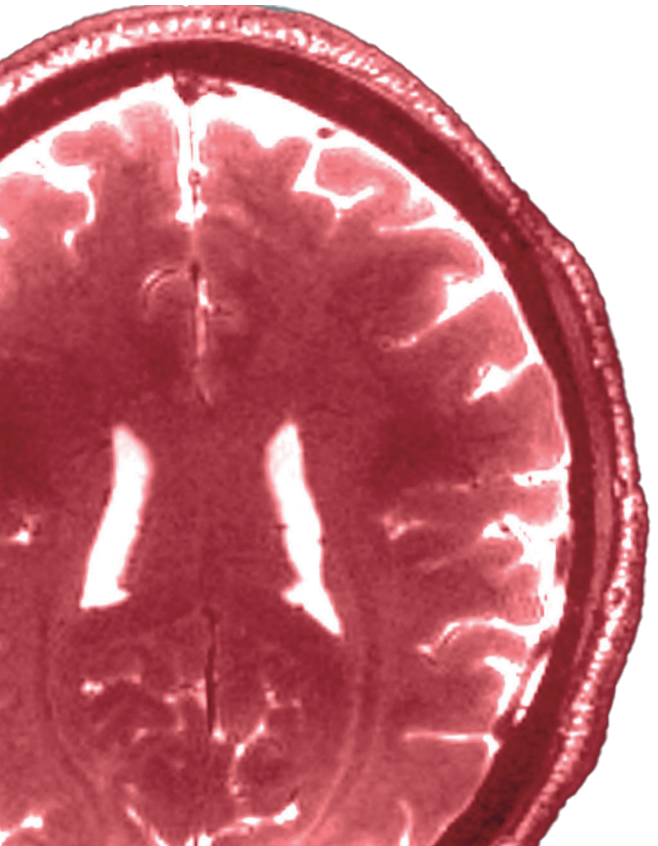

2

The basics of (f)MRI

This chapter gives an introduction to the basics of MRI[1]: nuclear magnetic resonance (NMR), using a quantum mechanical point of view before quickly moving over to the classic vector formalism. Having outlined the origin of the MR signal, the chapter describes the spatial encoding of the signal to form magnetic resonance images. The focus then shifts to MRI at UHF of 7 T before ending with the biophysics of fMRI.

2.1 NMR physics

2.1.1 Single protons

The effect of nuclear magnetic resonance arises from an intrinsic property of atomic nuclei: the spin, which is non-zero for a non-zero spin quantum number. In MRI, hydrogen (^{1}H) nuclei, i.e. protons with a spin quantum number of one half are the by far mostly used nuclei for imaging because of their high concentration in the body. A consequence of the spin is that these nuclei exhibit an intrinsic angular momentum $\hat{\mathbf{I}}$ corresponding to a magnetic moment $\hat{\boldsymbol{\mu}} = \gamma\hat{\mathbf{I}}$, with $\gamma = 42.576$ MHz/T being the gyromagnetic ratio of protons. The hat indicates operator notation, i.e. angular and magnetic moments are observable quantities.

In general, the state of a spin-one-half particle can be described with its eigenequation

$$|\Psi\rangle = c_\alpha |\alpha\rangle + c_\beta |\beta\rangle . \tag{2.1}$$

Eq. 2.1 describes the state of a proton as a superposition of all possible configurations of the two possible values of the spin quantum number (eigenvalues) $m = \pm 1/2$, labeled spin up (α) and spin down (β), respectively. $c_{\alpha,\beta}$ are

[1] If not stated otherwise, the literature used for this chapter is [22–24] and the classical textbooks of Haacke [25] and Bernstein [26].

complex coefficients. When placed into an external magnetic field of the form $\mathbf{B}_0 = \mathrm{B}_0\mathbf{e}_\mathrm{z}$, the longitudinal component of the magnetic moment interacts with the field. The energy associated to this field is discrete and can be obtained with the Hamiltonian (energy) operator

$$\hat{\mathrm{H}} = -\gamma \mathrm{B}_0 \hat{\mathrm{I}}_\mathrm{z}. \tag{2.2}$$

With $\hat{\mathrm{I}}_\mathrm{z} = \pm 1/2\,\hbar$, the energies are $\mathrm{E}_{\alpha,\beta} = \mp 1/2\gamma \mathrm{B}_0\hbar$, two quantised energy levels. Using the energy difference of the two states and Planck's energy-frequency relation yields the resonance frequency of the proton

$$\omega_0 = \gamma \mathrm{B}_0, \tag{2.3}$$

also referred to as the Larmor frequency.

2.1.2 Spin ensembles and macroscopic magnetization

Instead of investigating single protons (as it can be done with a Stern-Gerlach experiment), the majority of NMR applications (including MRI) measure the summed magnetization $\langle \mathbf{M} \rangle$ of a large number of particles (on the order of 10^{26} protons per sample).

$$\langle \mathbf{M} \rangle = \frac{1}{\mathrm{V}} \sum_{i=0}^{N-1} \langle \hat{\boldsymbol{\mu}} \rangle_i \tag{2.4}$$

with V being the volume and $\langle \hat{\boldsymbol{\mu}} \rangle$ being the expectation value of the magnetic moment. The state of this expectation value can be described using the formalism of a spin density operator. In thermal equilibrium, the spin density operator can be inferred from Boltzmann statistics yielding the bulk magnetization as the expectation value for the longitudinal component of the spin ensemble (assuming $\mathrm{k_b T} \gg \Delta \mathrm{E}$)

$$\mathbf{M}_0 = \frac{N}{V}\langle\hat{\boldsymbol{\mu}}_z\rangle = \rho_0\frac{\hbar^2\gamma^2 B_0}{4k_b T}\mathbf{e}_z. \tag{2.5}$$

Eq. 2.5 indicates that in thermal equilibrium, the bulk magnetization is parallel to axis of the main magnet field and scales linearly with its magnitude.

To describe the dynamics of the magnetization $\langle\mathbf{M}\rangle$ resulting from the spin ensemble, the Liouville differential equation needs to be solved. However, for most types of MR applications this is not necessary since in the regime of large ensembles of particles, quantum-mechanical expectations follow classical mechanics as stated by the Ehrenfest theorem. In fact, solving Liouville's equation results in equations of motion completely analogue to their pendant in classical mechanics. Therefore, it is sufficient to describe the dynamics of the spin system by means of a macroscopic magnetization vector ($\langle\mathbf{M}\rangle$ becomes now $\mathbf{M}$) obeying Newton's laws.

In the presence of an external magnetic field, a magnetic moment experiences a torque given by the cross-product $\mathbf{M}\times\mathbf{B}$. Following the rotation equivalent of Newton's second law (the time-dependent change of a system's total angular momentum $\mathbf{I}$ is equal to the torque applied to it) gives

$$\frac{d\mathbf{I}}{dt} = \mathbf{M}\times\mathbf{B}. \tag{2.6}$$

With the bulk magnetization being directly related to the total nuclear angular momentum (analogous to single protons) eq. 2.6 becomes

$$\frac{d\mathbf{M}}{dt} = \gamma\mathbf{M}\times\mathbf{B}. \tag{2.7}$$

This set of three ordinary differential equations describes the dynamics of the magnetization vector. Since the cross-product gives a new vector perpendicular to the plane spanned by both $\mathbf{M}$ and $\mathbf{B}$, the equations of motion describe a rotation of $\mathbf{M}$ about the axis of $\mathbf{B}$ called precession. The precession frequency

ω_0 is equal to the resonance frequency of the nucleus of interest, the Larmor frequency (eq. 2.3).

2.1.3 MR signal formation

At thermal equilibrium, the magnetization and the field vector point in the same direction resulting in the stationary magnetization $\mathbf{M} = \mathbf{M}_0$ (eq. 2.7 is zero) (Fig. 2.1A). Felix Bloch[27] proposed a fundamental technique to deflect the equilibrium magnetization by capitalizing on the magnetic resonance phenomenon, i.e. the effect that the motion of precession of single nuclei can be perturbed with magnetic fields oscillating at the Larmor frequency[28]. By applying an additional, weak, external field $\mathbf{B}_1$ ($\mathrm{B}_1 \ll \mathrm{B}_0$) such that the total external field becomes

$$\mathbf{B}_{\mathrm{ext}} = \begin{pmatrix} \mathrm{B}_1 \cos(\omega_0 t) \\ \mathrm{B}_1 \sin(\omega_0 t) \\ \mathrm{B}_0 \end{pmatrix}, \tag{2.8}$$

the magnetization can be tipped away from equilibrium and its transverse component $\mathbf{M}_{\mathrm{xy}} = \mathbf{M}_{\mathrm{x}} + i\mathbf{M}_{\mathrm{y}}$ starts to precess according to eq. 2.7 (Fig. 2.1B) with a mathematically negative direction of rotation if $\gamma > 0$ (clockwise). It is this component that leads to a measurable voltage induced in receiving coils according to Faraday's induction law.

To simplify the description of the effects the $\mathbf{B}_1$ field has on the magnetization vector, it is convenient to transform the coordinates of the stationary laboratory frame into ones that rotate about the axis of the main magnetic field $\mathbf{B}_0$. In such a coordinate system, eq. 2.7 becomes

$$\left(\frac{\mathrm{d}\mathbf{M}}{\mathrm{dt}}\right)' = \gamma \mathbf{M} \times \mathbf{B}_{\mathrm{eff}}. \tag{2.9}$$

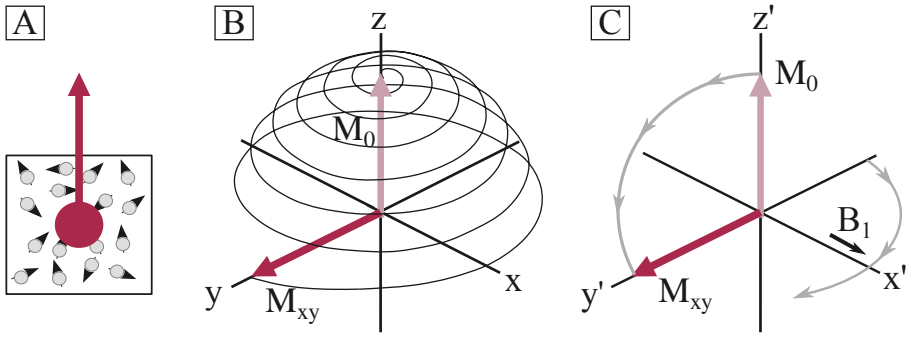

Fig. 2.1 Illustration of the vector formalism in the laboratory and the rotating frame of reference. (A) Bulk magnetization in thermal equilibrium emerging from a spin ensemble when being placed in an external magnetic field. (B) A short 90° RF pulse deflects the magnetization from its equilibrium position. In the laboratory frame, the trajectory of the magnetization forms a spiral. (C) In the rotating frame, the motion of the magnetization forms an arc with the RF-pulse appearing stationary.

The prime indicates a new coordinate system [x', y', z' = z]. In this system, the magnetization precesses about a new, effective magnetic field $\mathbf{B}_{\text{eff}}$ of the form

$$\mathbf{B}_{\text{eff}} = \mathbf{B} + \frac{\Delta\omega}{\gamma}\mathbf{e}_z, \tag{2.10}$$

where $\Delta\omega = \omega_0 - \omega$ and ω is the rotation frequency of the new coordinate system. If this frequency is chosen to match the Larmor frequency, the main magnetic field and the precession about it are effectively zero and $\mathbf{B}_{\text{eff}}$ reduces to $\mathbf{B}_1$. As the components of $\mathbf{B}_1$ rotate at the same frequency as the new frame of reference, they appear stationary, i.e. $\mathbf{B}_1 = [\mathrm{B}_1\ 0\ \ 0]^{\mathrm{T}}$. Within the rotating frame, the motion of the magnetization vector during the application of $\mathbf{B}_1$ can be understand as a tipping into the transverse plane (Fig. 2.1C). The angle by which $\mathbf{M}_{\text{xy}}$ is deflected from the z-axis is referred to as the flip angle (FA)

$$\alpha = \gamma \int_0^{\mathrm{T}} \mathrm{B}_1(\mathrm{t})\mathrm{dt}. \tag{2.11}$$

T is the time period during that $\mathbf{B}_1$ is applied. As the Larmor frequency is typically on the order of radiofrequencies, e.g. 297 MHz at 7 T, $\mathbf{B}_1$ is applied in form of short RF pulses with durations on the order of milliseconds.

2.1.4 Relaxation and contrast

In their seminal work, Bloch and colleagues[29] recognized that the measured signal was not permanent and introduced correction terms in eq. 2.7 to account for two phenomenological, independent processes called relaxation.

$\mathbf{T}_1$ relaxation

The first process, referred to as longitudinal or T_1 relaxation, describes the transition of the magnetization parallel to $\mathbf{B}_0$ toward its equilibrium (eq. 2.5) by means of energy transfer from the spin ensemble to its surroundings. This process is mediated by Brownian motion of the spins with respect to the medium they are embedded in for which reason this relaxation process is also referred to as thermal or spin-lattice relaxation. Quantitatively, the return of the longitudinal magnetization to its equilibrium is described by

$$\frac{dM_z}{dt} = \frac{(M_0 - M_z)}{T_1}, \tag{2.12}$$

with T_1 being the characteristic time constant of the relaxation process. Given an initial magnetization $\mathbf{M}_z(t = 0)$, the solution to eq. 2.12 is an exponential growth (right graph of Fig. 2.2) of the form

$$M_z(t) = M_z(t = 0)e^{-t/T_1} + M_0\left(1 - e^{-t/T_1}\right). \tag{2.13}$$

The transfer of energy depends on the random rotational motion of molecules, formally described by the correlation time τ_c, i.e. the time they require to rotate by one radian, and the Larmor frequency they are resonating at.

T_1 relaxation is most efficient if the tumbling rate, i.e. the frequency corresponding to the inverse of the correlation time, matches the Larmor frequency. Small, versatile molecules propagate through a medium more easily resulting in a broad range of possible frequencies. Only a fraction of this range matches the Larmor frequency, hence highly mobile molecules like hydrogen in free water exhibit a long T_1. In contrast, slow moving spins like those embedded in semisolid tissue have a relatively short T_1. At higher magnetic fields, the proportion of frequencies matching the Larmor frequency decreases as that frequency increases (eq. 2.3) resulting in a longer T_1 for protons in biological tissue. For mobile spins, a higher main magnetic field will not change T_1 considerably.

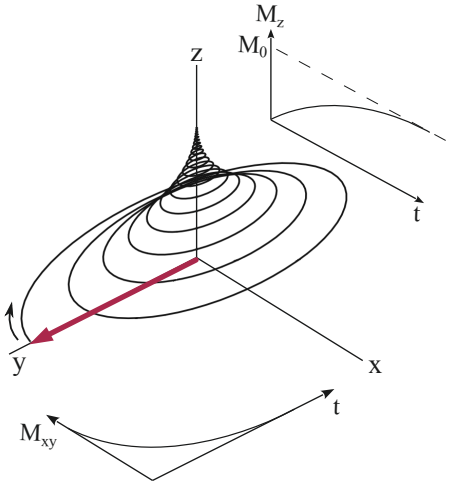

Fig. 2.2 Illustration of the relaxation processes. The magnetization vector after pulse application in the laboratory frame performs a rotational motion during relaxation. Projections of the individual components as functions of time in the rotating frame show the T_2 decay (lower graph) and the T_1 relaxation (upper graph) (adapted from [24]).

T_2 relaxation

The second relaxation process describes the loss of coherence between the individual magnetic moments in the spin ensemble forming the transverse magnetization. Therefore, this process is referred to as transverse or T_2 relaxation. Due to molecular motion, each individual spin exhibits a locally different magnetic field compared to the ensemble. The corresponding difference in Larmor frequencies results in a dephasing of the initially coherent spin system. Since this process is mediated by interactions between individual

spins, T_2 relaxation is also referred to as spin-spin relaxation. The loss of coherence manifests itself as a reduction of transverse magnetization, formally described by the differential equation

$$\frac{dM_{xy}}{dt} = -\frac{M_{xy}}{T_2}. \tag{2.14}$$

Using the concept of a flip angle (eq. 2.11), the transverse magnetization immediately after the RF pulse is $M_{xy}(t = 0) = M_0 sin(\alpha)$ and the solution to eq. 2.14 is given by an exponential decay (lower graph in Fig. 2.2) of the form

$$M_{xy}(t) = M_0 sin(\alpha) e^{-t/T_2}. \tag{2.15}$$

While the spin-spin interaction is of a stochastic nature, other systematic sources can lead to magnetic field perturbations and transverse relaxation. Any additional time-invariant perturbations of the magnetic field result in additional signal dephasing. However, because these perturbations are time independent, their effect can be reversed leading to the formation of signal echoes. Reasons for the additional perturbations can be gradients used for spatial encoding (see section 2.2) whose effect can be reversed by applying the same gradients with opposite polarity, leading to the formation of a gradient echo (GRE). Other sources can be main magnetic field imperfections or local susceptibility differences between adjacent structures. Because the effect of these susceptibility gradients on the signal is not know a priori, applying gradients to recall the signal is not possible. Instead, RF pulses are used to recover the signal in the form of spin echoes (SE, see sections 2.2.2.1 and 2.4.4.1 for further details). While susceptibility differences can cause imaging artifact at e.g. air/tissue interfaces, susceptibility differences caused by local changes of blood oxygenation play an important role in fMRI and will be treated in a later section.

Incorporating time independent field variations, the transverse relaxation is characterized by the time constant T_2^* according to

$$\frac{1}{T_2^*} = \frac{1}{T_2} + \frac{\gamma \Delta B_0}{2\pi} = \frac{1}{T_2} + \frac{1}{T_2'}, \tag{2.16}$$

with ΔB_0 as the additional, reversible field variations. Eq. 2.16 implies that $T_2^* \leq T_2$. At higher main magnetic fields, field variations caused by differences in susceptibility increase. Consequently, T_2^* relaxation times decrease at higher fields.

Albeit different magnetic field strengths should not affect T_2 relaxation in theory[30,31], real experiments always contain dynamic processes like diffusion and spin exchange between regions where magnetic field strengths differ. This can be captured by the "apparent" transverse relaxation time $T_2^{\dagger}$[32]

$$\frac{1}{T_2^{\dagger}} = \frac{1}{T_2} + \frac{1}{T_{2,\text{Diffusion}}} + \frac{1}{T_{2,\text{Exchange}}}. \tag{2.17}$$

The last two terms in this equation can be summarized as the dynamic dephasing regime, where diffusion and exchange reduce the net magnetization through additional phase dispersion of spins moving through regions of different susceptibility gradients. These inhomogeneities scale with the main magnetic field and cannot be refocused the same way as the time-invariant processes leading to additional decay as diffusion and exchange are random processes. As a result, the effectively measured T_2 shortens at higher main magnetic field strengths.

Because tissue types differ in their composition of differently mobile molecules, susceptibilities and exchange rates, they exhibit different relaxation times. Therefore, the contrast between tissues can be modulated by capitalizing on the different relaxation dynamics. Parameters with which contrast can be varied are repetition time (TR) defined as the time between two

RF excitation pulses in a pulse series and echo time (TE) defined as the time span between excitation and signal maximum, i.e. echo (see section 2.2.2).

In summary, the signal in an NMR experiment is generated by placing a sample in an external magnetic field resulting in a net magnetization vector parallel to it. With the application of short RF pulses whose frequency match the Larmor frequency of the nucleus of interest, the magnetization vector is tipped into the transverse plane where it starts precessing and consequently induces a measurable electromotive force in receiving coils. After the RF pulse, the equilibrium magnetization is restored and the dynamics of this process are characterized by the time constant T_1. Simultaneously, the transverse magnetization decays due to the loss of spin coherence characterized by T_2 and T_2^*. The full dynamics of the magnetization are described by the Bloch equations 2.7, 2.12 and 2.14, and contrast between different tissues can be obtained by means of signal weighting toward a specific relaxation process. However, next to contrasts due to differences in T_1 and T_2 are those reflecting physical and chemical interactions of protons between different tissue types. One is the contrast emerging from magnetization being transferred from free water protons to those bound to macromolecules and vice versa: a process called magnetization transfer which will be subject of the next section.

2.1.5 Magnetization transfer and the Bloch-McConnell equations[2]

The magnetization transfer (MT) contrast is generated by capitalizing on the exchange of magnetization between protons bound to semi-solid macromolecules and free water protons. The exchange is mediated by mainly two processes: chemical exchange, i.e. the physical exchange of water protons, and dipole-dipole cross relaxation. This refers to the interaction of

[2]This section is build upon the review articles of van Zijl et al. [33] and Sled [34].

neighboring magnetic moments through space, scaling with $1/r^3$ where r is the distance between the moments. Similar to T_1 relaxation, cross relaxation depends on the rotational mobility of the water protons and is extremely efficient in bound water. The majority of bound water is located within semi-solid tissue, e.g. white matter (WM) and GM while it has been shown that cerebrospinal fluid (CSF) exhibits no MT effect[35] and MT effects in blood are low due to a low concentration of macromolecules[36,37].

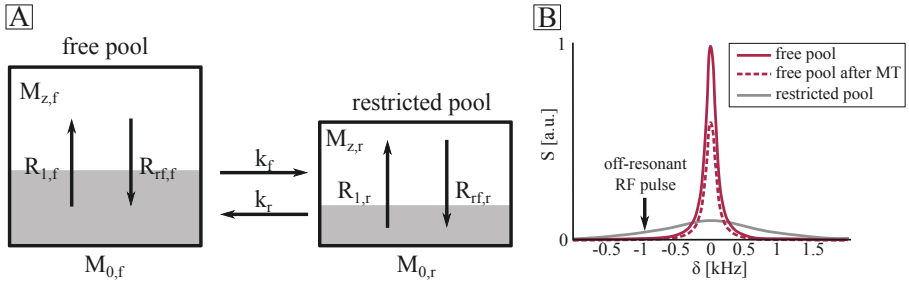

Fig. 2.3 Two pool MT model. (A) The free and the restricted (or bound) pool are modelled as separate reservoirs of longitudinal (non-shaded area) and saturated (shaded area) magnetization. The amount of saturation depends on the RF saturation rate R_{rf}. After RF application, the saturated magnetization relaxes back to equilibrium with its specific relaxation rate R_1. Simultaneously, magnetization is transferred between the two pools, described by the exchange rates k_f and k_r. (B) An RF pulse played out off-resonant can affect mainly the bound pool due to its broad absorption lineshape (width $\propto 1/T_2$) (gray curve). In contrast, the free pool's lineshape is considerably narrow (solid red line). With MT, the saturated magnetization of the bound pool exchanges with the unaffected magnetization of the free pool, hence reducing its magnitude (dashed red line) (adapted from [38–40]).

The simplest model of MT divides the tissue into two pools, a free water and a restricted, or bound water pool, which exchange magnetization between each other[35,41–43] (Fig. 2.3A). The bound pool exhibits a very short T_2 (on the order of 10 μs), too short to be directly detectable with conventional MRI. However, it is still possible to detect the bound pool indirectly by means of partially saturating its magnetization selectively. Via MT, the saturated magnetization is transferred to the free pool and becomes detectable. Saturation

can be performed using strong off-resonant RF pulses[3], i.e. fields not oscillating at the Larmor frequency but several hundred Hz away. This is possible because the spectral width of Larmor frequencies scales with the inverse of the transverse relaxation time, hence the bound pool exhibits a very broad spectral lineshape (width on the order of 10 kHz) while the lineshape of the free pool is considerably narrow (Fig. 2.3B). Therefore, an off-resonance RF pulse affects mainly the bound pool.

The temporal dynamics of transferable magnetization can be described using the Bloch-McConnell differential equations[41,47]:

$$\frac{dM_{x,f}}{dt} = -R_{2,f}M_{x,f} - 2\pi\delta M_{y,f} + \omega_1 sin(\phi) M_{z,f} \tag{2.18}$$

$$\frac{dM_{y,f}}{dt} = -R_{2,f}M_{y,f} + 2\pi\delta M_{x,f} - \omega_1 sin(\phi) M_{z,f} \tag{2.19}$$

$$\begin{aligned}\frac{dM_{z,f}}{dt} =& R_{1,f}(M_{0,f} - M_{z,f}) - k_f M_{z,f} + k_r M_{z,r} \\ & - \omega_1 sin(\phi) M_{x,f} + \omega_1 cos(\phi) M_{y,f}\end{aligned} \tag{2.20}$$

$$\frac{dM_{z,r}}{dt} = R_{1,r}(M_{0,r} - M_{z,r}) + k_f M_{z,f} - k_r M_{z,r} - W M_{z,r}. \tag{2.21}$$

Here, the subscripts f and r refer to the free and restricted, or bound pool, respectively. Subscripts x, y, and z denote the spatial components of the magnetization vector $\mathbf{M}$. R_2 ($R_2 = 1/T_2$) and R_1 are the transverse and longitudinal relaxation rates, respectively. δ is the off-resonance frequency of the RF pulses used to saturate the bound pool. The intensity of the RF pulse is given by the corresponding angular frequency $\omega_1 = \gamma|B_1|$, with B_1 being the complex RF pulse with phase ϕ. Because the transverse magnetization of the restricted pool decays rapidly, it is not shown as an explicit equation.

[3]For the sake of completeness, another technique based on on-resonant binomial pulses is mentioned here but a detailed description is beyond the scope of this thesis and can be found in [44–46].

As $T_{1,r}$ is not of a similarly large order as $T_{1,f}$[48], the longitudinal component $M_{z,r}$ experiences a saturation captured by equation 2.21. The process of transfer of this saturated magnetization from the bound to the free pool can be quantitatively described with the exchange rate k_r while the reverse transfer is described by k_f. The ratio of these rates reflects the ratio of the pool size, i.e. $k_r/k_f = M_{0,r}/M_{0,f}$ which, by definition, is equal to the pool size ratio F. The rate of bound pool saturation is given by $W = \pi\omega_1^2 G$ where ω_1^2 is a measure of the RF power and G describes the absorption lineshape of the restricted pool. For biological tissue, the lineshape is modelled as a Super-Lorentzian (gray lineshape in Fig. 2.3B) while the lineshape of the free pool is represented best by a Lorentzian[35] (red lines in Fig. 2.3B).

Since semi-solid tissue consists of both free and bound water, the classically observed longitudinal relaxation T_1 (= $T_{1,obs}$) is in fact a weighted combination of the free and bound pool relaxation times[41]. The relaxation rates are related to one another via

$$R_{1,f} = R_{1,obs} - \frac{k_f\,(R_{1,r} - R_{1,obs})}{R_{1,r} - R_{1,obs} + \frac{k_f}{F}}. \tag{2.22}$$

The MT effect provides a unique contrast between tissues depending on the concentration of bound water. Hence, semi-solid tissue can be selectively attenuated while liquid compartments like blood are to large extent unaffected: a contrast that will be exploited in chapter 6.

2.2 From signals to images

So far, signal generation and dynamics have been addressed. To perform imaging, these signals need to be assigned to unique spatial positions which can be achieved with a set of orthogonal gradient coils. Recalling that the precession frequency of the magnetization is directly related to the external

field (eq. 2.3), a linear modulation of the z-component of the external field as a function of space results in spatially dependent frequencies

$$\omega(\mathbf{r}) = \gamma(\mathrm{B}_0 + \mathbf{rG}). \tag{2.23}$$

r and **G** are the position and gradient vector with $\mathrm{G}_{\mathrm{x,y,z}} = \mathrm{dB}_\mathrm{z}/\mathrm{d(x,y,z)}$.

To encode the spatial information along one dimension, one gradient is superimposed on the main magnetic field. According to eq. 2.23, the linear varying field results in a varying Larmor frequency along the direction of the gradient. Conventionally, this *frequency encoding* gradient is applied along the x-axis while the signal is being recorded using analog-to-digital converter (ADC). Therefore, the gradient is also referred to as a *readout* gradient. During gradient application, the spin system accumulates a phase. Hence, the signal measured at time t is a superposition of all the transverse magnetization in the object weighted by a spatially dependent phase term

$$\begin{aligned} \mathrm{S(t)} &= \int_\mathrm{x} \mathbf{M}_\mathrm{xy}(\mathrm{x,t}) e^{-i\phi(\mathrm{x})} \mathrm{dx} \\ &= \int_\mathrm{x} \mathbf{M}_\mathrm{xy}(\mathrm{x,t}) e^{-i\gamma \int_0^\mathrm{t} \mathrm{G_x(t')xdt'}} \mathrm{dx}, \end{aligned} \tag{2.24}$$

with $\mathbf{M}_\mathrm{xy}$ being proportional to the spin density $\rho(\mathrm{x})$ along the x-dimension. Eq. 2.24 represents the Fourier transform of $\mathbf{M}_\mathrm{xy}$ sampled in the spatial-frequency domain. Applying the inverse Fourier transform to eq. 2.24 gives the spatial distribution of the magnetization along the x-axis in the spatial-position domain.

Obtaining unique information along the dimension orthogonal to the readout axis (e.g. the y-axis) cannot be achieved by means of simultaneous frequency encoding. The two gradients would add up leading to an encoding along a diagonal in the x-y-plane. This can be resolved by applying the

gradient before the readout for a short period of time. Similar to the frequency encoding gradient, a *phase encoding* gradient causes the spins to exhibit spatially dependent precession frequencies. After gradient application, the spin ensembles return to their initial Larmor frequency ω_0 while retaining the phase accrued during the gradient. Because phase is defined on the interval $[0, 2\pi)$, the phase information of a single encoding step is not unique. Hence, the acquisition, i.e. excitation, followed by phase encoding and readout, has to be repeated with different phase encodes which number matches that of the spatial positions to be discerned.

The dimension perpendicular to the x-y-plane can be encoded by means of *selective excitation*. During RF pulse application, a slice selection gradient is applied, altering the Larmor frequency as a function of z. Within a slice, the frequency range lies in the interval $[\omega_0 - \Delta\omega/2, \omega_0 + \Delta\omega/2]$. The slice selection gradient converts this frequency band into a band of spatial locations $[z - \Delta z/2, z + \Delta z/2]$ with Δz being the slice thickness. The relationship between $\Delta\omega$ and Δz is given by

$$\Delta z = \frac{\Delta\omega}{\gamma G_z} = \frac{2\pi\Delta f}{\gamma G_z}. \tag{2.25}$$

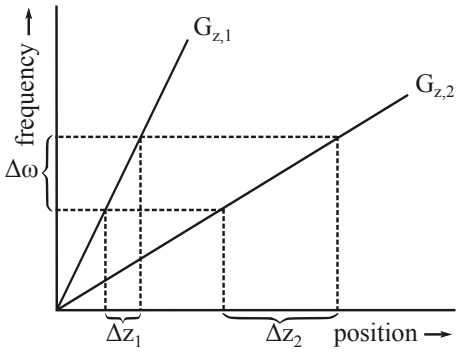

Fig. 2.4 Slice selection with gradients. The slice selecting gradient varies the Larmor frequency of the spins as a function of position along z. A pulse of a certain bandwidth $\Delta\omega$ excites spins within that frequency range which is converted to thinner or thicker slices if a relatively strong ($G_{z,1}$) or weak gradient ($G_{z,2}$) is applied (adapted from [26]).

To selectively excite the spins within the frequency band $\Delta\omega$, the RF pulse is designed such that its bandwidth is limited to that frequency spectrum.

That implies that in frequency domain, the shape of the slice profile is that of a rectangular window or mathematically, that of a rect function.

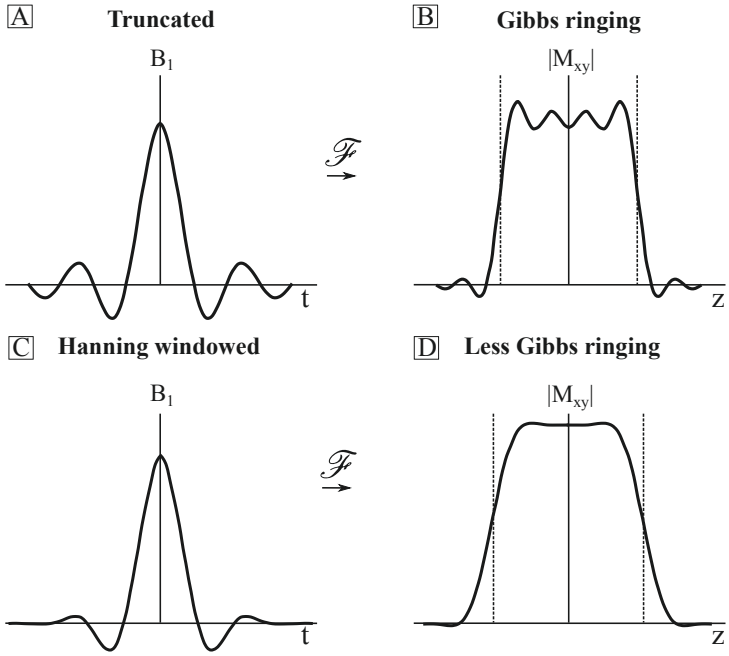

Fig. 2.5 RF pulse and resulting slice profile. (A) A truncated sinc pulse needed for practical imaging results in a slice profile with strong Gibbs ringing due to being convolved with a sinc function after Fourier transform (B). (C) Apodizing the pulse with a Hanning window results in a spatially smoother profile but a broad transition band, i.e. a less steep edge (D). A higher bandwidth increases the sharpness at the price of higher SAR (adapted from [25]).

Under the assumption of small flip angles, the slice profile in frequency domain obtained with an RF pulse is represented by the Fourier transform of that pulse. In other words, for flip angles $\leq 30°$, the Fourier transform of the rect function gives the time dependent RF pulse shape, i.e. a sinc pulse. For a perfectly sharp rect function an infinitely long sinc pulse would be necessary which is physically impossible. Therefore, the pulse must be truncated.

In frequency space, truncation, i.e. multiplication with a rectangular window, is a convolution with the Fourier transform of that window which is again a sinc. Therefore, truncation results in fluctuations of the slice profile, known as Gibbs ringing (Fig. 2.5A,B). To reduce these effects, the truncated pulse is windowed by an apodizing fuction, e.g. a Hanning window, which acts as a smoothing filter by tapering the RF amplitude at the end and the beginning of the RF pulse (Fig. 2.5C,D). This, however, has a detrimental effect on the sharpness of the slice profile. The profile can be improved by increasing the bandwidth of the pulse together with the gradient strength to maintain the same slice thickness. A higher bandwidth means increased RF power per unit time resulting in a higher specific absorption rate (SAR) which is a practical obstacle especially at UHF (see section 2.3.2).

Because application of the slice selection gradient results in a phase dispersion across the slice profile (identical to the effect the phase encoding gradient has) the phase needs to be negated to avoid unwanted signal loss. To this end, a rephasing gradient is applied with opposite polarity, typically at the end of the slice selecting gradient. If the slice selecting gradient is symmetric about the RF pulse, the gradient moment, i.e. the area under the gradient, is half the moment of the slice selecting gradient.

It is not strictly necessary to excite individual slices. As phase encoding is not restricted to a single dimension only, the third dimension can be phase encoded as well. To this end, instead of a thin slice, a thicker slab is excited and the z-direction is encoded similarly to the primary phase encoding direction. The signal equation for this case of *3D imaging* is similar to eq. 2.24, extended to three dimension:

$$\mathrm{S(t)} = \int_{\mathrm{V}} \mathbf{M}_{\mathrm{xy}}(\mathbf{r},\mathrm{t}) e^{-i\gamma \int_0^{\mathrm{t}} \mathbf{G}_{(\mathrm{t'})} \cdot \mathbf{r} \mathrm{dt'}} \mathrm{d}\mathbf{r}. \tag{2.26}$$

2.2.1 The k-space formalism

To better understand the spatial-frequency trajectory assigned by the gradient system, it is convenient to describe the spatial encoding in the frequency domain by means of spatial wave numbers: the **k**-vector. Defining the **k**-vector as

$$\mathbf{k}(\mathrm{t}) = \frac{\gamma}{2\pi} \int_0^{\mathrm{t}} \mathbf{G}(\mathrm{t'})\mathrm{dt'} \tag{2.27}$$

allows to interpret the signal acquisition as successively sampling a linear vector space, the k-space. In its essence, the k-space formalism describes the amount of spatio-temporal dephasing of the spin system due to the gradients, e.g. **k** = 0 means no dephasing due to gradients or for example just after excitation. Given the ordering of RF pulses and gradients, i.e. the pulse sequence, the timing of the acquisition of echoes and low or high spatial frequencies can be followed. This can be important in e.g. magnetization preparation sequences where the longitudinal magnetization is manipulated to induce a certain contrast before image acquisition is performed. As the magnetization relaxes back to equilibrium over time and low frequencies encode the image contrast (as opposed to high spatial frequencies which determine the details in an image) the time point of acquiring the center of k-space, i.e. small wave numbers or low frequencies, must be as close as possible to the time of preparation. This is realized in center-out encoding schemes where the k-space center is measured first. Variants of the center-out encoding scheme are used in chapters 5 and 6.

2.2.2 Discrete sampling of k-space: The pulse sequence

Having introduced the concept of k-space, the exact trajectory of how this space is filled is determined by the pulse sequence. MR sequences are typi-

cally shown as diagrams containing the RF pulse and the encoding gradients of one repetition loop. The majority of sequences can be categorized into two families, differentiated by the way the echo (section 2.1.4) is generated: Spin echo and gradient echo sequences.

2.2.2.1 Spin echo sequence

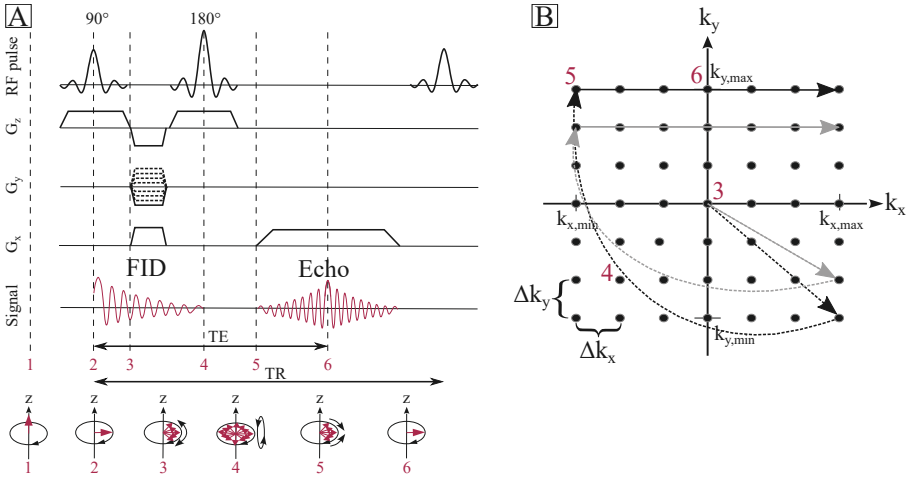

Fig. 2.6 Spin echo sequence. (A) Schematic diagram of a SE sequence. The signal maximum, i.e. echo, is measured at time TE and the sequence is repeated every TR with varying phase encoding gradient strength (dashed gradient lines). The time evolution of the spin ensemble at selected time points is shown below the diagram. (B) The corresponding k-space trajectory for the first (black) and second (gray) repetition with different PE encoding steps. The time points in A are marked (adapted from [49]).

A schematic of a SE sequence is shown in Fig. 2.6A. Starting from bulk magnetization M_0 (1), a 90° RF excitation pulse is applied during slice selection, creating transverse magnetization (2). The initially coherent magnetization starts to relax with T_2^* resulting in a signal called free induction decay (FID). The essential part in the SE sequence is that the phase dispersion is negated

using a 180° pulse[50] (4). This refocuses time-invariant inhomogeneities and an echo is formed at a time point after the 180° equal to the time difference between the center of the excitation and the refocusing pulse. The amplitude of the echo decays with T_2. The signal readout is timed such that the echo is formed in the center of k-space (6). The timing and strength of the gradients in the sequence yields the k-space sampling trajectory as shown in Fig. 2.6B. No in-plane encoding has been performed after excitation and slice selection, hence the trajectory starts at $k_y = k_z = 0$ (3). The first readout gradient in the sequence dephases the spins and, together with a negative phase encoding gradient $-G_{y,max}$, defines the k-space coordinate $[k_{x,max}\ k_{y,min}]$. The refoccusing pulse inverts the direction of dephasing between the spins resulting the k-space position to flip from $k_{x,max}$ to $k_{x,min}$ (5). During the readout gradient, which has twice the moment of the first dephasing gradient, the signal is sampled while k-space is traversed from $k_{x,min}$ to $k_{x,max}$.

Because in practice, k-space can only be sampled at discrete steps within a finite interval, the signal equation 2.26 needs to be approximated with finite sums yielding relationships between grid points in k-space and physical space:

$$\begin{array}{llll} x = u\Delta x & \Delta x = \dfrac{FOV_x}{M} & y = m\Delta y & \Delta y = \dfrac{FOV_y}{N} \\ k_x = v\Delta k_x & \Delta k_x = \dfrac{1}{FOV_x} & k_y = n\Delta k_y & \Delta k_y = \dfrac{1}{FOV_y}. \end{array}$$

Here, $FOV_{x,y}$ is the field-of-view in the x- and y-dimension, respectively, and is equal to the inverse of the sampling interval in k-space (Fig. 2.6B). The integer pairs u,v and m,n count the points in both reciprocal grids for the x- (k_x) and y- (k_y) coordinates, respectively. M an N are the maximum numbers of sampled grid points forming an M × N matrix. Dealing with trapezoidal gradients, eq. 2.27 can be discretized for the readout (RO) and phase encoding (PE) gradient as

$$\Delta k_x = \frac{\gamma}{2\pi} G_x \Delta t_{RO} \tag{2.28}$$

$$\Delta k_y = \frac{\gamma}{2\pi} \Delta G_y t_{PO}. \tag{2.29}$$

In the case of the readout, the descriptive parameter is the receiver full bandwidth $2\Delta\nu$ corresponding to the inverse of the dwell time Δt_{RO} which is defined as the interval between two adjacent digitized samples. In phase encoding, the parameter determining the step size is the gradient increment ΔG_y as it is more practical to vary than changing the duration of the gradient to avoid time inconsistencies between k-space center and periphery.

An important relationship between FOV and k-space sampling increment can be derived form the sampling process. Mathematically, it can be described by multiplying a continuous signal S_{cont} with a dirac comb and a rect function to take finite sampling ranges into account. This leads to a discretized signal[51]

$$S(k_x)_{dis} = S(k_x)_{cont} \cdot \Delta k_x \sum_{v=-\infty}^{\infty} \delta\left(k_x - v\Delta k_x\right) \cdot rect\left(\frac{k_x}{k_{x,max}}\right). \tag{2.30}$$

In case of symmetric boundaries, i.e. $k_{x,min} = -k_{x,max}$, inverse FT results in the spin distribution being convoluted with a comb and a sinc function

$$\rho(x)_{dis} = \rho(x)_{cont} \circledast \sum_{u=-\infty}^{\infty} \delta\left(x - \frac{u}{\Delta k_x}\right) \circledast \frac{1}{\pi\Delta x} sinc\left(\frac{x}{\pi\Delta x}\right). \tag{2.31}$$

Eq. 2.31 states that each data point in image space is copied with a periodicity of $1/\Delta k_x$ and is convolved with a sinc function which gives rise to the shape of the sampling point-spread function (PSF). The relationship between the sampling distance in k-space and the FOV is given by

$$\Delta k_x = \frac{1}{FOV_x}. \tag{2.32}$$

Choosing a sampling distance corresponding to a FOV larger than the object to be imaged violates the Nyquist-Shannon sampling theorem[52] which states that the rate with which a continuous signal is sampled must be at least twice the maximum frequency which needs to be resolved. Failing to meet this criterion results in the indistinguishability of frequencies, an artifact referred to as aliasing, i.e. signals outside the FOV will fold in. This artifact can be resolved using parallel imaging (PI) techniques (see section 2.2.3).

The RO direction was chosen in this example but the same description holds for the PE direction. By combining eq. 2.32 with eq. 2.28 and 2.29, the requirements on the encoding gradients can be calculated as

$$G_x = \frac{2\pi}{\gamma \Delta t_{RO} FOV_x} \tag{2.33}$$

$$\Delta G_y = \frac{2\pi}{\gamma t_{PE} FOV_y}. \tag{2.34}$$

In case of sequences where multiple k-space lines are acquired in a single excitation, eq. 2.31 above needs to be expanded by the Fourier transform of the transverse decay, which is a Lorentzian. Hence, next to the sampling PSF, a point is blurred due to the signal decay during readout. Keeping the sampling time below $\pi T_2^*/\sqrt{3}$ results in a Lorentzian full-width-half-maximum (FWHM) of less than the width of a pixel, hence no additional blurring.

2.2.2.2 Gradient echo sequence

The second family consists of gradient echo type sequences. The GRE sequence (Fig. 2.7A) is in its essence identical to its SE pendant with the important exception that the echo is generated by first prephasing the transverse magnetization using a frequency encoding gradient with opposite polarity followed by subsequent rephasing of the transverse magnetization. Fig. 2.7 illustrates that GRE sequences can generally be faster than SE sequences due to the absence of an 180° pulse. However, regarding a TR shorter than T_2^*,

two properties of the signal evolution must be considered: First, after readout, transverse magnetization is not completely dephased yet resulting in contamination of subsequent repetitions if not accounted for. One approach is to dephase all remaining M_{xy} prior to the excitation pulse by means of gradient and/or RF spoiling.

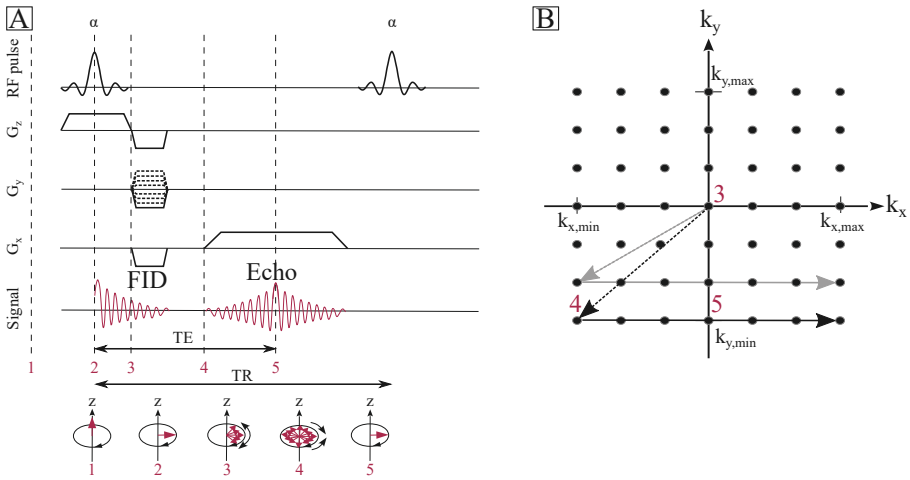

Fig. 2.7 Gradient echo sequence. (A) Schematic diagram of a GRE sequence. The echo is generated by rephasing previously dephased magnetization with gradients of opposite polarity. The evolution of the spin ensemble at selected time points is shown below the diagram. (B) The corresponding k-space trajectory for the first (black) and second (gray) PE step (adapted from [49]).

In the latter method, an additional phase, varying from shot to shot in a predefined manner, is applied to the RF pulse[53]. The second aspect is that because TR is also shorter than T_1, the longitudinal magnetization M_z will not fully relax back to equilibrium before the next excitation pulse. Instead, a steady state magnetization will emerge after a number of repetitions. Given T_1, TR and the flip angle α, the steady state magnetization in a spoiled GRE sequence is

$$M_z = \frac{M_0\left(1 - e^{-TR/T_1}\right)}{\left(1 - cos\left(\alpha\right)e^{-TR/T_1}\right)}. \tag{2.35}$$

The flip angle which maximizes the transverse magnetization is given by the Ernst angle

$$\alpha_{\text{Ernst}} = arccos\left(e^{-\text{TR}/\text{T}_1}\right) \tag{2.36}$$

and is smaller than 90°. The sequence which uses small α and short TR is called the Fast Low Angle SHot (FLASH) sequence[54].

2.2.2.3 Echo-planar imaging sequence

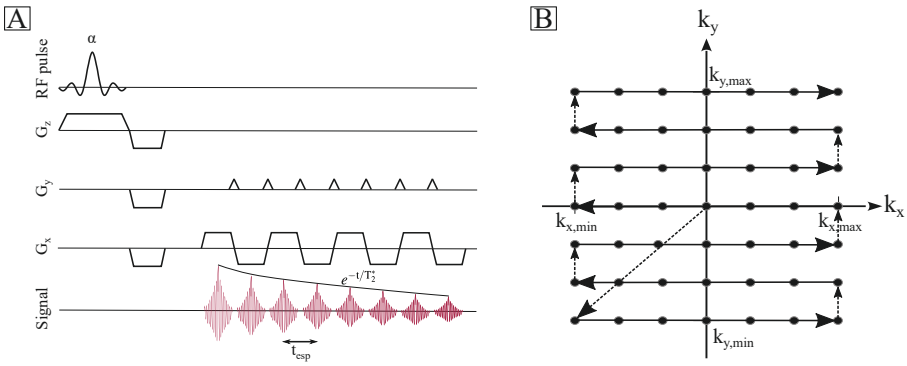

Fig. 2.8 Echo-planar imaging sequence. (A) Schematic diagram of an EPI sequence. A train of oscillating readout gradients samples the refocused echoes which decay with T_2^* along the readout. Phase encoding is achieved with small gradient blips between successive echoes. (B) K-space is traversed in a back-and-forth manner (adapted from [49]).

Although the FLASH sequence has come a long way in accelerating image acquisition relative to a classical GRE sequence, the Echo-Planar Imaging (EPI)[55] sequence shows an even higher time efficiency. This can be achieved by sampling the entire k-space with only a few excitations, i.e. shots. The sequence diagram of the single shot EPI variant is illustrated in Fig. 2.8A with corresponding k-space trajectory in Fig. 2.8B. Followed by the excitation of longitudinal magnetization (typically already in a steady state) with a flip angle α, phase and readout prephasing gradients set the start of the trajectory

to [$k_{x,min}$, $k_{y,min}$]. A series of fast oscillating readout gradients create an echo train decaying with T_2^* along the readout. The time between two successive echoes is referred to as the echo spacing t_{esp}. Phase encoding is realized by applying short gradient blips between the readout gradients of opposite polarity. The resulting k-space trajectory forms a "back-and-forth" pattern and after acquisition, odd lines have the be time-reversed to match the acquisition order of the even lines prior to image reconstruction. To further improve time efficiency, the echoes can be sampled during the ramping of the gradients. As this leads to non-equidistant sampling of k-space points, they need to be interpolated to a Cartesian grid, a processed known as re-gridding.

EPI is a very attractive sequence to measure dynamic processes like brain function as it can acquire a whole brain image in a few seconds with a spatial resolution on the order of a millimeter. In addition, the EPI readout can also be combined with various contrast preparation modules to introduce T_2-weighting as done in SE-EPI or to sensitize the signal toward changes in perfusion as done in e.g. Arterial Spin Labelling (ASL) or to changes in CBV as done in e.g. a technique called VAscular Space Occupancy (VASO) (see also section 2.4.4).

However, the superior temporal efficiency comes at a price of several artifacts, degrading image quality. Due to the high digitization rate of the readout, the T_2^* decay along the echo train plays only a role in the phase encoding dimension. In other words, the acquisition bandwidth along the PE direction is much smaller than along readout. Hence, the T_2^* decay is essentially mapped in this direction and because the criterion of no relaxation induced blurring ($T_{acq} \leq \pi T_2^*$) is generally not fulfilled, the PSF is broadened, hence images are more blurred in the PE direction.

The EPI sequence is more prone to artifacts related to B_0 inhomogeneities, one being geometric distortions (Fig. 2.9), i.e. spatial signal mismapping. Describing the inhomogeneity as a spatially varying additional

field caused by macroscopic susceptibility gradients $\Delta\mathbf{B}(\mathbf{r}) = \mathbf{G}_S(\mathbf{r}) \cdot \mathbf{r}$ and recalling that spatial encoding requires magnetic field gradients, signals are mis-localized in the presence of any additional (and typically unknown) field variation. As the gradient moment along PE accumulates in an EPI sequence, sampling errors do so as well which results in distortions to be the strongest along the PE direction. If the inhomogeneity gradient opposes the PE gradient, images are compressed whereas images are stretched if the field gradient enforces the PE gradient. The strength of these distortions is determined by the effective bandwidth. Along the PE direction, the bandwidth can be defined as the inverse of the echo spacing t_{esp} since this time span is the effective sampling time. Hence, reducing the echo spacing results in less distorted images. Although not as severe as distortions along PE, distortions can also occur along the readout axis, especially for low-bandwidth readouts. As inhomogeneity gradients scale with the main magnetic field, distortions are more severe at UHF.

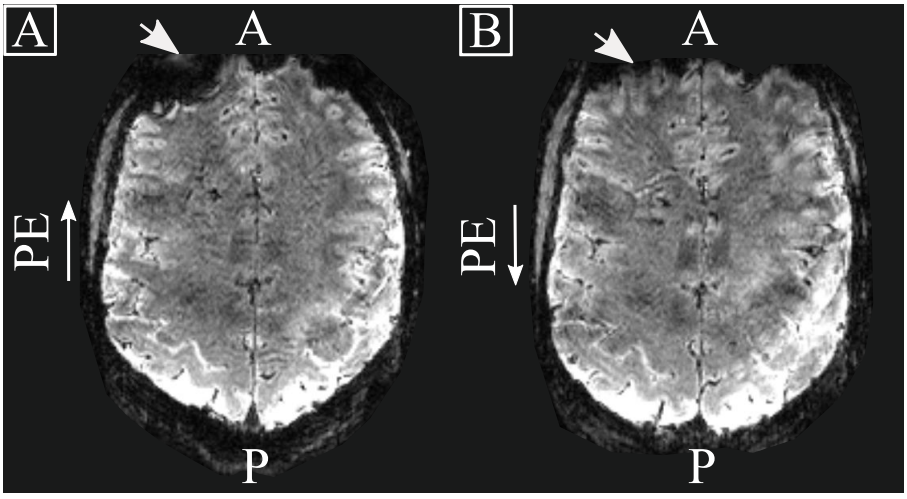

Fig. 2.9 Distortions in EPI. (A) Example transverse view of an EPI image acquired with a posterior-anterior PE direction. A region of high distortion close to the frontal sinus is highlighted by a white arrow. (B) Same image acquired with opposed PE encoding direction. Note the change in the direction of the distortion.

Macroscopic magnetic field variations are most pronounced near regions with high susceptibility changes, e.g. air cavities like the anterior skull base, the petrous bone or ear canals. Next to in-plane mis-localization, the z-component of the field gradient ($G_{S,z}$) leads to through-slice dephasing, i.e. signal dropouts in GRE-EPI sequences using an axial slice orientation. Spin echo sequences, including SE-EPI, do not exhibit this kind of artifact since 180° pulses refocus phase dispersion through the slice. Assuming perfect slice selection, the signal in a GRE-EPI acquisition can be expressed by[56]

$$S(\mathbf{r},t) = M_{xy}(\mathbf{r},0)\, e^{-t/T_2^*} sinc\left(\frac{\gamma}{2} G_{S,z} \Delta z TE\right). \tag{2.37}$$

Eq. 2.37 indicates that transverse relaxation of the signal is modulated by a sinc function depending on the strength of the inhomogeneity, the slice thickness Δz and the echo time. It is this modulation that causes signal attenuation and signal voids near areas of strong $G_{S,z}$. Reducing TE or slice thickness reduces signal drop-outs while the former is sometimes not practical due to other requirements on TE (see section 2.4.3). When choosing thinner slices, the amount of off-resonances present in a slice for a given through-slice gradient will be less and the sinc modulation reduced.

Typical for EPI sequences are aliasing artifacts, i.e. a ghost, shifted by $FOV/2$ with respect to the image (Fig. 2.10A). The ghost is also referred to as $N/2$ or Nyquist ghost. It arises when readout gradients of alternating polarity are used and can be caused by B_0 inhomogeneities, acoustic resonances of the gradient system, gradient heating, gradient amplifier/ADC delay or eddy currents. The latter can be considered to be the main source of Nyquist ghosts. As typically high gradient slew and switching rates as well as high gradient amplitudes are required in EPI, the induction of eddy currents in the gradient set is provoked. The currents result in a degradation in gradient switching efficiency and precision.

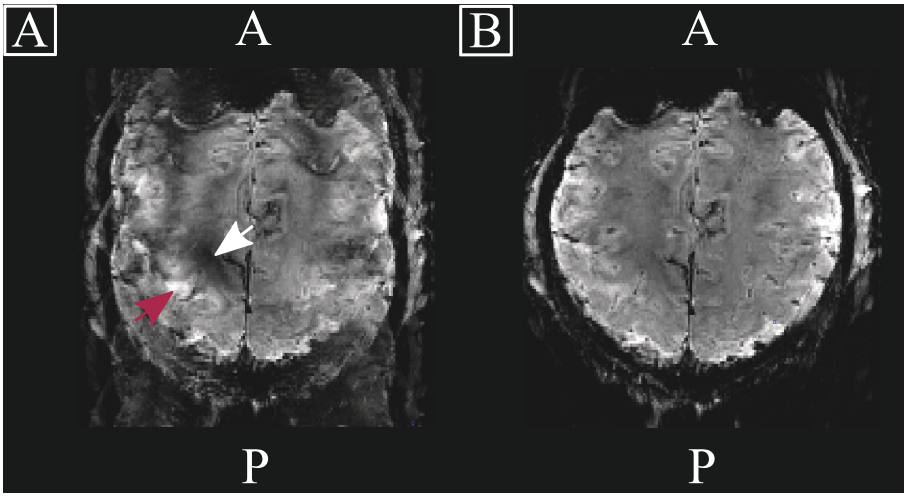

Fig. 2.10 Nyquist ghosts in EPI. (A) Example of a Nyquist ghost shifted by FOV/2 with respect to the true image. Note the phase artifacts, i.e. constructive (red arrow) and destructive (white arrow) interference patterns. (B) Same image after first order phase correction.

Although compensated for to a large extend by gradient pre-emphasis, i.e. adjustment of the gradient shape prior to the measurement to compensate gradient delays, some imperfection still remains causing small time delays between odd and even numbered readout lines. Consequently, as every other line needs to be time-reversed prior to image reconstruction, any small delay results in even and odd lines being shifted along readout with respect to one another. Considering odd and even lines separately, they represent images sampled with half the Nyquist frequency, hence aliased at half the FOV along the PE direction. Without the delay, i.e. in an ideal EPI dataset, the ghost in the even line image would cancel out with the ghost in the odd line dataset. However, according to the Fourier Shift theorem, a shift in k-space corresponds to a phase in image space and vice versa. Therefore, the shifted odd k-space lines lead to an additional image phase which exhibits no counterpart in the even line image, hence the ghosts are not perfectly canceled out. To account for

this phase error, a first order phase correction is typically performed by acquiring at least two alternating readouts without phase encoding prior to the actual EPI readout (Fig. 2.10B). From this readout, the delay, i.e. the phase ramp, is extracted and applied to correct the shift between alternate lines in PE direction.

2.2.3 The need for speed: MRI acceleration

An intrinsic obstacle with MRI is that it is a relative slow modality given that k-space needs to be sampled sequentially. Especially when large matrices need to be acquired, as in high spatial resolution laminar fMRI, gradient amplitudes and slew rates are reaching their limits due to constraints brought up by human physiology. Therefore, methods to accelerate the acquisition process are highly desirable.

One method, known as Partial Fourier (PF), exploits the Hermitian symmetry of k-space, i.e. $S(\mathbf{k}) = S^{*}(-\mathbf{k})$ where the star indicates the complex conjugate. Hence, it would suffice to acquire only one half of k-space. However, this implies the absence of any phase effects due to, e.g. B_0 inhomgeneities and negligible decay during k-space sampling which is often not the case. To account for these effects, more than one half of k-space, typically 5/8 to 7/8, is acquired to make sure that the center of k-space is within the sampled region (as phase effects may result in the center being eventually shifted into the unsampled region).

The simplest form to reconstruct a full data matrix is by filling the missing part with zeros prior to Fourier transform. As this results in neglecting high frequency information, zero filling has a detrimental effect on image resolution and acts like a smoothing filter in image space.

Alternative reconstruction algorithms try to synthesize the missing part of k-space using the sampled region. To account for the aforementioned phase effects, the symmetrical sampled center of k-space is used to reconstruct a

low resolution phase image which serve as a constraint in the reconstruction process. Methods include those synthesizing missing data directly[57,58] or in an iterative fashion[59–61] where the latter tend to be more robust against artifacts caused by high-frequency phase variations. For high resolution measurements at UHF, it is beneficial to keep PF acceleration to a minimum as high frequency components encode spatial resolution. Hence, zero-filling partly negates the effort being made in sampling large matrices. Furthermore, even if the omitted k-space region is synthesized, violation of the symmetry assumption as it is inherent in long EPI readouts with strong T_2^* decay during those causes PF reconstructions to be prone to artifacts, especially in areas of high-frequency phase effects, if too liberal PF factors are chosen.

With the development of many small receiver coils arranged in phased arrays[62], methods to accelerate image acquisition by means of parallel reception, known as (partial) parallel imaging (PI), have emerged rapidly. Originally, phased arrays were designed to boost SNR as each coil receives its own signal. Single images are obtained by simply combining the individual coil images taking, e.g. the root-sum-of-squares or, more preferably, by incorporating the coil's sensitivity profiles yielding optimal SNR. Besides gains in image quality, the spatially distinct reception profiles of different surface coils (Fig. 2.11A) can also be used to replace gradient encoding by coil spatial encoding, dramatically reducing scan time. To this end, k-space is undersampled by an acceleration factor R along the PE direction, i.e. only every R-th line in the PE direction is sampled. As this violates the Nyquist criterion, the FOV of an image corresponding the an R-fold accelerated k-space is reduced by the same factor resulting in an R-fold aliasing of the object, e.g. omitting every other line results in a doubled Δk_y and hence a halved FOV (eq. 2.32, Fig. 2.11B). Relying on the distinct coil sensitivity profiles, a class of image reconstruction algorithms are used to disentangle the aliased image. The techniques can be divided into two families[4]: those operating in image space

[4]For review of recent PI development, see Hamilton et al. [63] and Poser et al. [64].

and those synthesizing the missing k-space lines prior to Fourier transform. Commercially, the former is represented by techniques based on SENSitivity Encoding (SENSE)[65] while the most widely used representative of the latter is known as GeneRalized Partially Parallel Acquisitions (GRAPPA)[66,67].

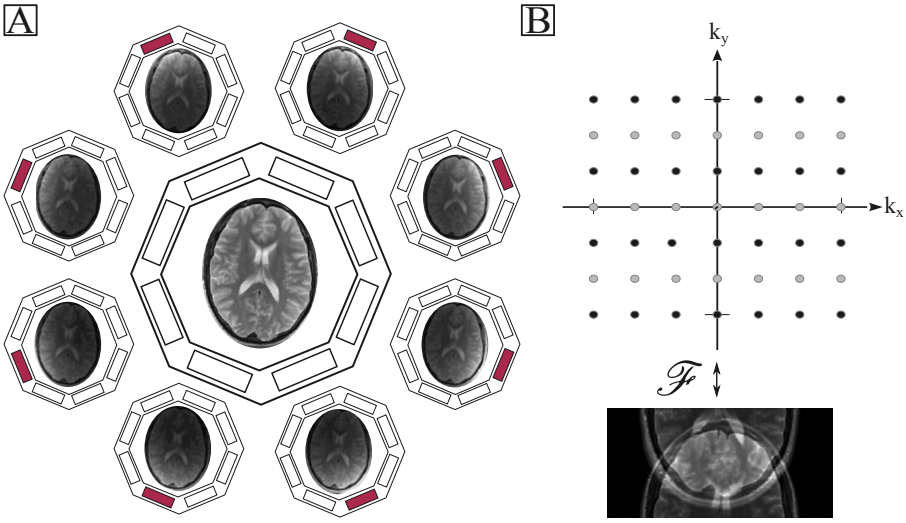

Fig. 2.11 Principle of parallel imaging (A) Each coil element in this exemplary 8-channel receive coil has its own sensitivity profile resulting in a spatially weighted image of the object for each channel. Combining all channels yields a fully covered image. (B) By omitting every second line (R = 2, shaded lines in B) in the k-space acquisition, the FOV is halved resulting in an aliased image. The image can be unfolded using the spatial distinct coil profiles in A (adapted from [68]).

2.2.3.1 SENSE

In SENSE[65], explicit coil sensitivities are used to unfold aliased pixels. Mathematically, the aliased signal at position y due to R-fold acceleration can be described by

$$S_i(y) = \sum_{j=0}^{N_A(y)-1} C_i\left(y + j\frac{FOV_y}{R}\right)\rho\left(y + j\frac{FOV_y}{R}\right), \qquad (2.38)$$

with $i = 0, 1, \ldots, N_C - 1$. N_C and N_A are the number of coils and pixel replicates at position y, respectively. C_i is the sensitivity of coil i and ρ is the desired full FOV image. Eq. 2.38 states that the measured image intensity S at position y is a superposition of the true value and values at position $jFOV_y/R$, weighted by the corresponding coil sensitivities C_i. If those are known beforehand, the system of equations can be solved for the unknown ρ, as long as $N_C \geq N_A$.

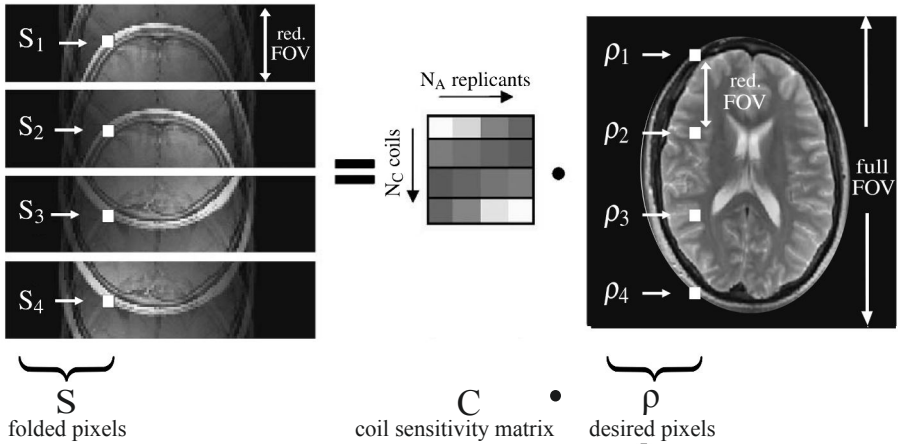

Fig. 2.12 Illustration of the SENSE algorithm. For an R = 4-fold accelerated acquisition with $N_C = 4$ separate receive coils, S consists of $N_A = 4$ aliased pixels in an reduced FOV (left side of the equation). The coils are sensitive toward different spatial locations, e.g. coil one is mostly sensitive toward ρ_1. By using this information, the desired full FOV image (right) can be calculated solving the inverse problem (adapted from [69]).

Eq. 2.38 can be written more generally as a matrix-vector multiplication

$$\mathbf{S} = \mathbf{C}\boldsymbol{\rho}, \tag{2.39}$$

with $\boldsymbol{\rho} \in \mathbb{C}^{N_A}$ being the underlying signal in the full FOV, $\mathbf{S} \in \mathbb{C}^{N_C}$ the aliased signal measured with each coil and $\mathbf{C} \in \mathbb{C}^{N_C \times N_A}$ the coil sensitivity matrix.

In case of Cartesian sampling, N_A is equal to the acceleration factor R. Typically, the number of coils is larger than the acceleration factor as sensitivities of neighboring coils are not entirely spatially distinct. Hence, $\mathbf{C}$ is overdetermined and eq. 2.39 is solved in a least-squares sense using the Moore-Penrose pseudoinverse

$$\boldsymbol{\rho} = \left(\mathbf{C}^{\mathrm{H}}\mathbf{C}\right)^{-1}\mathbf{C}^{\mathrm{H}}\mathbf{S}, \tag{2.40}$$

where $\mathbf{C}^{\mathrm{H}}$ denotes the complex conjugate transponse of $\mathbf{C}$. Coil sensitivities can be estimated using a separate, low resolution full FOV reference scan or a fully sampled k-space center when variable-density sampling schemes are employed. The individual coil images themselves can serve as a sensitivity proxy as well by dividing them with a root-sum-of-squares combined image followed by additional smoothing. The final image will be the combined full FOV image containing only magnitude information.

An inherent downside of all PI methods is the loss in SNR stemming from two factors: one is a $\sqrt{\mathrm{R}}$ reduction due to the acquisition of an R-fold smaller dataset. The other factor arises from the efficiency of the receiver coil to separate aliased pixels. This geometry- or g-factor represents a spatially varying noise amplification and depends on the properties of the receiver coil, i.e. how noise is correlated within and between channels, the k-space sampling scheme and the acceleration factor. Hence, the g-factor is used as a benchmark for optimization of RF coil designs, reconstruction algorithms and k-space sampling schemes. Taking together, the SNR of a fully sampled image relative to an image obtained with SENSE is given by

$$\mathrm{SNR}_{\mathrm{acc}} = \frac{\mathrm{SNR}_{\mathrm{full}}}{\sqrt{\mathrm{R}} \cdot \mathrm{g}}. \tag{2.41}$$

2.2.3.2 GRAPPA

Unlike SENSE, GRAPPA[66,67] synthesizes the missing k-space lines for each coil separately resulting in unaliased images per coil which can be subsequently combined.

The principle behind GRAPPA was developed by Sodickson et al. under the acronym SMASH which stands for SiMultaneous acquisition of Spatial Harmonics[66]. The key idea is that shifting k_y-lines by $m\Delta k_y$ can be achieved by modulating the coil-weighted version of the MR signal equation 2.26 with a spatial harmonic of order m

$$S_i\left(k_x, k_y + m\Delta k_y\right) = \int_x \int_y C_i\left(x,y\right)\rho\left(x,y\right) e^{-2\pi i\left(k_x x + k_y y\right)} e^{-2\pi i m\Delta k_y y} dxdy. \tag{2.42}$$

In GRAPPA, the problem of finding the harmonic is replaced by the problem of finding the relationship between neighboring lines. This is possible because the k-space representation of an image is convolved with the Fourier transform of a typically smooth coil sensitivity profile which represents a local object in frequency domain. Therefore, knowing the local relationship between lines (expressed as GRAPPA weights), one can synthesize missing lines using already acquired ones:

$$S_i\left(k_x, k_y + m\Delta k_y\right) = \sum_{j=0}^{N_C-1} w(m,i,j) S_j(k_x, k_y). \tag{2.43}$$

The weights are obtained from a fully sampled k-space calibration dataset, the autocalibration signal (ACS), which can be low resolution, i.e. the center of k-space, and present as part of the actual measurement or as a separate scan. To improve accuracy of the weights estimation, the ACS region is typically larger than the minimum amount of lines needed and also more than just one

point along the readout dimension is considered. This block of datapoints used for weights estimation is referred to as the GRAPPA kernel of size $N_x^{src} \times N_y^{src}$ which captures the local information of the coil sensitivity profiles in the frequency domain. Eq. 2.43 can hence be rewritten as

$$S_i\left(k_x, k_y + m\Delta k_y\right) = \sum_{j=0}^{N_C-1} \sum_{a=0}^{N_x^{src}-1} \sum_{b=0}^{N_y^{src}-1} w(m,i,j,a,b) S_j(k_x + a\Delta k_x, k_y + bR\Delta k_y) \tag{2.44}$$

or, using more compact matrix notation: $\mathbf{T} = \mathbf{wS}$, where $\mathbf{T} \in \mathbb{C}^{N_C(R-1)}$ are referred to as the missing target points, $\mathbf{w} \in \mathbb{C}^{N_C(R-1) \times N_C N_x^{src} N_y^{src}}$ is the aforementioned GRAPPA weighting matrix and $\mathbf{S} \in \mathbb{C}^{N_C N_x^{src} N_y^{src}}$ are the source points.

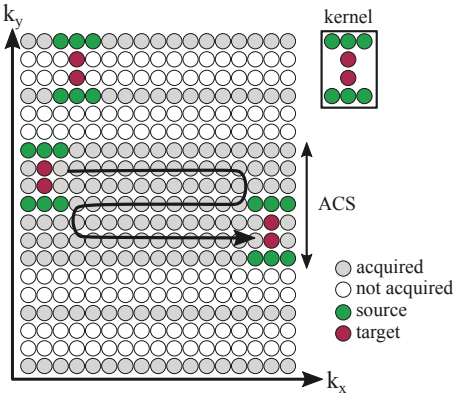

Fig. 2.13 Illustration of the GRAPPA algorithm. For an undersampling factor of R = 3, a kernel (size = 2×3) is defined collecting source and target points for all coils in a sliding-window manner within an ACS region (for visualization, the coil dimension is omitted). Solving for the weights which define the relationship between sampled and unsampled data, the same kernel is applied in the undersampled region synthesizing the target points using the previously determined weights (adapted from [70]).

Graphically illustrated in Fig. 2.13, the GRAPPA reconstruction can be seen as a two-step process where first, a translational invariant kernel slides through the ACS region, collecting a set of equations for all coils to obtain the weighting matrix by solving the inverse problem $\mathbf{w} = \mathbf{T}_{ACS} \cdot pinv(\mathbf{S})$, where *pinv* refers to the pseudoinverse. In the second step, the same kernel slides through the undersampled k-space regions and fill the target points using eq. 2.44. Similar to SENSE, GRAPPA suffers from reduced SNR due to less data sam-

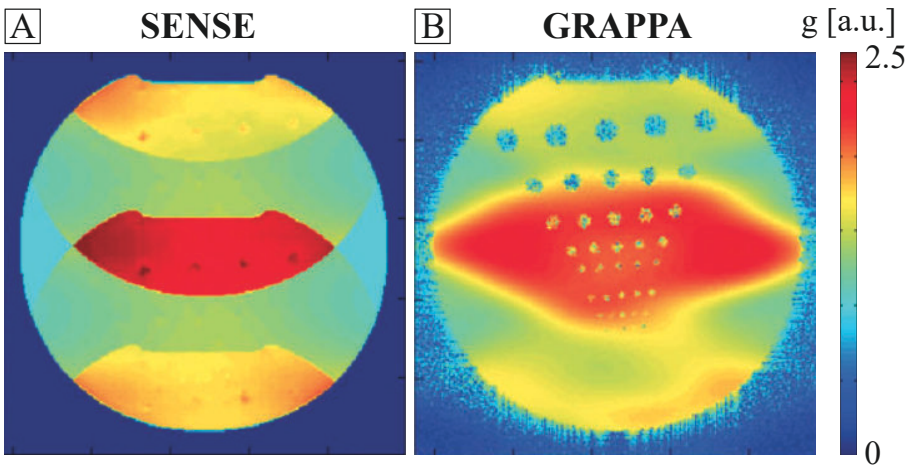

Fig. 2.14 G-factor comparison between SENSE and GRAPPA. (A) Using a 12-channel RF coil and an undersampling factor of 3, SENSE g-factor maps of a phantom show sharp edges and the strongest g-factor penalty in the center of the phantom as most of the pixels are aliased here. (B) In contrast, GRAPPA g-factor maps are smoother and the region of highest noise enhancement is slightly larger than for SENSE. However, both reconstructions lead to comparable noise enhancement characteristics (adapted from [70]).

pling and g-factor noise enhancement. Unlike SENSE, the g-factor is derived from the weights[70] resulting in a different noise enhancement characteristic. However, g-factors tend to be comparable as demonstrated in Fig. 2.14.

Parallel imaging techniques are highly synergetic with UHF[5]. The higher baseline SNR allows for higher acceleration without a penalty in image quality and constraints given by SAR (section 2.3.2) are easier to manage. Considering EPI, parallel imaging reduces the amount of B_0 inhomogeneity induced artifacts by reducing the echo spacing and the echo train length. Moreover, due to more pronounced far-field effects at UHF[72] (see section 2.3.1) the coils' sensitivity profiles reaches further in depth, opening up a wider range of possible acceleration factors.

[5]For details, see the review article by Pruessmann [71].

2.3 MRI at ultra-high fields

The aforementioned advantages of UHF regarding baseline SNR (eq. 2.5) and acceleration capabilities are opposed by problems due to transmission field inhomogeneity and safety considerations. These problems, techniques to solve them and further applications of those are subject of this section.

2.3.1 B_1 field distribution

In an ideal situation, the applied RF pulse affects the magnetization homogeneously over the entire sample. However, as the Larmor frequency increases at higher fields, the RF wavelength decreases. At 7 T, the RF wavelength is approximately 12 cm[73], approaching the size of the human brain. Under this circumstance, RF wave effects and frequency dependent dielectric properties of tissue must be considered.

In high dielectric material, the RF field is elliptically polarized and can be split into two circular polarized components[74]

$$\mathbf{B}_1^+ = \frac{\left(\mathrm{B}_{1,\mathrm{x}} + i\mathrm{B}_{1,\mathrm{y}}\right)}{2} \tag{2.45}$$

$$\mathbf{B}_1^- = \frac{\left(\mathrm{B}_{1,\mathrm{x}} - i\mathrm{B}_{1,\mathrm{y}}\right)^*}{2}, \tag{2.46}$$

where the variables in the above equations are complex quantities. $\mathbf{B}_1^+$ denotes the part of the RF wave rotating with the direction of precession, i.e. the transmission field. According to the principle of reciprocity[75–77], the e.m.f induced in a receiving coil is proportional to the negatively rotating field $\mathbf{B}_1^-$ of the applied RF field. Hence, $\mathbf{B}_1^-$ is referred to as the reception field. Assuming a rectangular pulse for simplicity, the measured signal can be expressed as

$$\mathrm{S} \propto \mathrm{M}_0 sin\left(\gamma \left|\mathbf{B}_1^+\right| \mathrm{T}\right) \left|\mathbf{B}_1^{-*}\right|, \tag{2.47}$$

where the argument $\alpha = \gamma \left| \mathbf{B}_1^+ \right| \mathrm{T}$ is the previously mentioned flip angle. At low frequencies, i.e. in the near-field regime, eq. 2.45 and 2.46 can be considered real quantities and their spatial distribution is identical. However, at high fields (high frequencies) a far-field condition is approached where phase effects leading to spatially distinct distributions of transmit and receive fields cannot be neglected[78,79] (Fig. 2.15A,B).

While the wave effects of the reception field are advantageous for parallel imaging as it introduces more spatial information in coil sensitivities, the spatial phase of the transmit field results in patterns of constructive and destructive interference. These are a major problem at UHF as a quadrature excitation mode (circularly polarized or CP^+ mode), which leads to a homogeneous flip angle distribution over the sample at lower fields[80], causes a non-uniform flip angle pattern and signal voids at UHF (Fig. 2.15C). Moreover, the spatially varying transmit field is followed by a spatially varying power deposition in tissue. Hence, aspects of RF safety are more critical at UHF.

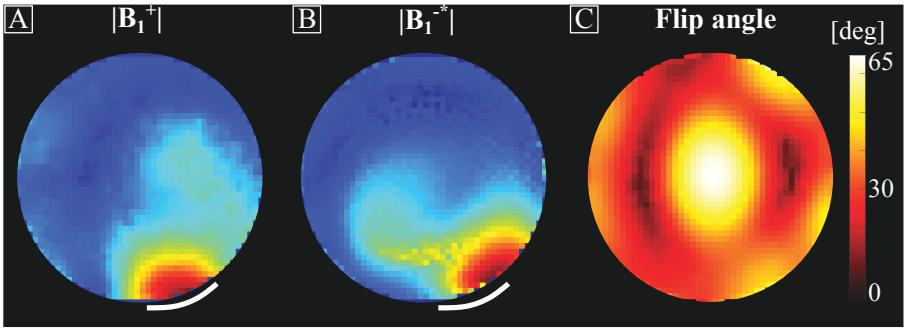

Fig. 2.15 Illustration of B_1 field distribution. (A) Magnitude of the transmit field of a single channel (highlighted as a white arc) measured in a phantom. Note the asymmetric and far-reaching transmission profile. (B) The corresponding reception field shows a rotation in opposite direction and a spatial shift between the maxima of B_1^+ and B_1^-. (A) and (B) are shown in arbitrary units and are individually scaled. (C) When transmitting in CP^+ mode, i.e. in quadrature, the resulting flip angle distribution is inhomogeneous with strong destructive and constructive interference pattern, know as the "central brightening effect".

2.3.2 Specific absorption rate (SAR)

The time-varying electrical field of the RF pulse deposits energy into conductive tissue. This absorbed RF energy is converted into heat which needs to be kept within safe limits. As a metric for RF induced tissue heating, the specific absorption rate (SAR), measured in $\mathrm{W/kg}$, was introduced[6]. Considering multiple transmit elements N_T (see next section), SAR in a voxel at location $\mathbf{r}$ can be expressed as[82]

$$\mathrm{SAR}(\mathbf{r}) = \frac{\sigma(\mathbf{r})}{2\rho(\mathbf{r})T} \int_0^T \left| \sum_{i=0}^{N_{T-1}} \mathbf{E}_i(\mathbf{r}) b_{1,i}(t) \right|^2 dt. \tag{2.48}$$

Here, $\sigma(\mathbf{r})$ and $\rho(\mathbf{r})$ are the sample-specific conductivity and mass density, respectively. $\mathbf{E}_i(\mathbf{r})$ is the complex-valued electrical field produced by the i-th transmit channel and $b_{1,i}(t)$ is the complex-valued RF pulse applied through that channel during time T.

The maximum allowed SAR is divided into global and local limits which apply to all field strengths. However, due to the higher frequency, more RF power is needed at high fields to achieve the same FA compared to low field systems. Up to a frequency of approximately 200 MHz, RF power follows an ω_0^2 rule[73,83]. Above 200 MHz, the power increase is less quadratic but still superlinear[84]. Another factor at UHF is that due to the transmission field heterogeneity, local SAR hotspots might occur. Hence local SAR limits are most critical in practice. Moreover, as SAR is also dependent on the temporal shape of the RF pulse, care should be taken in the design of specific RF pulses.

[6] For review of definitions and recent model developments, see Fiedler et al. [81].

2.3.3 Parallel transmission

Parallel transmission (pTx)[7] refers to a set of techniques used to overcome the B_1^+ inhomogeneity problem or to perform selective excitation. The basic concept of pTx is to use individually controlled transmit elements for excitation similar to parallel imaging where multiple channels are used for reception. According to the superposition principle, the individual B_1^+ fields of each channel are summed to produce a net transmit field inside the sample:

$$\mathbf{B}_1^+(\mathbf{r},t) = \sum_{i=0}^{N_T-1} \mathbf{B}_{1,i}^+(\mathbf{r},t) = \sum_{i=0}^{N_T-1} b_i(t)\Gamma_i(\mathbf{r}). \tag{2.49}$$

Here, $b_i(t)$ is the RF pulse transmitted through the i-th channel and $\Gamma_i(\mathbf{r})$ are maps of the i-th channel transmit sensitivity (c.f. Fig. 2.15A). The sensitivity information must be known prior to RF optimization. B_1^+ mapping techniques provide these information and many different methods exist to suit different applications[87–90].

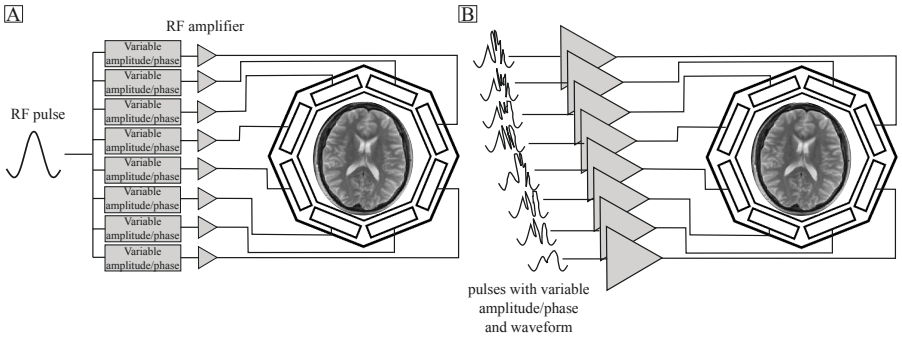

Fig. 2.16 Illustration of parallel transmission. (A) Schematic of RF shimming. Each element of the 8-channel transmit coil is driven with individually controlled amplitude and phase with identical RF waveform. (B) In full pTx, the RF pulse waveform, amplitude and phase is varied per channel (adapted from [91]).

[7] For review, see Padormo et al. [85] and Deniz [86].

Two classes of pTx methods can be defined: static RF shimming where the amplitude and phase of each channel is varied with a common RF pulse waveform (Fig. 2.16A) and dynamic pTx where the complex RF pulse is varied over time (Fig. 2.16B).

2.3.3.1 RF shimming

In RF shimming, eq. 2.49 can be rewritten as

$$\mathbf{B}_1^+(\mathbf{r},t) = b(t)\sum_{i=0}^{N_T-1} w_i \Gamma_i(\mathbf{r}), \tag{2.50}$$

i.e. the same RF pulse is applied for each transmit channel but the total transmit field is a complex weighted sum of the transmit sensitivities. By choosing the appropriate set of weights, the interference patterns can be modified such that the excitation field in dedicated Regions Of Interest (ROI) is more homogeneous. However, it was shown that when shimming one slice in e.g. the axial plane, the fields perpendicular to this slice become less homogeneous[92]. Therefore, static shimming is sufficient if either small ROIs are chosen or more transmit elements are available to increase the degrees of freedom.

Optimum weights can be obtained by minimizing a cost function in a least-squares sense

$$\mathbf{w} = \arg\min_{\mathbf{w}} \left\{ \| f(\mathbf{\Gamma w}) - \mathbf{M} \|_2^2 \right\}. \tag{2.51}$$

with $\mathbf{\Gamma} \in \mathbb{C}^{N_{ROI} \times N_T}$ containing the B_1^+ values of all N_T channels and N_{ROI} voxels within a ROI. $\mathbf{w} \in \mathbb{C}^{N_T}$ is a vector containing the shim settings, i.e. amplitude and phase for each channel and $\mathbf{M} \in \mathbb{C}^{N_{ROI}}$ the desired target distribution, e.g. homogeneous B_1^+. The function $f(\mathbf{\Gamma w})$ can be, e.g. the magnitude of $\mathbf{\Gamma w}$.

2.3.3.2 Dynamic pTx

Rather than to control the B_1^+ distribution, the goal of dynamic pTx is to manipulate the distribution of the transverse magnetization by means of solving the Bloch equations for multiple transmit channels. To simplify calculations, the small-tip-angle approximation (STA)[93] is typically employed, i.e. $M_z \approx M_0 = \text{constant}$, with which the transverse magnetization can be decoupled from M_z. Under this approximation, the desired target magnetization can be seen as a weighted Fourier transform of the RF pulse given a certain k-space trajectory. Grissom et al.[94] formulated a spatial-domain method to calculate, given a desired target magnetization, RF pulses under this formalism. The transverse magnetization $M(\mathbf{r})$ as a result of the Bloch equations under the STA for N_T transmit channels can be written as

$$M(\mathbf{r}) = i\gamma M_0 \sum_{i=0}^{N_T-1} \Gamma_i(\mathbf{r}) \int_0^T b_i(t) e^{i\gamma \Delta B_0(\mathbf{r})(t-T)} e^{-2\pi i \mathbf{k}(t)\cdot\mathbf{r}} dt. \tag{2.52}$$

The phase term $\gamma \Delta B_0(\mathbf{r})(t-T)$ in Eq. 2.52 is a result of the main magnetic field off-resonances captured in the quantity $\Delta B_0(\mathbf{r})$. Similar to the transmit sensitivity $\Gamma(\mathbf{r})$, this field map should be measured to correct for off-resonance effects. $b_i(t)$ is the RF pulse of the i-th channel with total duration T. Unlike the receive case (c.f. eq. 2.27), $\mathbf{k}$ is defined as the remaining gradient moment $\mathbf{k}(t) = \gamma/(2\pi) \int_t^T \mathbf{G}(t')dt'$, i.e. the transverse magnetization at time t only accrues phase due to the gradient played out at time t to the end of the pulse. Eq. 2.52 can be discretized in space and time and rearranged into a set of linear equations $\mathbf{M} = \mathbf{Ab}$ where the matrix $A \in \mathbb{C}^{N_s \times N_T}$ is the system matrix containing all information of the transmit sensitivities, off-resonances and k-space trajectory with N_s being the total number of samples.

Analogue to RF shimming, the desired RF pulses are obtained by solving a cost function which is typically regularized by means of Tikhonov regularization to penalize solutions with high integrated power:

$$\mathbf{b} = \arg\min_{\mathbf{b}} \left\{ \| f(\mathbf{Ab}) - \mathbf{M}_{\text{des}} \|_{\mathbf{W}}^2 + \lambda \| \mathbf{b} \|^2 \right\}, \tag{2.53}$$

with $\mathbf{M}_{\text{des}}$ being the target magnetization, λ the regularization parameter and $\mathbf{W}$ a diagonal $N_s \times N_s$ weighting matrix specifying ROIs. Eq. 2.53 can be solved using iterative, magnitude least squares (MLS) optimization[95].

The spatial domain framework can be flexibly adjusted to account for SAR or hardware limitations by means of additional regularization or constrained optimization and can incorporate arbitrary k-space trajectories. The trajectories can be broadly divided into two categories: those used for B_1^+ shimming and those used for selective excitation. In the case of shimming, the most widely used methods employ spokes trajectories[96] for slice/slab selective excitation and point-wise RF power deposition in k-space[97] for non-selective excitation. In the case of selective excitation, k-space trajectories need to incorporate high spatial frequencies to result in sharp excitation regions. For 2D applications, i.e. beams, typical trajectories are (variable density) spirals[98] or EPI[99] trajectories. The major advantage of pTx for the design of such selective pulses is the capability to accelerate the trajectory, analogue to parallel imaging. By replacing transmit k-space encoding with transmit sensitivity encoding, total pulse duration as well as off-resonance and relaxation effects can be reduced.

2.3.4 Adiabatic pulses

A class of pulses that is particularly useful at UHF are adiabatic pulses[100,101] as they can accomplish magnetization inversion[8] over a broad range of frequencies with a certain robustness against transmit field variations.

Recalling that the motion of magnetization in the rotating frame of reference describes a precession around an effective field $\mathbf{B}_{\text{eff}}$ (c.f. eq. 2.9, 2.10),

[8] Excitation is also possible with adiabatic pulses but is not explicitly treated in this thesis.

varying the effective field using amplitude modulation (as in conventional RF pulses) and frequency modulation of the pulse can result in the magnetization following the orientation change of that field. The condition for this to occur is known as the adiabatic condition

$$|\gamma \mathbf{B}_{\text{eff}}| \gg \left| \frac{d\alpha}{dt} \right|, \tag{2.54}$$

i.e. the magnetization follows the effective field if the precession frequency of the magnetization around that field is much larger than the rate the effective field changes its orientation. Fig. 2.17A illustrates the relationship between α and $\mathbf{B}_{\text{eff}}$.

To achieve adiabatic inversion over a range of off-resonance frequencies $\Delta\delta$, RF pulses can be designed analytically using amplitude $F_1(t)$ and frequency modulation functions $F_2(t)$, both normalized to unit amplitude[102]. The latter is converted into an RF phase when implemented on the MR scanner. The key relationship between these two functions is that they are complementary to fulfill the adiabatic condition at all times, i.e. if one function produces a small component of the effective field, the other must compensate for it and vice versa. The adiabatic inversion is illustrated in Fig. 2.17B-D for the general case that a spin ensemble exhibits a certain (in this case positive) off-resonance frequency δ. Just after the start of the pulse (very small Δt in Fig. 2.17B), the main contribution to the effective field produced by the pulse is the off-resonance component $\Omega F_2(t)$ with Ω as the frequency sweep amplitude. An off-resonance field component δ/γ adds to off-resonance component of the pulse. The transverse component, i.e. the pulse amplitude $|B_1|$ modulated by $F_1(t)$ is still small at this time. At the time t_δ, when the spin ensemble is on resonance (Fig. 2.17C), the off-resonance components cancel out and the effective field is solely determined by the amplitude modulation. Just before the pulse ends (Fig. 2.17D), the same condition as at the start of

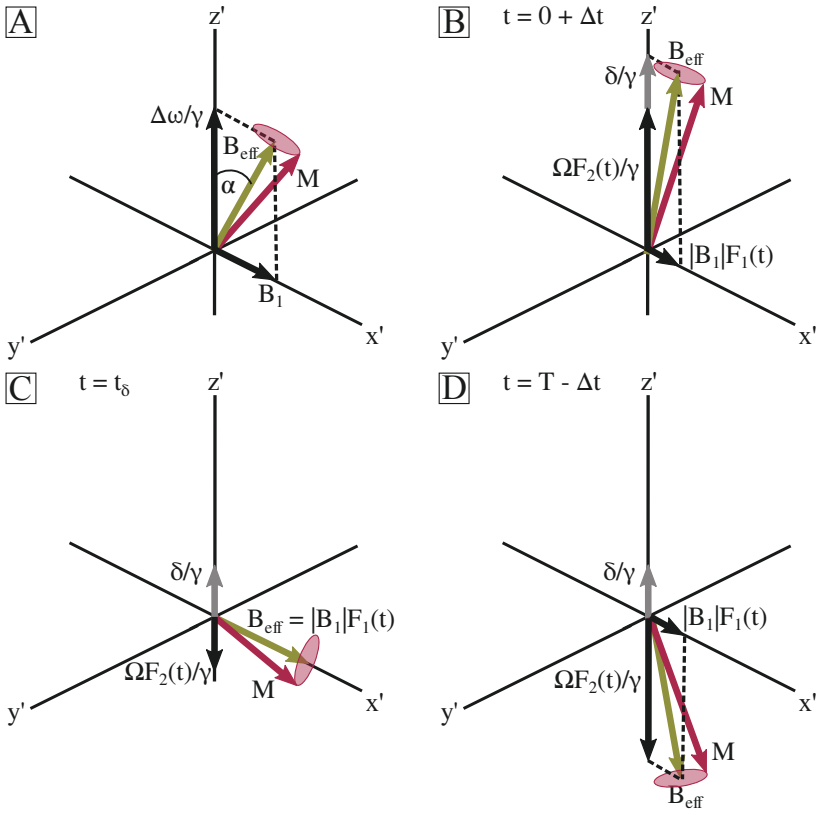

Fig. 2.17 Adiabatic inversion. (A) Illustration of the effective field, its components and the magnetization vector precessing around the field in the rotating reference frame. The rate the effective field changes its orientation ($d\alpha/dt$) determines the adiabatic condition. (B-D) Illustration of an adiabatic inversion at three different time points: Just after the start (B) and before the end (D) of the RF pulse, the effective field is dominated by the off-resonance field component. On-resonant (C), the field is given by the amplitude modulation (adapted from [102]).

the pulse applies, with the exception that the frequency modulation function has a reverted sign. Fig. 2.17B-D indicates two pulse design considerations: First, the amplitude of the frequency modulation must be at least equal to the off-resonance the pulse should affect, i.e. $\Omega \geq \Delta\delta/2$ (c.f. Fig 2.17D).

Second, the most critical point to fulfill the adiabatic condition is on-resonance when only the amplitude of the pulse determines the effective field (c.f. Fig. 2.17C). Hence, the RF amplitude must be above a certain threshold when passing through the center of the sweep. A commonly used adiabatic pulse is the Hyperbolic Secant (HS) which amplitude and frequency modulation are shown in Fig. 2.18 with the time points corresponding the Fig. 2.17B-D marked as red dots.

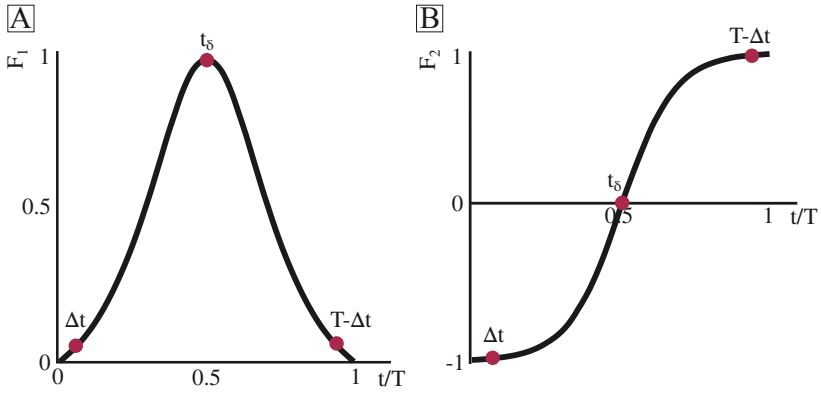

Fig. 2.18 Hyperbolic secant pulse. (A) Amplitude and (B) frequency modulation functions of the hyperbolic secant pulse. The time points corresponding to the adiabatic inversion shown in Fig. 2.17B-D are marked with red dots.

When designed carefully, adiabatic pulses do not necessarily need higher power than their non-adiabatic counterparts[102]. However, an adiabatic pulse designed for inversion cannot be directly used for refocusing due to the non-linear phase accrued along the pulse. A typical method to overcome this issue is to use another, identical pulse to refocus the phase dispersion[103] which results in some increased power deposition.

2.4 Biophysics of fMRI

Having focused so far on the physics of MRI, this section gives an overview of the biophysics of fMRI and how changes in vascular physiology can result in different fMRI contrasts.

2.4.1 Cortical vasculature

In order to satisfy its high energy demand (20 % of the total oxygen metabolism of the body[104]) the brain needs a robust blood supply which led to the development of a complex vaso-architecture.

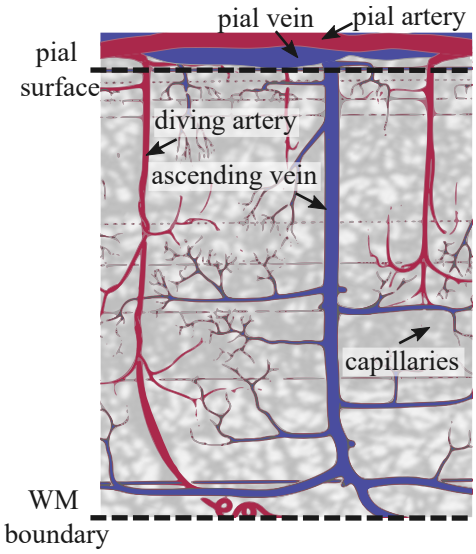

Fig. 2.19 Illustration of human cortical vasculature. Oxygenated blood flows from large pial arteries into diving arteries which branch into arterioles parallel to the cortical surface. These arterioles successively divide into smaller arterioles. Oxygen is exchanged in the capillary bed and deoxygenated blood is drained following a reverse order, i.e. from small venules into asceinding veins and finally into pial veins. Arteries are shown in red, veins in blue and the capillary bed is shown as a gray background mesh (adapted from [21]).

In their seminal work, Duvernoy et al.[21] described the human vascular architecture in the neocortex based on vessel location and degree of cortical penetration. Fig. 2.19 schematically illustrates the basic vascular architecture. Large pial arteries ($\varnothing = 150\ \mu\text{m} - 180\ \mu\text{m}$) supply the parenchyma with oxygenated blood. Diving, or intracortical arteries (ICA), perpendicular

to the cortical surface branch into the cortex. Their diameter ($\varnothing = 10\ \mu\text{m} - 75\ \mu\text{m}$) vary depending on how deep they reach. The deeper they reach, the more blood they need to supply, hence the thicker they are. Smaller arterioles branch parallel to the cortical surface and successively divide into smaller arterioles which branch into a network of fine capillaries ($\varnothing = 5\ \mu\text{m} - 8\ \mu\text{m}$)[21,105,106] where nutrients and water are exchanged with the parenchyma. Deoxygenated blood is collected horizontally via small venules, which successively merge into larger venules, until blood flows into ascending, or intracortical veins (ICV) ($\varnothing = 20\ \mu\text{m} - 125\ \mu\text{m}$). These run perpendicular to the surface, are again grouped according to their level of cortical penetration and drain blood into large pial veins ($\varnothing = 130\ \mu\text{m} - 380\ \mu\text{m}$) parallel to the cortical surface. Vessels smaller than approximately 10 μm are considered to belong to the microvasculature[106] whereas larger vessels are referred to as macrovasculature.

The blood volume fraction across the cortex varies substantially between micro- and macrovasculature. While the macrovasculature show a steady increase in density and hence in blood volume toward the pial surface[21], studies in post mortem human samples of the collateral sulcus[106] and in macaque V1[17] showed a relatively homogeneous microvascular density across the cortical ribbon. However, V1 exhibits a local maximum in central GM (granular layer IV)[17,21]. Work performed by Weber et al.[17] (Fig. 2.20A) and Tsai et al.[107] showed that the microvascular distribution reflects the metabolic demand of a specific region. This indicates that measuring signal changes at the microvascular level with fMRI serves as a good proxy for neuronal activity.

As the BOLD mechanism is driven by changes in oxygenation (see section 2.4.3)[9] the oxygen distribution across vessels must be considered. Fig. 2.20B shows the oxygen saturation S_{O_2} and its change ΔS_{O_2} as a function

[9] For a detailed review of how brain vascular is linked to hemodynamic responses, see Uludağ and Blinder [108].

of vessel size. While larger arterioles (first-branching-order, i.e. arterioles closest to the diving arteries) are close to fully oxygenated, arterioles closer to the capillary compartment exhibit decreased oxygenation (80 % for fith-branching-order). The steepest drop in oxygenation is in small venules similar to capillaries. The increased baseline oxygenation in medium and large sized venules may be explained by diffusion shunts between arterial and venous compartments as experimentally shown in mice[109]. As the oxygenation change is the strongest on the venous side of the vascular system, methods sensitive to those changes are weighted toward it. However, as further described in section 2.4.4, the weighting can be adjusted by using different MR contrasts sensitive toward different parts of the venous network.

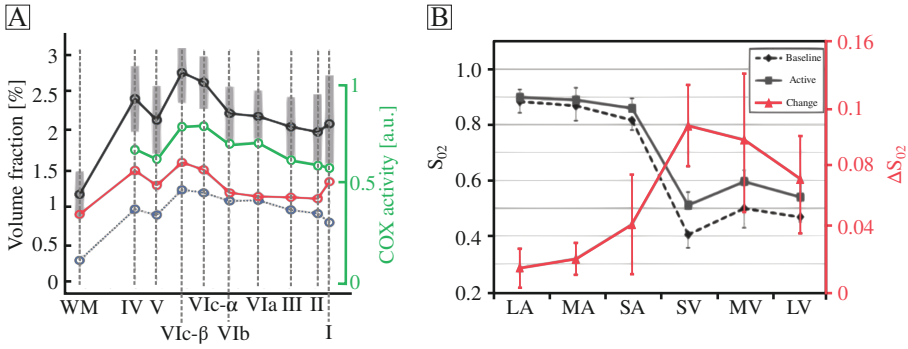

Fig. 2.20 Vascular density and oxygenation. (A) Blood volume fraction as a function of cortical depth (indicated by roman layer numbers) for capillaries (blue), non-capillaries (red) and total vasculature (black). The microvascular distribution mirrors the cytochrome oxidase (COX) staining (green) which reflect metabolic demand. (B) Oxygenation (black) and its change upon functional activity (red) for large (LA), medium (MA) and small (SA) arterioles/arteries, and large (LV), medium (MV) and small (SV) venules/veins. The lowest oxygenation and the highest change is observed in the venous compartment (adapted from [17] and [108]).

2.4.2 Neurovascular coupling

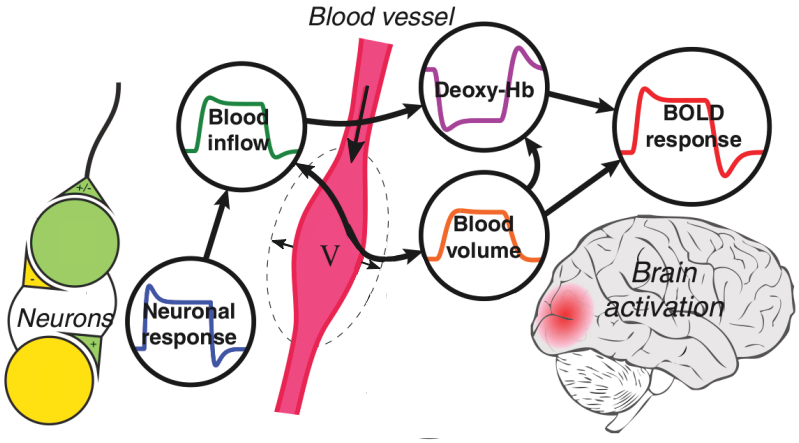

Fig. 2.21 Illustration of the neurovascular processes. Following neuronal response, a cascade of hemodynamic processes is set in motion. Blood flow and volume are increased upon activation. Increased CBF overcompensates the higher $CMRO_2$ resulting in a washout of deoxyhemoglobin (deoxy-Hb) at the locus of activity. CBV and Deoxy-Hb give rise to the BOLD response (adapted from [110]).

Neurovascular coupling describes a cascade of hemodynamic processes[10] following neuronal activity that result in the final BOLD response (Fig. 2.21). Due to neuronal activity, the local oxydative metabolism of glucose, i.e. the cerebral metabolic rate of oxygen ($CMRO_2$), is increased. To satisfy the higher oxygen demand, neurons release neurotransmitter mediating active vasodilation of large arteries and smaller arterioles caused by smooth muscle cells and pericytes. The initial vasodilation results in higher vascular diameter, hence reduced flow resistance which leads to an increase in cerebral blood flow (CBF). It is generally believed that this increased CBF drives in-

[10] whose regulatory mechanisms are not yet fully understood and are subject of current research, see e.g. the review articles of Phillips et al. [111] and Huneau et al. [112]

creased CBV in capillaries and post-capillary venules passively[113–115]. However, it was shown that pericytes surrounding capillaries likely play a role in actively controlling capillary diameter[116]. Moreover, endothelial cells containing aquaporin channels exhibit a strong contribution to the blood volume regulation in capillaries[117].

As the blood flow increases more than necessary to satisfy the increased oxygen demand, the concentration of deoxy-Hb decreases during activation. Both CBV and the amount of deoxy-Hb present in a given voxel determine the total MR signal within it[118,119]:

$$S^{rest,act} = \left(1 - CBV^{rest,act}\right) S_{Ex}^{rest,act} + \sum_i CBV_i^{rest,act} S_{In,i}^{rest,act}. \tag{2.55}$$

Eq. 2.55 describes the signal during rest and activity as a blood volume weighed average of extravascular (EV) signals S_{Ex} and intravascular (IV) signals $S_{In,i}$ where the index i counts through the vascular compartments, i.e. large veins and arteries, venules, arterioles and capillaries. With regard to the hierarchy of how much which vessel type contributes to the change in blood volume, the following order has been formed: In the case of microvasculature, most of the CBV change is expected to take place in the arterioles close to the locus of neuronal activity ($\approx$ 60 % contribution to the total CBV change) followed by the capillary ($\approx$ 30 %) and venule compartment ($\approx$ 10 %)[117]. For macroscopic vessels, it was shown that the response depends on the stimulus duration[120,121]. While large pial arteries show a strong CBV increase even for short stimuli ($\approx$ 40 % fractional CBV change), a small CBV change ($\approx$ 10 %) for large pial vessels was shown only for long stimuli (30 s) while pial arteries exhibit an even stronger volume increase[120]. Recently, Akbari et al.[122] estimated fractional CBV changes of ICAs and ICVs based on human CBV-weighted fMRI data. In line with previous animal studies[123,124], they showed a higher fractional change for ICAs ($\approx$ 19 % on average) than for ICVs ($\approx$ 4 % on average).

2.4.3 Susceptibility effects and BOLD contrast mechanism

In their seminal work, Ogawa et al.[1] discovered that the MR signal contrast between venous blood vessels and their surrounding tissue is dependent on the amount of deoxy-Hb present in these vessels. Deoxygenated blood is highly paramagnetic[125], resulting in a difference in susceptibility between a blood vessel and the tissues surrounding it, and thus magnetic field perturbations in and around the vessel. As the concentration of deoxygenated blood changes as a consequence of neuronal activity, the amount of signal dephasing as a result of field variations (eq. 2.15 and 2.16) varies accordingly.

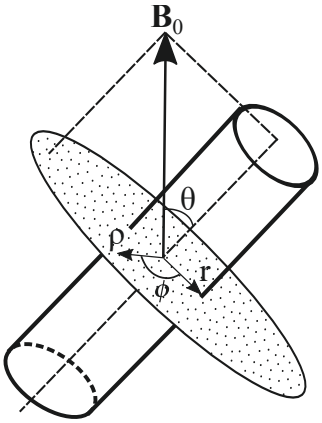

Fig. 2.22 Vessel geometry. Geometry of an infinitely long blood vessel with radius r and internal susceptibility χ_i tilted by an angle θ from the B_0-axis. A cross-section of the surrounding volume V with susceptibility χ_o parameterized with polar coordinates $\rho \in [0, R]$ and $\phi \in [0, 2\pi]$ is shown (adapted from [21]).

Describing a blood vessel as an infinitely long cylinder with radius r, the field variations can be calculated from Poisson's equation for magnetostatics. Using polar coordinates (Fig. 2.22), the field perturbation is given by[126]

$$\Delta B_0 = \begin{cases} 2\pi\Delta\chi B_0 (1-Y) \dfrac{r^2}{\rho^2} cos(2\phi) sin^2(\theta) & \rho > r \quad (2.56a) \\ 2\pi\Delta\chi B_0 (1-Y) \left(3cos^2(\theta) - 1\right)/3 & \rho \leq r \quad (2.56b) \end{cases}$$

with $\Delta\chi$ as the susceptibility difference between fully deoxygenated blood and surrounding tissue and Y as the oxygen saturation.

Eq. 2.56a describes the extravascular field perturbation as dipolar in shape which scales linearly with the amount of deoxy-Hb (1-Y) and quadratically with vessel radius. The sinusoidal dependency on the orientation relative to the magnetic field indicates that a vessel parallel to the main magnetic field produces no extravascular field variation whereas a vessel perpendicular to the field gives rise to a maximum field variation. Although it can be expected that the random orientations of the microvasculature in the parenchyma will result in no orientational dependent field variation, it has been demonstrated that the structured organization of the pial veins result in an orientation bias, i.e. the largest BOLD signal variation as a function of angle relative to B_0 was observed at the pial surface.[127].

As touched upon in section 2.1.4, water molecules diffuse in tissue which causes them to experience different fields and hence different dephasing regimes depending on the size of the vessels they are diffusion around. If the vessel diameter is much larger than the expected diffusion length of the water molecules during TE, the field variation the molecules experience can be considered time-invariant. In other words, the molecules experience the same field perturbation along their diffusion path throughout TE, hence the signal dephasing is of a *static* nature and give rise to the classical T_2^* signal loss. The exact value for the vessel diameter at which static dephasing dominates depends on the main magnetic field but is on order of tens of micrometers[113,128,129]. In contrast, if the vessel diameter is on the same order as the diffusion length, the molecules randomly experience a range of different field perturbations upon their trajectory. As this is time-dependent, the dephasing process is of a *dynamic* nature. This dephasing regime is most important for capillaries and small post-capillary venules.

In case of intravascular field variations, again, two types of dephasing regimes can be defined. Eq. 2.56b describes a net field offset within a vessel. As long as the molecules stay within that vessel, they dephase at a constant rate with respect to the vessel's surrounding, hence this process is of a static nature. In case of dynamic dephasing, multiple mechanisms have been proposed. They include a dynamic averaging effect, i.e. diffusion of water molecules around red blood cells giving rise to dephasing similar to the extravascular case, and rapid exchange of protons between sites of different susceptibility. Although hard to separate empirically, it is thought that the former mechanism is most likely the dominant contributor[130].

Referring back to eq. 2.55, the extra- and intravascular signals can be described by the monoexponential transverse relaxation process (eq. 2.15) where, in addition to the intrinsic transverse relaxation time, i.e. relaxation without deoxy-Hb, another relaxation process caused by deoxy-Hb is present[119,131]:

$$S_{Ex} = S_{0,Ex} e^{-\left(R_{2,0,Ex} + \sum_i R_{2,Hb,Ex,i}\right) TE} \tag{2.57}$$

$$S_{In,i} = S_{0,In,i} e^{-\left(R_{2,0,In} + R_{2,Hb,In,i}\right) TE} \tag{2.58}$$

Here, $S_{0,Ex}$ and $S_{0,In,i}$ are the baseline MR signals at TE = 0 ms for the extravascular and the intravascular compartments, respectively. $R_{2,0,Ex}$ and $R_{2,0,In}$ are the intrinsic relaxation rates for tissue and blood at Y = 100 %. The deoxy-Hb induced relaxation rates are a function of vessel type (artery, arteriole, capillary, venule, vein). The choice of TE is not arbitrary. To maximize the signal change in e.g. GM (eq. 2.57), TE needs to match the $T_2^{(*)}$ of GM as illustrated in Fig. 2.23. If TE is too short, there is only little time for dephasing to build up, i.e. the difference between the active and the baseline condition is low. For a too long TE, most of the signal has decayed already, resulting an a small difference between conditions.

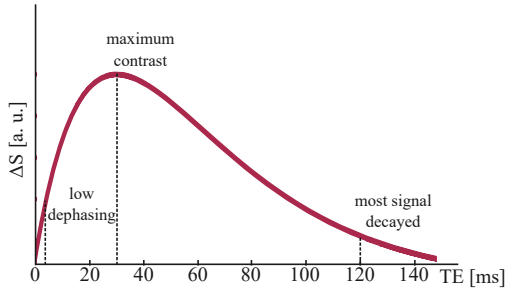

Fig. 2.23 TE dependency of the BOLD contrast. The GM signal change due to changes in T_2^* upon activity as a function of TE. The maximum contrast is achieved if TE = T_2^*.

Because upon neuronal activity the deoxy-Hb induced relaxation rates decrease, the MR signal decays at a slower rate, i.e. in an active state, the signal is higher. However, this positive BOLD response does not occur instantaneously, nor does it remain. As the BOLD response is a result of subsequent hemodynamic processes with different temporal characteristics, the time evolution of the BOLD response, referred to as hemodynamic response function (HRF), exhibits up to three distinct phases (Fig. 2.24).

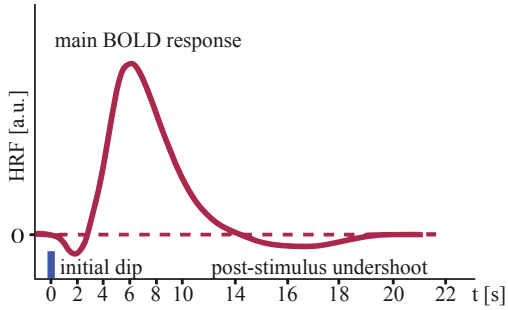

Fig. 2.24 Illustration of the hemodynamic response function. Time course of the BOLD response upon short stimulation (blue line) showing three distinct phases: initial dip (~2 s post-stimulus), main BOLD response (~6 s post-stimulus) and a post-stimulus undershoot (~10 - 12 s post-stimulus) (adapted from [132]).

Following stimulation, an inconsistently observed small signal decrease, the initial dip, occurs which last less than 2 s in humans[108]. Two explaining theories exist: one that an early increase in $CMRO_2$ creates an early hypo-oxygenation. Alternatively, an increase in arterial CBV, which has been shown to happen prior to changes in blood oxygenation[133], might cause the dip provided that the relaxation time of arterial blood is shorter than that of the extravascular space. Approximately 6 s post-stimulus, the main positive BOLD

response follows. After stimulus cessation, the BOLD response does not return to zero but a post-stimulus undershoot is typically observed which can last for more than 30 s[108]. The explaining mechanisms are highly controversial. One early theory was that due to the delayed vascular compliance of the post-capillary venous vesculature CBV returns to baseline slowly[114] but alternatives such as $CMRO_2$ recovering more slowly to baseline than CBF have been proposed as well[11].

2.4.4 Sensitivity and spatial specificity in laminar fMRI

Summarizing the previous three sections, ideally, high-resolution fMRI measures signal changes at the level of the microvascular compartment (small arterioles, capillaries and venules) as this is most confined to the locus of neuronal activity. However, the BOLD contrast, as a result of a chain of hemodynamic events, reflects changes of blood oxygenation which occurs mainly post-capillar and the susceptibility effects scale with vessel diameter which introduces a bias toward large venous vasculature. In humans, the density and diameter of large ICVs increases from deep to superficial layers[21] and it has been shown that the extravascular field effect of large pial veins affects the entire parenchyma, not only the superficial cortical layers[127,135]. Hence, venous macrovasculature results in a bias toward the pial surface. However, it is possible to obtain more microvascular sensitivity, i.e. more spatial specificity, by refocusing static field effects using SE-BOLD fMRI.

2.4.4.1 GRE- vs. SE-BOLD laminar fMRI[12]

The GRE-BOLD contrast is the most sensitive contrast[130,136] as it measures signal changes of *all* vasculature which exhibits a change in oxygenation.

[11] For review, see Uludağ et al. [108] and van Zijl et al. [134].
[12] For a detailed review, see Koopmans and Yacoub [128]

However, its specificity is impaired due to the aforementioned bias toward large venous vessels. Using refocusing pulses, i.e. the SE-BOLD contrast, static dephasing effects are (to a large extend) refocused and only dynamic dephasing contributes to the measured signal change. This is illustrated in Fig. 2.25 in the case of EV effects. As dynamic dephasing is dominant around microvasculature, SE-BOLD is more specific than its GRE counterpart (Fig. 2.26).

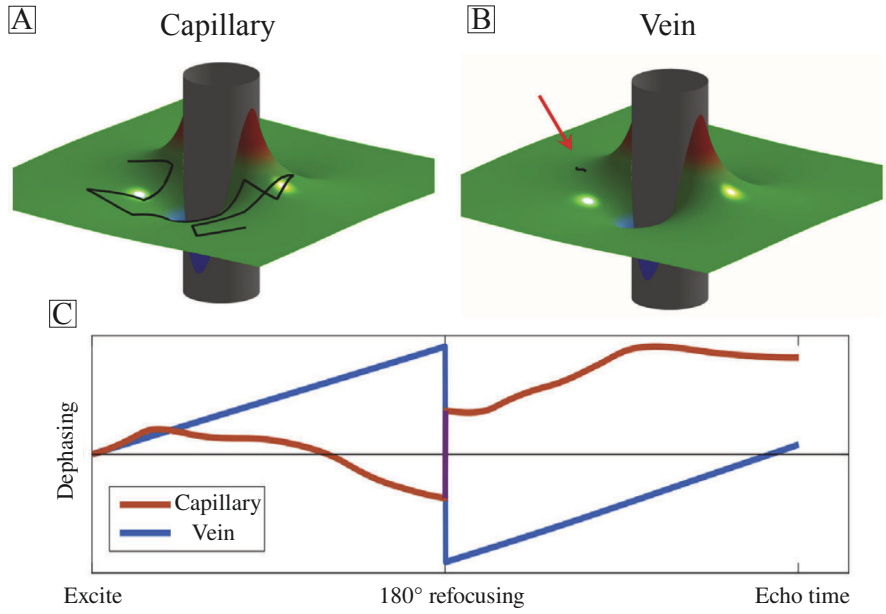

Fig. 2.25 Extravascular dephasing around capillaries and veins. (A) Random diffusion path (black line) of a water proton around a capillary (modelled as a cylinder). The proton experiences a range of different field variations, dipolar in shape (colored surface). (B) Same as in (A) but around a large vessel. Note that for visualization purposes, the diffusion path (red arrow) is scaled relative to the vein. In reality, the path would stay the same but the vein would be several orders of magnitude larger. As the field does not change much with respect to the diffusion path of the proton, the dephasing is static. (C) Accumulated dephasing along the diffusion trajectory around the capillary (red line) and the vein (blue line) in the time between excitation and echo time. In case of SE-BOLD, a 180° refocusing pulse is played out at TE/2 inverting the dephasing. In case of static regime, almost all dephasing has been refocused whereas the dephasing around the capillary is not identical before and after the 180° pulse, hence a net dephasing is observed (adapted from [128]).

Intravascular field effects add to the bias problem in both GRE- and SE-BOLD type of sequences as baseline CBV increases toward the pial surface. A straightforward approach to reduce IV signal contributions is to exploit the short T_2/T_2^* of venous blood at UHF when the TE is tuned toward the TE of GM. It should be noted however, that in case of GRE-BOLD, unspecific EV

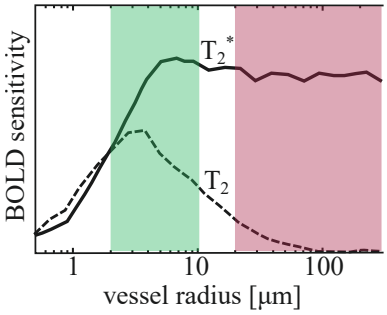

Fig. 2.26 BOLD specificity. Monte Carlo simulation of BOLD signal change as a function of vessel radius for T_2- (dashed line) and T_2^*-weighted (solid line) sequences at 9.4 T (TE_{GRE}/TE_{SE} = 20/30 ms, 3 % CBV, $Y_{rest}/_{act}$ = 0.77/0.85). SE-BOLD is more sensitive toward the microvascular compartment (green shaded area) whereas GRE-BOLD is sensitive to all vasculature, especially larger vessels (red shaded area) (adapted from [129]).

dephasing scale we TE, i.e. when TE $\approx T_2^*$ of GM at 7 T, IV contributions are close to zero but EV field effects are maximized.

A consideration regarding SE-BOLD is its practical sequence implementation as fMRI requires a relatively high time efficiency compared to MRI (seconds vs. minutes). EPI readouts[137] improve temporal efficiency but as they are inherently T_2^*-weighted, only the central k-space echo is purely T_2-weighted while the rest of the readout train exhibits a varying degree of additional T_2'-weighting. Because this T_2'-weighting can re-introduce contributions from macrovasculature, the EPI readout train can be segmented[138] to reduce macrovascular impact. However, this comes with the downside of prolonged scan time and sensitivity toward shot-to-shot B_0 differences which can introducing artifacts[139,140]. As an alternative to SE-EPI, GRAdient- and Spin-Echo (GRASE)[141] 3D readouts[142] using a train of refocusing pulses with short EPI readouts in between have been proposed.

While SE-BOLD shows a higher specificity, it comes with downsides, e.g. lower temporal efficiency, lower contrast-to-noise, i.e. sensitivity, lim-

ited volume coverage, higher RF power deposition and sensitivity toward B_1^+ inhomogeneities.

2.4.4.2 CBV-weighting as a non-BOLD alternative[13]

As neuronal activation triggers a variety of hymodynamic responses, other, non-BOLD functional contrasts can be used for fMRI. They have the potential to overcome the venous bias and to provide a more quantitative interpretation of underlying signal change.

Indicated by eq. 2.55, cerebral blood volume changes upon activation. Depending on stimulus duration, the majority of CBV change happens at the level of small arterioles and capillaries. Hence, CBV-weighted laminar fMRI is expected to provide a more specific measure of functional activity.

The most widely used method to achieve CBV-weighted fMRI is VASO[144,145] which working principle is schematically illustrated in Fig. 2.27B. It relies on suppressing blood signal by means of signal inversion and capitalizing on different T_1 relaxation times between blood and GM. At a certain inversion time (TI), matching the blood nulling time, the signal is read out using EPI. To account for T_2^*-weighting during the readout, CBV-weighted images are interleaved with non-CBV-weighted images. As both sets have the same T_2^*-weighting, the BOLD contamination can be accounted for. The slice-saturation slab-inversion VASO (SS-SI-VASO)[146] method required some careful TI calibration to achieve the blood nulling when imaging the region of interest and as T_1 relaxation times become longer at UHF, SS-SI-VASO tend to be less time efficient[14].

[13] For a detailed review of CBV-weighted and other non-BOLD contrasts, see Huber et al. [143]

[14] Note that recent VASO developments achieve CBV-weighting by simple T_1-weighting using variable flip angles to circumvent the need of signal inversion, hence greatly improving temporal efficiency at the cost of less sensitivity toward CBV changes [147, 148]

Alternative to blood nulling, which represents a negative functional CBV contrast, CBV-weighting can also be achieved by means of GM signal suppression (Fig. 2.27C). The resulting signal change is hence positive. GM suppression can be achieved by exploiting MT effects (section 2.1.5) as extensively studied in chapter 6.

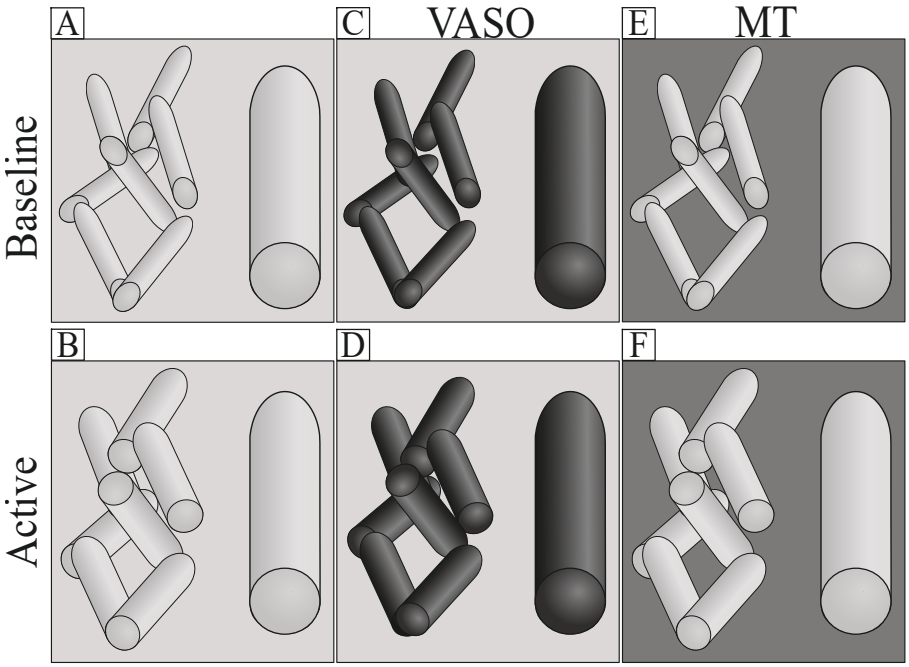

Fig. 2.27 Illustration of CBV-weighting. (A) Considering a voxel containing a network of small vessels (small cylinders) and a large vessel, the signal intensity of GM and blood is almost identical. Note that this is the case at short TE, where little dephasing and hence little BOLD effects are present. (B) Because there is no contrast between EV and IV space, an activity induced change in CBV, as indicated by larger microvascular vessels compared to (A), is not visible as the net signal within the voxel stays the same between functional activity and baseline. (C-D) Nulling the blood compartment as done in VASO results in a negative signal change upon activation, driven by microvasculature. (E-F) In contrast, saturating GM signal instead of blood with e.g. magnetization transfer (MT) results in a positive signal change.

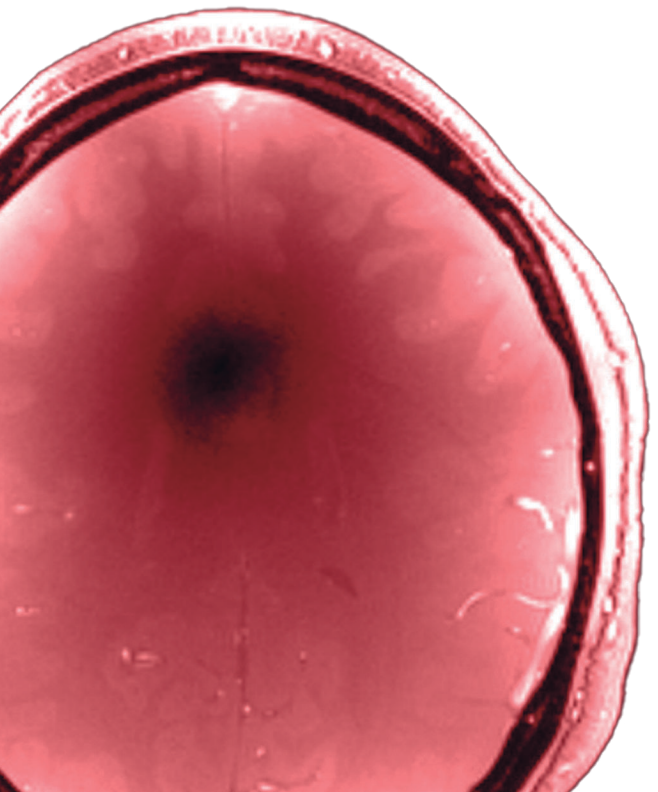

3

An 8/15-channel Tx/Rx head neck RF coil combination with region-specific B_1^+ shimming for whole brain MRI focused on the cerebellum at 7 Tesla

---

Associated publication: **Pfaffenrot, V.**, Brunheim, S., Rietsch, S. H. G., Koopmans, P. J., Ernst, T. M., Kraff, O., Orzada, S., and Quick, H. H. "An 8/15-channel Tx/Rx head neck RF coil combination with region-specific B_1^+ shimming for whole brain MRI focused on the cerebellum at 7 Tesla". In: *Magn. Reson. Med.* 80 (2018), pp. 1252–1265.

Abstract

The human cerebellum is an interesting, yet challenging brain structure to study using functional magnetic resonance imaging (fMRI) at ultra-high fields (UHF) due to its anatomical location and the problem of transmit field (B_1^+) inhomogeneity at UHF. Especially when the cerebellum is to be studied as part of a larger network including parts of the neocortex and/or spinal cord, the small field-of-view (FOV) provided by commercial radiofrequency (RF) coils is an obstacle.

In this work, we evaluated an 8/15-channel transmit/receive (Tx/Rx) head neck RF coil combination with region-specific B_1^+ shimming for whole-brain MRI with focus on improved fMRI of the cerebellum at 7 Tesla. To this end, an 8-channel transceiver RF head coil was combined with a 7-channel receive only array. The noise parameters and acceleration capabilities of this 8Tx/15Rx coil setup were compared with a commercially available 1Tx/32Rx RF head coil. Region-specific B_1^+ shimming was applied when using the 8Tx/15Rx RF coil. To evaluate the capability for fMRI of the cerebellum and the neocortex, temporal signal-to-noise ratio (tSNR) and statistical non-parametric maps for finger-tapping experiments with 14 healthy subjects were acquired by using a variable slice thickness gradient-echo echo-planar (VAST GE-EPI) fMRI sequence.

The enlarged FOV of the 8Tx/15Rx coil in combination with region-specific B_1^+ shimming increased homogeneity of the transmission field and tSNR in caudal cerebellar regions. Temporal SNR losses in cranial parts were reduced. This resulted in more highly significant voxels in the caudally activated areas and identical patterns in the cranial cerebellar parts during a finger-tapping task. In the case of the neocortex, RF shimming of the transmit field resulted in reduced sensitivity losses compared to the coil combination without B_1^+ shimming.

We conclude that compared to the 1Tx/32Rx RF coil, the presented 8Tx/15Rx RF coil combination successfully improves fMRI of the human cerebellum at 7 T and allows for whole-brain coverage including spinal cord. A clear tSNR gain in caudal cerebellar regions is shown and fMRI of the neocortex is possible.

3.1 Introduction

The functional role of the human cerebellum has been studied for about a century[150,151]. With the progress in functional MRI (fMRI)[1,64], it has been shown that the cerebellum's contribution exceeds sensorimotor function[152–154] and that the cerebellar vermis is involved in the extinction of conditioned fear[155]. Given that anxiety disorder is one of the most common mental disorders[156], in-depth knowledge of the underlying functional network and the cerebellum's contribution are important prerequisites for new therapy approaches.

The interest in neuroscience applications continuously drives magnetic field strengths beyond the clinical established field strengths of 1.5 T and 3 T. Ultrahigh-field (UHF) magnets of 7 T and higher provide opportunities to satisfy the increased demand of detailed spatial information, increased SNR, and functional contrast. Because the signal changes caused by susceptibility-induced changes in the magnetic field accompanied by neural activity scale quadratically with the main magnetic field strength at the capillary level[157], fMRI at higher fields becomes more sensitive to the locus of neuronal activity[119,158]. With the available higher SNR at 7 T, Marques et al.[159] performed high-resolution gradient-echo (GRE) imaging of the cerebellum revealing cerebellar cortical layers. Van der Zwaag et al.[160] used the increased blood oxygenation level dependent (BOLD) contrast at 7 T and a relatively high spatial resolution of 1.2 mm isotropic to map the digits of right-handed participants in the cerebellum, similar to the well-studied homunculus in the primary somatosensory cortex.

However, many fMRI experiments at UHF are designed for only depicting individual structures of the brain in more detail without taking the full system (e.g. neocortex, cerebellum, spine) into account. This is primarily because of the undesired trade-off between high spatial and high temporal resolution for large FOVs and the obstacles introduced by UHF. In particular, excitation field (B_1^+) inhomogeneities caused by the decreased RF wavelength[79]

need to be compensated by introducing new RF hardware and excitation methods like B_1^+ shimming[161]. For larger regions of interest, the B_1^+ shimming concept can be extended to a slice-by-slice[162] or a slab-wise[163] transmission optimization. Moreover, design of spoke pulses[164] in a simultaneous multi-slice acquisition have shown promising results at 7 T[165] and 9.4 T[166].

Additionally, the stronger vulnerability of UHF imaging to susceptibility-induced image distortions near air-filled cavities like the mastoid antrum[167,168] is also challenging, especially when imaging the cerebellum. Its physical location in the posterior cranial fossa and anatomical diversity, combined with its small size of one-ninth of the volume of the neocortex, renders the cerebellum a challenging region of interest for UHF MRI[169,170]. In addition, commercially available RF head coils at 7 T are primarily optimized for imaging the cerebrum and impaired caudal image contrast inversions as well as limited excitation fidelity have been reported[97,171–174].

The primary target of this work was to improve cerebellar fMRI at 7 T, while measuring as much of the remaining brain structures, including spinal cord. Therefore, an 8-channel transceiver (Tx/Rx) RF head coil[175] was combined with a 7-channel receive-only (Rx) array[176] to form an 8Tx/15Rx coil combination setup. Variable slice-thickness (VAST) GRE-EPI[177] fMRI was used to reduce through-slice signal dropouts near the cerebellum and to adjust the resolution with focus on the cerebellum. To improve RF homogeneity, a region-specific RF shimming procedure, i.e. different static RF shims for different anatomical locations was applied. The benefits and disadvantages of this approach were systematically evaluated by comparing the 8Tx/15Rx RF coil with an 1Tx/32Rx commercially available RF coil from NOVA Medical (Wilmington, MA) in terms of B_1^+ homogeneity, noise correlation, g-factors, temporal SNR (tSNR), and second-level t-statistics in a basic finger-tapping fMRI experiment at 7 T.

3.2 Materials & methods

3.2.1 Radiofrequency coil hardware

In this work, a 1Tx/32Rx head coil from NOVA Medical (Fig. 3.1A) served as a reference. The FOV coverage of this coil setup in the z-direction was measured to be 21 cm. This coil allows a fixed circular polarized (CP^+) excitation profile only. However, for a better comparison with the other RF coil setup, dielectric shimming was applied. Three pads of dimensions 17 x 11 x 1 cm^3 (L x W x H) filled with high dielectric material (calcium titanate, ε_r = 110) were used to passively shim the RF field at the location of the cerebellum[178]. In detail, two dielectric pads were placed next to both ears canals and one in the neck of each subject (Fig. 3.1A, red arrows), as recommended by Teeuwisse et al[178].

To enlarge the FOV in the z-direction toward the cerebellum and more caudal regions while simultaneously increasing the local SNR in those, an RF head coil combination consisting of two individual RF coils was used. One part is a transceiver head coil consisting of eight microstripline elements with meanders arranged in octagonal shape (Fig. 3.1B), as previously described in Orzada et al[175]. This coil provides a wider measured FOV coverage of 31 cm for RF excitation in the z-direction. The 8-channel transceiver RF coil was combined with a 7-channel Rx-only RF array[176] (Fig. 3.1C, top view; Fig. 3.1D, bottom view). This array consists of six hexagonally arranged overlapping loop elements with a seventh loop placed in the middle. The 7-channel Rx array was placed occipitally in the 8Tx/Rx head coil in a way that the cerebellum of each subject was optimally covered with the array's sensitivity profile (Fig. 3.1E). The 8-channel Tx/Rx head RF coil and the 7-channel Rx-only RF array together form an 8Tx/15Rx RF array. For anatomical reference, the inion of the skull was positioned on the central channel of the receiver RF array (channel two). No additional dielectric pads were used in this setup, as the 8-channel transceiver coil allows RF shimming.

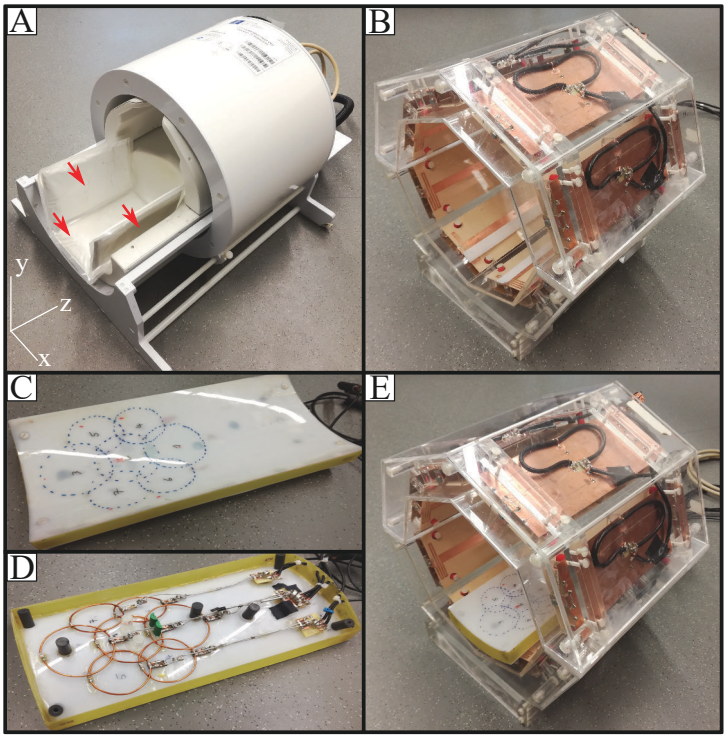

Fig. 3.1 RF hardware. (A) The 1Tx/32Rx RF head coil with dielectric pads (red arrows) was used as a reference and compared with an 8-channel transceiver coil consisting of eight individual microstripline elements with meanders arranged in octagonal shape (B). (C,D) In addition, a 7-channel Rx-only array was used to augment signal detection in the cerebellum when using the 8Tx/Rx coil. Six overlapping loops are arranged in hexagonal shape with the seventh loop positioned in the center (C, top view; D, bottom view). (E) The 7Rx RF array was positioned occipitally inside the 8Tx/Rx coil to boost SNR at the location of the cerebellum.

The amplitudes and phases of the transceiver's individual transmit channels were controlled by a custom RF shimming setup, including online specific absorption rate (SAR) supervision[179]. For RF coil safety assessments, finite integration technique simulations (Microwave Studio, CST, Darmstadt, Germany) of the 8Tx/Rx were performed. For coil model validation, the coil was first loaded with a homogeneously filled elliptical phantom (ε_r = 45.3,

σ = 0.84 $\Omega^{-1}m^{-1}$). Subsequent dosimetric measurements of the H-field at 297 MHz were performed to validate the model. To this end, a field probe (Dosimetric Assesment System, SPEAG, Zurich, Switzerland) was immersed in the phantom and systematically moved by a computer-controlled 3-axis positioning apparatus, while the 8Tx/Rx head coil was driven in CP^+ mode by an 8-channel custom Butler matrix.

Based on the coil model, the SAR was estimated during scans using virtual observation points[180]. Those were calculated from CST simulations for Duke and Ella from the virtual family[181] as well as Hugo from the visible human project[152], each in two different positions within the coil. The 6-min SAR for the worst-case scenario in this combined model was taken for restricting the forward RF power. To ensure safe use of the 8Tx/Rx coil while RF shimming, the worst-case 10 g SAR over all RF shims was used as an upper boundary, assuming all input power goes into this worst-case shim. To verify that the 7-channel Rx-only coil was adequately detuned during RF transmission, dosimetric measurements of the E-field were performed with a similar setup as described above. The E-field was measured with and without the 7-channel Rx-only array along three top–down lines in z-direction (Fig. 3.2A,B) covering the receive-only elements. The results in Fig. 3.2C-E show that the E-field during transmit does not change within error margins when using the detuned 7Rx array indicating that the 7Rx array can be safely used for measurements. Note that the shown measurement error represents the expanded uncertainty of all error sources.

Each of the two in-house-built RF coils was connected to its own custom-built 8-channel transmit/receive switchbox containing low impedance preamplifiers. The transmit part of the transmit/receive switchbox connected to the Rx-only array was terminated with 50 Ω.

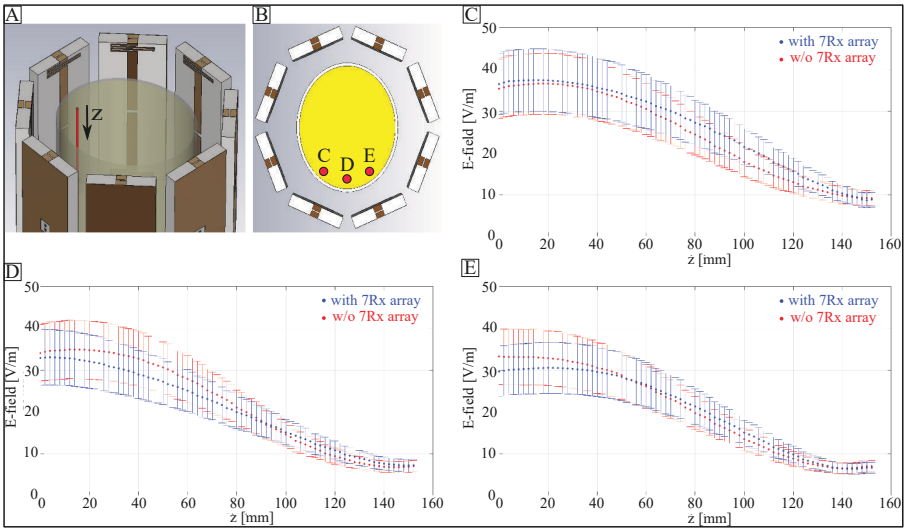

Fig. 3.2 Detuning verification. (A) Schematic of the 8Tx/Rx RF coil loaded with a tissue simulating phantom. (B) Top view of the measurement setup. To evaluate the detuning capability and the safe use of the 7-channel Rx array, the E-field along the z-dimension at three different positions corresponding to the rows of loop elements of the array was measured.(C-E) For all three positions, the E-field measurements with and without the Rx array are identical within the measurement uncertainties demonstrating sufficient detuning of the 7-channel Rx array.

3.2.2 Coil performance on a 7 T MR system

The MRI measurements were performed on a 7 T whole-body research system (MAGNETOM 7 T, Siemens Healthcare, Erlangen, Germany). Fourteen healthy subjects (11 males, 3 females, 32.6 $\pm$ 5.1 years) participated in this study. The local ethic committee approved all in vivo MRI measurements, the volunteers provided written consent, and no neurological diseases were known at the time of measurement. Before the functional measurements, noise correlation coefficients and SENSE[65] g-factor maps were calculated online for every subject and both RF coils using a quality assurance sequence. The SNR decrease resulting from parallel imaging was calculated in terms of g-factors

in two transverse slices. One slice was aligned to be parallel to the medial part of the arbor vitae of the cerebellum and going straight through the fourth ventricle. The other slice with identical orientation was shifted by a multiple of slice thickness $\Delta z = 3$ mm cranial to depict the cerebrum. For each subject, these positions were noted and applied for both RF coil setups in the same way.

3.2.3 Region-specific RF shimming

One key concept of this work is the application of multiple B_1^+ excitation patterns to exploit the RF shimming capability and the large FOV of the 8Tx/Rx head coil to cover the cerebellum with optimal signal while maintaining whole-brain coverage.

Before RF shims could be computed, single-channel B_1^+ maps were measured using B1TIAMO[88,182]. B_1^+ maps were acquired in three slices, each with a thickness of 22.5 mm. These slices defined three regions of interest (ROI): One comprising the caudal part of the cerebellum, one the cranial part and the last ROI was in the middle of the neocortex (see Fig. 3.7). Based on the transmission field information, phase-only RF shims were computed. These shims serve the purpose to maximize flip angle (FA) homogeneity with sufficient high average FA in the caudal cerebellum, the cranial cerebellum and the motor cortex. One cost function to improve homogeneity within a ROI is the coefficient of variance (CoV)[92,183], defined as

$$\mathrm{CoV} = \mathrm{std}\left\{\left|B_1^+\right|\right\} / \mathrm{mean}\left\{\left|B_1^+\right|\right\}. \tag{3.1}$$

However, it is well known that minimizing this cost term alone results in reduced B_1^+ efficiency[184]. Then, a homogeneous excitation with sufficient high average FA may require too high RF peak power and exceed SAR limits. To counteract low average FA, the RF shimming cost function used in this work

was the average of the B_1^+ magnitudes regularized with their CoV. The resulting cost function is then a trade-off between an excitation with a high but inhomogeneous FA distribution and a homogeneous but inefficient excitation similar to the approach described in Metzger et al[185]. The cost function is given by

$$\Theta = \left(\text{mean} \left\{ \left| \sum_{i=0}^{N_T-1} \Gamma_{i,j} w_i \right| \right\} \right)^{-1} + \lambda \text{CoV} \left\{ \left| \sum_{i=0}^{N_T-1} \Gamma_{i,j} w_i \right| \right\} \tag{3.2}$$

and was minimized using a simplex search algorithm in MATLAB 2016a (The MathWorks Inc., Natick, MA, USA). In eq. 3.2, $\mathbf{\Gamma} \in \mathbb{C}^{N_{ROI} \times N_T}$ is the transmit sensitivity matrix containing the B_1^+ values of N_T transmit elements and N_{ROI} voxels in a region of interest. The vector $\mathbf{w} \in \mathbb{C}^{N_T}$ contains amplitudes and phases of the transmit elements. The regularization parameter λ was chosen to be $\lambda = 0.05$ using L-curves based on one pilot B_1^+ map. Because different RF shims in different ROIs may result in different flip angles, SNR may differ between those regions. To counter inter-regional transmit field variations, the driving amplitudes of all transmit elements for one shim were normalized to the amplitude corresponding to the minimum achieved FA. The amplitude corresponding to this FA was used as the reference amplitude in the scanner settings.

For a quantitative estimation of the RF shimming performance, FA homogeneity was estimated by the CoV given in eq. 3.1[186,187]. The argument of the function was the FA values obtained from three ROIs in the FA maps. The group averaged variance coefficient was compared within three different settings: The 1Tx/32Rx coil using the CP^+ mode and dielectric pads, the 8Tx/15Rx coil combination with CP^+ excitation and the coil combination with region-specific RF shimming.

3.2.4 Functional MRI measurements

To evaluate the RF coil's performance for fMRI of the cerebellum and the neocortex, a finger-tapping block design experiment was conducted to obtain robust functional activation patterns. Each participant was instructed to perform a self-paced tapping task of the fingers of the right hand with a tapping rate higher than 1 Hz if the magnet bore was illuminated with red light. In the case of blue or no illumination, the subjects should rest. The tapping rate was not recorded during scans. The paradigm included 10 blocks of movement and 10 blocks of rest, each lasting for 28 s. Each task block contained 10 measurements followed by a rest block of 10 measurements. The first and last scan in the time series of 202 measurement repetitions exhibited no color coding and were used to inform the participant of the start and end of the experiment. Presentation software Version 20.0 (Neurobehavioral Systems, Berkeley, CA) was used to trigger condition switching. Data were acquired with the three RF coil and excitation settings as described in the previous section. The order was pseudo-random between subjects. In all three cases, the location of significant voxels in the cerebellum should consist of the transition region of lobules V and VI ipsilateral to the tapping hand. Lobulus VIII, divided into the sublobuli VIIIa and VIIIb on the same cerebellar hemisphere, should also show significant functional activation[188].

3.2.4.1 Variable slice thickness EPI

To acquire functional data, the VAST 2D single-shot GRE-EPI technique[177] was used (Fig. 3.3A). It has the ability to adjust the individual slice thickness depending on position by changing the amplitude of the slice-selecting gradient within one fMRI measurement. This has three advantages for cerebellar fMRI: First, imaging of the whole brain volume can be accelerated. It takes fewer slices to obtain whole-brain coverage when using partially thicker slices.

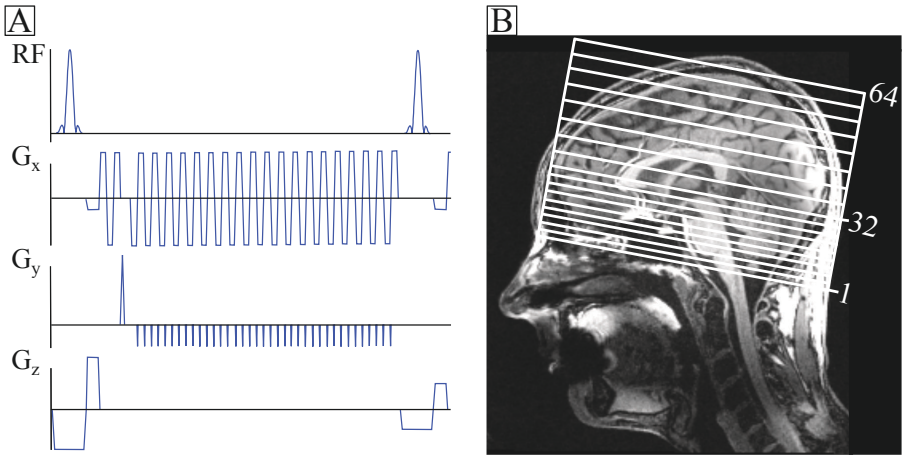

Fig. 3.3 VAST-EPI sequence. (A) Diagram of the VAST GRE-EPI sequence in the transit region between two blocks with different slice thickness. The higher amplitude of the slice-selecting gradient G_z (left) results in thinner slices in the cerebellum, whereas the lower G_z gradient amplitude (right) leads to thicker slices for the neocortex. (B) The whole-brain coverage is achieved with 64 slices of which 32 were used to sample the cerebellum and the other 32 sampled the rest of the brain.

In this work, high spatial resolution was not the primary goal, but whole-brain coverage with focus on the cerebellum in a reasonable amount of time. Second, region-specific RF shimming can be easily implemented. In this consecutive slab-by-slab excitation pattern, a trigger was implemented in the sequence to control the switching between the individual RF shim settings via a custom-built RF modulator system[179]. Finally, the original purpose of the sequence was to minimize through-plane signal loss near air-filled cavities by using thinner slices in these locations. Because the cerebellum is adjacent to the auditory canals[167], VAST GRE-EPI is well-suited for fMRI of this structure. Although the focus of this work was primarily on the cerebellum, the sequence was also used to estimate potential for large FOV fMRI measurements by sampling the whole brain. In particular, the brain was sampled with 64 slices, of which the first 32 covered the cerebellum (Fig. 3.3B). The RF shim condition

was changed after the first 16 and 32 slices, respectively. The other parameters used in VAST EPI acquisitions were TR/TE = 2800/22 ms, acquisition time = 9:41 min resulting in 202 volumes, matrix size = 128 x 128, distance factor = 0 %, 1.5 mm isotropic resolution of the first block, 1.5 x 1.5 x 3 mm^3 resolution of the second block, FOV = 192 x 192 mm^2, FA = 78° (Ernst angle), partial Fourier factor 7/8, GRAPPA R = 3 with 48 phase-encoding reference lines, readout bandwidth = 1302 Hz/pixel, echo spacing = 0.87 ms.

A high-resolution structural T_1-weighted MPRAGE scan served as an anatomical reference for postprocessing steps. The parameters were: TR/TE/TI = 2500/1.54/1100 ms, acquisition time = 6:13 min, 256 sagittal slices, matrix size = 384 x 336, 0.7 mm isotropic resolution, FA = 4°, partial Fourier factor = 6/8, GRAPPA 3 with 48 phase-encoding reference lines; readout bandwidth = 570 Hz/Px, echo spacing = 54.7 ms.

3.2.5 Data processing and analysis

Except for one step, postprocessing was performed with SPM12 Version 6906 (Welcome Trust Centre for Neuroimaging, London) in MATLAB 2016a. The anatomical T_1-weighted image was manually reoriented such that the center of the fourth ventricle was located at the coordinates x = 1, y = -44, z = -29 of the spatially unbiased infratentorial template (SUIT)[189]. After segmentation and bias field correction, a cerebellar mask was generated and manually corrected with MRIcron Version 12.0[190] to serve as the anatomical reference.

From the image series of 202 functional images, the first and the last scan were excluded from analysis. The remaining volumes were slice time–corrected before interpolation onto a 1.5 mm isotropic grid using cubic splines with MATLAB. Then, spatial postprocessing steps using SPM12 and the SUIT toolbox (Version 3.1) were applied. The functional volumes were manually reoriented similar to the anatomical data set and subsequently

realigned. The mean EPI image was used for coregistration with the T_1-weighted image.

After postprocessing, the coregistered functional data were evaluated using a first-level general linear model (GLM). Activation was modeled by convolving a boxcar function, representing the tapping paradigm, with a canonical hemodynamic response function. To remove slowly varying signal drifts, a high-pass filter (128 s cut-off) was used. The six rigid-body realignment parameters were used as nuisance regressors in the design matrix. To account for respiratory motion and heartbeat, the robust Weighted Least Squares toolbox[191] was used. Although gross motion and physiologically induced artifacts can be corrected to certain extend, residuals may remain[192] which represent non-stationary noise sources along the timeline of measured volumes. The toolbox relaxes the assumption of time-independent variance made within the general linear model. It uses a mild exclusion by estimating the noise along the timeline in a first pass and then weights each brain volume by the inverse of this estimate in a second pass. This results in less contribution from images affected by motion, but also sporadic hardware-associated artifacts like RF spikes. This toolbox was used because the cerebellum is surrounded by dense vasculature and the particular anatomical location of the cerebellum leads to more susceptibility to heartbeat and respiratory motion[170,193]. The resulting individual β-maps were normalized based on the affine transformation information obtained from the structural images using the normalization algorithms of the SUIT toolbox.

It has been shown that parametric group-level analyses suffer from elevated error rates when the group size is less than 20[194,195]. Non-parametric tests can overcome this issue. Therefore, a group-level analysis was performed using the Statistical non-Parametric Mapping toolbox[196] (version 13) in SPM12. The 14 normalized β-maps were smoothed with a Gaussian kernel of 3 mm. The images served as independent parameters in the non-parametric

equivalent of a one-sample t-test for each measurement condition. A total of 10000 permutations was used. As recommended by the developer of the toolbox, mild variance smoothing with the same kernel width as used for the β-maps was applied to increase statistical power in the case of experiments with degrees of freedom of less than 20. This procedure resulted in pseudo t-statistics.

In case of the neocortex, postprocessing and analysis were similar to the procedure described above with the exception that the T_1-weighted reference was reoriented to match the MNI coordinate space. Realigned functional data were coregistered to this standard space prior to statistical testing.

3.2.5.1 Temporal SNR

For each participant, the first 100 functional images were separately realigned and coregistered to the T_1-weighted image without any temporal postprocessing. Temporal efficiency maps (i.e. tSNR/$\sqrt{\text{TR}}$[197]), were calculated by voxel-wise-dividing the mean value by the SD derived from the timeline. The individual maps were normalized to the SUIT template and averaged across participants to form group-level maps.

3.3 Results

3.3.1 Large FOV imaging

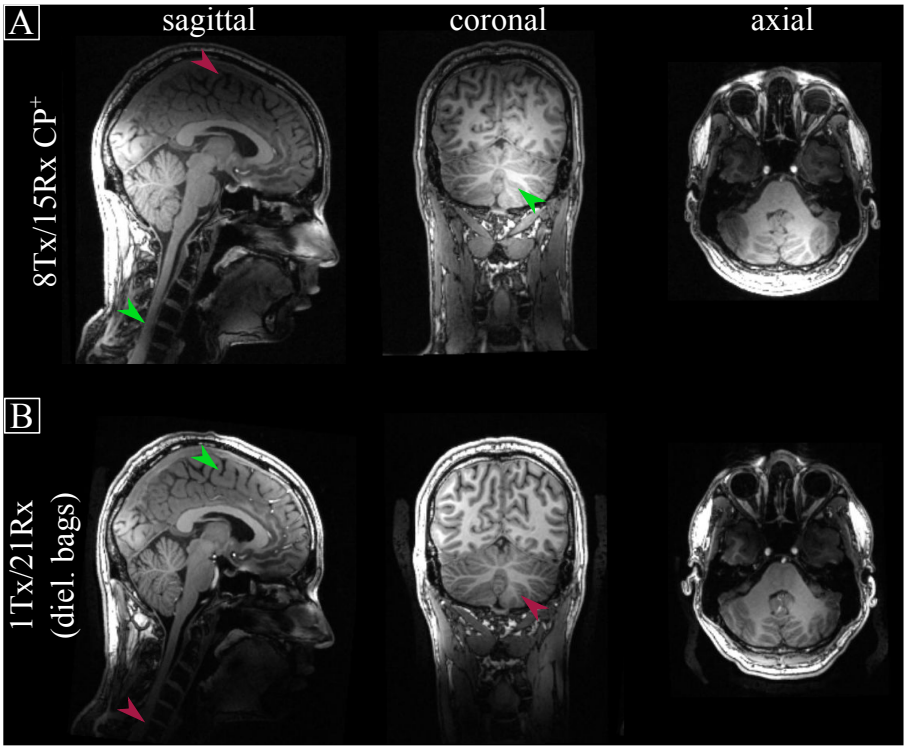

Fig. 3.4 Comparison of brain coverage. (A) Exemplary T_1-weighted images of one subject acquired with the 8Tx/15Rx coil combination setup using CP^+ mode. (B) Same subject measured with the 1Tx/32Rx reference coil. Regions of signal gains and losses are highlighted with green and red arrows, respectively.

For one subject, Fig. 3.4 shows example high resolution T_1-weighted images acquired with the 8Tx/15Rx coil combination operating in CP^+ mode (Fig. 3.4A) and with the 1Tx/32Rx reference coil (Fig. 3.4B). With the 8Tx/15Rx RF coil, the whole-brain (including spinal cord) can be visualized

in one FOV whereas the 1Tx/32Rx reference coil primary visualizes the cerebrum. The 8Tx/15Rx coil improves signal intensity in the cerebellum and in more caudal regions (green arrows in 3.4A) at the cost of lower signal intensity in the cerebrum (red arrow in 3.4A). The reference coil performs the opposite, with high intensity at the neocortex (green arrow in 3.4B) but low signal intensity at caudal regions (red arrows in 3.4B). Both image groups where scaled identically without correcting for receive field bias. Please note that in this comparison, the reference coil was used with dielectric pads whereas no region-specific RF shimming was used when scanning with the 8Tx/15Rx coil as the MPRAGE sequence was not adjusted to load different excitation modes. Hence, further gains in caudal regions, e.g. reduced signal inhomogeneity in the cerebellum, and more signal in cranial parts can be expected with region-specific shimming (see also Fig. 3.9 and 3.10).

3.3.2 Coil performance on a 7 T MR system

Fig. 3.5 illustrates the parallel imaging performance for both RF coils in one representative subject. Axial SENSE 1/g maps are shown at the location of the cerebellum (Fig. 3.5A) and the neocortex (Fig. 3.5B) for five different acceleration factors with anterior–posterior (AP) phase-encoding direction. For visualization, axial anatomical images are shown on the left. Please note that the anatomical images are not identically scaled to aid visualization. As expected, the g-factor is higher for the 8Tx/15Rx coil compared to the 1Tx/32Rx RF coil at both locations, because of the reduced number and unequal distribution of the receive elements of the 8Tx/15Rx coil. However, the average g-factor over all subjects was almost identical for an acceleration factor of R = 3 being used in this work. At the cerebellum (Fig. 3.5A), the g-factor was 1.100 ± 0.005 and 1.050 ± 0.011 for the 8Tx/15Rx and the 1Tx/32Rx coil, respectively. At the location of the neocortex (Fig. 3.5B), the corresponding

g-factor was 1.110 $\pm$ 0.008 and 1.040 $\pm$ 0.004, respectively. With an SNR reduction of approximately 10 % for the 8Tx/15Rx RF coil at both anatomical locations, these results indicate that a 3-fold acceleration is a reasonable compromise between image acceleration and SNR loss.

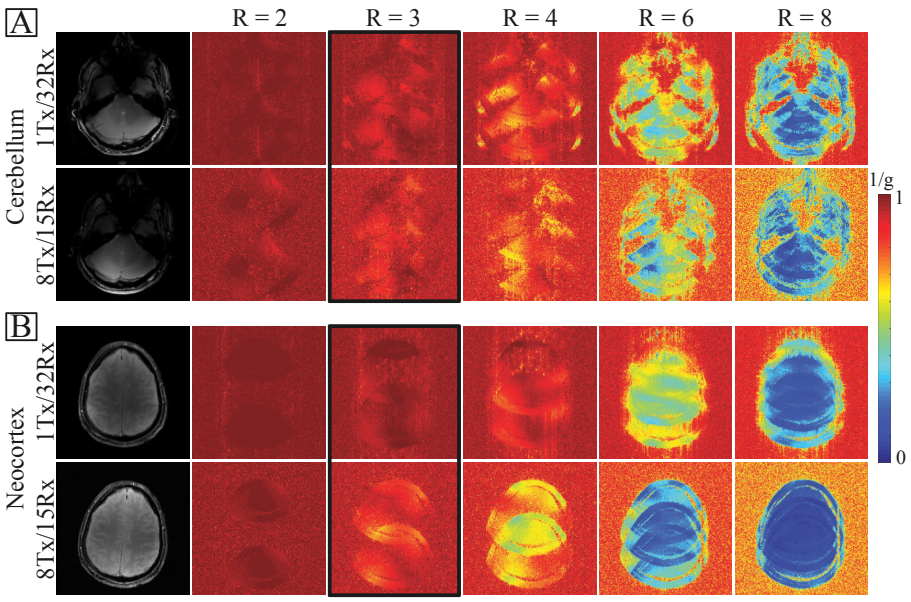

Fig. 3.5 G-factor maps. (A) Axial 1/g maps for the 1Tx/32Rx coil and the 8Tx/15Rx coil at the location of the cerebellum for five different acceleration factors (R). Anatomical images are shown on the left for orientation. fMRI experiments were performed with R = 3 (black box). (B) 1/g maps for the neocortex at the level of the motorcortex.

Fig. 3.6 shows the noise correlation coefficient matrix for the 8Tx/15Rx (Fig. 3.6A) and the 1Tx/32Rx RF coil (Fig. 3.6B), averaged over all subjects. The corresponding SD is shown in Fig. 3.6C,D, respectively. The average off-diagonal correlation coefficient of the 8Tx/15Rx and the 1Tx/32Rx RF coil was 0.112 (Fig. 3.6A) and 0.07 (Fig. 3.6B), respectively. In terms of maximum noise correlation, the 8Tx/15Rx coil exhibited a correlation coefficient of 0.42 compared to 0.49 for the 1Tx/32Rx head coil. Channel five of

the receive-only array showed relatively high values for mean and SD of the correlation coefficient compared to other channels in the 8Tx/15Rx RF coil (Fig. 3.6A,C). These could be attributed to the corresponding transmit/receive switch of the connected switch box. The transmit/receive switch of this element was damaged during the measurements, leading to decreased SNR of channel five of the receive-only array. However, this finding has no significant influence on the overall results.

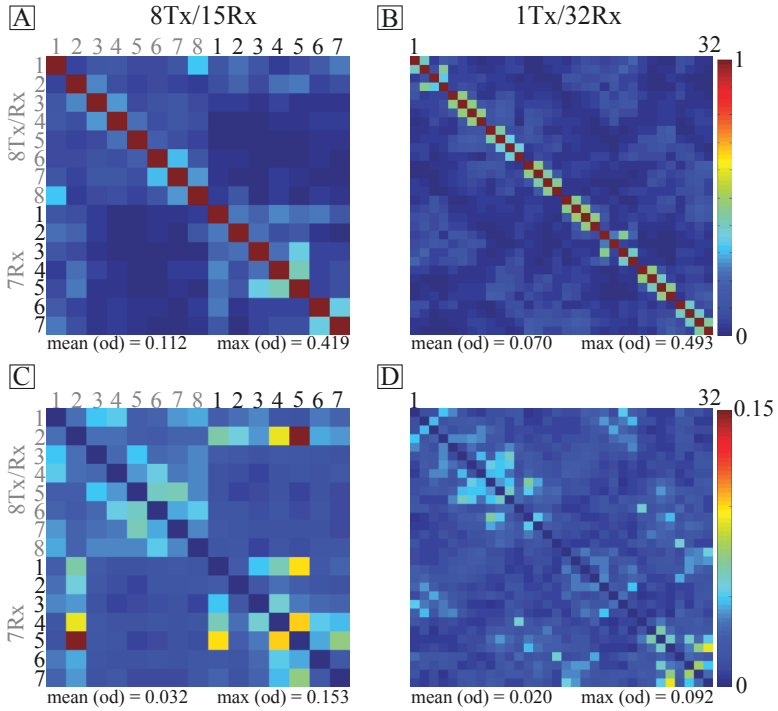

Fig. 3.6 Noise correlation. (A) The noise correlation coefficient for the 8Tx/15Rx and (B) the 1Tx/32Rx RF coil averaged over all subjects. (C,D) The corresponding SD over subjects. The mean and maximum of the off-diagonal (od) elements are shown for both quantities and RF coils. The transmit/receive switch of the fifth element of the 7Rx array was damaged during the measurements, as indicated by the increased SD of that particular channel in C. However, this finding has no significant influence on the overall results.

3.3.3 Region-specific RF shimming performance

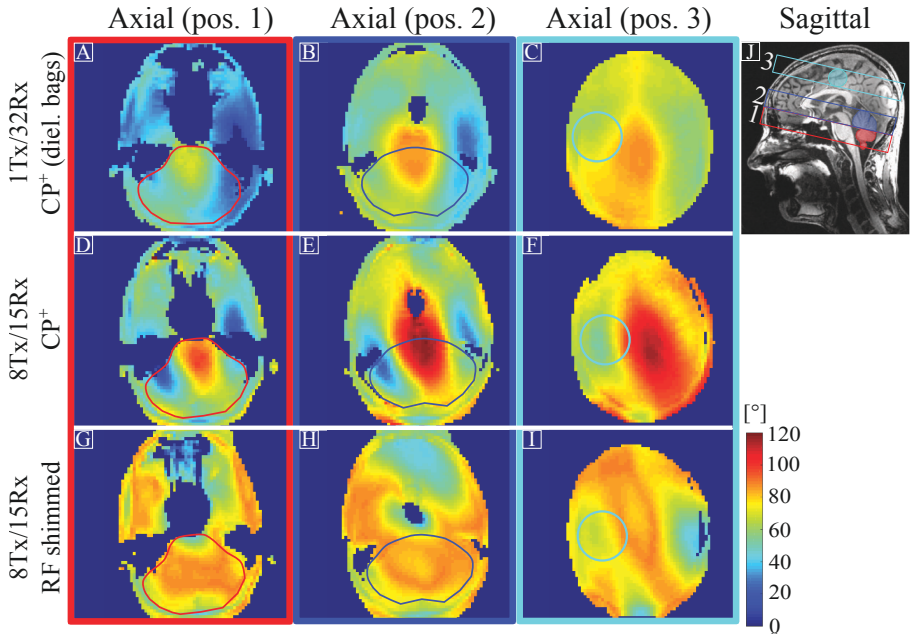

Fig. 3.7 Flip angle maps. Example axial flip angle maps obtained with the 1Tx/32Rx coil (A–C), the 8Tx/15Rx coil using CP^+ mode (D–F), and the 8Tx/15Rx coil with region-specific shimming (G–I) at the location of the caudal cerebellum (A,D,G, red volume in J), the cranial cerebellum (B,E,H, blue volume in J), and the neocortex (C,F,I, motor cortex highlighted as turquoise volume in J), respectively. The location of the cerebellum and the motor cortex in the corresponding FA maps are marked as colored ROIs.

The FA distributions of the 1Tx/32Rx coil using dielectric pads, the 8Tx/15Rx RF coil with CP^+ excitation, and the 8Tx/15Rx coil using region-specific RF shimming is shown in Fig. 3.7 for the same subject as in the g-factor comparison (Fig. 3.6). From left to right, the axial FA maps correspond to the locations of the caudal cerebellum (Fig. 3.7A,D,G, red volume in 3.7J), the cranial cerebellum (Fig. 3.7B,E,H, blue volume in 3.7J), and the neocortex (Fig. 3.7C,F,I), respectively. The motor cortex is highlighted as a turquoise volume in Fig. 3.7J.

The qualitative comparison between the 1Tx/32Rx RF coil and the 8Tx/15Rx coil using RF shimming indicates a more homogeneous FA distribution with a target FA value of 90° for both ROIs within the cerebellum. Especially within the caudal part of the cerebellum, the larger FOV along the z-direction together with RF shimming increases the transmit capability remarkably. Quantitatively, the group-averaged CoV within the caudal part (red ROI in Fig. 3.7A,D,G) of the cerebellum was 0.26 ± 0.04 for the 1Tx/32Rx, 0.27 ± 0.04 for the 8Tx/15Rx coil with CP^+ mode, and 0.1 ± 0.02 for the 8Tx/15Rx RF coil with region-specific RF shimming. Within the cranial part (blue ROI in Fig. 3.7B,E,H), the corresponding CoV was 0.19 ± 0.03, 0.27 ± 0.03 and 0.08 ± 0.02 respectively. Because a lower CoV represents higher homogeneity[186], these results indicate an overall increase in FA homogeneity within and a decrease in FA variance between subjects when using the 8Tx/15Rx RF coil with region-specific shimming. With this approach, the signal transmission was improved for the cerebellum. In the case of the neocortex with focus on the left motor area, homogeneity in all three cases was identical but RF shimming allowed for a higher maximum available FA.

3.3.4 Functional MRI performance

3.3.4.1 Temporal SNR

Fig. 3.8 shows tSNR maps of the 8Tx/15Rx coil normalized to the tSNR of the 1Tx/32Rx RF coil, reflecting the gain and loss when using the 8Tx/15Rx RF coil in an fMRI experiment of the cerebellum. For CP^+ excitation, the 8Tx/15Rx RF coil setup exhibits increased sensitivity within the central caudal regions of the cerebellum compared to the 1Tx/32Rx coil (lower part in Fig. 3.8A). The tendency of the 8Tx/15Rx coil setup to increase tSNR in central structures can be redirected to the transmit profile (c.f. Fig. 3.7E) and/or

the shape and sensitivity profile of the receive-only RF array. Within upper cerebellar regions, strong losses up to 30 % can be observed due to the non-optimized transmission profile. Losses in the lateral parts of the caudal cerebellum are visible as well. In contrast, using region-specific RF shimming (Fig. 3.8B) increases and homogenizes the gain within the lower cerebellar parts while simultaneously decreases the tSNR loss in upper structures. As it can be expected, the closer the structure of interest is located to the center of the head coil, the better the 1Tx/32Rx RF coil performs.

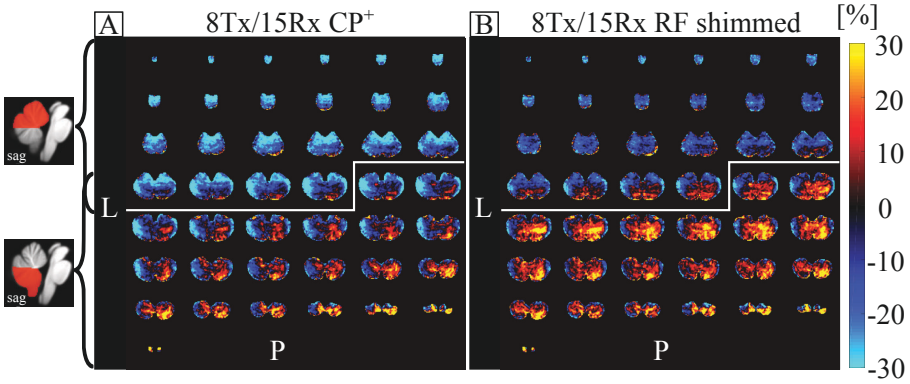

Fig. 3.8 Temporal SNR comparison. Axial, cerebellar sensitivity maps, i.e. tSNR of the 8Tx/15Rx coil normalized to the tSNR of the 1Tx/32Rx RF coil, displaying gains and losses when using the 8Tx/15Rx coil with CP^+ excitation (A) and with region specific RF shimming (B). The transition region between the cranial and caudal part of the cerebellum is highlighted with a white bar. Anatomical and sagittal views are shown on the left for orientation. Where the color changes to hot coloring, the 8Tx/15Rx coil outperforms the reference.

3.3.4.2 Second-level fMRI results

To examine whether the changes in sensitivity would influence the observation of functional activation in a finger-tapping fMRI experiment, second-level pseudo t-statistics were performed. The pseudo t-maps, acquired with the 1Tx/32Rx coil (Fig. 3.9A,D,G) indicate significant voxels in the expected areas. In comparison, the 8Tx/15Rx coil with CP^+ mode (Fig. 3.9B,E,H) results

in fewer significant voxels within cerebellar lobuli V and VI, but in similar t-values in lobule VIII. This can be explained by the inhomogeneous excitation pattern of the 8Tx/15Rx coil when the RF field is not properly shimmed. Using region-specific RF shimming (Fig. 3.9C,F,I), a homogeneous excitation with the Ernst angle resulting in similar t-statistics compared with the 1Tx/32Rx coil in the cranial cerebellar lobule can be observed (3.9A,C). However, in lobule VIII, the 8Tx/15Rx coil with RF shimming outperforms the 1Tx/32Rx coil (Fig. 3.9D,F). These results are consistent with the findings in the tSNR evaluation, indicating increased sensitivity of the 8Tx/15Rx coil in the caudal parts of the cerebellum with similar performance in the cranial cerebellum when using region-specific RF shimming.

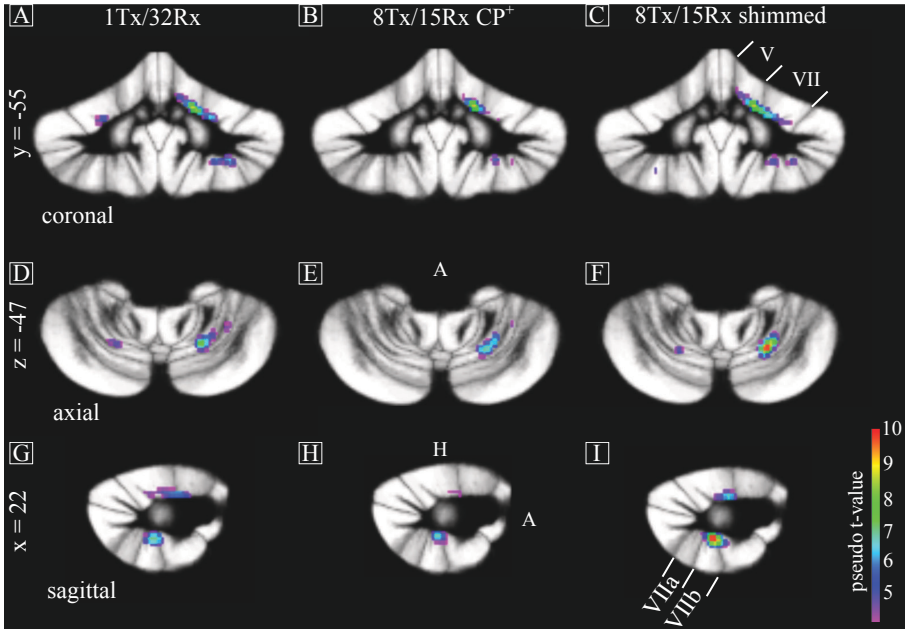

Fig. 3.9 Second-level fMRI results of the cerebellum. Pseudo t-maps ($p \leq 0.05$ FWE corrected) overlaid on the SUIT maximum probability template (coordinates given in SUIT space in mm) shown for the 1Tx/32Rx RF coil (A,D,G), the 8Tx/15Rx coil in CP^+ mode (B,E,H), and the 8Tx/15Rx coil with region-specific RF shimming (C,F,I). Number and location of the cerebellar lobuli of interest are shown in C and (I.

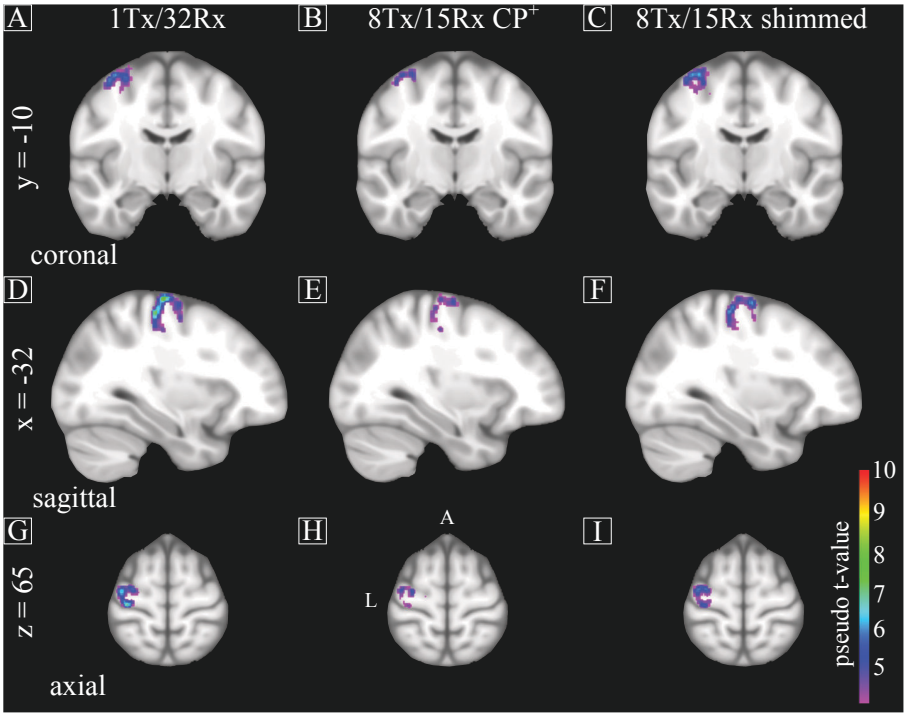

Fig. 3.10 Second-level fMRI results of the motorcortex. Pseudo t-maps ($p \leq 0.05$ FWE corrected) overlaid on the MNI template (coordinates in mm) shown for the 1Tx/32Rx RF coil (A,D,G), the 8Tx/15Rx coil in CP^+ mode (B,E,H), and the 8Tx/15Rx coil with region-specific RF shimming (C,F,I).

Fig. 3.10 shows the group-level fMRI results of the motorcortex. As expected, using the 1Tx/32Rx results in higher t-values in the motorcortex (Fig. 3.10A,D,G) compared to the 8Tx/15Rx coil (Fig. 3.10B,E,H) due to the high density of receiver elements. However, a large amount of sensitivity can be gained by tailoring the RF field toward the motorcortex (Fig. 3.10C,F,I). These results indicate that although only a quarter of the receiving elements are available for the neocortex, the sensitivity of the coil in combination with RF shimming is sufficient to acquire fMRI signal changes in finger tapping experiments.

3.4 Discussion

In this work, an 8Tx/15Rx RF coil combination with a region-specific B_1^+ shimming method were presented. With this setup, improved BOLD-fMRI of the human cerebellum could be performed. Simultaneously, the neocortex and more caudal brain regions could be included in the same FOV and robust BOLD responses in the motorcortex were measured. The performance of this RF coil setup and RF excitation method were evaluated and compared with a commercially available 1Tx/32Rx head coil.

The chosen approach to improve RF excitation during fMRI of the cerebellum uses different static phase-only B_1^+ shims in different anatomical regions along the z-dimension. This region-specific RF shimming method is a pragmatic and easy to implement approach in a 2D acquisition method. Furthermore, the used excitation method is easily transferable to commercially available parallel transmission–capable RF hardware. In the case of the cerebellum, region-specific RF shimming using the 8Tx/15Rx coil significantly improves FA homogeneity compared to the dielectrically improved CP^+ mode of the 1Tx/32Rx coil (Fig. 3.7). The comparisons between CP^+ mode and RF shimming within the 8Tx/15Rx coil indicate that it is this shimming capability that, together with the improved receive sensitivity due to the larger FOV along the z-dimension (Fig. 3.4), ultimately translates into higher tSNR (Fig. 3.8) and t-values in fMRI of the cerebellum (Fig. 3.9). Because of the ability to actively adjust the transmission pattern instead of using dielectric pads, less variance in RF homogeneity and in maximum FA could be observed. This could be enhanced by including the magnitude of the B_1^+ field in the optimization process, and therefore increase the degrees of freedom. However, the main advantage of the phase-only RF shimming approach is to avoid solutions of the cost function in which most of the RF power is applied on only a few number of channels, and, in combination with an unevenly distributed RF power per channel, potentially emerging local SAR hotspots. Because ho-

mogeneous excitation of the cerebellum was the primary goal, we restricted ourselves to phase-only RF shims. Outside the context of a finger-tapping fMRI experiment, increased transmission field homogeneity can potentially lead to a higher possibility in finding significant BOLD responses in the entire cerebellum.

Given the high density of receiving elements, the 1Tx/32Rx reference coil exhibits a higher image SNR in the neocortex than the 8Tx/32Rx coil, resulting in higher t-values in motor areas, as expected (Fig. 3.10). However, Fig. 3.10 also demonstrates that optimizing the transmit field to achieve an excitation with the Ernst angle in the ROI can at least partly compensate the 4-fold lower number of receiving elements in that area. Hence, the used coil setup combined with region-specific RF shimming offers to possibility to focus on study the cerebellum more precisely as part of a larger network.

In principle, more than three B_1^+ shims can be used to maximize B_1^+ homogeneity over the entire brain. As it has been shown, a generalized slab-wise multiband approach can lead to homogeneous excitation when using approximately 12 coronal slabs, each with a thickness of 12 mm, one to two B_1^+ mapping slices per slab, and a 16-channel Tx/Rx RF coil[163]. In general, time efficiency in acquisition and evaluation of B_1^+ maps, shim, or pulse calculation and sequence preparation decreases with the number of maps. Moreover, the calculation of RF pulses is more time-consuming than solving an optimization problem for static RF shimming, rendering multiband pulse design that aims for homogeneous whole-brain excitation more time-consuming in real applications. However, calculations can be performed during the structural scan, and a slab-wise approach is more time-efficient and reasonable than a slice-wise optimization, given slow spatial variations of B_1^+. Because static RF shims were applied without further optimization of transmit k-space trajectories, this slab-wise RF shimming approach is designed for 2D acquisitions. In a 3D acquisition, other techniques like k_t-points[97] have to be applied to

account for B_1^+ inhomogeneities. Another option for B_1^+ homogenization in 2D acquisitions is the design of spoke pulses[164,198] in a slab-wise[163] or in a simultaneous multislice manner[165,166]. However, the design of those pulses requires gradient trajectory optimization and may prolong experiment preparation time. Our RF optimization approach aims to provide a pragmatic solution to the problems of achieving large FOV coverage along with RF homogeneity and high SNR in the cerebellum while, at the same time, still being able to investigate potentially widely separated areas of the neocortex. Conditions hard to meet with conventional RF hardware at 7 T. Hence, our RF optimization approach may be attractive for time critical studies examining patient cohorts[199,200].

In this work, the VAST GRE-EPI method was used successfully with a 2-block acquisition design to acquire whole human brain images, whereby the main focus was on the cerebellum. The sequence parameters were chosen to obtain whole-brain coverage while sampling as fast as possible. However, a large FOV is in direct contrast to a fast sampling rate. Therefore, for the given parameters and a large FOV body gradient coil, a TR of 2.8 s was the minimum time to sample the brain with 64 slices. This TR is acceptable for functional paradigms in a block design, but event-related designs require faster sampling rates of, for example, 2 s[155]. However, as it has been shown that enlarging slice thickness in upper parts of the brain decreases measurement time[177], making the VAST technique superior over a 2D acquisition with an identical smaller slice thickness within the entire FOV. By using VAST, the focus was on the cerebellum, decreasing through-plane signal loss and sampling the cerebellum with a 1.5 mm isotropic resolution. Although the used resolution may drive the data to be partially in a physiological noise–dominated regime for the neocortex[201], where tSNR and therefore the sensitivity to detect changes in BOLD is approximately insensitive to FA variations[202], the data become thermal noise–dominated as soon as one operates in a low-SNR regime. This can be achieved either through small voxels or through reduced

baseline SNR in the first place. In this work, the SNR-starved regimes were the ROIs where improved excitation can increase sensitivity and therefore the ability to detect BOLD contrast. To decrease image acquisition time, portions of the neocortex could be neglected from the FOV to achieve a TR of 2 s or less. However, this depends on the specific experiment.

Because of non-equidistant slice positioning, a clear limitation of VAST is that it cannot be easily combined with a 2D simultaneous multislice acquisition[203]. Here, slice-specific or slab-specific B_1^+ shims can be combined in a multiband spoke RF pulse to achieve homogeneous excitation, while maintaining high spatial and temporal resolution[163,165]. The spoke pulses, however, come with tradeoffs between B_1^+ homogenization, SAR[204] (which is generally higher in simultaneous multislice applications), and off-resonance robustness[205]. Especially the latter can be a problem for cerebellar fMRI, as the performance of spoke pulses worsen near the ear canal cavities[206]. Solutions to this issue were recently presented[205,206], but they exhibit their own drawbacks. The VAST-EPI method with region-specific phase-only RF shimming addresses the problems of B_1^+ inhomogeneity and through-slice dephasing simultaneously in a pragmatic manner. However, a limit is given on further homogeneity improvement with phase-only as well as magnitude and phase RF shimming, because of the limited degrees of freedom especially for large ROIs.

Although the number of the receive elements of the 1Tx/32Rx RF coil is more than twice as high, it comes as no surprise that this RF receive array has a lower mean noise correlation coefficient compared with the presented 8Tx/15Rx coil setup. However, in terms of maximum noise correlation, the 8Tx/15Rx coil is preferable compared with the reference coil. The variance between measurements (Fig. 3.6C) indicates that element five of the receive-only array exhibited strong variation, which was caused by a damaged external transmit/receive switch. However, the overall findings in this work indicate that the damaged switch has no significant effect on the con-

clusions. Because of the higher number of receive elements and their equal distribution, the 1Tx/32Rx coil exhibits lower noise amplification when using parallel imaging. With moderate acceleration factors like R = 3 used in this work, the coil setups exhibited similar SNR losses of 5 % and 10 % for the 1Tx/32Rx and the 8Tx/15Rx RF coils, respectively. Using the receive-only array is beneficial for acceleration at the location of the cerebellum, because of its positive effect on image SNR. However, the position of the receive elements was not optimal for acceleration in the AP phase-encoding direction. As most of the fMRI studies use an AP phase-encoding direction, this direction was chosen.

Overall, a higher number of RF receive channels would improve the general capabilities to cover the whole brain and more caudal anatomies with high signal as dense as possible. Dedicated RF hardware can provide further acceleration potential, and improved transmit/receive switches could decrease noise correlation. Along with the excitation method being applied in this work, the different functional contributions of the cerebellum and its connectivity to cerebral and/or spinal structures can be revealed more easily using UHF MRI.

3.5 Concluding remarks

An 8Tx/15Rx RF coil combination together with a region-specific RF shimming method was presented for improving fMRI of the human cerebellum at 7 T, while covering as much of the brain and the spinal cord in the same FOV. The RF coil performance was compared with a conventional 1Tx/32Rx head coil with dielectric pads for passive RF shimming serving as reference. Although less than half of the coil elements were used for the 8Tx/15Rx RF coil, the results presented in this study show a significant gain in sensitivity for task-related BOLD responses in the cerebellum when using region-specific RF shimming.

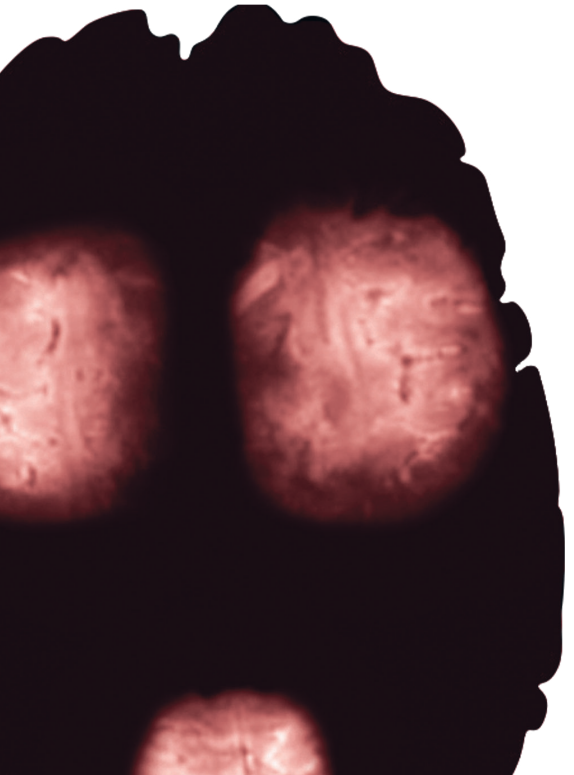

4

Zoomed imaging for high coverage laminar fMRI

Abstract

Sub-millimeter functional MRI is a promising technique to study brain function at the level of cortical layers opening up the possibility of inferring the direction of information flow. However, as many brain regions are organized in long-range networks, covering all regions within the same field-of-view (FOV) at high spatial *and* temporal resolution posses a major challenge for laminar fMRI.

In this work, we used parallel transmission (pTx) technology and designed 2D RF pulses to selectively excite multiple, specific areas of interest. The exclusion of unwanted signals enables higher parallel imaging (PI) acceleration capability which, in turn, allows all regions of interest to be imaged at high spatio-temporal resolution. Using 3D GRE-EPI to image a hypothetical network, we investigated the acceleration improvement using this zoomed imaging approach. Furthermore, we explored additional acceleration capabilities using phase-constrained (PC) parallel imaging and theoretically evaluated the improvement of PC PI by tailoring the 2D RF pulse transmit phase.

The results indicate that with zoomed imaging, all relevant areas can be covered and the image quality of those is improved compared to a non-pTx EPI sequence, where, to meet the identical volume TR, some areas could not be covered within the same FOV. Aiming for an identical net acceleration factor between pTx and non-pTx EPI, the quality improvement stems not from reduced g-noise but from an optimal excitation when using 2D RF pulses. It is shown that zoomed imaging can theoretically benefit from PC parallel imaging if optimal phase conditions are provided. This can be achieved by capitalizing on the 2D RF pulse' capability to shape the phase pattern of the target regions.

We conclude that zoomed multi-FOV imaging together with PC parallel imaging with optimal phases is a promising method to scan multiple, widely

spaced regions with high spatio-temporal resolution and increase the temporal efficiency of laminar fMRI.

4.1 Introduction

The previous chapter demonstrates the necessity for large FOV RF hardware to cover the entire brain and how the inhomogeneity problem at UHF can be addressed in a pragmatic fashion. But it also shows the general dilemma of obtaining high spatio-temporal resolution and large coverage: When the areas of interest can be covered in a small FOV, high spatial resolution is well compatible with fast sampling. However, to acquire a whole network of multiple, potentially widely spaced areas at high spatial resolution, the FOV must be increased accordingly. Encoding of such large matrices comes at the price of either slow sampling or a higher needed acceleration through parallel imaging (PI), whereby the latter strongly impairs the image SNR.

To overcome the encoding limits of RF coils and to allow for higher spatio-temporal resolutions, methods were proposed which try to reduce the aliasing and hence the burden on PI reconstruction by means of outer volume suppression[207,208] or inner volume excitation[209,210]. However, these approaches share a common disadvantage: they are unable to examine long-range connections because they can only be tailored to a single specific region of interest (ROI).

In this chapter, initial results of an approach to cover multiple, widely spaced brain areas within the same FOV at high spatial resolution using 2D RF pulses and parallel transmission (pTx) for selective excitation are presented. By excluding signals of no interest, image encoding of large matrices can be highly accelerated without too strong SNR penalty, as demonstrated recently[211–213]. In addition to selective excitation, we explore through numerical simulations additional acceleration capabilities capitalizing on phase-constrained (PC) parallel MRI[214–216], in particular the concept of virtual conjugate coils (VCC)[217].

4.2 Theory

4.2.1 Aliasing reduction by zoomed imaging

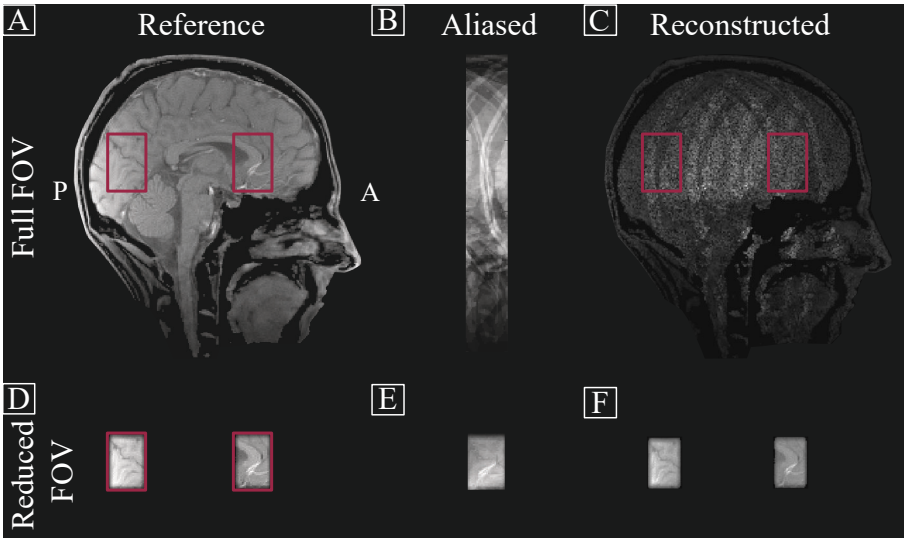

Fig. 4.1 Illustration of aliasing reduction through zooming. (A) Full FOV reference image. Two target regions are shown as red rectangles. (B) 8-fold undersampling results in an 8-fold smaller FOV and strong aliasing (AP PE direction). (C) Due to the limited amount of coil variation along the PE direction, the reconstructed image exhibits strong g-noise and aliasing artifacts. (D) Exciting only the ROIs, each FOV/4 in size, results in an effectively 2-fold aliased image as shown in (E) (ROIs exactly on top of each other). (F) As the ROIs are far away from each other and do not overlap with unwanted regions, the coil sensitivities are unique enough to disentangle the folded FOV without g-noise penalty.

Fig. 4.1 illustrates, based on simulations, how zoomed imaging reduces aliasing. Fig. 4.1A shows an example of a full FOV, fully sampled reference image acquired with 16 coils which was retrospectively 8-fold undersampled resulting in an aliased image as shown in 4.1B. Because the coil sensitivities do not vary enough relative to the amount of aliased pixels, the reconstructed image shown in Fig. 4.1C exhibits strong noise amplification and aliasing artifacts. However, as only two regions are of interest, most of the image encoding can

be considered wasteful. By exciting only the ROIs (red rectangles in 4.1A,C and D) the burden on the PI reconstruction is relaxed as only one forth of the FOV is excited in this example. Additional 8-fold undersampling is equivalent to a reconstruction problem of a 2-fold accelerated, full FOV image as the ROIs are exactly on top of each other and hence two pixels are aliased (Fig. 4.1E). Because the ROIs are far away from each other, they are covered by unique coil sensitivity profiles which results in an almost perfect reconstruction.

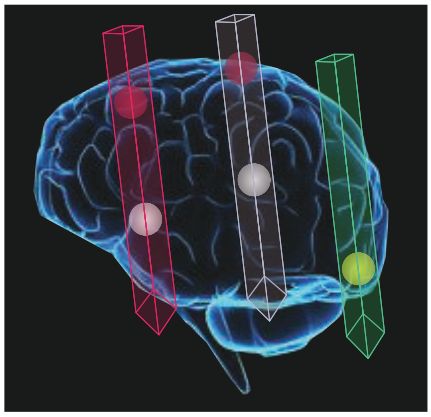

Fig. 4.2 Illustration of zoomed multi-FOV imaging. A hypothetical network comprising the left and right insula (white ROIs), areas around the left and right superior fontal sulcus (red ROIs) and the primary visual cortex (yellow ROI) is shown as five red ROIs. To cover all the ROIs within one FOV would require almost whole-brain coverage. Instead, the ROIs can be selectively excited using 2D RF pulses whose exemplary excitation patterns are shown as colored beams. By skipping PE lines, those beams are aliased and PI can be leveraged to disentangle them.

The selective simultaneous excitation of multiple ROIs can be achieved with 2D RF pulses whose target magnetization pattern forms "beams" (Fig. 4.2). Sampling acceleration leads to overlap of these beams which can be resolved using PI. Hence, the optimal beam placement depends on the spatial distribution of the ROIs and the receiver coil's sensitivity profiles. But other factors like the transmit sensitivities and the sampling limits of the used imaging sequence, e.g. nerve stimulation limits or the amount of distortions, need to be considered as well (see section 4.5).

FOV placement and PI reconstruction can in principle be performed in two ways: (a) A FOV which is large enough to cover the largest ROI in the set is encoded using no or only small in-plane acceleration. All ROIs are

then superimposed in one image. Similar to Simultaneous Multi-Slice (SMS) reconstructions[218,219], each ROI can be reconstructed individually. (b) Alternatively, a large FOV covering all ROIs and high 2D acceleration factors are chosen and the aliased ROIs are reconstructed using classical 2D-SENSE/2D-GRAPPA. Note that this approach essentially results in shifted aliasing patterns as in 2D-CAIPIRINHA[220]. Since k-space undersampling is equivalent to FOV reduction and, from a sampling perspective, 2D-SMS is equivalent to 3D volumetric imaging with 2D-CAIPIRINHA[221] both approaches are expected to lead to similar results. In this work, the latter is chosen because it has the practical advantage that the ROIs are reconstructed at the right position in the full FOV and no additional changes in the reconstruction is needed.

4.2.2 Phase-constrained parallel MRI for further acceleration

In the previous example (Fig. 4.1D-F), the FOV placement and acceleration was chosen such that two ROIs are collapsed exactly on top of each other. Considering this, the question arises whether further acceleration is possible. Any additional acceleration would result in aliasing within the reduced FOV which is difficult to disentangle given the limited amount of coil sensitivity variation. However, by incorporating the phase information into the reconstruction, the conditioning of the reconstruction problem can be improved.

4.2.2.1 Virtual conjugate coils

For k-space reconstructions, the virtual conjugate coil (VCC)[217] concept has been proposed. The measured signal $S_i(\mathbf{k})$ of coil element C_i can be expressed as

$$S_i(\mathbf{k}) = \int_V C_i(\mathbf{r})\rho(\mathbf{r})e^{i\phi(\mathbf{r})}e^{-2\pi i\mathbf{kr}}d\mathbf{r} = \mathscr{F}\{D_i(\mathbf{r})\rho(\mathbf{r})\}, \qquad (4.1)$$

where $\rho(\mathbf{r})$ is the spin density distribution and $\phi(\mathbf{r})$ is the object phase due to, e.g. B_0 inhomogeneity, the used contrast or the used sequence. D_i is the effective coil sensitivity incorporating the coil phase pattern and the background phase and $\mathscr{F}$ denotes Fourier transform operation. The Hermitian symmetric signal is given by

$$S_i^*(-\mathbf{k}) = \int_V C_i^*(\mathbf{r})\rho(\mathbf{r})e^{-i\phi(\mathbf{r})}e^{2\pi i(-\mathbf{k})\mathbf{r}}d\mathbf{r} = \mathscr{F}\{D_i^*(\mathbf{r})\rho(\mathbf{r})\}, \tag{4.2}$$

The signal in eq. 4.2 can be seen to be measured from a fictitious coil with effective sensitivity D_i^*. This virtual coil can be incorporated into the GRAPPA framework by expanding the number of used coils, i.e.

$$S_{i+N_C}(\mathbf{k}) = S_i^*(-\mathbf{k}). \tag{4.3}$$

All $2N_C$ coils are used for the reconstruction and final single coil images of the physical coils are combined. Effectively, eq. 4.3 denotes that in the GRAPPA kernel calibration process, the source points are extended by their complex-conjugate counterpart from the mirrored side of k-space to fit to one target point. Hence, additional encoding capability is provided.

4.2.2.2 Influence of background phase

Intuitively, the additional phase information can be seen as an additional coil. Therefore, analogous to optimal undersampling patterns for physical coils, there is an optimal phase distribution maximizing its benefit. In their original work, Blaimer et al.[217] described the impact of the background phase on the reconstruction by taking the extreme case of a single physical coil and a 2-fold acceleration as an example. Here, the only difference between two aliased pixels is the phase difference between them. Blaimer et al. showed that in this example, two pixels are maximally different if their signals are 90° out of

phase which can be realized by a linear phase ramp across the image. However, in reality the background phase consists of receiver and object phase which may vary considerable across the image, especially for T_2^*-weighted EPI readouts (see section 4.5).

The VCC concept is a natural extension to the described zoomed multi-FOV imaging approach. Fig. 4.3A-C shows the reconstruction of an 8-fold accelerated zoomed acquisition (same as in Fig. 4.1D-F). Doubling the acceleration factor to create an effective 4-fold acceleration results in aliasing within the small FOV (Fig. 4.3D) which cannot be reconstructed using coil sensitivities alone (Fig. 4.3E). However, when capitalizing on PC reconstruction with optimal phase distribution, most of the signal can be recovered (Fig. 4.3F).

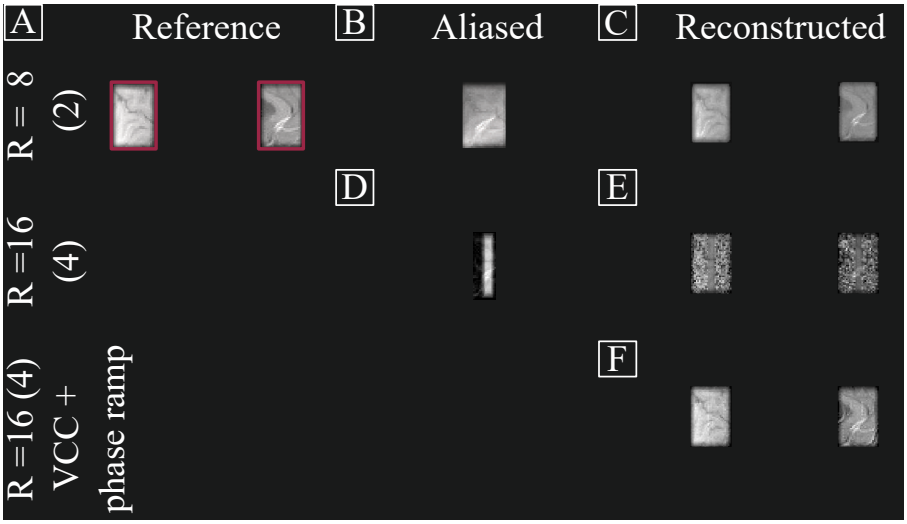

Fig. 4.3 PC reconstruction of small FOVs. (A-C) Reduced FOV excitation and the reconstruction of an 8-fold undersamling (same as in Fig. 4.1D-F). (D) Doubling the acceleration results in aliasing within the small FOV which cannot be disentangled using coil sensitivities alone as shown in (E). (F) By using VCC and optimal phase difference within the ROI, the image can be recovered.

Provided that the background phase is known, recent work has shown that an RF pulse phase can be calculated which yields an optimal phase distribution when applied to full FOV images using tailored spatially selective pulses[222,223]. In our work, we theoretically explore the effect of extending the described zoomed multi-FOV imaging approach to tailor magnitude and phase of the desired magnetization pattern in 3D GRE-EPI.

4.3 Materials & methods

Scans were conducted on a 7 T system (MAGNETOM 7 T, Siemens Healthcare, Erlangen, Germany) using the custom 8Tx/Rx coil as described in chapter 3. Only the transceiver coil and not the 7Rx-only array was used for the initial pilot experiment. The scanner was equipped with a large FOV body gradient coil with maximum gradient amplitude of 28 mT/m and slew rate of 170 mT/(m*ms). One male subject was scanned after giving informed consent according to the guidelines of the local ethics committee.

4.3.1 MR data acquisition

4.3.1.1 B_0 and B_1^+ mapping

After B_0 shimming, whole-brain B_0 maps were acquired using a dual-echo 3D GRE sequence. Parameters were: TR/TE1/TE2 = 30/1.03/3.03 ms, 4 mm isotropic resolution, 8° FA, 50 x 50 x 44 matrix size, 1560 Hz/px bandwidth, acquisition time = 1:49 min. The unwrapped[166] phase difference was used as the field offset ΔB_0 (eq. 2.52).

A transmit phase-encoded[90], T_2- and T_2^*-compensated DREAM sequence[89] was used to obtain complex transmit sensitivity maps. Parameters were: TR1/TR2 = 6.0/7.1 ms, TE1/TE2 = 1.98/3.86 ms, FA = 7°, nominal preparation pulse FA = 65°, 4 mm isotropic resolution, 64 x 64 x 19

matrix size, 1240 Hz/px bandwidth, 12 transmit PE steps, acquisition time = 1:30 min.

4.3.1.2 3D GRE-EPI sequence

To assess how high-resolution EPI can benefit from zooming, we investigate the coverage of a hypothetical network as shown in Fig. 4.2. It comprises the left and right insula (white ROIs in Fig. 4.2) and areas around the superior frontal sulcus (SFS, red ROIs), i.e. parts of the superior frontal gyrus (SFG) and the middle frontal gyrus (MFG). As an additional component, we included the primary visual cortex (V1, yellow ROI) to maximize the distance between the ROIs.

3D GRE-EPI[197] images with and without 2D RF pulses were acquired. In case of pTx, the following parameter were used: Sagittal orientation with AP as primary (PE_y) and LR as secondary (PE_z) phase encoding direction, TR/TE = 75/23 ms, 16° nominal FA (Ernst angle), FOV_{read} = 231 mm, 288 x 216 x 192 matrix size, 0.8 mm isotropic resolution, GRAPPA R = 4 x 4, volume TR (TR_{vol}) = 3600 ms, 6/8 partial Fourier (PF) factor along PE_y, 914 Hz/px bandwidth, 1.27 ms echo spacing, 6.03 ms pulse duration.

For reference, a 3D EPI sequence with conventional slab selective excitation was used with the following parameter: transverse orientation, AP as PE_y, TR/TE = 71/27 ms, 16° nominal FA, FOV_{read} = 192 mm, 240 x 240 x 48 matrix size, 0.8 mm isotropic resolution, GRAPPA R = 4 x 1, TR_{vol} = 3500 ms, 6/8 PF factor, 906 Hz/px bandwidth, 1.27 ms echo spacing, 2.56 ms pulse duration, bandwidth-time product (BWTP) = 22.6. Please note that in order to stay within comparable TR_{vol} without too strong acceleration, the coverage of the insula needed to be sacrificed.

For both sequences, 50 volumes were acquired to assess image quality by means of temporal efficiency, i.e. $tSNR/\sqrt{TR_{vol}}$.

4.3.2 pTx pulse calculation

All calculations and analysis were performed in MATLAB 2016a (The MathWorks Inc., Natick, MA, USA). 2D RF pulses were calculated using the spatial domain method[94] under the small tip approximation[93]. A variable density spiral-in transmit k-space trajectory[224] was chosen with a FOV of 200 mm, a resolution of 5 mm and a 2-fold undersampling outside of the high density center k-space portion. The trajectory and corresponding gradients are shown in Fig. 4.4.

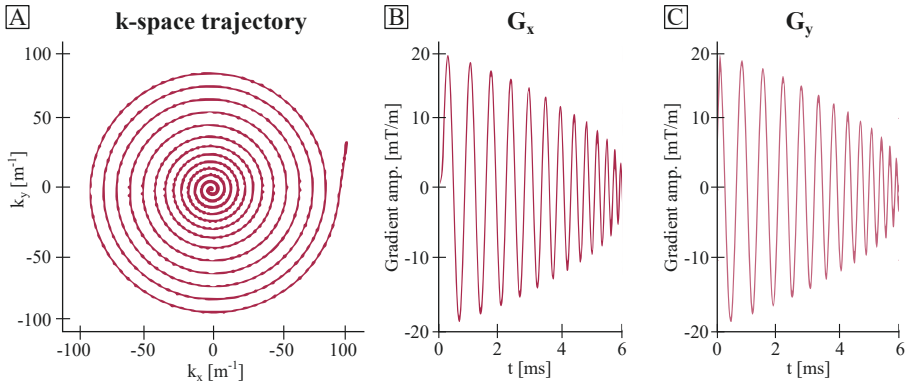

Fig. 4.4 Transmit k-space trajectory. (A) Spiral-in transmit k-space trajectory and (B,C) corresponding gradients.

The beam placement was chosen to cover all the five ROIs with as few as possible beams. To this end, we chose the long axis of the beams to be normal to the transverse plane and hence parallel to the readout direction (as schematically shown in Fig. 4.2). The targets themselves were defined semi-automatically. First, the regions were drawn as a NIFTI mask on the MNI template using ITK-SNAP[225] Version 3.6.0 (www.itk-snap.org). Then, the receive channel combined FID image of the DREAM dataset was transformed to the MNI template using the normalization tools of SPM12 Version 7487 (Wellcome Trust Centre for Neuroimaging, London). The inverse transformation

was subsequently applied to the target mask to create a target in subject space. The cost function (eq. 2.53) was minimized using the magnitude least-squares (MLS) optimization[95] with multi shift conjugate gradients least squares[226]. The resulting FA distributions were visualized with Bloch simulations.

4.3.3 Data reconstruction

Data were reconstructed offline using custom-written MATLAB routines. All EPI scans were noise prewhitened prior to the reconstruction. For the pTx EPI, GRAPPA[67] was calibrated on a 64 x 64 autocalibration (ACS) dataset using a 5 x 4 kernel. For the reference EPI, the calibration region was 48 x 36 with the same kernel size. The PF reconstruction was performed using POCS[60] with four iterations.

To assess whether the data quality would already benefit from a VCC reconstruction without optimal transmit phase, we implemented the VCC concept with additional regularization of the virtual coils[227] into our GRAPPA reconstruction. Intuitively, the VCC concept is not compatible with PF as VCC relies on data which has been omitted in PF. However, as it has been demonstrated recently[228], reconstructing the symmetrically sampled center part of k-space using VCC-GRAPPA and the periphery using standard GRAPPA can still improve the reconstruction quality. Hence, we followed the approach as described by Kettinger et al[228]. The noise enhancement penalty of the reconstruction was assessed by computing the g-factor using the pseudo-multiple-replica method[229] with 100 replicas.

4.3.4 Transmit phase optimization

Following the work of Kettinger et al.[223], we optimized the phase pattern imprinted by the 2D RF pulses (in the following referred to as RF phase) to result in less g-factor penalty in VCC-GRAPPA. To this end, the receiver and the intrinsic object phase must be known. We used the ACS data of

the full FOV non-pTx 3D EPI as an auxiliary scan on which ESPIRiT[230] was applied to estimate complex-valued coil sensitivities (example coil phase shown in Fig. 4.5A) which were subsequently used to extract the object phase (Fig. 4.5B) from the ACS image. Once known, the optimum phase can be calculated by minimizing a cost function containing the g-factor of a SENSE reconstruction.

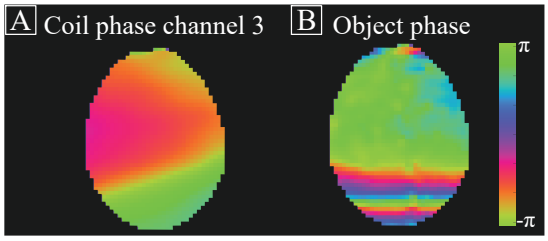

Fig. 4.5 Coil and object phase. (A) Transverse slices showing an example phase of the third receiver channel as extracted with ESPIRiT. (B) Intrinsic object phase of the full FOV non-pTx 3D GRE-EPI.

The SENSE problem (eq. 2.39) can be extended with the virtual conjugate coils by incorporating the background phase into the sensitivity matrix and expanding the set of equation:

$$\begin{bmatrix} \mathbf{S} \\ \mathbf{S}^* \end{bmatrix} = \begin{bmatrix} \mathbf{D} \\ \mathbf{D}^* \end{bmatrix} \boldsymbol{\rho} = \mathbf{D}_{\mathrm{VCC}} \boldsymbol{\rho}. \tag{4.4}$$

Similar to the original SENSE problem, the g-factor at voxel k in VCC-SENSE can be calculated as:

$$g_k = \sqrt{\left[\left(\mathbf{D}_{\mathrm{VCC}}^{\mathrm{H}} \mathbf{D}_{\mathrm{VCC}}\right)^{-1}\right]_{k,k} \left(\mathbf{D}_{\mathrm{VCC}}^{\mathrm{H}} \mathbf{D}_{\mathrm{VCC}}\right)_{k,k}}. \tag{4.5}$$

The sum-of-squares of eq. 4.5 was used as the cost function in a simplex search minimization where the optimum phase was initialized with a phase ramp spanning $\pi/2$ over the FOV. The RF target phase, i.e. the phase profile imprinted by the 2D RF pulse, is then the difference between the optimum and the object phase.

However, the initial simplex search does not take physical feasibility into account, i.e. the output phase is not always smooth. Hence, we performed an iterative polynomial fitting procedure varying the order from two to six. In the routine, voxels exhibiting a phase jump of larger than $\pi/2$ with respect to their surrounding were iteratively excluded from the binary mask defining the target region. This resulted in smooth phase maps maintaining the phase difference between aliased voxels with the exception of those exhibiting large phase jumps.

After obtaining the desired RF phase profile, the magnetization target was extended to be complex at the pTx pulse calculation stage. Hence, the cost function was minimized using least-squares as opposed to MLS.

4.4 Initial results

4.4.1 Zoomed imaging

Fig. 4.6A-C shows the excitation target as defined on the MNI template. Applying the inverse normalization transformation results in the target being in the space of the B_1^+ maps (Fig. 4.6D-F, cross-sectional views indicated by dashed lines). The simulated FA distribution obtained with a CP^+ excitation mode is shown in Fig. 4.6G-I for reference. Using all field information and the transmit k-space trajectory as shown in Fig. 4.4A, a 2D RF pulse exciting the target regions with the Ernst angle is calculated. The resulting simulated FA distribution is shown in Fig. 4.6J-L indicating a homogeneous excitation of the target regions with a root-mean-squared error (RMSE) of 24.6 %.

The average over 50 volumes for the zoomed 3D-EPI and for the reference EPI are shown in Fig. 4.7D-F and Fig. 4.7G-I, respectively. For anatomical reference, Fig. 4.7A-C shows an MPRAGE acquired during the study presented in chapter 3.

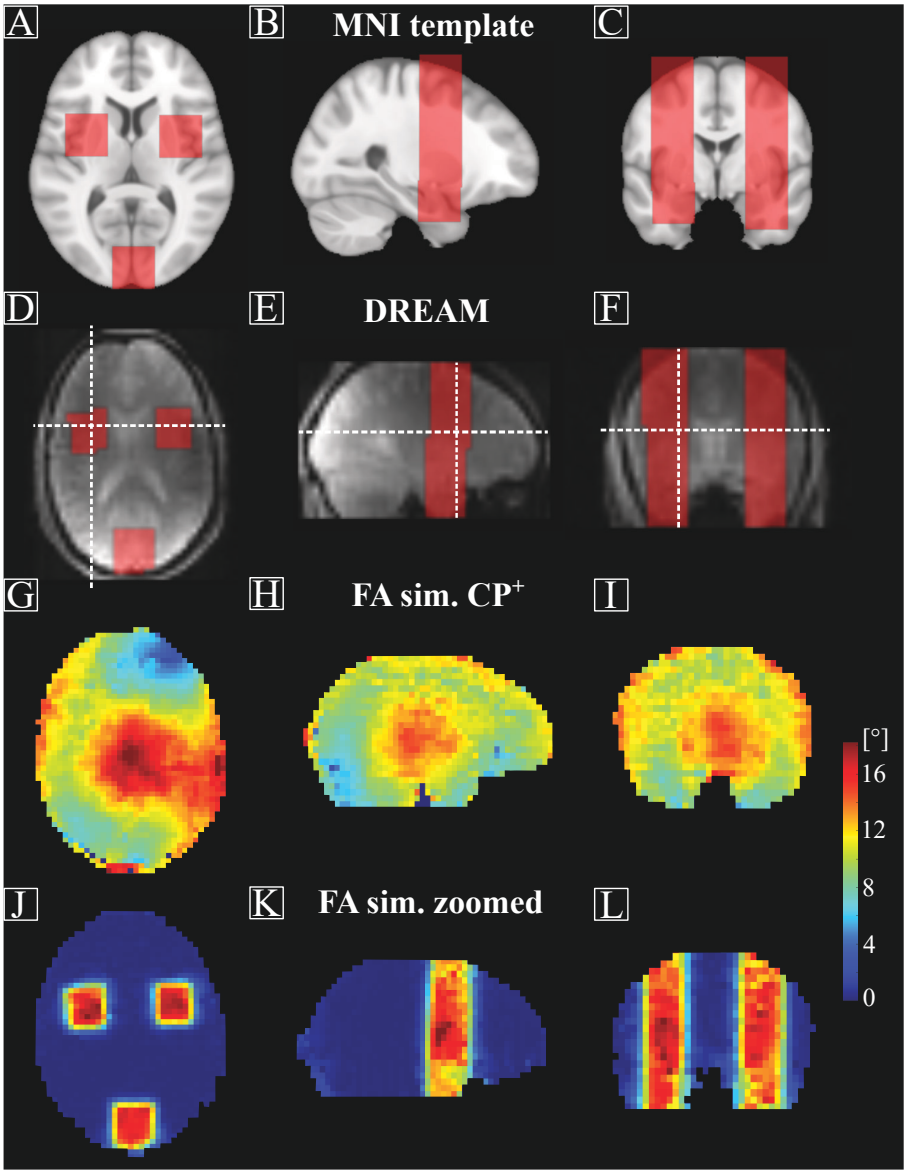

Fig. 4.6 Target definition & FA simulation. (A-C) Magnetization target defined on the MNI template. (D-F) The same target transformed into the coordinate space of the DREAM FID image. (G-I) Simulation of the resulting FA distribution when using conventional CP^+ mode and (J-L) when applying the calculated 2D RF pulse.

The dashed lines in Fig. 4.7A-C indicate the cross-sectional views and the white arrows show example ROIs. Please note that the EPI distortions were not corrected and, due to different angulations, differ between zoomed EPI and non-pTx EPI. For reference, Fig. 4.7H includes the coronal cross-section (dashed line) corresponding to that cross-section shown in 4.7B.

Using the 2D RF zooming approach, all ROIs (Insula, SFS, V1) could be covered within one FOV (Fig. 4.7D-F). In contrast, staying within the same range of TR_{vol}, the reference scan (Fig. 4.7G-I) could only cover the SFS and V1. In case of the full FOV reference, aliasing artifacts are present at the location of V1, seen best on the transverse view in Fig. 4.7G (red arrows). This can be explained by the high acceleration factor along PE_y relative to the number of receive channels. In contrast, aliasing artifacts are absent in the zoomed case (Fig. 4.7D) as the signal of unwanted regions is to a large extend suppressed. Using tailored 2D RF pulses results in more signal in superior brain regions like the SFS (green arrows in Fig,4.7E,F) compared to the reference (red arrows in 4.7H,I) which can be attributed to the inferior excitation profile of the CP^+ mode (Fig. 4.6G-I).

This is also reflected in the tSNR efficiency (Fig. 4.8). The V1 region exhibits comparable tSNR between zoomed and non-pTx EPI (mean $\pm$ std within ROI: 2.80 $\pm$ 0.82 and 2.61 $\pm$ 0.83, respectively) due to the sufficient transmit and receive sensitivity at this location (the coil elements are closest to the back of the head). In contrast, tissue around the SFS shows higher tSNR in the zoomed case (2.10 $\pm$ 0.48) compared to the reference (1.43 $\pm$ 0.36). Temporal SNR in the insula was 2.60 $\pm$ 0.66 for the zoomed EPI. In general, all ROIs exhibit equal or higher tSNR when using tailored 2D RF pulses.

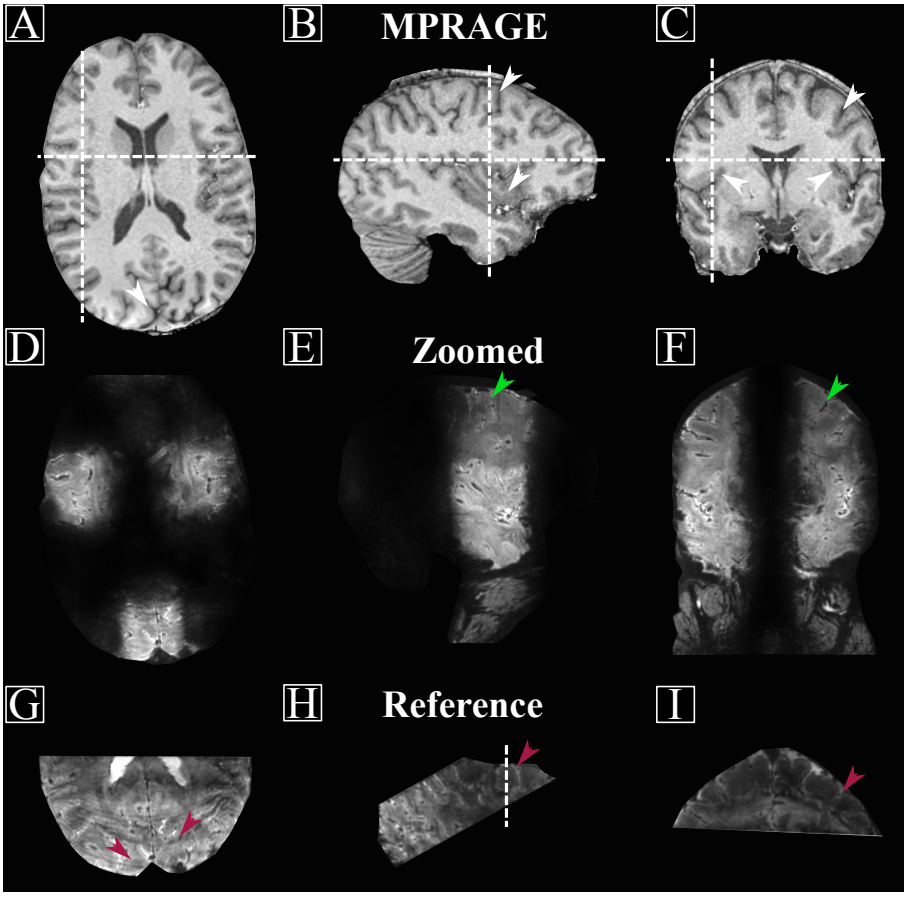

Fig. 4.7 Image quality. (A-C) T_1-weighted MPRAGE of the subject acquired during the study presented in chapter 3. Cross-sections and example ROIs are highlighted with white dashed lines and white arrows, respectively. (D-F) Average over 50 volumes acquired using zooming. High coverage of all ROIs as well as good image quality of the superior brain (green arrows) are visible. (G-I) In contrast, the reference exhibits low signal in these regions (red arrows in H and I), residual aliasing in V1 (red arrows in G) and not enough coverage to cover the insula. (For anatomical reference, the dashed line in H corresponds to the dashed vertical line in B.)

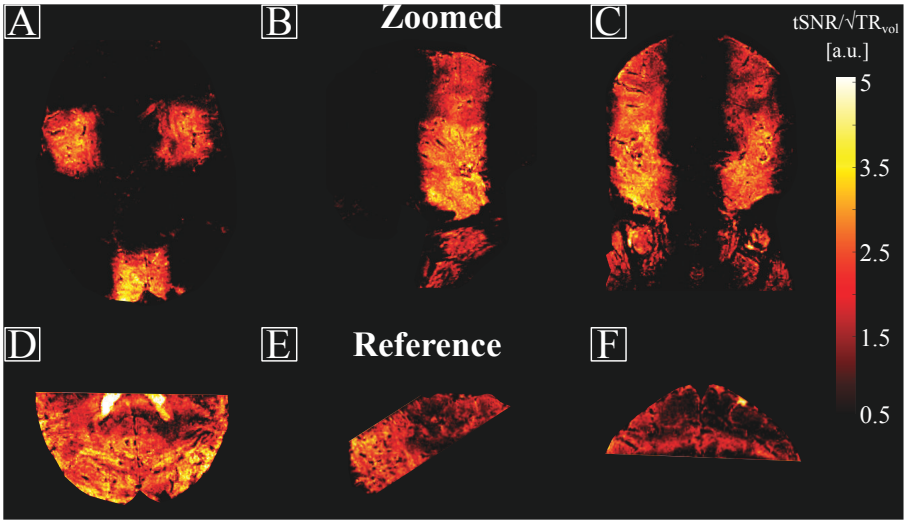

Fig. 4.8 tSNR comparison. (A-C) tSNR efficiency of the zoomed 3D EPI. (D-F) Efficiency of the full FOV reference. tSNR is approximately equal in posterior areas but higher in anterior/superior areas in case of zooming.

4.4.2 Noise amplification

To estimate how acceleration could benefit from zooming and VCC reconstruction, we calculated g-factors using the pseudo-multiple-replica method. Fig. 4.9A-E shows transverse 1/g-maps of the zoomed 3D EPI for a plane covering V1 and the insula (Fig. 4.9B,C, white dashed line in 4.9A) as well as for a slice covering the SFS (Fig. 4.9D,E, red dashed line in 4.9A). For both slices, a non-VCC, i.e. standard GRAPPA, and a VCC-GRAPPA reconstruction are shown. Fig. 4.9F-J shows the same comparison for the non-pTx 3D EPI. G-factors averaged within the ROIs are shown below each panel.

In both sequences, the RF coil exhibits a tendency of inferior PI capability on the right side of the FOV (more green/blue areas on the right of each slice in e.g. Fig. 4.9B or I). Comparing g-factors between zoomed EPI

and the reference indicate that noise amplification is slightly higher for the zoomed case. This can be explained by the amount of FOV reduction zooming could achieve: In total, approximately FOV/4 is excited, hence the total nominal acceleration factor of 16 corresponds to a total effective acceleration factor of approximately four in the zoomed case. However, on the one hand only a perfect excitation pattern would result in an exact 4-fold FOV reduction. Because some residual unwanted excitation is present (e.g. the red arrows in Fig. 4.10A), the effective acceleration factor is slightly higher than four. On the other hand the coil encoding burden is also unevenly distributed as more of the FOV is excited along PE_z (LR). This can be seen especially in the ROIs covering the insula which exhibit relatively high noise amplification (anterior ROIs in Fig. 4.9B and D). Because the acquisition was 4-fold accelerated along PE_z but the FOV was only reduced by approximately a factor two due to zooming, the ROIs in the folded image overlap significantly with one another (Fig. 4.10C). However, g-factors in areas covered by both sequences are of similar order but the zoomed EPI was able to include all ROIs in one FOV within an acceptable TR_{vol}.

The quantitative, averaged g-factors in Fig. 4.9B,C and D,E show a tendency that using VCC to reconstruct zoomed 3D EPI images leads to marginally better reconstructions although differences are very small. This tendency is not reproduced in the reference EPI (g-factor in 4.9H slightly higher than in 4.9G). These results indicate that 3D GRE-EPI with 6/8 PF is not very benefiting from VCC. At least if only the inherent object phase is taken into account.

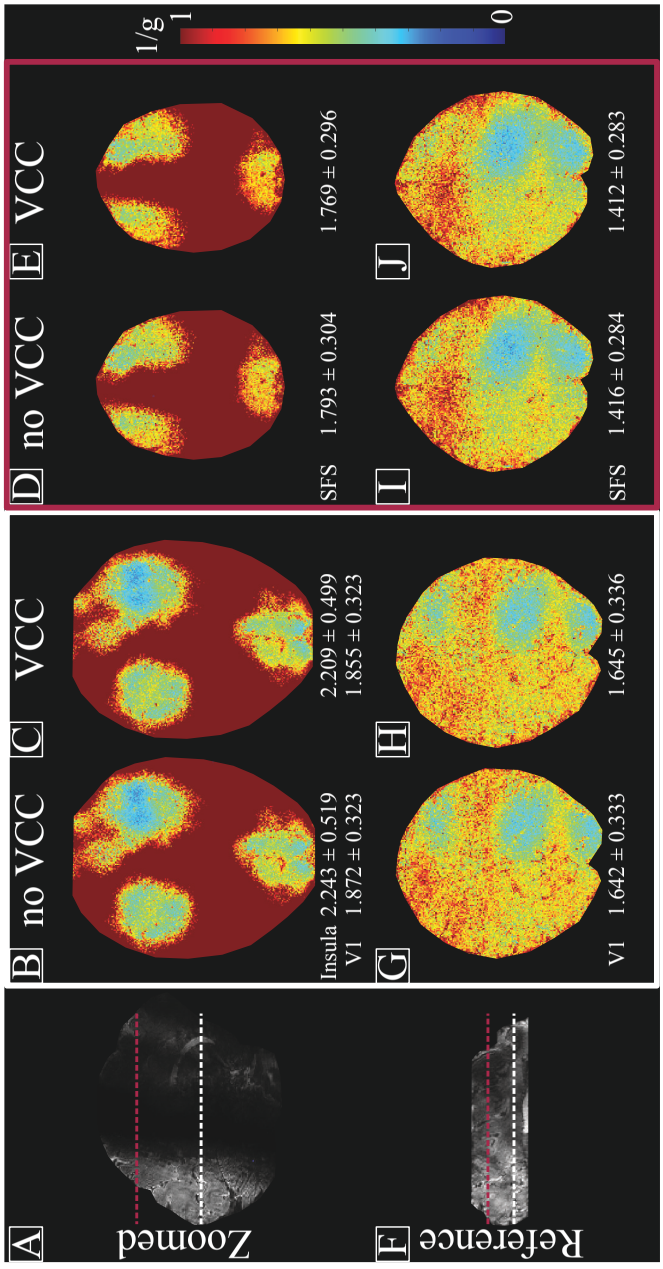

Fig. 4.9 G-factor comparison. (A-E) Transverse 1/g-maps for the zoomed 3D EPI showing one slice which covers V1 and the insula (B,C, white dashed line in A) and one which covers GM around the SFS (D,E, red dashed line in A). Standard and VCC reconstruction are compared and the mean and standard deviation of the g-factor within the ROIs are shown below each panel. (F-J) Same comparison for the non-pTx 3D EPI. Note that the images were not reoriented to allow for full visual inspection.

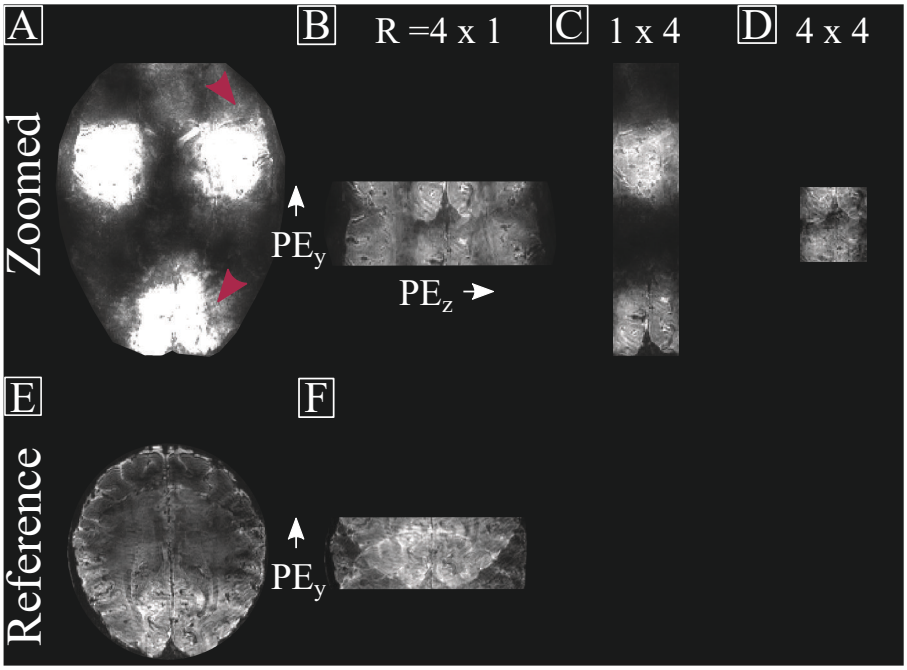

Fig. 4.10 Aliasing patterns. (A) Reconstructed volume average of the zoomed EPI windowed such that residual unwanted excitation as indicated by the red arrows are better visible. (B) Aliasing patterns when accelerating along PE_y, (C) along PE_z and (D) along both dimension. Overlap is high for the anterior ROIs when undersampling along PE_z. (E,F) Full and undersampled FOV for the non-pTx EPI.

4.4.3 Transmit phase optimization

To assess the theoretical feasibility of tailoring the RF phase to optimize the VCC reconstruction of zoomed imaging, phases and SENSE g-factors were simulated. For visualization purposes, acceleration was simulated along PE_z (LR) alone as the overlap in this dimension is the largest.

Fig. 4.11 shows optimization results for a 4-fold accelerated acquisition taking the coil and object phase as shown in Fig. 4.5 into account. As the object phase is almost constant along PE_z at the location of the ROIs (Fig. 4.5),

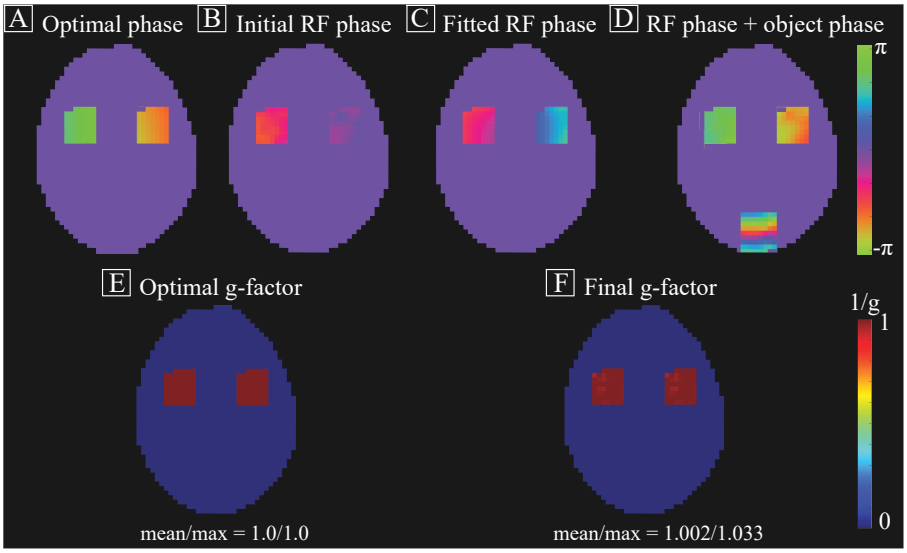

Fig. 4.11 4-fold acceleration along PE_z with optimal RF phase pattern. (A) Optimal phase distribution between the ROIs for LR PE encoding. The ROIs as a whole are 90° out of phase given the slow varying object phase along PE_z. (B) RF phase as the result of the simplex search leading to exactly the phase pattern in A. (C) Resulting phase pattern when fitting a polynomial to the initial RF phase. (D) The total image phase, i.e. fitted RF phase + object phase closely resembles the optimum phase distribution. (E) With the optimal phase, the g-factor is one, i.e. the reconstruction is theoretically perfect. (F) With the fitted RF phase, the final g-factor is close of being optimal.

the benefit of VCC using only the intrinsic phase information is limited. The optimal phase in Fig. 4.11A shows that for a perfect reconstruction, i.e. a g-factor of one (Fig. 4.11E), the ROIs as a whole need to be 90° out of phase, as expected since they completely overlap in an 4-fold smaller FOV (Fig. 4.10C). The RF phase as a result of the simplex search leading to exactly this optimal phase is shown in Fig. 4.11B. Fitting a polynomial to the initial RF phase while maintaining the phase difference between aliased voxels results in a phase as shown in Fig. 4.11C. Together with the phase of the object, the resulting phase pattern (Fig. 4.11D) closely resembles the optimum, reflected

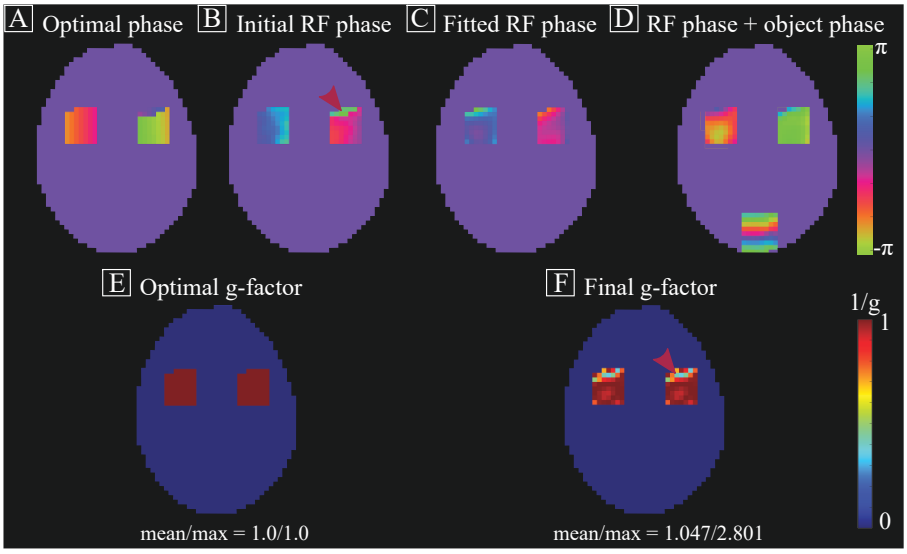

Fig. 4.12 8-fold acceleration along PE_z with optimal RF phase pattern. (A) Due to the aliasing within the small ROIs, the optimal phase shows a phase ramp along PE_z and also a discontinuity of some voxels with respect to their surrounding. (B) To meet this phase jump, the initial RF phase exhibits a discontinuity (red arrow) which is hard to achieve in practice. (C) By excluding the sets of aliased voxels which show this jump, the fitted RF phase pattern is smooth and (D) together with the object phase lead to a phase pattern agreeing well with the optimum. (E) The g-factor for the optimum phase is one. (F) As some voxels were excluded in the fitting, they exhibit a higher g-factor (red arrow). However, on average, the final g-factor is close to optimal.

by near optimal g-factors (Fig. 4.11F). Note that for aiding visual comparability between optimal (Fig. 4.11A) and final phase (Fig. 4.11D), a global phase offset was added to Fig. 4.11D.

In Fig. 4.12, the results for a more ambitious acceleration factor of eight are shown. Here, the optimal phase in Fig. 4.12A has a clear phase ramp within the ROIs along PE_z to account for additional aliasing within the small FOVs. The optimal and hence the initial RF phase as shown in Fig. 4.12B exhibit a discontinuity (red arrow in 4.12B) between a few voxels and their

surrounding. This phase jump cannot be resolved by a phase offset of all voxels within the aliased set. To meet the necessity of a smoothly varying RF phase, these voxels are ignored when obtaining the final RF phase as shown in Fig. 4.12C. The combined RF and object phase (Fig. 4.12D) are in an overall good agreement with the optimum except for the excluded voxels which show a higher g-factor in Fig. 4.12F compared to the rest (red arrow in 4.12F). However, on average, the final g-factor is close to the optimum and the RF phase is physically feasible.

To estimate how the excitation quality is affected by imposing an explicit RF phase, Bloch simulations were performed using 2D pTx RF pulses optimized for both image magnitude and phase. For reference, Fig. 4.13A shows the FA distribution as the result of the MLS optimization without RF target phase definition. Fig. 4.13B and C show the FA when imposing a smooth RF phase for a 4-fold acceleration (Fig. 4.13F) and for an 8-fold acceleration (Fig. 4.13G), respectively. As expected, imposing a target RF phase in a least-squares optimization decreases the excitation fidelity as indicated by increased RMSE. The more varying the RF phase needs to be, the higher the RMSE (Fig. 4.13C compared to Fig. 4.13B). However, the increase can be considered tolerable as the FA patterns still exhibit the desired shape and sufficient homogeneity within the ROIs. In contrast, imposing a discontinuous RF phase as shown in the case of Fig. 4.13H, where the initial RF phase prior to polynomial fitting was set as the target, results in a degraded quality of the excitation profiles (Fig. 4.13D) as indicated by the high RMSE. Especially at the location of the phase discontinuity (red arrow in 4.13D), excitation quality is poor. Note the high degree of similarity between the phase patterns in Fig. 4.13F and G and those shown in Fig. 4.11C and Fig. 4.12C, respectively.

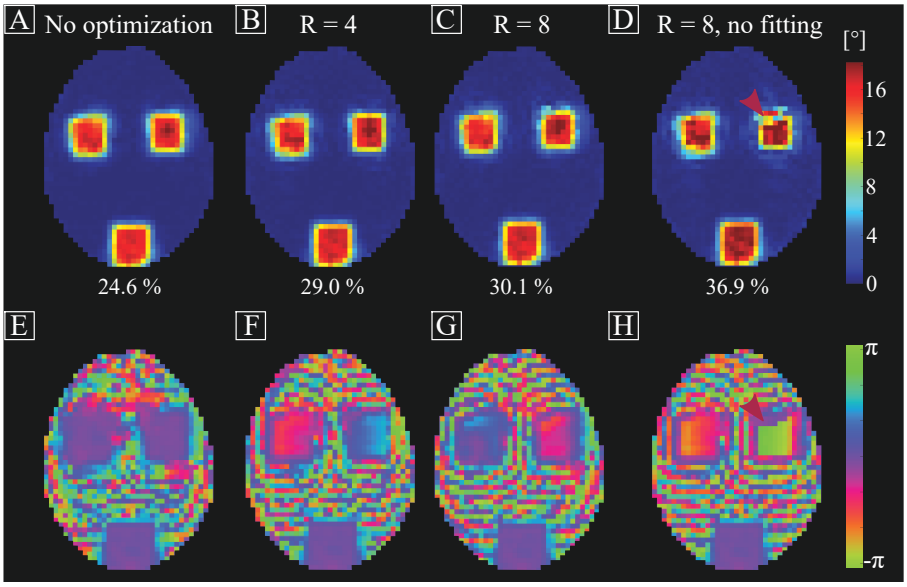

Fig. 4.13 Bloch simulations of target FA and RF phase.(A-D) Bloch simulations of the target FA distribution in the case of (A) MLS minimization, i.e. no explicit RF phase defined, (B) LS optimization for a 4-fold acceleration, (C) an 8-fold acceleration and (D) an 8-fold acceleration where the target RF phase was set to the initial phase prior to polynomial fitting. The FA profile shows impaired excitation fidelity at the location of the phase jump (red arrows in D and H). The excitation's RMSE is shown below each panel. (E-H) Simulated RF phase patterns. Note the similarity of the phase shown in F and G to those shown in Fig. 4.11C and Fig. 4.12C, respectively.

4.5 Discussion

In this work, the effect of the simultaneous selective excitation of multiple ROIs with 2D pTx RF pulses on image quality, coverage and acceleration capabilities was investigated using experiments and numerical simulations.

Scanning multiple, potentially widely separated ROIs of a network requires a large FOV coverage, hardly compatible with the demand of high spatio-temporal resolution needed for laminar fMRI. However, typically not

all of the brain contributes to a certain network. For instance, if the neuroscientific question in mind comprises the interaction of attention with the perception of certain sensory stimuli, then only those areas associated with attention and perception are of interest. Those areas can be efficiently covered with selective excitation by means of 2D RF excitation, i.e. zooming.

The qualitative (Fig. 4.7) and quantitative (Fig. 4.8) results indicate that with zooming, widely spaced ROIs like the insula, the SFS and V1, can be covered within one FOV which was not possible with an acquisition using standard slab selective excitation without accepting losses in sampling speed and/or image quality. In fact, to cover all ROIs in one FOV would require almost whole brain coverage using non-pTx EPI. For reference: with a 32 Rx-only head coil, typically a total 8-fold acceleration is feasible without too strong SNR penalty. With this acceleration, Whole-brain coverage at 0.8 mm isotropic resolution can be achieved in approximately 5 s. With the zoomed FOV approach, all relevant areas can be scanned within 3.6 s with a 4 x 4 undersampling, i.e. an acceleration twice the number of available receiving elements. It can be expected that the total 16-fold acceleration with the 8Tx/Rx head coil can be translated to a total acceleration factor of 32 using modern, commercially available multi-channel transceiver head coils. Investing all additional acceleration capability into undersampling along the secondary PE direction as TE needs to meet the optimal BOLD condition, TR_{vol} can be reduced to approximately 1.2 s. Regarding optimal TE, the relatively long duration of the 2D RF pulse (6.03 ms) may be intuitively seen as problematic. However, because the transmit k-space trajectory was spiral-in (Fig. 4.4), the bulk of the RF excitation is performed at the center of k-space which is sampled last. Hence, T_2^*-decay during the pulse and unnecessary TE extension can be seen to be less of an issue.

The results in Fig. 4.7 and Fig. 4.8 also demonstrate that the image quality and tSNR of the target regions is equal or better compared to the non-pTx

acquisition. However, the g-factor comparison between zoomed and non-zoomed acquisition (Fig. 4.9) indicates that the improved image quality is not due to an reduced g-noise penalty (e.g. Fig. 4.9D and 4.9I). In fact, the sequence parameters were chosen in such a way that the comparison between the two acquisition strategies is as fair as possible which includes an approximately identical net acceleration factor. Alternatively, the FOV of the non-pTx EPI could have been enlarged to also cover the insula. This would require an approximately doubled total acceleration factor to meet the same TR_{vol} which would render the resulting images unusable. Given the same net acceleration, it can be expected that noise enhancement is similar between the two sequences, as shown in Fig. 4.9. It must be noted however that imperfect suppression of unwanted signals (c.f. Fig. 4.10A) needs to be taken into account when developing an acceleration strategy for zoomed acquisitions.

The explanation for the improved image quality of the zoomed acquisition in Fig. 4.7 and 4.8 needs to be sought in Fig. 4.6G-L. A beneficial side effect of the selective excitation is that the ROIs are excited with the Ernst angle and that the excitation within the beams is homogeneous. Using a non-pTx excitation in CP^+ mode, as typical for single channel transmit systems, results in suboptimal excitation FA in certain areas (c.f. frontal part of the brain in Fig. 4.6G, red arrows in Fig. 4.7H,I and Fig. 4.8E,F). As the acquisition is in the thermal noise-dominated regime, optimal FA leads to an substantial gain in tSNR[201]. Using spokes[96,231] or the recently introduced concept of universal pulses[232] extended to slab-selective excitation can resolve the issue of transmission field non-uniformity in non-zoomed acquisitions.

Analogue to finding the optimal distribution of aliased voxels in an acquisition using CAIPIRINHA, the optimal beam placement depends on the overlap of the ROIs in the accelerated image and on the coil's receiving sensitivity profiles. However, other factors need to be considered as well. Analogue to the acceleration of the acquisition, acceleration of the transmit k-

space traversal and hence the fidelity of the excitation profile depends on the coil's transmit sensitivity. For the used coil configuration in this work (see Fig. 3.1B), transmit profiles vary the most in the transverse plane hence the design of RF pulses exciting beams perpendicular to this plane benefits the most from the pTx capability. Since primary phase encoding is typically performed anterior-posterior to allow more tolerable distortion in fMRI, a sagittal orientation, i.e. a readout along the head/feet direction parallel to the direction of the beams, and PE encoding of the short axes was chosen. Because the bandwidth of the readout direction is much higher compared to the PE direction, the coverage along the long axis of the head comes more or less 'for free'. The resulting acquisition of additional areas may provide helpful landmarks (e.g. the temporal lobe in Fig. 4.7G) in the (co)registration of laminar fMRI data which require special attention (for review, see Polimeni et al.[233]). In addition, readout along the long axis comes with the advantage of reduced impact of aliasing with residual unwanted signals. For instance, beams and readout direction could have been chosen from left to right to cover all ROIs with the same number of beams. However, all unwanted residual signal along the entire head/feet axis would overlap with the ROIs increasing the burden on the PI reconstruction. Another practical consideration are nerve stimulation limits which are typically reached faster with a readout along the head/feet dimension. However, no limits were reached during the acquisitions, sequence simulations using typical 7 T gradient coils did not show any limits violation and sagittal readouts have been successfully used recently[234]. In future work, an algorithm could potentially be designed which optimizes the beam placement in terms of coverage and acceleration given the target ROIs and the mentioned constraints. In addition, acceleration capabilities and signal quality using modern high-density RF transceiver coils can be investigated.

The g-factor comparison between conventional and VCC-GRAPPA reconstruction of the experimental data (Fig. 4.9) indicates that image quality

improvements of PF accelerated 3D GRE-EPI data using VCC are limited. This can be explained by two observations: First, k-space Hermitian symmetry of GRE-EPI is inherently perturbed due to the long sampling time of a full EPI echo train relative to T_2^*, especially at high spatial resolution. Hence, acceleration by means of relying on k-space symmetry is limited and violation of the symmetry assumption can cause artifacts if not taken into account in the reconstruction[227]. Second, the usage of partial Fourier itself, as typically needed for laminar fMRI at UHF to account for the shorter T_2^*, limits the benefit of VCC because this method relies on signals which have been omitted in PF. Our findings in Fig. 4.9 are in line with those presented in the study performed by Kettinger et al.[228] showing that with a 4-fold acceleration and a PF factor of 6/8, the SNR gain using a VCC reconstruction is close to zero. However, the comparison presented in Fig. 4.9 and in the study of Kettinger et al. do not take other than the coil and object phase variations into account.

Using the example of image acceleration along PE_z (left/right), the possibility to improve the VCC reconstruction[222,223] of the zoomed acquisition was theoretically investigated (Fig. 4.11-4.13). It was first noticed, that the object phase of the full FOV reference scan does not vary substantially along PE_z at the locations of the anterior ROIs (Fig. 4.5). Hence, little gain in the image quality can be expected. By optimizing the RF phase to result in a 90° phase difference between the ROIs in case of a 4-fold acceleration (Fig. 4.11) the theoretically achievable g-factor is close to the optimum. The benefit of VCC-GRAPPA with optimum phase in zoomed multi-FOV imaging can be seen more clearly when the acceleration is further increased to an extend where the voxels are overlapping within the ROIs. This extreme aliasing cannot be resolved by coil sensitivities alone, but capitalizing on a optimized phase differences, the reconstruction can be improved drastically (Fig. 4.12). However, physical feasibility needs to be taken into account as otherwise excitation quality is impaired (Fig. 4.13D,H).

At this point, some practical considerations of target phase optimization need to be discussed: Section 4.4.3 shows phase optimization results for a 1D acceleration only. But as the zoomed experiment was accelerated in two dimension, the VCC phase optimization approach needs to be adapted to 2D. Although technically feasible, this could potentially degrade the theoretical gain in image quality because the anterior ROIs would alias with the posterior ROI (c.f. Fig. 4.10D) which exhibits a strong varying object phase (Fig. 4.5 and 4.11D). As this may result in a strong varying optimal phase pattern, the demand of a smooth phase resulting in this optimal phase may be more difficult to meet. In addition, optimization was only performed on a single slice chosen such that it contains the maximum number of aliased voxels. As it is likely that the object phase varies along the direction of the beam, the RF phase optimization needs to be extended to 3D. This implies the necessity for 3D rather than 2D pTx RF pulses. Although initial work has shown that inner volume excitation with 3D RF pulses is feasible[235,236], the pulses or the RF pulse calculation are impractically long, and, to the best of our knowledge, the extension to several ROIs is yet to be shown. Finally, other sequences than GRE-EPI are more compatible to VCC and may benefit more from phase optimization because of slow varying object phases and/or less k-space asymmetry. All these mentioned considerations open up directions for future research.

4.6 Concluding remarks

This chapter presents an approach to scan multiple long-range connections at sub-millimeter resolution within one field-of-view. To this end, a large coverage, multi-transmit RF coil and 2D RF pulses were used to excite only the areas of interest in a 3D GRE-EPI sequence. The zooming approach can cover all relevant areas and the image quality of those is improved compared

to a non-pTx EPI sequence, where, to meet the identical volume TR, some areas could not be covered within the same FOV. It is shown that zoomed imaging can theoretically benefit from phase-constrained parallel imaging if optimal phase conditions are provided. This can be achieved by capitalizing on the 2D RF pulse' capability to shape the phase pattern of the target regions. The results presented in chapter 3 and in this chapter show that at present, high resolutions and time-efficient coverage of all relevant areas are possible but the SNR gains using the pTx capability of the 8-channel transceiver coil are traded with the SNR losses due to the lack of receive channels compared to commercially available RF coils. To beat current standards, high-density multi-transmission RF coils (see, e.g. Rietsch et al.[237] and section 7.1 of the general discussion) are needed. Together with the method presented in this chapter, the possibility is opened up to cover multiple, widely spaced regions with high spatio-temporal resolution and high SNR. This might push the limits of temporal efficient laminar fMRI being so far restricted to small field-of-views.

This research was funded by the DFG grant 310872863. We thank Philipp Ehses (German Center for Neurodegenerative Diseases (DZNE), Bonn, Germany) for providing the basic code for the reconstruction and Desmond Tse (Center for Functional and Metabolic Mapping, Western University, London Ontario Canada) for providing the toolbox for pTx calculation.

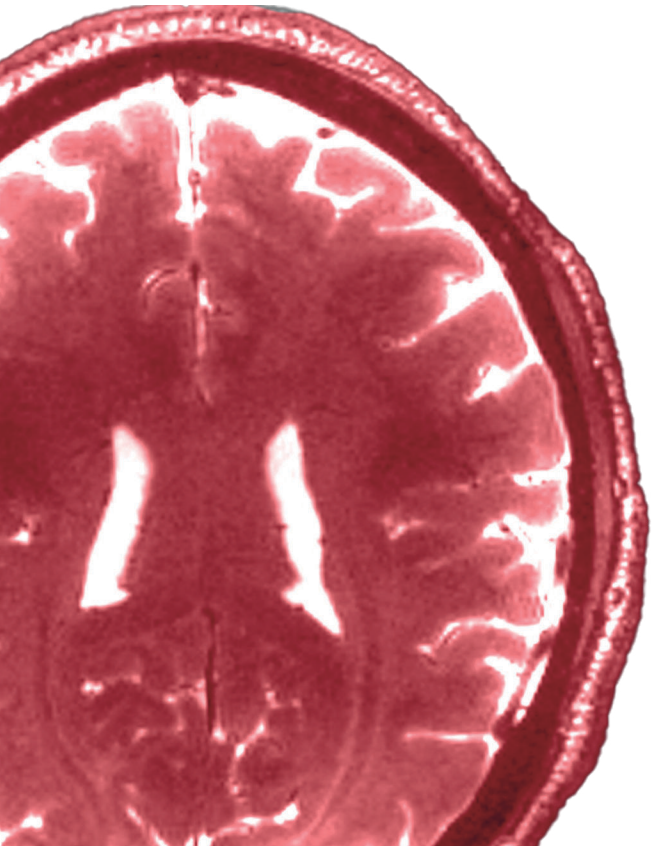

5

Laminar fMRI using T_2-prepared multi-echo 3D FLASH

Associated publication: **Pfaffenrot, V.**, Voelker, M. N., Kashyap, S., and Koopmans, P. J. "Laminar fMRI using T_2-prepared multi-echo FLASH". in: *NeuroImage* 236 (2021).

Abstract

Functional MRI using BOLD contrast at a sub-millimeter scale is a promising technique to probe neural activity at the level of cortical layers. While GRE-BOLD sequences exhibit the highest sensitivity, their signal is confounded by unspecific extravascular (EV) and intravascular (IV) effects of large intracortical ascending veins and pial veins leading to a downstream blurring effect of local signal changes. In contrast, SE-fMRI promises higher specificity toward signal changes near the microvascular compartment. However, the T_2-weighted signal is typically sampled with a gradient echo readout imposing additional $T_2^{'}$-weighting.

In this work, we used a T_2-prepared (T_2-prep) sequence with short GRE readouts to investigate its capability to acquire laminar fMRI data during a visual task in humans at 7 T. By varying the T_2-prep echo time (TE_{prep}) and acquiring multiple gradient echoes (TE_{GRE}) per excitation, we studied the specificity of the sequence and the influence of possible confounding contributions to the shape of laminar fMRI profiles. By fitting and extrapolating the multi-echo GRE data to a $TE_{GRE} = 0$ ms condition, we show for the first time laminar profiles free of $T_2^{'}$-pollution, confined to gray matter. This finding is independent of TE_{prep}, except for the shortest one (31 ms) where hints of a remaining intravascular component can be seen. For $TE_{GRE} > 0$ ms a prominent peak at the pial surface is observed that increases with longer TE_{GRE} and dominates the shape of the profiles independent of the amount of T_2-weighting. Simulations show that the peak at the pial surface is a result of static EV dephasing around pial vessels in CSF visible in GM due to partial voluming. Additionally, another, weaker, static dephasing effect is observed throughout all layers of the cortex, which is particularly obvious in the data with shortest T_2-prep echo time. Our simulations show that this cannot be explained by intravascular dephasing but that it is likely caused by extravascular

effects of the intracortical and pial veins. We conclude that even for TE_{GRE} as short as 2.3 ms, the $T_2^{'}$-weighting added to the T_2-weighting is enough to dramatically affect the laminar specificity of the BOLD signal change. However, the bulk of this corruption stems from CSF partial volume effects which can in principle be addressed by increasing the spatial resolution of the acquisition.

5.1 Introduction

The increased signal-to-noise ratio and sensitivity of functional magnetic resonance imaging (fMRI) at ultra-high ($\geq$ 7 T) magnetic field strengths enable researchers to spatially map brain responses on a sub-millimeter level in humans. At this high-resolution scale, fMRI can probe neuronal activity at the level of cortical columns[239–241] and layers[242–247]. Especially layer fMRI promises to be of particular value for neuroscientists by elucidating directionality of interactions between distinct brain areas[234,248,249] and testing computational theories of brain function[250].

The contrast mechanisms in fMRI can be coarsely classified into blood oxygenation level dependent (BOLD) and non-BOLD contrasts. Detailed reviews on the pros and cons of BOLD and non-BOLD methodologies are given in Koopmans et al., 2019[128] and Huber et al., 2019[143], respectively. All contrast mechanisms have in common, that they link neuronal activity to hemodynamic changes being measured with fMRI. Therefore, the spatio-temporal characteristics of the fMRI signal are given by vascular physiology and MRI parameters[110,115,119,129,251,252]. In the case of BOLD fMRI, it is well known that a gradient echo (GRE) BOLD weighted sequence has a high sensitivity toward activity induced signal changes. However, its sensitivity stems from intravascular (IV) and extravascular (EV) field effects at the level of capillaries and larger draining veins. While the capillary compartment is close to the neuronal source of activity, intracortical veins (ICV) drain blood downstream perpendicular to the cortex and merge into pial veins parallel to the cortex[21]. EV effects due to static dephasing i.e. negligible spin diffusion around the vessel, increase downstream due to an increase in ICV density from deep to superficial layers and due to long ranging EV effect of pial veins on the parenchyma. This downstream effect blurs local activity over a larger spatial scale decreasing specificity of GRE BOLD[113,253]. IV effects add to the drain-

ing vein problem due to increasing cerebral blood volume (CBV) of veins toward the surface[115]. However, given typical echo times at high field strengths, IV effects are assumed to be negligible[119,129,209]. Nevertheless, a systematic bias toward the pial surface in GRE BOLD layer fMRI is observed[244,246,254]. In contrast, a spin echo (SE) weighted BOLD experiment is most sensitive toward T_2-changes around small vessels. Here, the EV contrast mechanism around small capillaries is of a dynamic nature i.e. not refocusable with a 180° pulse whereas EV effects around large veins are refocused. Taking together, these characteristics lead to higher specificity toward the capillary compartment at the price of lower sensitivity relative to a GRE sequence[128,130,136].

Several studies have investigated characteristics of T_2- and T_2^*-weighted BOLD fMRI at different field strengths and different echo times in simulation[119,129,252,255,256] and in experimental studies[209,257–260]. In the context of neuroscientific application, a practical implementation of T_2-weighting either requires fast readouts and/or high parallel imaging acceleration. As an example, T_2-weighting is combined with echoplanar imaging (EPI) readout modules to increase sampling efficiency[137]. However, during the long signal readout, unspecific $T_2^{'}$-effects can re-emerge which can be addressed by segmenting the EPI readout at the cost of reduced temporal resolution. To the best of our knowledge, the systematic assessment of the effect of additional $T_2^{'}$-weightings during the readout on the specificity of laminar BOLD responses has so far only been performed in animals at 4.7 T[138].

As an alternative to SE-EPI, T_2-prepared (T_2-prep) sequences with short 3D FLASH readouts[261] have been proposed to minimize additional $T_2^{'}$-pollution and geometric distortions encountered in EPI. In this work, we designed a T_2-prep sequence for laminar fMRI applications. We analyzed the signal characteristics of this sequence via numerical simulations and performed a multi-echo laminar fMRI study targeting primary visual cortex at 7 T. Our goals were two-fold. First, we were interested in the capability of

this technique to acquire laminar fMRI data as done previously[148]. Second, by varying the T_2-prep TE and acquiring multiple gradient echoes per excitation, we studied the specificity of the sequence and the influence of possible confounding contributions from EV and potential IV effects to the shape of laminar fMRI profiles in humans.

5.2 Materials & methods

5.2.1 MR data acquisition

Data were acquired on a 7 T system (MAGNETOM 7 T, Siemens Healthcare, Erlangen, Germany) equipped with a 32 channel head coil (NOVA Medical Inc.). Six subjects (3 male, 3 female; 27.3 $\pm$ 3.4 years old) were scanned after giving informed consent according to the guidelines of the local ethics committee. B_0 shimming and B_1 calibration was performed locally on primary visual cortex.

5.2.1.1 Structural scans

In a session separate from the functional sessions, a T_1-weighed MPRAGE was used to acquire a whole brain structural dataset with 0.75 mm isotropic resolution. The following parameters were used: Sagittal orientation, matrix size 320 x 320 x 256, TE/TR/TI = 1.48/2500/1100 ms, bandwidth 560 Hz/px, flip angle (FA) 6°, GRAPPA R = 2, acquisition time = 5:58 min, no fat saturation, WURST pulse[262] for inversion.

5.2.1.2 Functional scans

Functional data at three different spin echo times (TE_{prep}) of 31 ms, 50 ms and 70 ms were acquired in a pseudo-random order on three different days

using a T_2-prepared 3D FLASH, center-out encoded sequence shown in Fig. 5.1A. The T_2-prep module consisted of a $90°_x$ hard pulse (1 ms duration) followed by two $180°_y$ adiabatic pulses. Using Bloch simulations (mrsrl.stanford.edu/~brian/blochsim/), we compared several adiabatic pulses as summarized in table 5.1. The design objectives were RF power and an inversion efficiency of > 95 % for transmission fields $B_1 \geq 5$ μT within a frequency range of $\Delta B_0 = \pm 100$ Hz. The comparison led to the decision to use an adiabatic Gaussian pulse[102] (13 ms duration, $\beta = 3.03$, frequency sweep $\Omega = 500$ Hz) in the experiments.

Tab. 5.1 Modulation functions of the compared adiabatic inversion pulses $B_1(t) = F_1(t)\exp(-2\pi i F_2(t))$, $|t| \leq T/2$, $T \equiv$ total pulse duration, $\Omega \equiv$ total frequency sweep.

Pulse	$F_1(t)$	$F_2(t)$
HS[a]	$\operatorname{sech}(\beta t)$	$-\frac{\mu}{2\pi}\log(\operatorname{sech}(\beta t))$
Gaussian[b]	$\exp\left(-\frac{\beta^2\tau^2}{2}\right)$	$\int \frac{\Omega}{2}\frac{\operatorname{erf}(\beta\tau)}{\operatorname{erf}(\beta)}\,dt$
Sin/Cos[c]	$\sin\left(\pi\frac{\tau}{T}\right)$	$-\int \frac{\Omega}{2}\cos\left(\pi\frac{\tau}{T}\right)dt$
HS4[d]	$\operatorname{sech}(\beta\tau^n)$	$\iint \Omega\operatorname{sech}^2(\beta\tau^n)\,d\tau dt$
WURST[e]	$1-\left\lvert\cos\left(\pi\frac{\tau}{T}\right)\right\rvert^n$	$\frac{\Omega}{2}\tau\left(\frac{\tau}{T}-1\right)$

[a] [101] $\beta = 375$ rad/s, $\mu = 5$
[b] [102] $\beta = 3.03$, $\Omega = 500$ Hz, $-1 \leq \tau \leq 1$
[c] [263] $\Omega = 800$ Hz, $0 \leq \tau \leq T$
[d] [102] $\Omega = 800$ Hz, $n = 4$, $-1 \leq \tau \leq 1$
[e] [264] $\Omega = 1500$ Hz, $n = 20$, $0 \leq \tau \leq T$

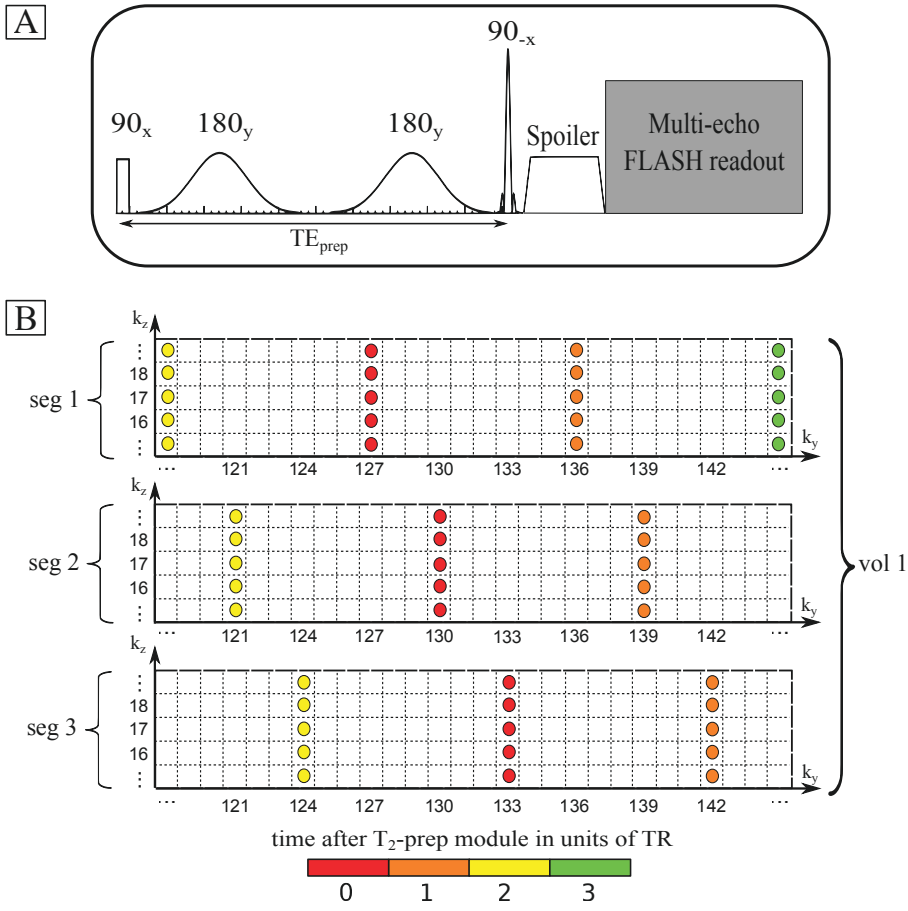

Fig. 5.1 T_2-prep sequence. (A) Schematic of the sequence. The used T_2-prep module consists of a 90°$_x$ hardpulse followed by two adiabatic Gaussian 180°$_y$ pulses. The echo at TE_{prep} is brought back to the longitudinal axis with a broadband 90°$_{-x}$ sinc pulse which simultaneously excites the so far not influenced fat. Unwanted transverse magnetization is spoiled prior to a multi-echo 3D FLASH readout. (B) Sampling scheme of one multi-echo volume. In order to minimize the effects of T_1-relaxation which introduces unwanted, non-T_2-weighted magnetization, both phase encode dimensions are segmented and acquired center-out. k_y is 3-fold undersampled and 3-fold segmented. Each k_z-line is preceded by a T_2-prep module i.e. 32-fold k_z-segmentation. The k-space coordinates are given as numbers on the axis of each segment, respectively.

A broadband $90°_{-x}$ sinc pulse (2 ms duration, 3 kHz bandwidth) was used to flip the spin echo back to the longitudinal axis while simultaneously excite the thusfar not affected fat magnetization, as shown in the simulations in Fig. 5.2A and B (relaxation effects were neglected). In combination with a spoiling gradient, this pulse acted as a fat saturation pulse[265]. When operating at the SAR limit, a single adiabatic pulse achieved $\approx 6.5\ \mu$T and a minimum inversion of 97.7 % at $\pm$ 100 Hz which corresponds to a refocusing efficiency of 95.6 % at $\pm$ 100 Hz for the entire module. Fully sampled representative images ($TE_{prep}/TE_{GRE}/TR_{seg}$ = 50/2.24/526 ms) acquired with a rect pulse and a sinc pulse are shown in Fig. 5.2C and D, respectively.

The T_2-weighted longitudinal magnetization (M_z) was read out using a multi-echo 3D FLASH sequence. A 252 x 252 x 32 matrix was acquired with an isotropic resolution of 0.75 mm. Targeting primary visual cortex (V1), the imaging slab was symmetrically placed around the calcarine sulcus of which its position was localized using a HASTE sequence[266]. For each functional run, four equidistant gradient echoes were acquired using monopolar readout gradients with a bandwidth of 790 Hz/px at echo times (TE_{GRE}) ranging from 2.25 ms to 11.94 ms. Echo spacing was 3.23 ms, TR_{GRE} was 15.2 ms, the duration of the excitation pulse was 1 ms and FA was 6° for all TE_{prep}. The primary phase encoding direction (PE_y) was 3-fold undersampled. To reduce the effect of unwanted T_1-relaxation which would result in a loss of T_2-contrast along the long readout, both phase-encode dimensions were sampled center-out and PE_y was additionally 3-fold segmented, resulting in the pattern shown in Fig. 5.1B. The partition encoding direction (PE_z) was 32-fold segmented, i.e. each PE_z-line was preceded by a T_2-prep module. With this sampling strategy, the time between two consecutive T_2-prep modules (TR_{seg}) was 501.3 ms, 520 ms, and 540 ms for the respective TE_{prep}. The effective volume TR (TR_{vol}) was 48.12 s, 49.92 s and 51.84 s, respectively.

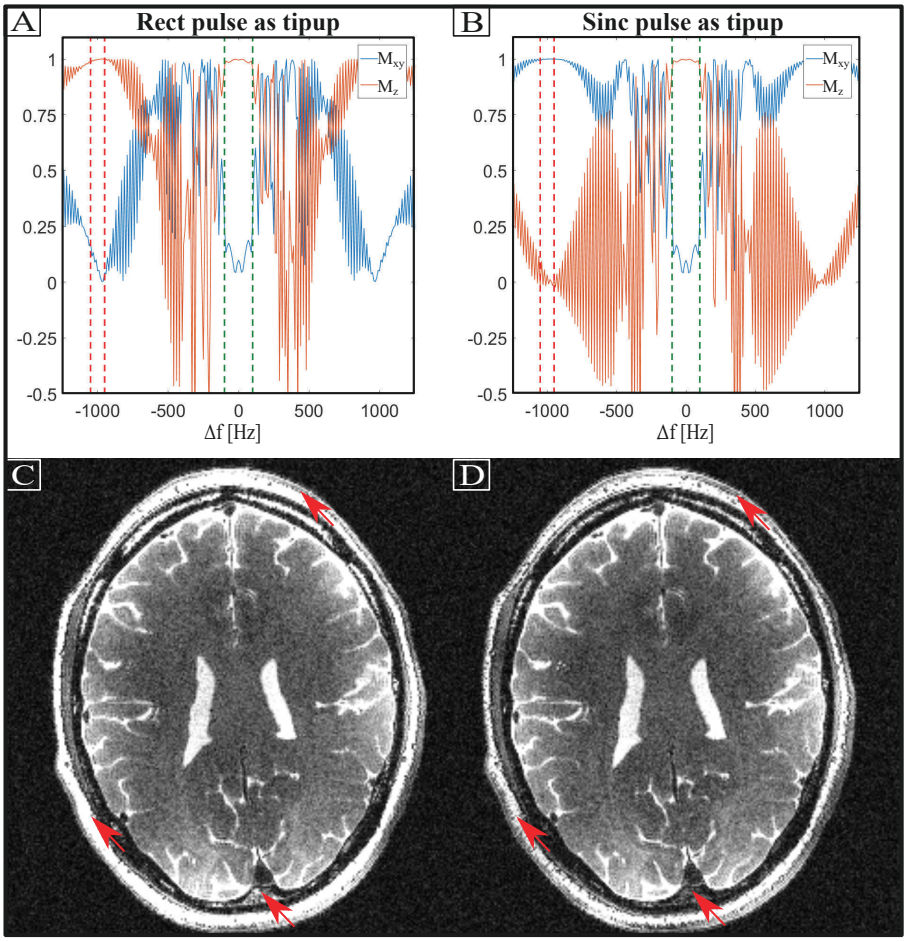

Fig. 5.2 Simulation of the T_2-prep module and the effect of different tipup pulses. (A) Bloch simulation of the entire T_2-prep module prior to the spoiler gradient using the same rect pulse for excitation and tipup. The area of interest is highlighted with green dotted lines indicating a homogenously refocused profile with a minimum refocused Mz of 96.7 % at $\pm$ 100 Hz. Using the rect puls has no effect on the fat signal (red dotted lines). (B) By changing the tipup pulse to be a broadband sinc pulse, the area of interest is not altered (95.6 % at $\pm$ 100 Hz) but the fat spins are excited leading to low residual M_z of fat. M_{xy} is spoiled by the subsequent gradient. (C-D) Fully sampled images acquired with a rect pulse (C) and a sinc pulse (D) as tipup. Note the reduced fat signal (red arrows). We attribute the remaining fat signal to T_1-relaxation during TR_{seg} given the short T_1 of fat at around 330 ms[267].

To avoid influences of a different steady state of the first volume with respect to the rest of the functional run, one dummy volume preceded each run. In addition, each block of PE_y lines within a T_2-prep segment was preceded by two dummy lines to avoid residual influences of unwanted signal instabilities in the first few readouts. The effect of acquiring PE_y dummy lines is shown in Fig. 5.3A.

5.2.1.3 Functional experiments

A flickering checkerboard block design was used to induce activity in V1. Given the long volume TR, functional sessions were split into five runs to reduce the impact of the main magnetic field drifts on our narrowband refocusing pulses (see Fig. 5.3B and C). Each run contained four "rest" blocks (gray screen with red fixation cross) and four "active" blocks during which the subject attended an 8 Hz flickering radial checkerboard with a center red fixation cross. The checkerboard started 6 s before an actual "active" volume to start sampling at the peak of the BOLD response. The duration of a single block was 96.24 s, 99.84 s and 103.68 s for the respective T_2-prep TEs. Sixteen volumes were acquired per run with two volumes per block. Acquisition time for one run was 16:10 min, 16:46 min and 17:23 min, respectively. Between runs, the participants had a break of up to five minutes inside the scanner. After the break the transmitter frequency was re-adjusted to reduce the impact of frequency drifts. Stimuli were presented using code written in MATLAB (The MathWorks, Natick, MA) based on the Psychophysics Toolbox[268,269] (Version 3.0.15).

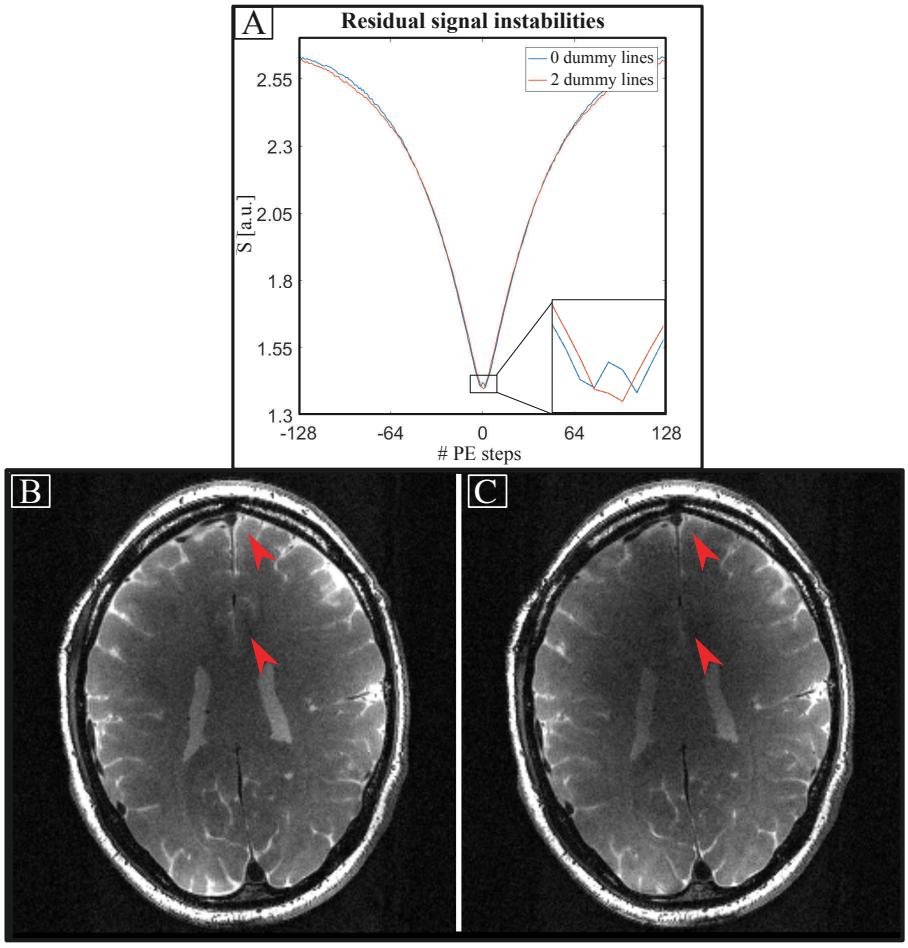

Fig. 5.3 Acquisition stability. Measured signal with no phase encoding gradients without (blue) and with (red) two dummy PE_y-lines in one T_2-prep segment. Here, the segment was the entire k-space i.e. one T_2-prep module was applied. A strong T_1-relaxation along the readout can be observed. The local signal maximum at the center of k-space in the case of no dummy line acquisition likely stems from residual influences of unwanted signal instabilities in the first few readouts. Acquiring two dummy lines avoids this effect. (B-C) The effect of frequency drift during the readout. The fully sampled images were acquired with a TE_{prep} of 31 ms at the start of a run (B) and after 24 minutes scanning without frequency adjustment (C). The red arrows indicate areas of decreased refocusing efficiency of the adiabatic pulses highlighting the necessity for short runs with in-between frequency adjustment.

5.2.1.4 Additional quality measures

In the time period between the two refocusing pulses in the T_2-prep module (Δt) the signal is susceptible to spin diffusion. Through increasing TE_{prep}, we also increased Δt which might cause the dephasing around large vessels to move from a static to a more dynamic regime (i.e. signal changes around large vessels become more pronounced in SE imaging at later TE_{prep}). In theory, the presence of diffusion shortens the transverse relaxation time, leading to the apparent relaxation $T_2^{\dagger}$[270]. To test whether this is a concern in our data, we acquired multi-echo data without functional stimulation to map $T_2^{\dagger}$. In particular, we re-scanned the first subject at TE_{prep} = 31 ms, 40 ms, 50 ms, 60 ms and 70 ms (810 Hz/px bandwidth, 0.75 mm isotropic resolution). Six gradient echoes were acquired with a bipolar readout and a TE_{GRE} ranging from 2.24 ms to 10.29 ms with an echos spacing of 1.61 ms for each TE_{prep}. To account for low SNR, in particular at long TE_{prep}, we measured three fully-sampled k-spaces, filtered each with a Hanning window and averaged the reconstructed images to reduce the noise. Since each TE_{prep} is additionally T_2'-weighted, we used these multi-echo GRE data to fit a mono-exponantial decay function on a voxel basis to estimate a TE_{GRE} = 0 ms dataset for each TE_{prep}. In a second pass, $T_2^{\dagger}$-decay was fitted on these interpolated data using a mono-exponential model to obtain a $T_2^{\dagger}$-map. The apparent relaxation time is related to a relaxation without diffusion by $1/T_2^{\dagger} = 1/T_{2,0} + 1/12 G_{sus} \gamma^2 D \Delta t^2$[271], where γ is the gyromagnetic ratio, $T_{2,0}$ is the relaxation time absent of diffusion, D is the diffusion constant and G_{sus} is the gradient caused by local susceptibility changes. To test whether our data are better represented by a model including diffusion effects, we compared the mono-exponential model (see also section 5.2.5) with one of the form $a \cdot \exp\left(-2\Delta t \left(b + c\Delta t^2\right)\right)$ on signal obtained from GM, WM and CSF segmentations in the occipital lobe.

As additional quality assurance measures, we acquired a multi-echo dataset without T_2-preparation to estimate T_2^* in a typical experimental

setting in this study using the same mono-exponential fitting routine as described above (see also section 5.2.6).

To test the reproducebility of our functional acquisitions, we repeated the TE_{prep} = 31 ms measurement for the first subject several days after the first session (see Fig. 5.20).

5.2.1.5 Data reconstruction

The functional data were reconstructed using custom-written MATLAB routines. After merging segments, GRAPPA[67] was calibrated on fully-sampled autocalibration (ACS) data. To this end, a 9-fold segmented acquisition without undersampling resulting in a fully-sampled, contrast-matched image followed the dummy volume before the actual functional scans start. Data were Fourier transformed in PE_z and a slice- and echo-specific kernel (kernel size 9 x 6) was used. The large kernel size serves to capture high-frequency information while the contrast-matched ACS data and the echo-specific calibration aim to avoid aliasing artifacts due to residual fat signals. The single coil images were combined using echo-specific coil-sensitivity profiles estimated with the SENSE1 algorithm to reduce the noise floor in high-resolution images[272]. All runs and T_2-prep TE acquisitions were put in the same intensity scale in order to be able to average signal changes across runs.

5.2.2 Data pre-processing

5.2.2.1 Structural scans

The structural dataset was corrected for receive bias fields using *spm_preproc* and was further processed with FreeSurfer[273] Version 6.0 with the *-cm* flag and with 50 iterations in *-mris_inflate* to create two surfaces. One marks the boundary between GM and WM (hereafter referred to as WM boundary) and

one corresponds to the pial surface. The output brain mask was manually edited and fed into a second pass of FreeSurfer to correct for any erroneous pial surface estimation in the first pass. The quality of the surface generation is visualized in Fig. 5.4.

5.2.2.2 Functional scans

One run of the first subject of the TE_{prep} = 31 ms dataset was discarded due to excessive motion. The remaining runs per T_2-prep TE were pre-processed using MATLAB code based on SPM12 Version 7487 (Welcome Trust Centre for Neuroimaging, London). In particular, volumes were realigned within each run. To this end, an echo-averaged, biasfield-corrected image was calculated and segmented to create a brain mask. The mask served as weights within *spm_realign*, reducing the influence of the fat rim onto motion estimates. To account for motion between runs, the biasfield-corrected volume average of the third TE_{GRE} within each run was realigned between runs.

Registration to the structural image was performed in two steps. First, the aforementioned volume average of the first run was manually registered using ITK-SNAP[225] Version 3.6.0 (www.itk-snap.org). The resulting transformation matrix was applied to the averaged, registered volume in all subsequent runs. In the second step, the initialized transformation matrix was refined utilizing a modified version of *spm_coreg* which was executed at high resolution and was adapted to include a weighting volume. The registration quality is visualized in Fig. 5.4.

All transformation matrices were concatenated and a single resampling operation was applied. Temporal signal-to-noise ratio (tSNR) was quantified on the OFF-labeled volumes of all runs after linear signal detrending.

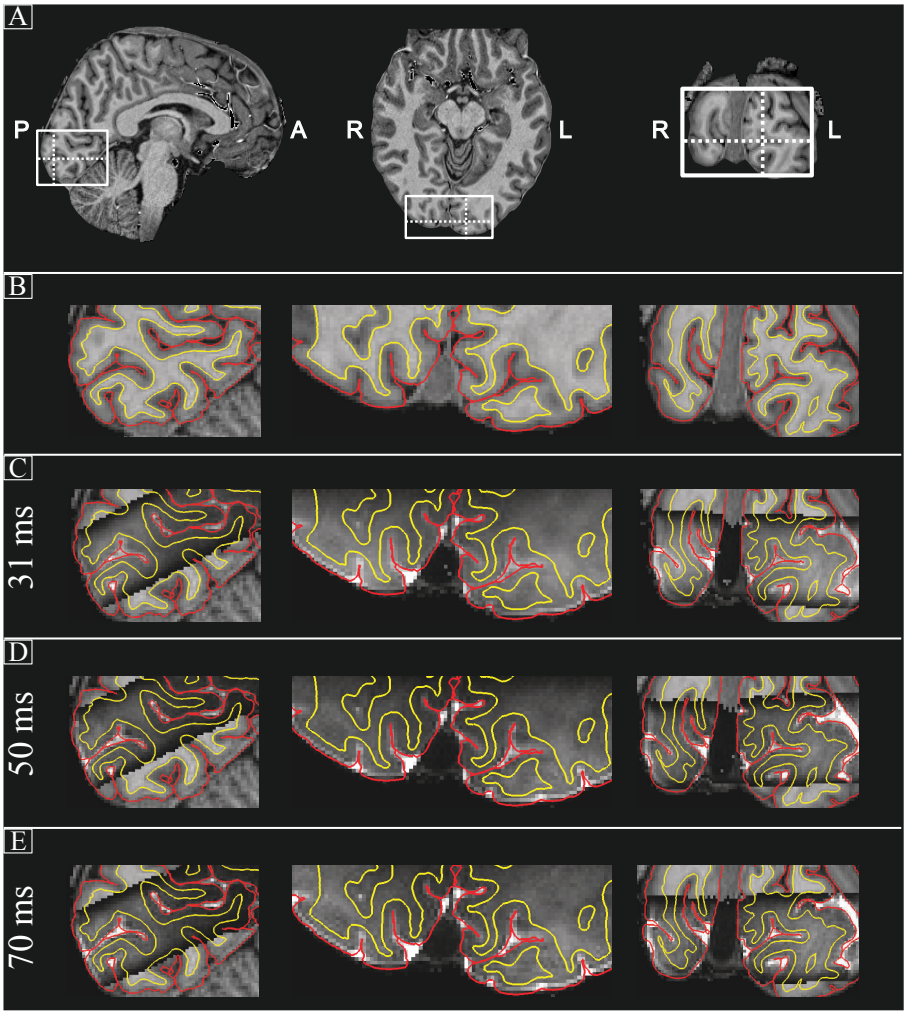

Fig. 5.4 Quality of surface generation and registration. (A) T_1-weighted structural reference of the first subject. The zoomed areas shown in panel (B – E) are highlighted with white boxes. Sectional planes are shown as dotted lines. (B) WM (yellow) and pial (red) surfaces generated by FreeSurfer are overlaid on the structural scan. Visually, surfaces were extracted correctly in primary visual areas. The registered, OFF-labeled mean functional image overlaid on the structural reference for the runs corresponding to a TE_{prep} of 31 ms (C), 50 ms (D) and 70 ms (E) indicate good registration since the surfaces correctly match GM/CSF and GM/WM boundaries.

5.2.3 Activation map estimation

For the first subject, an activation map to assess the general activity pattern was created. At the used resolution and its associated SNR level a voxelwise map is noisy, not very informative, and above all, not representative of the analysis methods in our work. Our purpose of having small voxels was not to analyze them in isolation, but to group voxels sensibly in the analysis afterwards, i.e. as layers (similar approaches are found in columnar fMRI and pattern classifier high-resolution fMRI). For the activity map visualization we therefore used anatomically informed, three-step smoothing in the form of a modified version of the function *LN_GRADSMOOTH* from the LAYNII software distribution[274] version 1.6.0 archived in Zenodo. In short, this smoothing approach uses an adaptive 3 mm smoothing kernel that prevents averaging different tissue types together. Input data to determine the compartments were the MPRAGE data where large venous vessels were masked out using the T_2^*-map (Fig. 5.10B) and the average functional image. This way, WM, GM, CSF, and large pial vessels were smoothed separately.

5.2.4 Laminar profile extraction

In order to extract cortical profiles from the functional data, two ROIs, each targeting positive activation in the posterior calcarine sulcus of a hemisphere, were drawn on the inflated brain in FreeView Version 2.0 (see Fig. 5.12S-T). Only vertices corresponding to a reported cortical thickness between 2.3 mm and 3.5 mm within these ROIs were taken into account. Inside GM, 20 equidistant layers were sampled from the spatial functional data. In addition, to examine effects outside GM, sampling continued into WM and into CSF, for the same distance as inside GM resulting in a total of 60 spatial positions spanning three times the cortical thickness.

5.2.5 Data analysis

To account for between-run intensity offsets, all runs were globally scaled relative to the first one. Each run was high-pass filtered with a cutoff period of 4 x block duration (i.e. 385 s – 414 s depending on TE_{prep}). Because of the long volume TR and the time shift of the active condition we averaged time points of the signal corresponding to the OFF and ON condition across runs, respectively. This resulted in a 60 x 4 matrix (position along surface normal x TE_{GRE}) for each condition and TE_{prep}. To account for edge effects at the boundaries of each run's time series as a result of high-pass filtering[275] we excluded the first and the last two volumes of each run prior to averaging across volumes.

For each cortical bin and condition, a mono-exponential decay function was fit to the data using MATLAB's Levenberg-Marquardt nonlinear least squares algorithm. With this, we obtained a hypothetical TE_{GRE} = 0 ms profile for both conditions. By taking the difference between the ON and the OFF state we obtained laminar activation profiles. We hypothesized that the cortical profiles at TE_{GRE} = 0 ms exhibit a spin echo behavior i.e. almost no EV effects around large vessels and no IV effects given sufficiently strong T_2-weighting. In contrast, with increasing TE_{GRE}, we expect an increasing EV effect through increased $T_2^{'}$-weighting around large venous vessels while IV signals (and effects) should be further attenuated to be below detection threshold.

It is known from theory that the GRE signal dephasing needs to follow a continuous function at all times[131,276]. This means that at TE_{GRE} = 0 ms, the temporal derivative of the decay function needs to be zero resulting in an initial "shoulder" at very short TE_{GRE}. To assess if our data are better represented by a model as developed by Yablonskiy and Haacke[131], we fitted a function of the following form to our data:

$$f(TE) = \begin{cases} a \cdot \exp\left(-b \cdot TE^2\right), & TE < TE_{crit} \\ c \cdot \exp\left(-d \cdot TE\right), & TE \geq TE_{crit}, \end{cases} \tag{5.1}$$

where the parameters a and b are given by

$$b = -0.5 f'_{TE \geq TE_{crit}}(TE_{crit}) / (f_{TE \geq TE_{crit}}(TE_{crit}) \cdot TE_{crit})$$
$$a = -0.5 f'_{TE \geq TE_{crit}}(TE_{crit}) / \left(\exp\left(-b \cdot TE_{crit}^2\right) \cdot b \cdot TE_{crit}\right)$$

as defined by the boundary conditions

$$f'_{TE<TE_{crit}}(0) = 0$$
$$f'_{TE<TE_{crit}}(TE_{crit}) = f'_{TE \geq TE_{crit}}(TE_{crit})$$
$$f_{TE<TE_{crit}}(TE_{crit}) = f_{TE \geq TE_{crit}}(TE_{crit}).$$

TE_{crit} is the critical echo time at which the shoulder of the decay changes into a mono-exponential decay. The critical echo time is given by $TE_{crit} = 1.5\delta\omega^{-1}$, where $\delta\omega$ is a characteristic frequency shift caused by venous vessels containing deoxyhemoglobin. We distinguished between two cases: a) a microvascular network inside GM with $\delta\omega = 4/3\pi\Delta\chi\gamma B_0(0.95 - Y)$ and b) large vessels inside CSF perpendicular to the main magnetic field as an upper limit of EV dephasing around pial veins with $\delta\omega = 2\pi\Delta\chi\gamma B_0(0.95 - Y)$. Here, $\Delta\chi = 0.84 \times 10^{-7}$[119] is the susceptibility difference between oxygenated and fully deoxygenated blood, γ is the gyromagnetic ratio and Y is the oxygenation fraction. Upon activity, Y changes from 0.6 to 0.7[119,277], resulting in a TE_{crit} of 6.5 ms and 9.1 ms at 7 T for GM during rest and activity, respectively. For large vessels, TE_{crit} is 4.3 ms and 6.1 ms, respectively.

5.2.6 Simulations

In this study, we aimed to maximize sensitivity toward signal changes of the capillary bed while at the same time being as insensitive as possible toward signal changes in and around the large veins. To estimate a reasonable parameter space and to try to predict the signal behavior upon parameter changes, we followed Markuerkiaga et al.[255] and designed a simple four-compartment model, i.e. GM, venous and arterial blood and CSF. CSF was modeled to investigate EV effects of pial veins in this compartment. For simplicity, perfect spoiling was assumed.

Let n be the number of T_2-prep segments and m be the number of excitation pulses within one T_2-prep segment with n = 1...N, and m = 0...M, respectively. We denote longitudinal magnetization at any given time as $M_z^{n,m}$, and we use the following abbreviations throughout the derivation:

$$\begin{aligned} E_\Delta &= \exp\left(-\Delta t/T_1\right) \\ E_1 &= \exp\left(-TR_{GRE}/T_1\right) \\ E_{1,seg} &= \exp\left(-TR_{seg}/T_1\right) \\ E_2 &= \exp\left(-TE_{prep}/T_2\right) \\ E_2^* &= \exp\left(-TE_{GRE}/T_2^*\right) \end{aligned}$$

where the time between the $90°_{-x}$ pulse and the first excitation pulse (α-pulse) is Δt = 13.1 ms. Starting with a certain longitudinal magnetization $M_z = M_0$, M_z after the first T_2-prep module just before the readout is given by

$$M_z = M_0\left(1 - E_1\right) + M_z^{1,m-1}. \tag{5.2}$$

After the m-th α-pulse, M_z becomes

$$M_z^{1,m} = M_0\left(1 - E_1\right) + M_z^{1,m-1}\sin\left(\alpha\right)E_1. \tag{5.3}$$

The transverse magnetization along the readout train is calculated as

$$\begin{aligned} M_{xy}^{1,m} &= M_z^{1,m-1} \sin(\alpha) E_2^* \\ &= M_0 (1 - E_1) \sin(\alpha) E_2^* + M_{xy}^{1,m-1} \cos(\alpha) E_1. \end{aligned} \tag{5.4}$$

Assuming a short Δt, the longitudinal magnetization after the n-th T_2-prep module can be approximated as:

$$\begin{aligned} M_z^{n,0} &\approx M_z^{n-1,M} E_2 \\ &\approx \left[M_0 \left(1 - E_{1,seg}\right) + \left(M_z^{n-1,0} + \varepsilon\right) E_{1,seg} \right] E_2. \end{aligned} \tag{5.5}$$

Here, the error term $\varepsilon = \varepsilon(\alpha, TR, T_1, n)$ takes into account that $M_z^{n-1,M}$ is approaching a steady state during the readout train between two successive T_2-prep modules and therefore differs from $M_z^{n-1,0}$ (see Fig. 5.8A). Eq. 5.5 raises the importance of reducing the time between two consecutive T_2-prep modules since non-T_2-weighted magnetization creeps into the readout. Eventually, $M_z^{n,0}$ reaches a steady state and becomes

$$M_z^{n,0} \approx M_0 E_2 \left(1 - E_{1,seg}\right) / \left(1 - E_{1,seg} E_2\right). \tag{5.6}$$

Taking all N T_2-prep shots into account, we used eq. 5.2-5.4 to simulate the signal evolution throughout the sequence during activity and rest. To this end, reasonable assumptions of relaxation rates and their changes must be made. The used tissue parameters are summarized in Tab. 5.2 and reflect cortical depth and, implicitly, vessel size dependent variations of $T_2^{(*)}$ and CBV (Fig. 5.5). If not otherwise specified, the parameters were taken from simulation studies of Markuerkiaga et al.[255] and Uludağ et al.[119]. The blood volume distribution was taken from Duvernoy[21] and Lauwers et al.[106]. Changes in T_2^* in CSF were taken from Markuerkiaga[278] and Uludağ et al.[119].

Tab. 5.2 Tissue parameters used in the simulations. Three 'cortical' bins, referred as deep, middle and top, were used to evaluate depth specific changes in $T_2^{(*)}$ during rest and activity.

Compartment	T_2 [ms]		T_2^* [ms]		T_1 [ms]	Volume fraction [%]	
	OFF	ON	OFF	ON		OFF	ON
GM (deep)	48.1	48.6	29.4[a]	30.0	2000[e]	98.20	98.03
GM (middle)	46.8	47.7	27.5[a]	28.5	2000[e]	96.92	96.63
GM (top)	47.2	48.2	27.0[a]	28.4	2000[e]	96.92	96.63
Ven. blood (deep)	20.5[b]	29.7[b]	6.5[a]	8.6	2600[e]	1.23	1.34
Ven. blood (middle)	20.5[b]	29.7[b]	6.5[a]	8.6	2600[e]	2.13	2.32
Ven. blood (top)	20.5[b]	29.7[b]	6.5[a]	8.6	2600[e]	2.34	2.55
Art. blood (deep)	68.1	67.1	14.6	14.9	2600[e]	0.57	0.63
Art. blood (middle)	68.1	67.1	14.6	14.9	2600[e]	0.95	1.05
Art. blood (top)	68.1	67.1	14.6	14.9	2600[e]	0.80	0.88
CSF	900.0[c]	903.0	160.0[d]	170.5[e]	4425[f]	94.29[g]	93.89[h]

[a] taken from [255] and confirmed that the values are within range of our measured T_2^*-map
[b] [279]
[c] [280]
[d] Estimated from a T_2^*-map and a VOI in CSF
[e] [278]
[f] [281]
[g] Assumed to be $1 - \sum_{i=1}^{3} \left(CBV_i^{veins} + CBV_i^{art.}\right)$, with i counting the bin index
[h] Estimated to change due to a 7 % CBV change in pial veins [121]

Since T_2^* relaxation time can vary due to its dependency on local B_0 homogeneity we estimated T_2^* values for GM and venous blood in a typical experimental setting used in this study. To this end, we applied the same fitting procedure as described in the previous section to the non T_2-weighted data

(see section 5.2.1.4) and averaged T_2^*-values in volumes of interest (VOI) targeting GM around the calcarine sulcus and venous blood in the sagittal sinus (see Fig. 5.10A). These measured values were used as a verification of the T_2^*-values taken from Markuerkiaga et al.[255] as reported in Tab. 5.2 since those reflect cortical depth specific changes. To evaluate these changes explicitly, we divided the cortical depth into three bins resembling cortical layers V-VI (referred to as deep) layer IV (middle) and layers I-III (top) and averaged $T_2^{(*)}/\Delta T_2$ within those bins (Fig. 5.5). In order to distinguish depth specific contributions of different compartments we separated the blood compartment into laminar vasculature (both arteriolar and venous) and into intracortical veins as a function of cortical depth. Following Uludağ et al.[119], we estimated depth- and contrast-specific changes of EV and IV transverse relaxation times. The change in IV $T_2^{(*)}$ was simulated as constant throughout cortical depth. To test the effect of different static EV dephasing in CSF onto the shape of laminar profiles we performed simulations with a variety of different T_2^* changes around the value reported in Tab. 5.2.

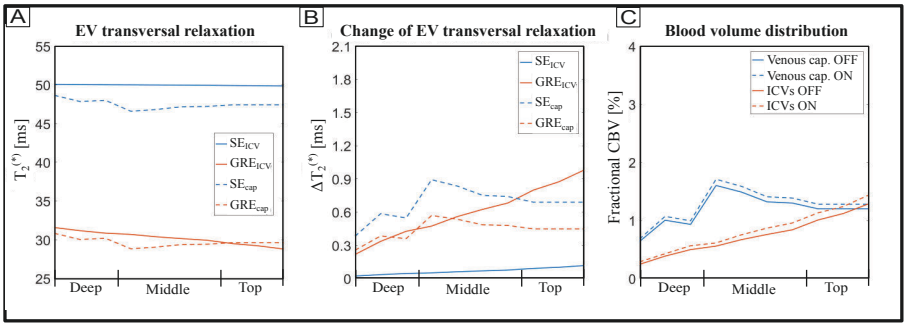

Fig. 5.5 Model parameters. (A) Extravascular $T_2^{(*)}$ and (B) its change upon activity as a function of cortical depth for a SE and a GRE sequence used in the simulations. Solid lines represent EV $T_2^{(*)}$ due to ICVs, dashed lines due to capillaries, respectively. (C) Fractional CBV for venous capillaries and ICVs during rest and activity. The cortical depth was subdivided into three bins, referred to as 'deep', 'middle', and 'top'. To obtain the values as summarized in table 5.2, parameters within these bins were averaged.

Because unwanted T_1-relaxation between T_2-prep segments puts an upper limit on the choice of TR and consequently TE_{GRE}, the only "free" parameters to choose were TE_{prep} and flip angle. We simulated the signal at rest and during activation with T_2-prep TEs ranging from 5 ms to 70 ms and a FA of 1° to 20°. TR_{GRE} and TE_{GRE} were taken as mentioned in the acquisition section. To aid visualization, TE_{GRE} was extended by five additional gradient echoes at the same echo spacing and we add a hypothetical TE_{GRE} = 0 ms to visualize a SE condition. The signal was computed as

$$S = (1 - CBV)\, S_{Ex} + CBV S_{In} \tag{5.7}$$

with S_{Ex} and S_{In} being the extravascular and intravascular signal, respectively. CBV is the combined volume fraction of ICV, venous and arterial microvasculature (arterioles) as given by the values in Tab. 5.2 (graphically shown in Fig. 5.5C). In detail, the microvascular distribution was simulated as being 40 % arterial and 60 % venous[105,255]. The fractional CBV change of the entire microvascular volume was taken as 16.6 %[119] of which the arterial and venous part contribute 60 % and 40 %, respectively[117]. For long stimulus durations as used in this study, it has been shown that large venous vessels also dilate to a certain extend[120,121]. As an upper limit, we assumed the baseline blood volume of the pial veins to be equal to the parenchymal CBV. Taking the results from Kim and Kim[121] Supplementary Fig. S3C, we estimated a cortical depth dependent fractional CBV change for ICVs and a fractional CBV change of 7 % for pial veins. The functional signal change was calculated as $\Delta S = S_{ON} - S_{OFF}$. For the cortical bin close to the pial surface, a partial voluming effect was simulated by taking 50 % of signal change in CSF as part of the superficial bin. Moreover, a worst-case scenario regarding the EV effect of pial veins on the parenchyma was assumed i.e. vessels of 200 μm diameter perpendicular to B_0 inducing a $\Delta T_2^{(*)}$ additional to the intravoxel change of dephasing in the top bin.

5.3 Results

5.3.1 Adiabatic pulse comparison

Fig. 5.6 shows Bloch simulations of magnetization inversion as a function of transmit B_1 and off-resonance ΔB_0 obtained with adiabatic pulses of 15 ms (Fig. 5.6 first row) 13 ms (second row) and 9 ms (third row). The region where the pulse should achieve an inversion of > 95 % is highlighted with a white box. The power integral of the normalized, complex pulses, calculated as $P = \sum_i \left(R_i^2 + I_i^2\right)$, where R and I are the real and imaginary part and i counts the sampling points, is shown in the title of each panel, respectively. For better comparison, the power integral is shown relative to that of the 15 ms hyperbolic secant (HS) pulse.

Originally designed for broadband inversion, the HS4 (Fig. 5.6D,I,N) and the WURST pulse (Fig. 5.6E,J,O) produce a too broad inversion at a too high power deposit for the purpose of this work. The HS (Fig. 5.6A,F,K) and the Gaussian (Fig. 5.6B,G,L) pulse exhibit a more narrowband inversion profile at lower power. The Sin/Cos pulse (Fig. 5.6C,H,M) results in an inversion profile of intermediate bandwidth.

Among all compared pulses, the Gaussian is the most power efficient pulse to achieve the desired inversion in the target region. Fig. 5.7 compares the Gaussian pulse at 13 ms duration with a 15 ms HS pulse as reference in more detail. The HS pulse (β = 375 rad/s, μ = 5) achieves a broadband inversion over a range of $\pm$ 250 Hz (Fig. 5.7A). However, the efficiency fluctuates with ΔB_0 for a B_1 of 4 μT to 6 μT and tend to decrease for $B_1 > 8$ μT as shown in the zoomed image in (Fig. 5.7C). The inversion obtained with an adiabatic Gaussian pulse (β = 3.03, $\Omega = 500$ Hz frequency sweep) inverts spins in a narrower frequency range (Fig. 5.7B,D). However, within this range, the inversion is more robust against B_1 and B_0 variations (Fig. 5.7D).

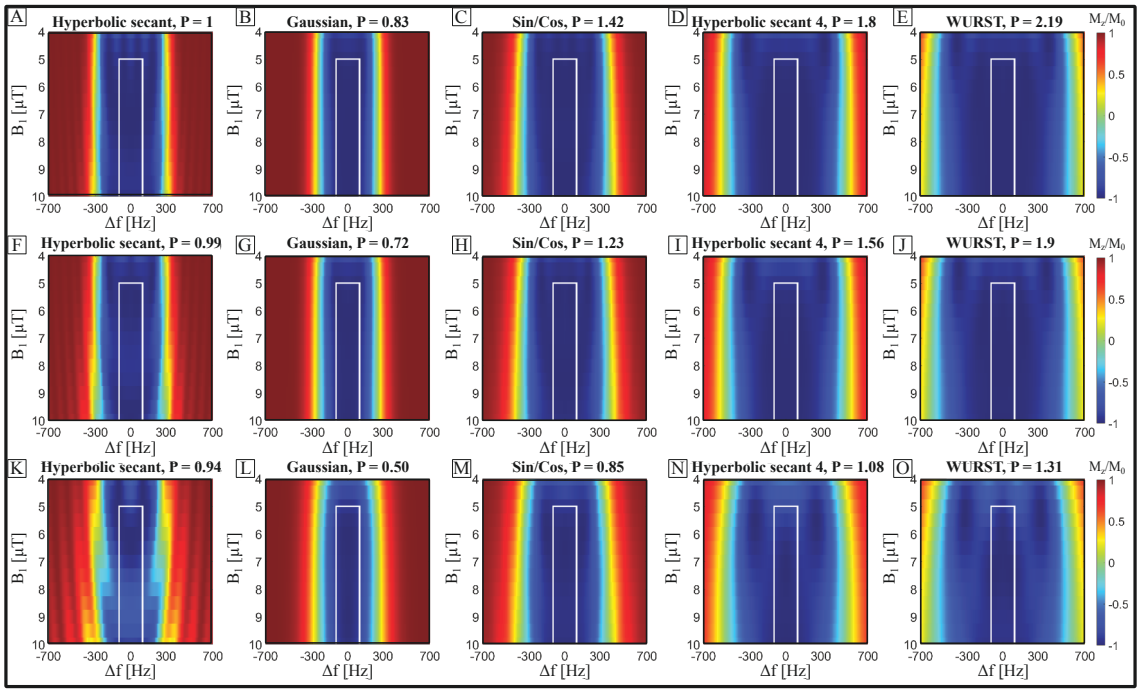

Fig. 5.6 Adiabatic pulse comparison. Bloch simulations of inversions as a function of transmit B_1 and off-resonance ΔB_0 obtained with adiabatic pulses of 15 ms (first row) 13 ms (second row) and 9 ms (third row). In each panel, the white box shows the target region ($>$ 95 % inversion) and the power integral relative to the 15 ms HS pulse (A) is written in the respective title. Originally designed for broadband inversion, the HS4 (D,I,N) and the WURST pulse (E,J,O) result in a too high power deposit. Among the narrowband alternatives (HS (A,F,K), Gaussian (B,G,L), Sin/Cos pulse (C,H,M)) the Gaussian pulse is the most power efficient.

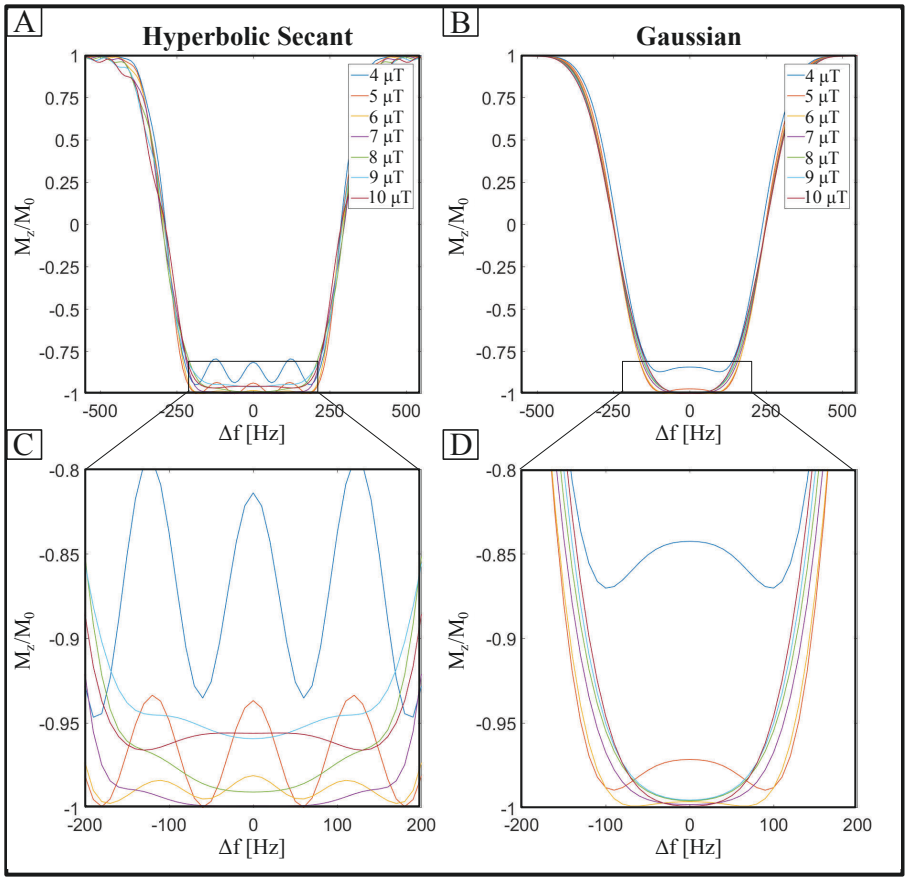

Fig. 5.7 Detail look on HS and Gaussian pulse. The HS pulse (A,C) achieves an overall broader inversion but the efficiency fluctuates with B_0 and B_1. The inversion obtained with the Gaussian pulse (B,D) is within the target range of $\pm$ 100 Hz and more robust against field variations at a 28 % lower power deposit.

Since the adiabatic pulses represent the bulk of the applied RF power, care must be taken in the pulse design to stay within SAR limits, especially with repeated T_2-prep module application. In this comparison, the Gaussian pulse is 28 % more SAR efficient.

5.3.2 Simulations

Fig. 5.8A shows the simulated longitudinal magnetization of GM after 32 T_2-prep dummy shots as a function of GRE shots for a FA of 6° and a TE_{prep} of 30 ms with 32-fold segmentation (blue curve) and 8-fold segmentation (red curve). The curves correspond to a segment TR of TR_{seg} = 501.3 ms and TR_{seg} = 1778.1 ms, respectively. Segmentation comes with a trade-off: The downsides of using higher segmentation factors is that there is less M_z available at the start of the readout and the total acquisition time increases due to the repeated T_2-prep modules. The benefit is that with shorter segments there is less T_1-relaxation, resulting in less non-T_2-weighted signal to re-emerge. The latter is especially important with respect to the intravascular compartment as due to blood's short T_2^*, re-emerging non-T_2-weighted (i.e. non-nulled) signal can lead to relatively large signal changes at the short GRE-TEs used.

Fig. 5.8B shows the signal change in GM as a function of TE_{GRE}. The gray area depicts the range of measured TE_{GRE}. For standard GRE sequences (blue line) the signal change at TE_{GRE} = 0 ms starts at a negative value due to a change in CBV (eq. 5.7) and increases up to $TE_{GRE} = T_2^*(\mathrm{GM})$. In case of the used T_2-prep sequence (red, yellow and purple curves), the T_2 prepared signal exhibits a net positive change due to changes in EV T_2. With increasing TE_{prep}, the signal decay during preparation results in a shift of the maximum signal change toward lower TE_{GRE}. In addition, the initially very strong dependency on TE_{GRE} (blue curve in gray area) is leveling off with stronger T_2-weighting resulting in weak (red and yellow curve) or no (purple curve) additional signal increase with longer TE_{GRE}. This behavior is due to coupled changes in T_2 and T_2^*.

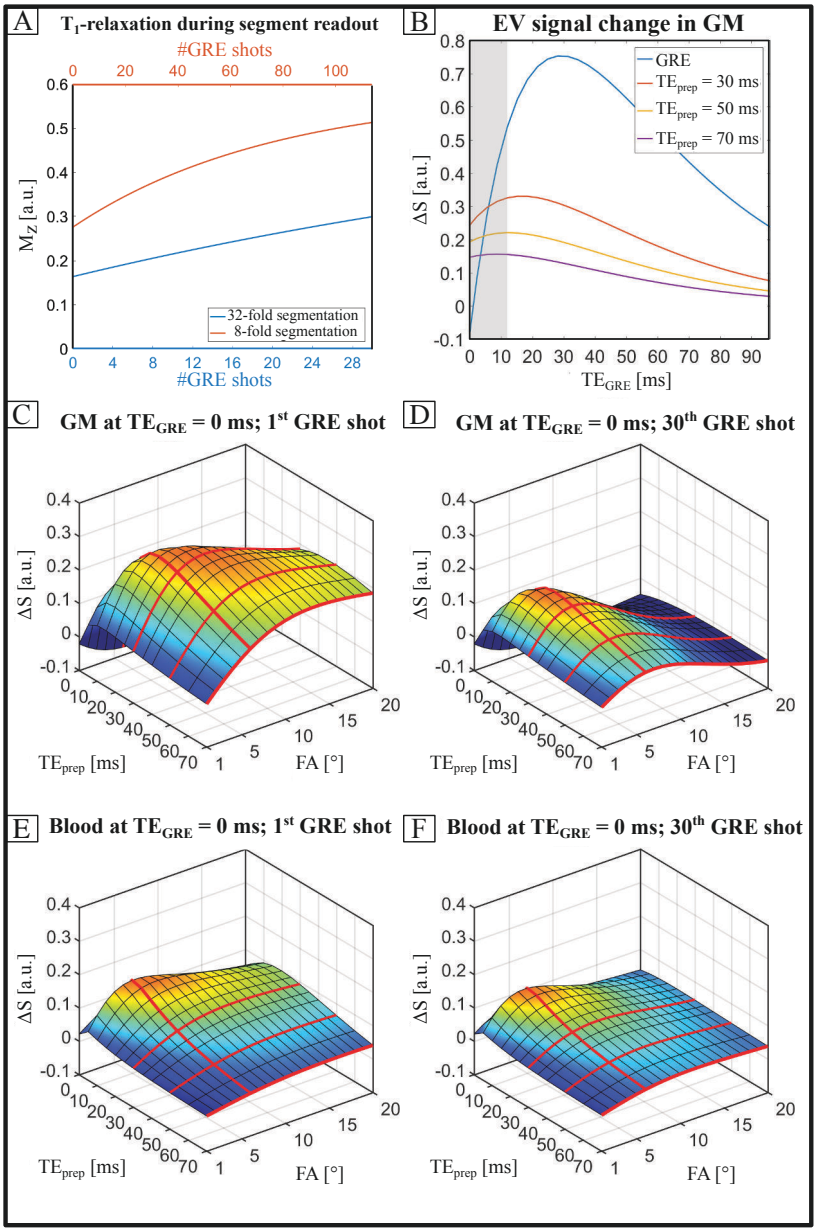

Fig. 5.8 Simulation of signal behavior. (A) Longitudinal magnetization of GM as a function of GRE shots for a FA of 6° with 32-fold segmentation (blue curve) and 8-fold segmentation (red curve).

(B) Signal change as a function of TE_{GRE} for a GRE sequence (blue line) and for the used sequence with different amounts of T_2-weighting (red, yellow and purple lines). The shaded gray area indicates the TE_{GRE} range used in the experiments. Please note the steep ascend in the blue curve in this region whereas the heavily T_2-weighted purple curve is relatively flat. (C-F) Functional signal change in GM (C,D) and venous blood (E,F) at TE_{GRE} = 0 ms immediately after a T_2-prep module (C,E) and at the end of the segment (D,F) as a function of TE_{prep} and FA. The crossing of the red lines depict the chosen parameters for the FA and TE_{prep}. With a FA of 6°, we maximize the sensitivity toward signal changes in GM along the entire readout train (C and D). Additionally, by using long TE_{prep}, we avoid the early maximum of venous blood contributions (E and F).

Functional signal changes as a function of TE_{prep} and FA induced by changes in T_2 in GM and in venous blood are shown in Fig. 5.8C-D and Fig. 5.8E-F, respectively. The crossing of the red lines depicts the chosen FA and T_2-prep TEs. Immediately after the T_2-prep module, signal change in GM is maximized for a TE_{prep} of $\approx$ 30 ms and a flip angle of $\approx 10^{\circ}$ (Fig. 5.8C). However, at the end of the readout, repetitive application of excitation pulses with such large flip angles leads to a low baseline signal, effectively reducing the sensitivity toward changes in GM as shown in Fig. 5.8D. On the other hand, when exciting with flip angles slightly lower than the Ernst angle[282], signal change in GM is maximized during the entire readout.

In the case of venous blood, signal change is maximized for very short TE_{prep} and high FA. With increased TE_{prep}, the signal change declines rapidly due to the short T_2 of venous blood. These results suggest that, to be sensitive to T_2-modulated signal changes in GM during the readout of a segment while reducing sensitivity toward IV changes, low FA and long TE_{prep} have to be used.

5.3.3 T_2-prepared multi-echo imaging

Fig. 5.9 shows time-averaged images in the rest condition of the first subject for a TE_{prep} of 31 ms (Fig. 5.9A,B,C), 50 ms (Fig. 5.9D,E,F) and 70 ms (Fig. 5.9G,H,I) and for the first and last gradient echo. Note that the images corresponding to different TE_{prep} were scaled individually to allow better visual inspection. Within each TE_{prep}, images were scaled relative to the first TE_{GRE}. In general, the overlay on the structural reference shows good realignment quality owing to the absent distortions of the FLASH acquisition (Fig. 5.9A,D,G, see also figure 5.4).

A transverse view of the cross-section highlighted by the white dashed line in Fig. 5.9A is depicted for the first gradient echo (Fig. 5.9B,E,H) and the last echo (Fig. 5.9C,F,I). Increased T_2-contrast can be seen with increased TE_{prep}. Importantly, at TE_{prep} = 31 ms, signal of venous vessels is not effectively nulled compared to later spin echoes as shown by the red arrows in Fig. 5.9B,E,H. This is highlighted by normalized projections shown in Fig. 5.9J,K at the first and last TE_{GRE}, respectively, taken along the dashed line in Fig. 5.9I. With additional T_2'-weighting, exemplified with the last gradient echo (Fig. 5.9C,F,I), intravascular signal is further reduced as indicated by the red arrows in Fig. 5.9C.

Fig. 5.10 shows maps of the transverse relaxation times acquired for the first subject. The $T_2^\dagger$-map (Fig. 5.10A) depicts the expected low GM/WM contrast in the highlighted area[283]. Please note that $T_2^\dagger$-values outside of this area are prone to errors since the T_2-prep module was calibrated to accurately weight the signal in the visual cortex. $T_2^\dagger$ values inside GM (one slice of a VOI shown as red ROI in the zoomed view) and WM (green ROI) are 47.9 $\pm$ 5.8 ms and 54.6 $\pm$ 5.2 ms, respectively. This is in good agreement with previously reported $T_2^\dagger$ relaxation times measured with a similar approach[271]. Please note that an estimation of venous blood $T_2^\dagger$ was not possible with the used TE_{prep} assuming a blood T_2 shorter than our minimum TE_{prep}[279].

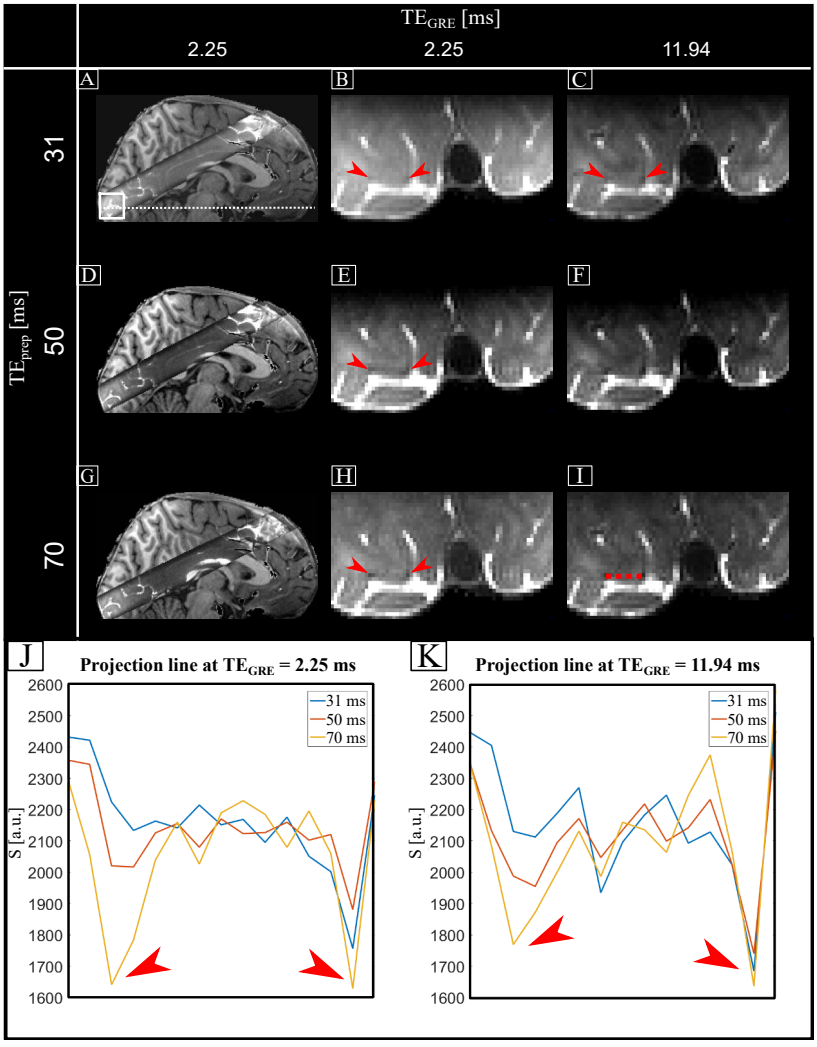

Fig. 5.9 T_2-prepared multi-echo imaging. Average OFF-labeled image of the first subject at TE_{prep} = 31 ms (A,B,C), 50 ms (D,E,F) and 70 ms (G,H,I) and for the first and last TE_{GRE}. Note that the images along TE_{prep} were scaled individually to allow better visual inspection. Within each TE_{prep}, images were scaled relative to the first TE_{GRE}. The sagittal overlay on the T_1-weighted image shows good realignment between functional data and anatomical reference (A,D,G). In V1, a transverse slice (white, dashed line inside white box in A) depicts increased T_2-contrast with increasing TE_{prep} (B,E,H). Red arrows indicate decreasing signal intensity inside venous vessels. This is highlighted by the normalized projections (J-K) along the red, dashed line in panel I. At 31 ms TE_{prep}, the venous signal is not nulled as effectively as in later spin echoes. Increasing TE_{GRE} shows increased T_2'-weighting (C,F,I) with strong signal attenuation in the mentioned veins (exemplified by red arrows in C), as expected.

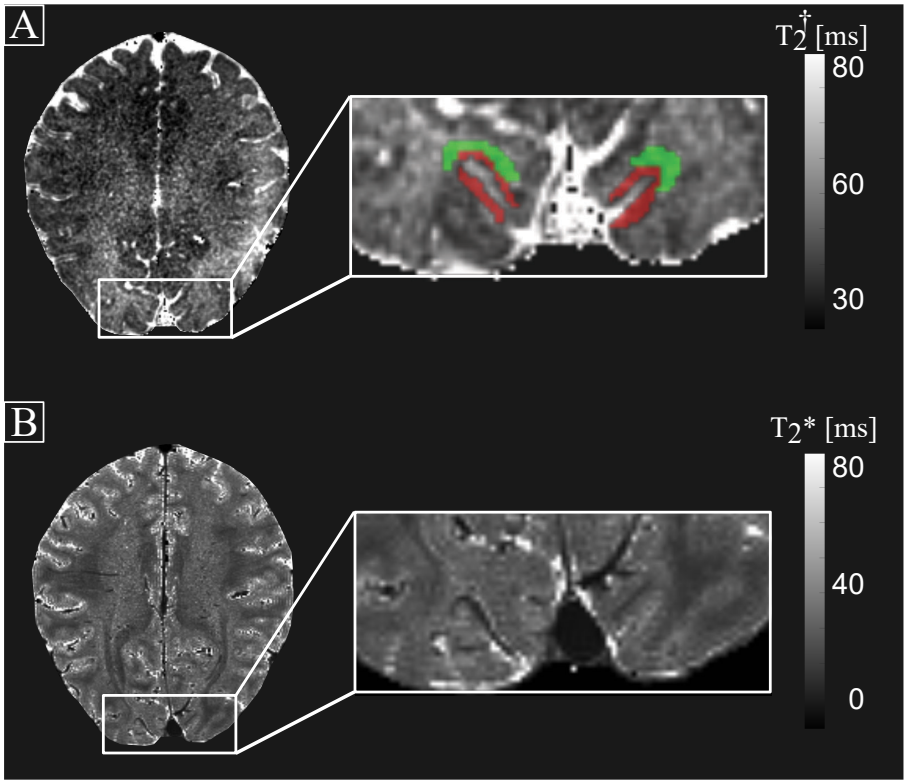

Fig. 5.10 $T_2^{\dagger,*}$-weighting accuracy. (A) $T_2^{\dagger}$-map acquired for the first subject shows the expected low WM/GM contrast in the zoomed area. ROIs of WM and GM are shown in green and red, respectively. (B) T_2^*-map acquired without T_2-preparation.

The calculated T_2^*-map based on a multi-echo dataset without T_2-preparation using the same fitting procedure as described in section 5.2.5 is shown in 5.10B. T_2^* values inside GM and in the sagittal sinus are 28.0 $\pm$ 0.7 ms and 6.1 $\pm$ 0.1 ms, respectively. These are in good aggreement with previously reported relaxation times at 7 T[119,284,285].

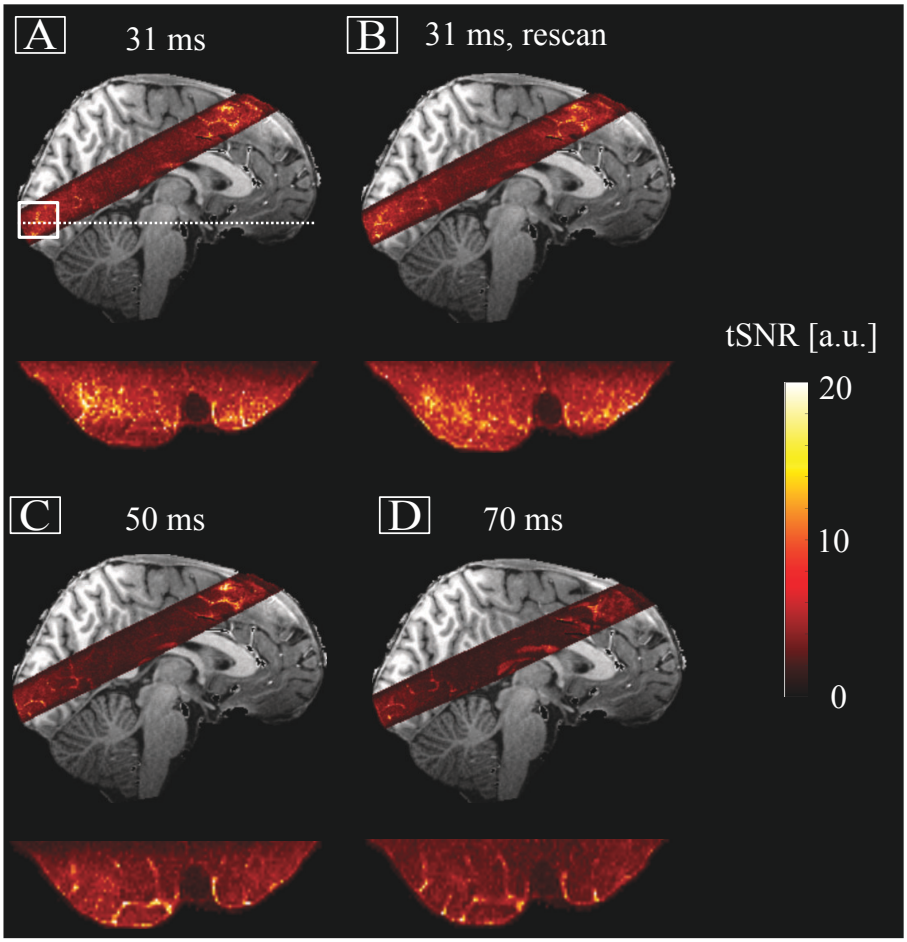

Fig. 5.11 Temporal stability. Temporal SNR-maps of the first subject overlayed on the structural image at TE_{prep} of 31 ms (A), the 31 ms rescan (B), 50 ms (C) and 70 ms (D). The zoomed transverse view of the cross-section in the white box in (A) is shown below the corresponding sagittal view. Since increased T_2-weighting effectively reduces the amount of available signal in a steady state, tSNR is reduced with increased TE_{prep}. In VOI targeting GM of the primary visual cortex tSNR was 10.6 $\pm$ 2.1 (A), 10.1 $\pm$ 2.0 (B), 6.7 $\pm$ 1.4 (C) and 5.7 $\pm$ 1.3 (D).

To estimate the temporal stability of T_2-prepared laminar fMRI, we quantified tSNR over the functional timeline. For the first subject, Fig. 5.11A-D shows tSNR-maps overlayed on the structural reference and zoomed transverse views on the visual cortex for each TE_{prep}. Owing to the increased T_2-weighting of M_z with increased TE_{prep}, the available baseline signal is reduced resulting in decreasing tSNR with increasing TE_{prep}. In Fig. 5.11C and D, CSF shows high tSNR with respect to the rest of the tissue due to its long T_2 (see Tab. 5.2) whereas in Fig. 5.11A-B, the tSNR maps do not show a considerable contrast. Notably, tSNR in the scan-rescan experiment (Fig. 5.11A and B) is identical within error margins indicating a stable data acquisition. When averaging tSNR in VOI targeting GM in the primary visual cortex, we find a subject average tSNR (mean $\pm$ std) of 8.6 $\pm$ 1.9, 6.1 $\pm$ 1.2 and 4.8 $\pm$ 0.6, for a TE_{prep} of 31 ms, 50 ms and 70 ms, respectively. The results shown in Fig. 5.11 also suggest that with longer TE_{prep} the sequence becomes more sensitive toward long-living T_2-components like CSF.

5.3.4 Functional activation maps

In Fig. 5.12 activation maps are shown for the first subject as a function of TE_{GRE} and TE_{prep}, respectively. Fig. 5.12A and B depict the structural reference of the left calcarine sulcus while 5.12C shows the corresponding T_2^*-map. Locations of big veins are highlighted with white arrows. Fig. 5.12D-R show activation maps for all measured and extrapolated echo times. For a nonzero TE_{GRE}, signal change increases mainly around large veins inside CSF. At TE_{GRE} = 0 ms (5.12D,I,N), signal change occurs mainly inside GM for $TE_{prep} > 31$ ms. Interestingly, a negative signal change is observed around big veins at TE_{GRE} = 0 ms and to a lower extend at the first measured TE_{GRE}. At later TE_{GRE}, this becomes a strong, positive signal change. Given the long stimulus duration, these negative signal changes can be attributed to a vasodilatation of large vessels[120,121].

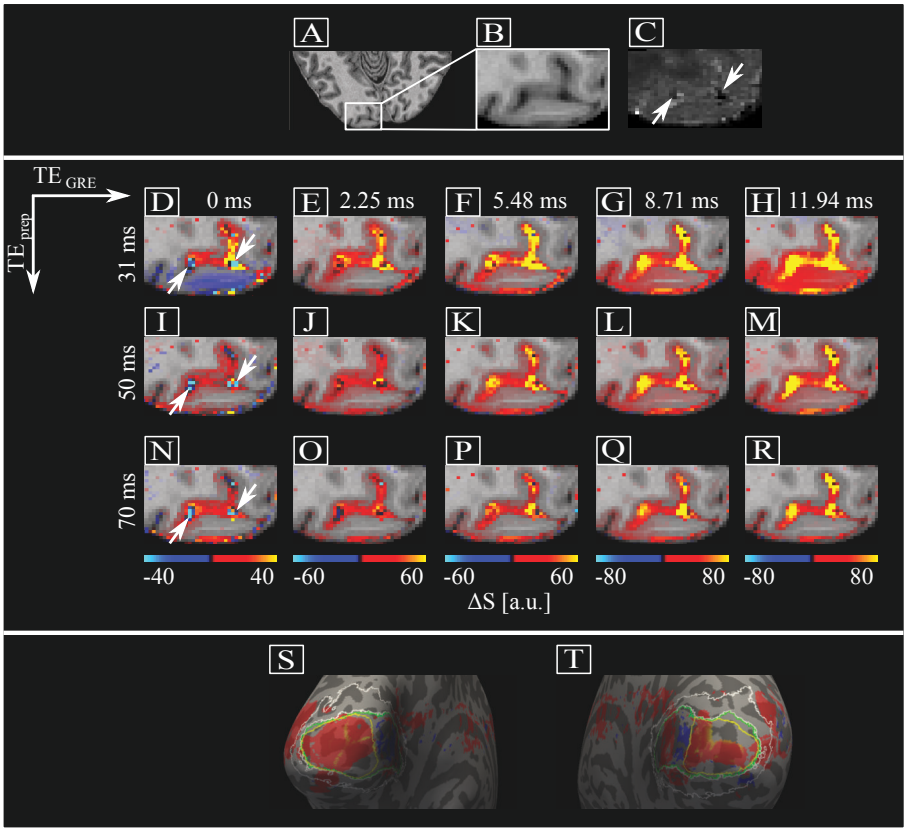

Fig. 5.12 Activation maps from smoothed data and ROI selection. (A-C) Anatomical references showing the T_1-weighted image of the first subject (A), a zoomed area highlighting left V1 (B) and a corresponding T_2^*-map (see Fig. 5.10B for details) (C). (D-R) Activations maps calculated from anisotropically smoothed data (3 mm smoothing kernel) for all measured and extrapolated echo times. They show increased signal change with longer TE_{GRE} mainly around veins, a positive signal change mainly in GM for the case of TE_{GRE} = 0 ms (D,I,N) and a negative signal change around large vessels (white arrows in C,D,I,N) for the same TE_{GRE}. (S-T) The echo-average signal change overlayed on the left (S) and right (T) inflated hemisphere. The ROI for the subsequent laminar analysis covers the positive signal change in the posterior part of V1 (yellow contour). Full V1 (green contour) and V2 (white contour) are shown for reference.

5.3.5 Laminar profiles

The subject averaged profiles at rest shown in Fig. 5.13A-C clearly demonstrate the expected systematic signal decrease with longer TE_{GRE} and longer TE_{prep}. The shaded areas correspond to the standard error of the mean over all subjects.

The profiles of functional signal change are shown in Fig. 5.13D-F. Most prominently, the measured signal change in the pial compartment (i.e. veins and CSF) increases approximately linearly as a function of TE_{GRE} for all TE_{prep} (see also Fig. 5.12D-R) and likely resembles the EV effect in CSF which has a relatively long T_2^*. All measured profiles exhibit a peak in CSF (red arrows). In the extrapolated TE_{GRE} = 0 ms spin echo condition (blue profiles), signal change is close to zero in CSF and attenuated at the GM/CSF boundary.

This is in line with the argumentation that EV dephasing around large pial veins is refocused and therefore not contributing to the overall fMRI signal in a SE experiment[119,138]. Interestingly, even with a small amount of additional $T_2^{'}$-weighting, i.e. at GRE echo times as small as 2.25 ms, the signal change at the pial surface becomes a dominant feature for all TE_{prep}.

In middle and deep GM, the dependency on TE_{GRE} is not identical across different amounts of T_2-weighting as highlighted by black and blue arrows, respectively. In the case of TE_{prep} = 31 ms (Fig. 5.13D), signal change increases with longer TE_{GRE}. For longer TE_{prep} (black and blue arrows in Fig. 5.13E,F) this is not the case. This indicates toward either a not completely nulled IV component at shorter TE_{prep} or EV effects.

In Fig. 5.14A, simulations of compartment specific signal changes are shown for the deep layer. The gray shaded area highlights TE_{GRE} corresponding to our measurements. EV signal changes show a mild increase with increasing TE_{GRE} within the measured range for a TE_{prep} of 30 ms (brown solid line, see also Fig. 5.8B).

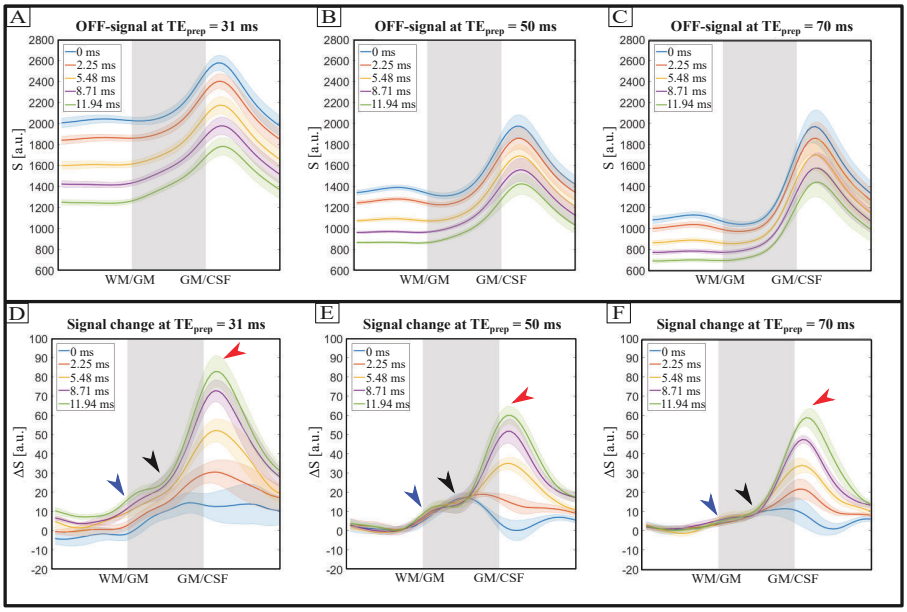

Fig. 5.13 Measured average laminar profiles. (A-C) Average signal profiles at rest sampled across cortical depth exhibit the expected signal decrease with longer TE_{GRE} and TE_{prep}. The shaded area correspond to the standard error of the mean. (D-F) Functional signal change exhibits a prominent peak at the pial surface increasing with additional T_2'-weighting (red arrows). At TE_{prep} = 31 ms (D), signal change in the middle (black arrows) and deep (blue arrows) parts of GM also show an increase with TE_{GRE} which is absent for later TE_{prep} (E and F).

For longer TE_{prep}, this increase is absent (solid pink and green line). In case of IV contributions, signal changes decrease with longer TE_{prep} and TE_{GRE} (dashed lines). While approaching the pial surface, the tendency of EV signal changes to increase with increasing $T_2^{'}$-weighting becomes more pronounced due to the rise of baseline blood volume toward the pial surface (Fig. 5.14B and C) but again this behavior is more pronounced in cases of less T_2-weighting (solid brown lines). In all cases, IV signal changes decrease with longer TE_{GRE}. Due to its long T_2^* (see Tab. 5.2), CSF, included in the top layer simulations, shows a strong dependency on TE_{GRE} (Fig. 5.14C, dotted-dashed lines).

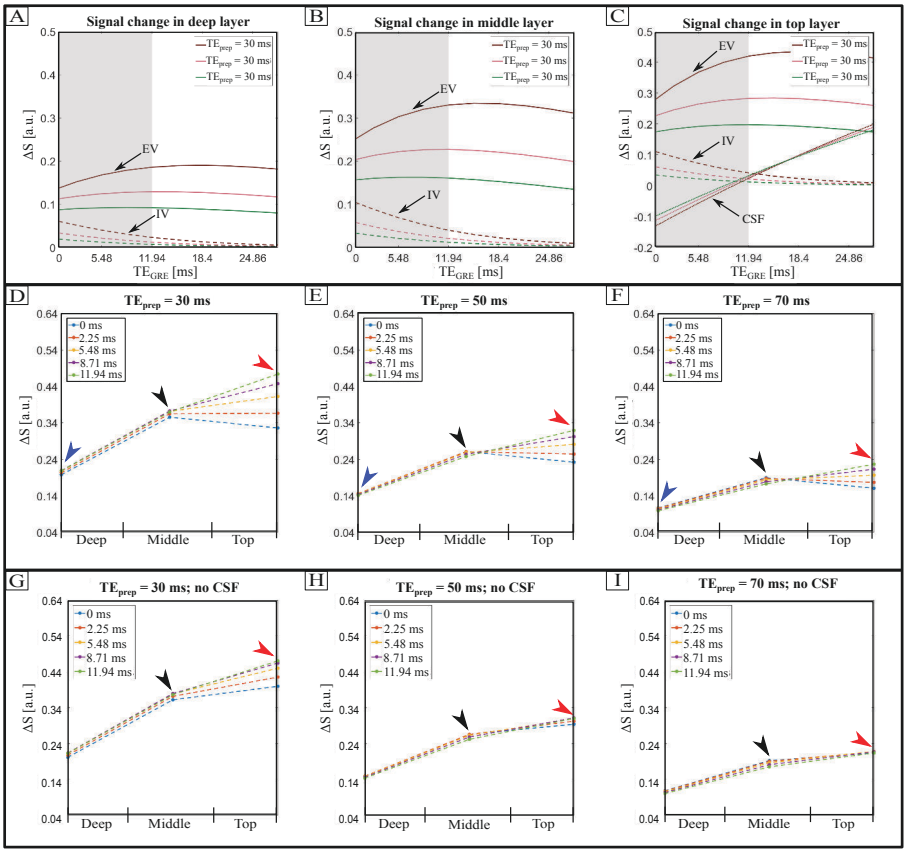

Fig. 5.14 Simulated laminar profiles. Signal change as a function of TE_{GRE} and TE_{prep} in deep (A), middle (B) and top (C) layers. See main text for detailed explanations. By combining the volume-weighted contributions of all compartments, artificial laminar profiles were generated for a TE_{prep} of 30 ms (D), 50 ms (E) and 70 ms (F). Signal changes as a function of TE_{GRE} in the top (red arrow) correspond well with the measured profiles if taken partial voluming with CSF into account. In case of a TE_{prep} of 30 ms (D), middle (black arrow) and deep (blue arrow) layers do not exhibit a strong increase with longer TE_{GRE} as shown in the measurements. Assuming no EV effect in CSF (G-I) and a worst-case scenario regarding EV effects of pial veins onto the parenchyma shows no increase in signal change in the top layer for the longest TE_{prep} under consideration (I). This argues toward a considerable amount of EV signal change in CSF.

By combining all compartments, we created artificial laminar profiles (Fig. 5.14D-F) which exhibit similar TE_{GRE} dependencies in top layers (red arrows) compared to the measured profiles shown in Fig. 5.13. Note that in case of a TE_{prep} of 30 ms, the signal increase in deep and middle layers (blue and black arrows in Fig. 5.14D) is not as pronounced compared to the measurements (blue and black arrows in Fig. 5.13D). By removing the contribution of CSF (Fig. 5.14G-I), no strong $T_2^{'}$-effect in top layers is visible for long TE_{prep} arguing toward a considerable EV effect in CSF. To test a variety of different static EV dephasing in CSF and its effect onto the shape of laminar profiles, we simulated a ΔT_2^* of 6 ms to 14 ms in steps of 2 ms. The results shown in Fig. 4.15 indicate the same TE_{GRE} behavior for all TE_{prep} and all ΔT_2^* with the only difference being the scale of the signal increase in the top bin.

To delimit the possible mechanisms leading to the deviation between simulations and measurement of signal changes in deep and middle layers for TE_{prep} = 30 ms (blue and black arrows in Fig. 5.13D and 5.14D), we conducted our simulation with an IV T_2 of 200 ms representing the case of not fully nulled blood signal. In this scenario, the T_2-preweighting is not strong enough yet such that additional $T_2^{'}$-weighting results in a positive IV signal change to take place with increasing TE_{GRE} until $TE_{GRE} = T_2^*(\text{blood})$ (dashed lines in Fig. 5.16A,B; see also Fig. 5.8B). The resulting profiles in Fig. 5.16C,D exhibit a signal increase until $TE_{GRE} = T_2^*(\text{blood})$ before declining again. Importantly, this behavior is visible over the entire cortical depth, also at long TE_{prep} (Fig. 5.16D) which is not observable in the measured profiles in Fig. 5.13D,E arguing against an IV source. In contrast, an increase in the change of GM T_2^* upon activity results in profiles shown in Fig. 5.16E,F which strongly mimic the intracortical behavior seen in Fig. 5.13D-F.

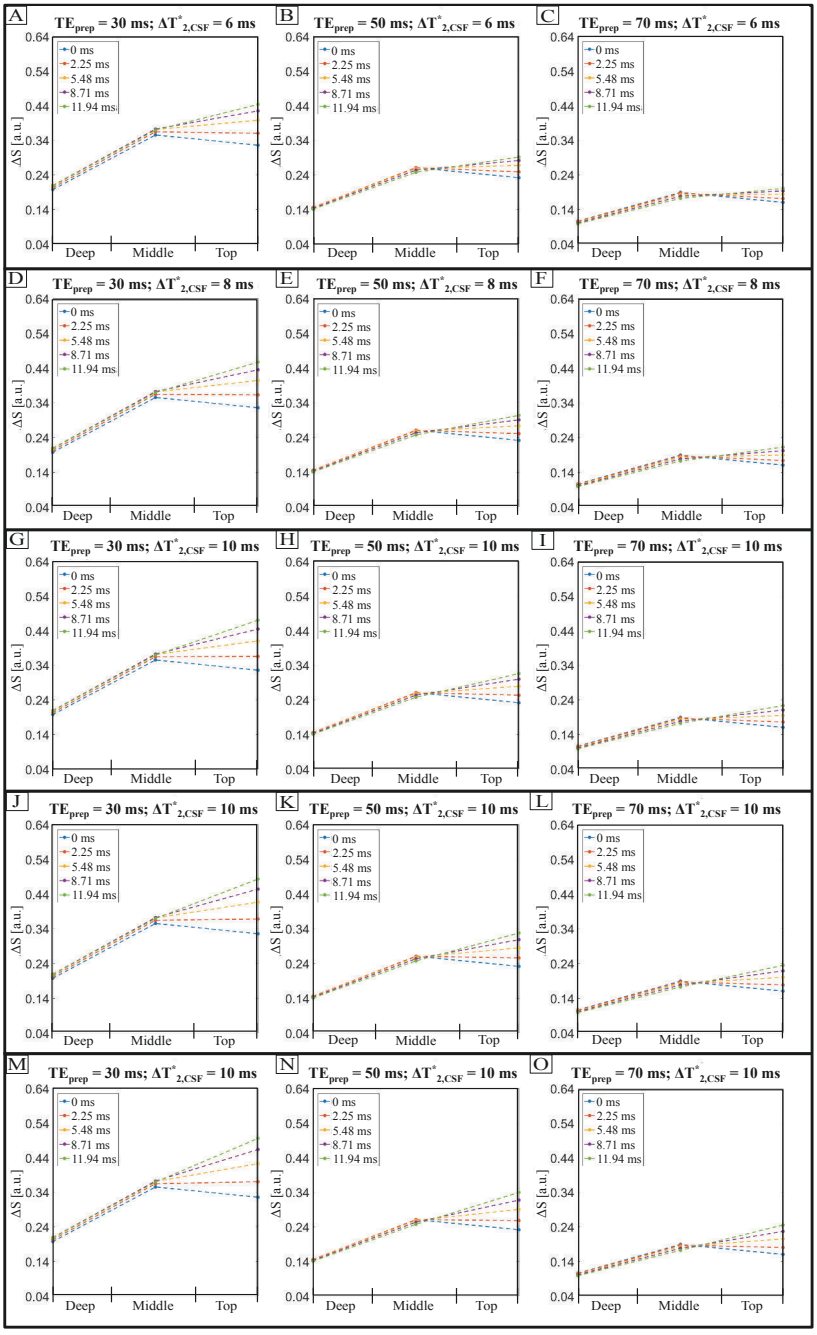
A
TE_prep = 30 ms; ΔT*_2,CSF = 6 ms
B
TE_prep = 50 ms; ΔT*_2,CSF = 6 ms
C
TE_prep = 70 ms; ΔT*_2,CSF = 6 ms
D
TE_prep = 30 ms; ΔT*_2,CSF = 8 ms
E
TE_prep = 50 ms; ΔT*_2,CSF = 8 ms
F
TE_prep = 70 ms; ΔT*_2,CSF = 8 ms
G
TE_prep = 30 ms; ΔT*_2,CSF = 10 ms
H
TE_prep = 50 ms; ΔT*_2,CSF = 10 ms
I
TE_prep = 70 ms; ΔT*_2,CSF = 10 ms
J
TE_prep = 30 ms; ΔT*_2,CSF = 10 ms
K
TE_prep = 50 ms; ΔT*_2,CSF = 10 ms
L
TE_prep = 70 ms; ΔT*_2,CSF = 10 ms
M
TE_prep = 30 ms; ΔT*_2,CSF = 10 ms
N
TE_prep = 50 ms; ΔT*_2,CSF = 10 ms
O
TE_prep = 70 ms; ΔT*_2,CSF = 10 ms
0 ms
2.25 ms
5.48 ms
8.71 ms
11.94 ms
ΔS [a.u.]
0.64
0.54
0.44
0.34
0.24
0.14
0.04
Deep
Middle
Top

Fig. 5.15 Test of different EV effects in CSF. All panels show the same TE_{GRE} behavior for all TE_{prep} and all ΔT_2^* with the only difference being the scale of the signal increase in the top bin.

Those profiles exhibit a similar TE_{GRE} behavior in deep and middle layers for all TE_{prep} conditions indicating a stronger than expected EV contribution to the laminar profiles.

To estimate whether this EV contribution is driven by micro- or macrovasculature we looked at the EV effects of the capillaries and the ICV in isolation. Fig. 5.17A,B shows the signal change resulting from changes in EV dephasing around microvasculature (solid lines) and IV effects in capillaries (dashed lines). EV effects are strongly modulated with TE_{prep} but stay approximately constant as a function of TE_{GRE} for a TE_{prep} of 30 ms (solid brown line). With stronger T_2-weighting, signal changes decrease (solid pink and green line). In combination with decreasing IV contribution with longer TE_{GRE} and TE_{prep}, the corresponding laminar response (Fig. 5.17C,D) is decreasing as a function of TE_{GRE} for all TE_{prep}. In contrast, the EV effect of ICV exhibits no dynamic dephasing component (approximately zero signal change at TE_{GRE} = 0 ms) and is building up with longer TE_{GRE} (Fig. 5.17E,F). The difference between the shown signal responses of capillaries and larger veins can be explained by the difference in the strength of the effect. Around microvasculature, the static EV effect is not as prominent as around large vessels. Therefore, depending on the amount of additional T_2-preweighting and its associated shift in the sensitivity curve (Fig. 5.8B), the EV static effect around capillaries can decrease while at the same time increase for larger vessels. This results in a net increasing signal change with longer TE_{GRE} and along cortical depth (Fig. 5.17G,H). Taking this together, the signal increase in deep and middle GM at TE_{prep} = 31 ms as shown in Fig. 5.13D can be seen to stem from EV signal changes around veins but with a stronger than expected EV effect (see Fig 5.16D).

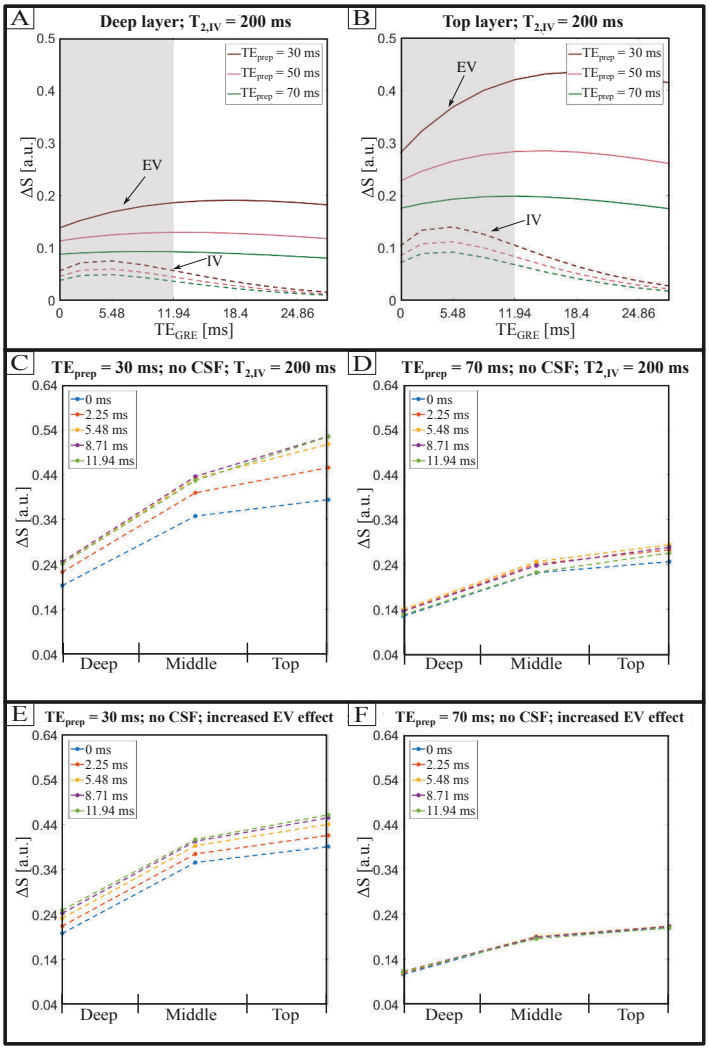

Fig. 5.16 Alternative model parameters. (A-D) The simulations in Fig. 5.14D show a disparity with respect to the measurements in Fig. 5.13D in terms of TE_{GRE} dependence. To assess if the model assumed a too short blood T_2 leading to a too strong IV suppression, we set blood T_2 to a large value of 200 ms. (C,D) shows that this results in an increase with longer TE_{GRE} over the entire cortical depth even at longer TE_{prep} (D) which is absent in the measured profiles (blue and black arrows in Fig. 5.13E,F) arguing against a dominant IV contribution. (E,F) Increasing the neural activity induced change in T_2^* in GM in the model results in profiles with a strong TE_{GRE} in the 30 ms TE_{prep} case (E), but not at longer TE_{prep} (F), very similar to the results seen in Fig. 5.13. Pial vessels or ICV could be the source of such elevated ΔT_2^* values.

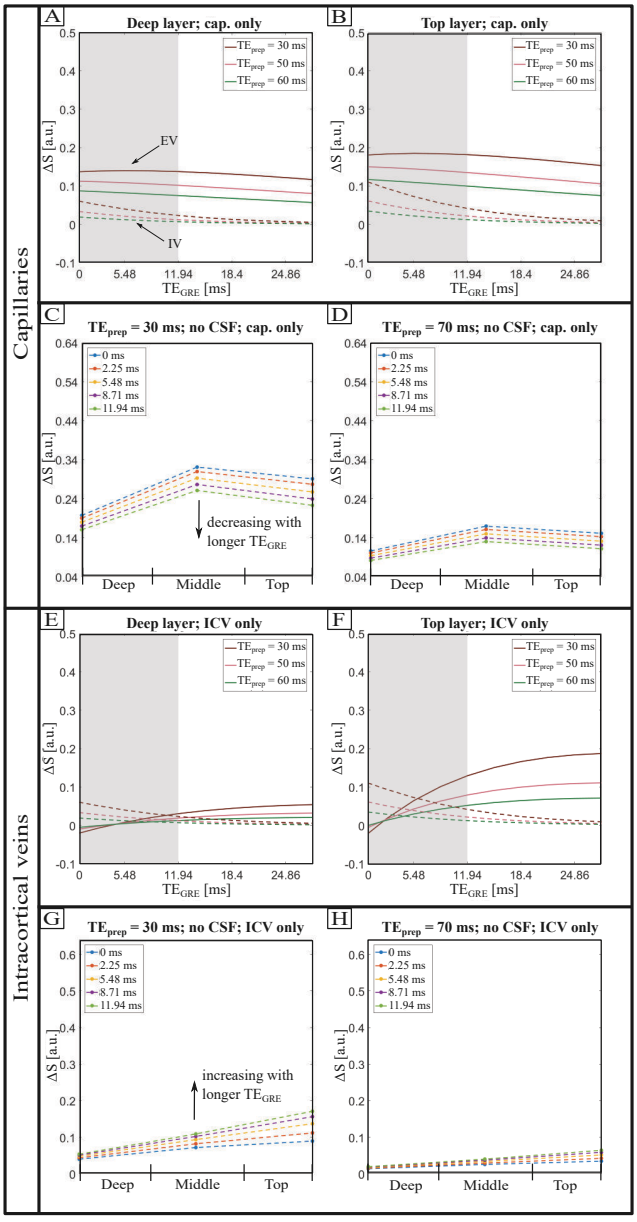

Fig. 5.17 Simulated laminar profiles of capillaries and intracortical veins in isolation. Signal change as a function of TE_{GRE} and TE_{prep} in deep (A,E) and top (B,F) layers simulated for the microvascular (first row) and the macrovascular (third row) compartment inside GM. In case of capillaries, laminar profiles exhibit a signal decrease with longer TE_{GRE} (C,D) whereas the profiles for the macrovascular compartment (G,H) show an increase in signal with longer TE_{GRE} and along cortical depth. The difference between the shown signal responses of capillaries and larger veins can be explained by the difference in the strength of the effect. Around microvasculature, the static EV effect is not as prominent as around large vessels.

5.3.6 Fitting accuracy

We assessed whether our data are more susceptible to diffusion with increasing inter-pulse duration Δt between the two refocusing pulses, which would shorten the apparent $T_2^{\dagger}$, by comparing the employed mono-exponential model with a model containing a diffusion term $c = 1/12 G_{sus} \gamma^2 D$ in units of $1/sec^3$.

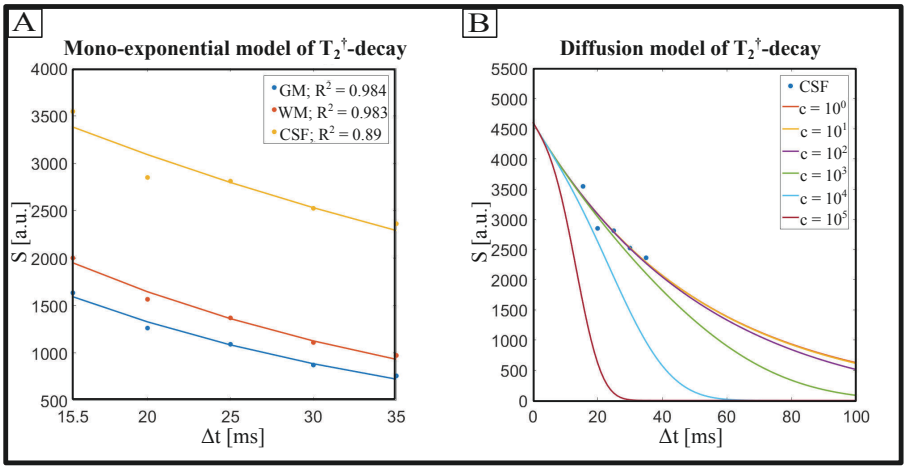

Fig. 5.18 Test of $T_2^{\dagger}$-decay model. The signal decay of GM, WM and CSF is represented quite well with a mono-exponential model (A). Assuming CSF signal to be the most sensitive toward diffusion effects, the diffusion model represents the signal the best of the diffusion ($c = 1/12 G_{sus} \gamma^2 D$) approaches zero.

The results in Fig. 5.18A show that the signals follow a mono-exponential decay quite well, as indicated by the R^2 of the fits (shown in the legend of panel A). Fig. 5.18B shows the CSF signals, since these are assumed to exhibit the strongest sensitivity toward diffusion effects, and decay functions obtained with the diffusion model with increasing influence of the diffusion term c. A strong influence of additional diffusion would cause the signal at later TE_{prep} to approach zero more rapidly which is absent

in our data. In fact, the data shown here are represented best if c approaches zero, i.e. when the diffusion in CSF is negligible.

It is well known that in theory the GRE signal decay deviates from a mono-exponential behavior at short TE_{GRE}[131,276]. We evaluated whether our data are better represented by a model as developed by Yablonskiy and Haacke[131], which we refer to as "short TE model" (Eq. 5.1). For each subject (Fig. 5.19A-L), we fitted the short TE model (dashed lines) and a mono-exponential decay (solid lines) to our data at rest (brown dots representing the data, brown lines the fits) and activity (green dots/lines). The critical echo times are marked with red dots. For the fits at rest, the corresponding R^2 is written in the legend. We repeated the fitting procedure for an average over subjects (Fig. 5.19M,N). One can see, that for each individual subject and for the subject average, the mono-exponential model (solid lines) fits our data always better than the short TE model (dashed lines), especially for GM where the long TE_{crit} result in an too early transition into the "shoulder" of the decay. We additionally evaluated the goodness of the fits as a function of oxygenation fraction (Fig. 5.19O,P). For GM (Fig. 5.19O), the short TE model never fits our data as good as the mono-exponential model, even at unrealistically low Y. For CSF (Fig. 5.19P), the quality of the short TE model fit approaches that of the mono-exponential model asymptotically with lower oxygenation fractions. However, in the range of physiological plausible values of Y, (0.5 – 0.7), the short TE model does not represent the data better than a mono-exponential model.

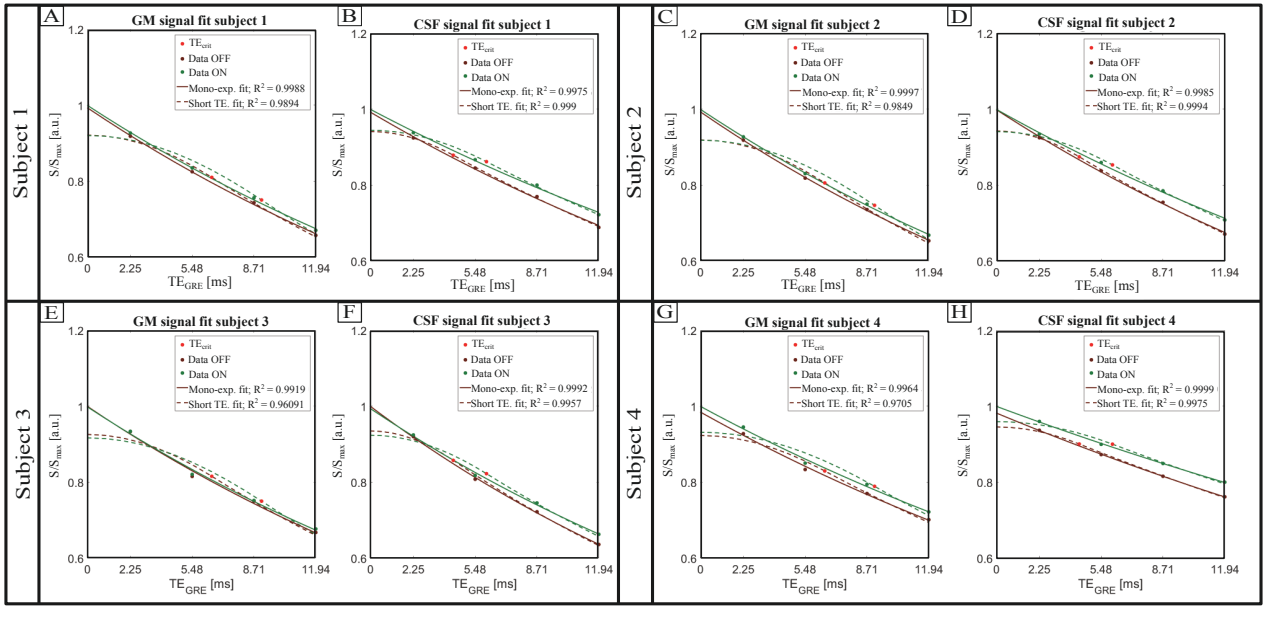

Fig. 5.19 Test of different signal decay models at short TE_{GRE}. See main text for description.

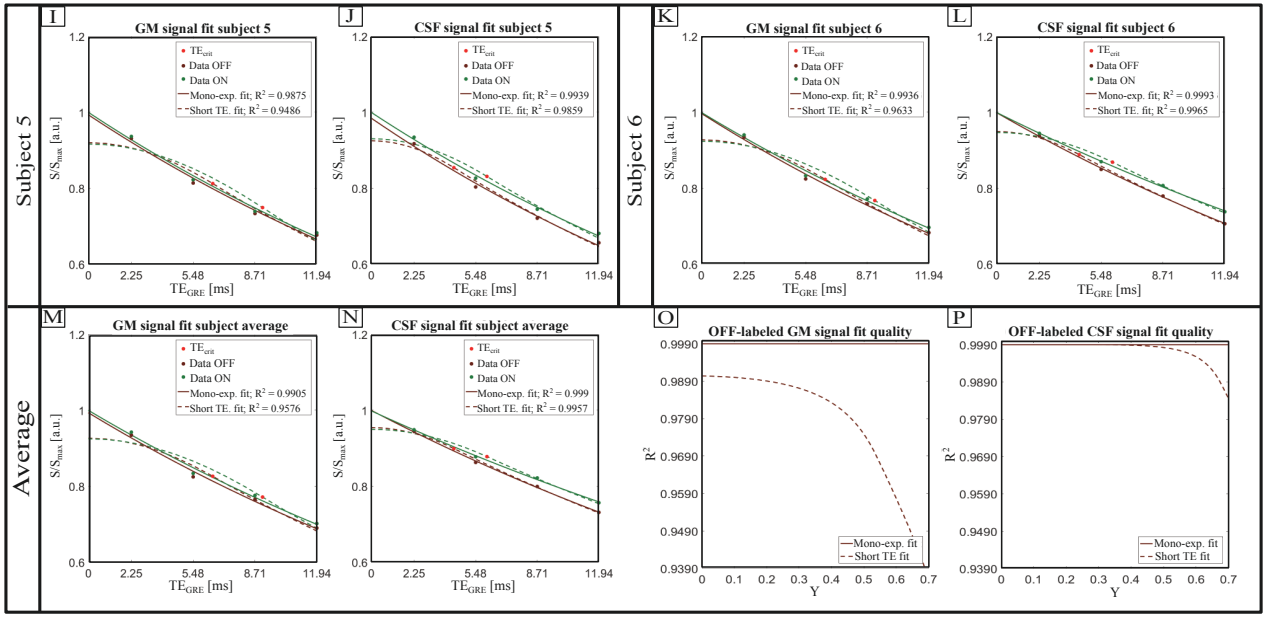

Fig. 5.19 Continued.

Fig. 5.20 shows the scan-rescan results for the first subject scanned at TE_{prep} = 31 ms. The extrapolated profiles at rest (Fig. 5.20A,B) corresponding to the case of TE_{GRE} = 0 ms are shown in blue with shaded areas representing the 95 % confidence interval of the fit. Note the narrow interval indicating a good quality of the fit. The similarity of profiles suggests reliable extraction of cortical signals. The profiles of functional signal change (Fig. 5.20C,D) exhibit similar features between the scan and the rescan i.e. both show increasing signal change over the entire cortical depth with longer TE_{GRE}.

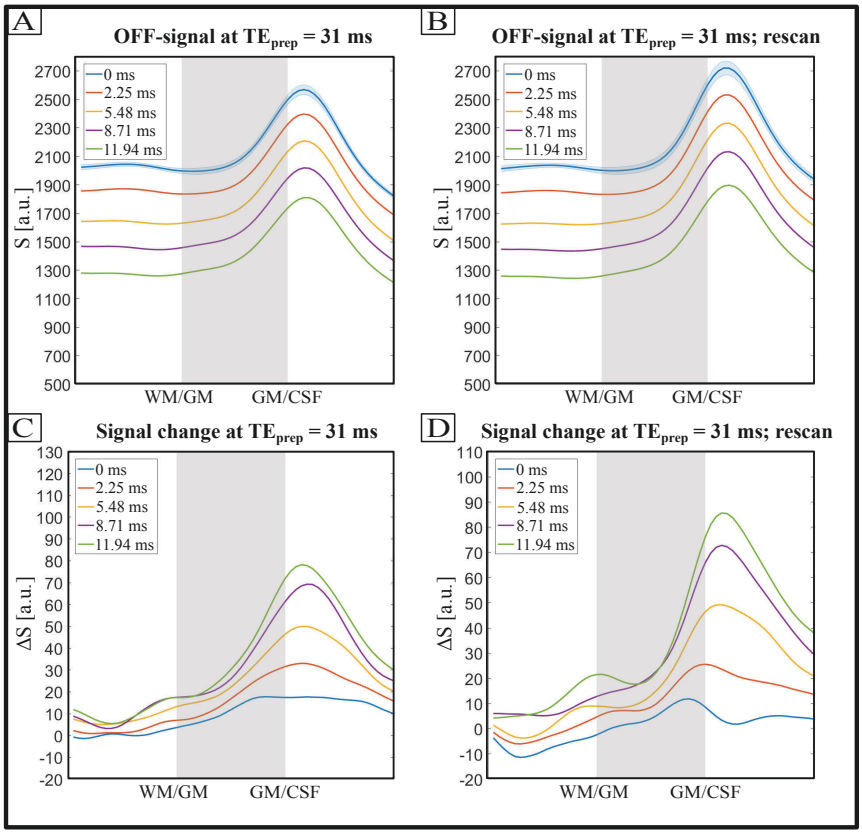

Fig. 5.20 Scan-rescan experiment. (A,B) Profiles at rest sampled across cortical depth during the scan (A) and the rescan (B). The narrow confidence interval of the fit (blue shaded area) indicates a good quality of the fit. The Profiles of functional signal change (C,D) exhibit similar trends between the two measurements.

5.4 Discussion

In this work, we used a T_2-prepared multi-echo FLASH sequence, assessed its capacity to acquire T_2-weighted laminar fMRI profiles and systematically analyzed signal contributions from different vascular and non-vascular compartments in T_2-weighted and T_2^*-weighted BOLD via simulations and multi-echo functional experiments. Our findings can be summarized into three main observations discussed in turn below:

(1) The profiles of the fitted TE_{GRE} = 0 ms exhibit a strong specificity at TE_{prep} = 50 ms and 70 ms, whereas for the shortest TE_{prep} of 31 ms, the signal change at the pial surface does not completely go to zero.
(2) The pial component exhibits a strong TE_{GRE} dependency.
(3) There is a clear difference in the TE_{GRE}-dependent behavior of functional signal change in the case of TE_{prep} = 31 ms versus the cases of TE_{prep} = 50 ms and 70 ms.

(1) After removing the $T_2^{'}$ contributions by extrapolating to a TE_{GRE} = 0 ms case, the fitted profiles (blue curves in Fig. 5.13D-F) are confined to GM. However, for the shortest TE_{prep}, a non-zero signal change at the pial surface is observed. The fitted profiles reflect mostly EV dynamic dephasing changes of GM signal around microvasculature. However, a small IV compartment might be present at the shortest TE_{prep} which disappears with longer TE_{prep}, as most of the IV signal has decayed already. While early studies suggest a rather short venous blood T_2 of 22 ms at 4.7 T[286] and 9 ms at 9.4 T[287], recent parametric mapping studies report longer values, 21 ms at 7 T[279] and 15 ms at 11.7 T[288]. Functional experiments at 9.4 T[257] as well as Monte Carlo simulations of SSFP sequences[252] underpin these findings of longer blood T_2 than previously thought. We find support as well since our qualitative results in Fig. 5.9 suggest that a considerable amount of pial venous blood signal is still present with a TE_{prep} of 31 ms whilst it is

absent at longer TE_{prep}. Given our T_2^*-measurements (Fig. 5.10B) and other experiments at 7 T[284,285,289], venous blood T_2^* at baseline oxygenation can be seen to be around 7 ms supporting a longer blood T_2. Unfortunately, in our $T_2^\dagger$-mapping experiment (Fig. 5.10A) we were not able to confirm this due to our long minimum TE_{prep}, which was limited by the length of the RF pulses in the T_2-prep module. The significant decay associated with this TE_{prep} in conjunction with the relatively short blood T_2, resulted in SNR starved measurements of blood in the sagittal sinus. Nevertheless there is increasing evidence that IV effects based on changes in T_2 are present at TE_{prep} lower than GM T_2 which indicates that for an effective suppression of these components, longer echo times or additional diffusion gradients around refocusing pulses are needed[287,290]. Taking venous blood T_2 as given by Table 5.2, our simulations (Fig. 5.14A-C) show a remaining IV effect at TE_{GRE} = 0 ms for a TE_{prep} of 30 ms. This is in line with a simulation study of SE-BOLD signal changes[256], showing that for echo times shorter than GM T_2, intravascular contributions from big vessels contribute significantly. In case of our experimental data, remaining IV contributions are visible as a peak at the pial surface. At longer TE_{prep}, IV effects are close to zero, in line with Monte Carlo simulation studies[129,252]. A recent study performed by Pérez-Rodas et al.[291] investigated the intravascular BOLD contributions in balanced SSFP sequences and compared the experimental results with simulations of SE-BOLD signal changes at 3 T, 9.4 T and 14.1 T. At 9.4 T, the simulation results show that IV SE-BOLD signals of large vessels at 50 ms are absent which agree with our 7 T findings of close to zero signal changes at the pial surface for TE_{GRE} = 0 ms (cf. blue curve in Fig. 5.13E).

(2) By extrapolating to a TE_{GRE} = 0 ms case, no peak is observable in CSF at TE_{prep} TEs of 50 ms and 70 ms, indicating refocused EV effects around pial veins. These findings seem to be inconsistent with respect to the SE-BOLD simulation study of Pflugfelder et al[256]. While the simulations predict

that, at 7 T, EV effects in CSF reduce laminar specificity at TE_{prep} of 50 ms and longer, our experiments show refocused EV effects in this compartment. In terms of sensitivity, Pflugfelder et al. predict that sensitivity peaks at a TE_{prep} of around 35 ms at 7 T whereas our experimental $TE_{GRE} = 0$ ms profiles exhibit a maximum sensitivity at a TE_{prep} of 50 ms. Possibly, these discrepancies can be explained by simulation parameter choices not corresponding to the parameters in our experiment.

Although the diffusion coefficient in CSF is approximately three times larger than in GM[292], the dephasing effect around large pial vessels at typical diameters between 130 μm and 380 μm[21] can still safely be considered static given the TE_{prep} used in this work (average diffusion length is 17.5 μm at 70 ms TE_{prep} with a diffusion coefficient of 3.0×10^3 mm^2/s of free water at a temperature of 37°C[293]). Another effect which may result in dynamic dephasing in CSF is bulk motion i.e. pulsation of CSF. To have an influence on the magnetic environment during the T_2-prep module the periodicity of this motion has to be in the order of tens of milliseconds which is unlikely given that the motion is expected to act like a low-pass filtered heartbeat.

By changing our TE_{prep}, we also change the spacing between the 180° pulses. This changes the sensitivity to diffusion effects and is captured in a measure called "apparent T_2" ($T_2^{\dagger}$)[271]. A longer TE_{prep} could therefore result in higher sensitivity toward diffusion effects around large vessels in CSF. In other words: EV effects in CSF would move from a static to a more dynamic dephasing regime. The signal change as a function of TE_{prep} would then behave non-monoexponentially. However, we did not find evidence for this for the range of TE_{prep} used (see Fig. 5.18).

It must be noted that although EV effects in CSF are likely to be refocused at TE_{GRE} = 0 ms and IV contributions are nulled at TE_{prep} = 50 ms and 70 ms, our results in Fig. 5.12 show a negative signal change in CSF at this TE_{GRE} and TE_{prep}, possibly due to a CBV increase of large vessels given

the long stimulus durations[120,121]. As a consequence, the decreased signal change in GM at pial boundary in Fig. 5.13E,F could either be explained by low vascular densities in layers one and two[21] or by partial voluming with negative CSF signal changes. However, the latter can potentially be addressed by sequence design (see discussion below).

(3) An intuitive explanation of the difference between Fig. 5.13E,F with respect to 5.13D would be the intrasvascular signal not having fully decayed at 31 ms TE_{prep}. However, our simulations (Fig. 5.14A-C) show that a dominant IV component would lead to a decrease in signal changes with longer TE_{GRE}. Furthermore, when modifying the IV component's T_2 value to an unrealistically large value to simulate reduced IV suppression, the simulations show a signal increase in all T_2-prep conditions (Fig. 5.16A-D) which is not observed in the measured profiles shown in Fig. 5.13E,F. This simplistic explanation of IV effects being the main source of signal changes thus is not correct.

Instead, the reason for the Fig. 5.13E,F appear to show TE_{GRE} independence in contrast to 5.13D, the explanation for this has to be sought in Fig. 5.8B. Simply put: changes in T_2 and T_2^* are not independent. This is visualized in Fig. 5.8B, where TE_{GRE} dependency of the EV effect is shown for the GRE scenario and all T_2-prep echo times. The peak of optimal sensitivity can clearly be seen to move to the left when increasing T_2 preweighting. This results in a relatively flat section in the TE_{GRE} sensitivity curve for 50 ms and 70 ms TE_{prep} for our TE_{GRE}-range used. Therefore, the difference under (3) can be explained as predominantly being driven by EV effects which due to the T_2-pre-weighting show different TE_{GRE} dependencies for different T_2-prep TEs. We argue that the source of this EV effect is likely attributed to larger venous vessels because our simulation results in Fig. 5.17A-D show that a dominant microvascular EV contribution would lead to a net decrease in signal change with longer TE_{GRE}. Instead, EV effects around ICVs (Fig. 5.17E,F) lead to a net increase in signal change (5.17G,H) as observed in Figure 5.14.

However, assuming changes in T_2^* of the size as reported in Tab. 5.2 results in some discrepancy between simulation (Fig. 5.14D) and measurement (Fig. 5.13D) in deep (blue arrows) and middle (black arrows) layers. A stronger than expected static EV effect could explain this discrepancy (Fig. 5.16E). These could be caused by pial or intracortical veins or both. In recent publications, the extravascular effect of large veins were studied in task fMRI at 9.4 T[135], at 7 T[294] and in resting-state fMRI at 7 T and 3 T[127], all using GRE-EPI. All found a considerable EV effect of pial veins on the parenchyma even at deeper cortical depths which could explain the increase in signal change in deep and middle layers in our measured data (Fig. 5.13D). Another possible source would be ascending ICVs as well as the horizontal collecting veins that connect the capillaries to the ascending ICVs. The latter would not affect spatial specificity in laminar experiments a lot, but the former would.

The profiles at 50 ms and 70 ms TE_{prep} appear to be independent of TE_{GRE}, falsely suggesting no T_2' contribution. This is a consequence of the T_2 pre-weighting as the optimum TE_{GRE} of the sensitivity curve shifts toward shorter TE_{GRE} (Fig. 5.8B, Fig. 5.14A-C). This should be taken into account when dealing with SE data acquired with T_2'-pollution since already at a TE_{GRE} = 2.25 ms (at 7 T), unspecific EV effects are noticeable (Figs. 5.13, 5.14, 5.16). In terms of specificity, using T_2-weighted sequences will always be better than a pure GRE sequence and is it up to the user to decide how much T_2' corruption is considered acceptable. For instance, Goense and Logothetis[138] used varying segmentation factors in SE-EPI to investigate the effect of echo train length on the shape of laminar activation profiles acquired with a high-resolution (0.5 mm in plane) in monkeys at 4.7 T. They showed that activity at the pial surface is absent only when using a very short acquisition window of 7.7 ms (16-fold segmentation). This means that even the highest spatial frequencies still needed to be acquired less than 4 ms away from the

spin echo in order for the $T_2^{'}$-effects not to dominate. This may seem a bad prospect for SE-EPI or any other efficient sampling scheme to acquire spin echo data. Fortunately however, our work shows that although some extravascular dephasing around veins is seen throughout all layers of the cortex, by far the largest effect is seen at the surface (often used in argumentation whether venous effects are dominant in layer profiles or not) and this peak stems predominantly from extravascular effects in the CSF compartment. By optimizing the T_2-weighting to suppress unwanted intravascular draining vein effects, the sequence has become sensitive to EV BOLD changes in CSF with its long T_2, and Pflugfelder et al. showed that this can significantly reduce specificity in voxels at the GM-CSF boundary[256]. But as this compartment is outside the cortex, these CSF effects are only problematic through partial volume effects which could in theory be addressed through higher resolution sequences, possibly exploiting anisotropy[295]. In other words, the worst $T_2^{'}$-pollution of laminar profiles through EV vein effects appears to be a problem of engineering (reducing partial volume effects) as opposed to a fundamental biophysical one which cannot be solved through sequence resolution increase.

In this work, technical challenges regarding the generation of T_2-contrast and its sustainability during the signal readout must be addressed. The simulation result in Fig. 5.8A suggests that T_1-relaxation and its adverse effect on the desired T_2-contrast must be minimized as pointed out earlier[261]. This is particularly important for high resolution applications due to the long readouts involved. During those, IV non-T_2-weighted signals can re-merge due to blood's short T_2^*, leading to relatively large signal changes at short GRE-TEs. Secondly, T_2-weighted M_z reaches a new (lower) steady state during the readout resulting in an inhomogeneous signal distribution across k-space and blurring in image space.

In order to reduce these confounding effects, we maximally segmented the partition encoding dimension which required a high number of T_2-prep

modules per unit time. To address the resulting higher power deposition, we designed low-power, narrow bandwidth adiabatic pulses (see Fig. 5.6 and 5.7). With 3-fold acceleration and 3-fold segmentation of the primary phase encoding direction, we reduced the segment TR such that the remaining, maximum T_1-relaxation effect was around 22 % of M_0. Given the center-out encoding scheme, the influence of this residual relaxation can be considered small. With a lower amount of k_z-segmentation, T_1-induced blurring can also be reduced by using variable FA along k_z[296] as it has been done in other magnetization preparation studies[297,298]. However, a loss of T_2-weighting can only be addressed by a repetitive application of the T_2-prep module.

Our laminar experiments (Fig. 5.13) suggest that the acquisition of four gradient echoes per excitation is sufficient to extrapolate to a condition without $T_2^{'}$-weighting given the good quality of the fit (Fig. 5.20A,B). To fit the data, we chose as short as possible TE_{GRE} to not unnecessarily prolong TR and a simple mono-exponential model. However, it is well known that in theory the signal decay deviates from a mono-exponential behavior at short TE[131,276], which may introduce a bias in our signal fitting and modeling. We assessed if a higher-order exponential model do fit our data better than a simple mono-exponential (Fig. 5.19) and conclude that the latter model is the better representation of our data.

As an alternative to multi-echo imaging, temporal resolution and tSNR can greatly be improved by performing an experiment with an as short as possible single TE_{GRE}. For instance, using 750 μs long excitation pulses and asymmetric echoes, a TE_{GRE} of 1.18 ms can be achieved with standard gradient coils at 7 T. With a TE_{prep} of 50 ms in combination with partial Fourier in the partition encoding direction, the volume TR for our slab of 32 slices can be reduced to 10 s. With a different partial Fourier reconstruction strategy[61], the volume TR can further be reduced to approximately 6-7 s. Such short acquisition times would additionally help to provide a high amount of averaging

needed to counteract the intrinsically low sensitivity given that the baseline signal has to reach a steady state and is reduced by a substantial amount with more T_2-weighting. To further increase time efficiency besides using partial Fourier, our simulations suggest that a lower than utilized number of dummy shots is sufficient to reach a steady state. Moreover, by using a pseudo-random spoiling scheme along with RF-spoiling within the T_2-prep module, the confounding effect of any residual transverse magnetization can be reduced and possibly the number of dummy lines in the readout. Of all these measures, reducing the readout time by omitting a multi-echo acquisition is the most efficient one, but comes at the price of additional $T_2^{'}$-pollution as data can no longer be extrapolated to $TE_{GRE} = 0$ ms. We have also investigated acceleration capabilities of multi-echo data by using a joint reconstruction approach[299], given in the appendix. Unfortunately, our findings indicate that the shared information between echoes used in the reconstruction resulted in non-unique single echo profiles prohibiting correct fitting and interpretation of the measured data.

5.5 Concluding remarks

We showed that the acquisition of robust laminar responses to a visual stimulus with T_2-prepared, multi-echo FLASH is feasible at 7 T. By varying both SE and GRE echo times we could investigate signal contributions from different vascular and non-vascular compartments to the shape of laminar fMRI profiles.

Scanning at multiple GRE echo times allowed us to extrapolate to a laminar profile at $TE_{GRE} = 0$ ms. To our knowledge these are the first T_2-weighted laminar profiles devoid of $T_2^{'}$ pollution reported and are well confined to GM. They look very similar for the three different T_2-weightings, except for the shortest T_2-prep echo time where an additional intravascular component can be observed on top of this general shape.

As soon as $T_2^{'}$ is introduced, even at 2.25 ms TE_{GRE}, strong effects at the pial surface can be seen, partial voluming into the superficial layers. Our simulations show that this is predominantly caused by EV dephasing in CSF. Additionally, another, weaker, static dephasing effect is observed throughout all layers of the cortex, which is particularly obvious in the data with shortest T_2-prep echo time. Our simulations show that this cannot be explained by intravascular dephasing but that it is likely caused by extravascular effects of the intracortical and pial veins. The simulations also explain why this effect is hidden but nevertheless present in the longer T_2-prep TE data through the shift in optimal TE_{GRE} sensitivity curves induced by T_2 weighting. These results can be used as a guideline when designing efficient T_2-weighted sequences in terms of how much specificity loss is considered acceptable. For example, in Fig. 5.13D, the relative distance of the blue and the red line with respect to zero can serve as an estimate of $T_2^{'}$-pollution inside GM. The CSF compartment then indicates an upper bound of the static dephasing sensitivity to be expected. The finding that the bulk of profile corruption at non-zero $T_2^{'}$-weighting stems from CSF bodes well for more efficient T_2-weighted sequences provided partial volume effects are kept to a minimum.

Appendix A Joint multi-echo reconstruction

Introduction

To accelerate multi-contrast MRI, Bilgic et al.[299] proposed a method wherein multiple echoes are reconstructed jointly within the GRAPPA framework. The principle is to treat additional contrast as additional coils by including them in the GRAPPA kernel calibration. As the individual contrasts exhibit little extra information in terms of encoding sensitivity, echoes are shifted with respect to one another in k-space using caipi blips between readouts to achieve complementary k-space coverage. In the reconstruction process, a GRAPPA kernel is fitted across contrasts and subsequently applied to create jointly reconstructed multi-echo data (Fig. 5.21).

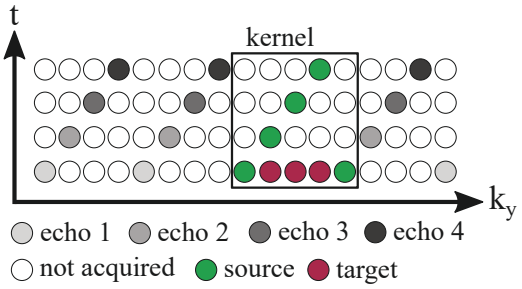

Fig. 5.21 Illustration of the joint GRAPPA algorithm. Joint GRAPPA reconstruction of four echoes for an undersampling factor of R = 4. The echoes are shifted with respect to one another and a kernel uses the additional information as source points to reconstructed the missing target points (coil and readout dimensions are omitted for visualization, adapted from [299]).

We were interested in whether this approach could accelerate the multi-echo T_2-prep acquisition without comprising the data quality. As unique echo information is imperative to extrapolate to a TE_{GRE} = 0 ms condition and to understand how different contributions of $T_2^{'}$ dephasing would affect the shape of the measured laminar profiles, we introduced an sampling strategy additional to the segmentation approach to verify the fidelity of the signal (see next section).

Materials & methods

We performed a similar laminar fMRI experiment as described in section 5.2.1.3 in one subject. The T_2-prep sequence had the following parameters: 256 x 256 x 32 matrix size and 0.75 mm isotropic resolution. Four equidistant echoes were acquired with a bipolar readout and a bandwidth of 700 Hz/px. A small gradient blip was implemented between the readout lobes to shift the echoes with respect to one another. TE_{GRE} were 2.88/4.84/6.8/8.76 ms, echo spacing was 1.96 ms. TE_{prep} was 50 ms and TR was 11.2 ms. The secondary PE was 8-fold segmented and both PE directions were sampled center out. The primary PE direction was 8-fold undersampled which would result in an approximately 2-fold net acceleration factor in a joint reconstruction.

To compare the joint reconstruction with conventional GRAPPA, we needed to modify the sampling scheme to obtain usable single echo images with standard GRAPPA reconstructions. To this end, we introduced the tGRAPPA sampling strategy[300] in our fMRI experiment, i.e. the sampling pattern was permuted over volumes such that after R volumes, a fully-sampled k-space was obtained. This was used as ACS data to reconstruct the R volumes and the procedure was repeated in a sliding window fashion, i.e. for each set of R volumes, a separate ACS region and GRAPPA kernel was used. Moreover, combining two subsequent volumes resulted in effectively 4-fold accelerated single echo images which could be reconstructed with GRAPPA. To characterize the differences between GRAPPA and tGRAPPA reconstructions, we first performed a separate acquisition of 50 volumes without functional stimulation. The joint reconstruction approach was implemented in our offline reconstruction pipeline, single coil images of an fMRI experiment were combined using sum-of-squares and subsequently processed as described in sections 5.2.2.2 and 5.2.4.

Results & discussion

Fig. 5.22 shows the first image of the time series without functional stimulation reconstructed with conventional GRAPPA (Fig. 5.22A) and with tGRAPPA (Fig. 5.22B) with R = 4. A clear gain in image SNR can be seen with tGRAPPA which could be attributed to the fact that the data themselves are used as ACS and a full k-space can be used to train the GRAPPA kernel. This may result in a better conditioning of the kernel estimation and prevents discrepancies between ACS and actual data which could be useful in especially long fMRI runs. Another advantage of tGRAPPA for fMRI could be that given that the kernel is re-calibrated every R volumes, dynamic physiological changes are captured in the reconstruction which might help to improve the temporal stability of the time series, e.g. adapting to phase effects as a result of breathing.

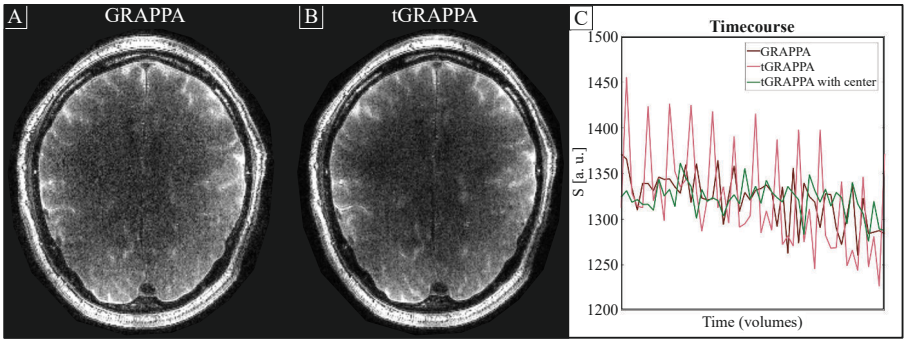

Fig. 5.22 Comparison between GRAPPA and tGRAPPA. (A,B) First image of a time series of 50 volumes reconstructed with GRAPPA (A) and with tGRAPPA (B) showing a clear gain in image SNR with tGRAPPA. (C) Timecourse of the GM signal in V1 showing a signal fluctuation with an R-fold periodicity when using tGRAPPA (pink line) compared to GRAPPA (brown line). Ensuring that the high-energy center of k-space is always acquired for each volume, the instabilities can be greatly reduced (green line).

Fig. 5.22C shows the timecourse of GM signal in V1 and illustrates a problem with tGRAPPA: Because the undersampling pattern varied across volumes, it occurred that the center k-space echo was not in the set of acquired lines. As this portion of k-space is crucial for the image signal, errors in the tGRAPPA reconstruction translate into large errors in the final image, seen as signal intensity fluctuations with a 4-fold periodicity (comparing the brown with the pink timecourse in Fig. 5.22C). We attempted to alleviate this issue by ensuring that the high-energy center of k-space was always acquired in each volume (corresponding to five extra center lines at the start of each volume). This greatly reduced the signal instabilities (green line in Fig. 5.22C). Residual fluctuations may be further reduced by using denoising techniques based on Independent Component Analysis (ICA)[301–303] or by including the signal intensity variations in the general linear model provided that the frequency of the artifact is not within the band of the desired fMRI intensity variations.

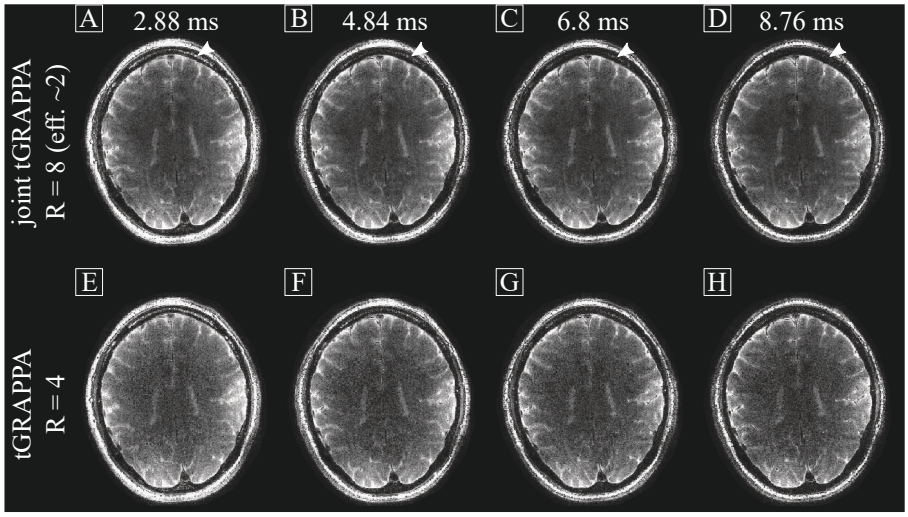

Fig. 5.23 Comparison between joint tGRAPPA and tGRAPPA. (A-D) Joint tGRAPPA reconstruction of the first volume of the fMRI experiment for all measured TE_{GRE}. As the effective acceleration factor is approximately two, g-noise is low. Qualitatively, the images show a T_2^* decay as indicated by the white arrows highlighting subcutaneous fat. (E-H) Corresponding tGRAPPA reconstruction with an effective acceleration factor of four showing a higher g-noise, as expected.

Fig. 5.23 shows images of the first volume of the laminar fMRI experiment for all measured TE_{GRE} and for the joint tGRAPPA (Fig. 5.23A-D) and the single echo tGRAPPA reconstruction (5.23E-H), respectively. Qualitatively, the jointly reconstructed images exhibit a lower g-noise compared to the single-echo images as the effective acceleration factor is halved. Furthermore, the jointly reconstructed images exhibit a T_2^* decay as indicated by the white arrows in Fig. 5.23A-D highlighting the decay of subcutaneous fat signal.

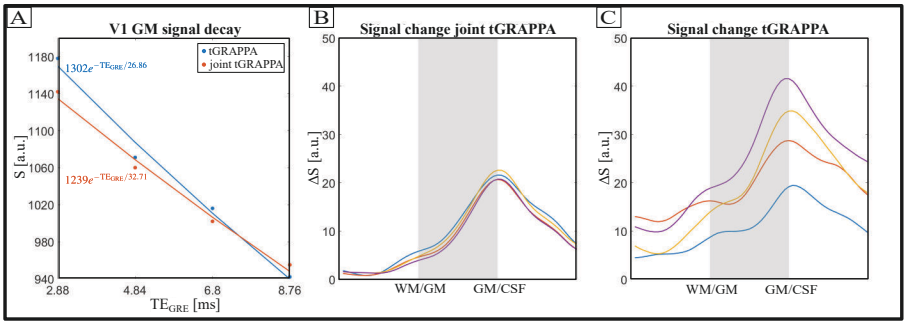

Fig. 5.24 Signal decay and laminar profile comparison between joint tGRAPPA and tGRAPPA. (A) T_2^* decay of GM signal in V1 at rest for tGRAPPA (blue curve) and joint tGRAPPA (red curve). The dots represent the measured data and the curves are non-linear fits. The joint tGRAPPA curve shows a strong deviation from the reference resulting in a strong overestimation of the T_2^*. (B,C) Profiles of signal change as a function of cortical depth for the joint reconstruction (B) and the individual reconstruction (C). The jointly reconstructed profiles exhibit no variation with TE_{GRE} compared to the reference. Moreover, the signal change intensities in B seem to be an average of those shown in C.

In Fig. 5.24, a quantitative comparison between joint tGRAPPA and single-echo tGRAPPA is shown. Fig. 5.24A shows the T_2^* decay of GM signal in V1 at rest for tGRAPPA (blue dots/line) and joint tGRAPPA (red dots/line) along with the fitted mono-exponential functions. The curves indicate that the joint tGRAPPA reconstruction results in lower signal intensity for the shortest TE_{GRE} and a higher intensity for the longest compared to individual reconstructed echoes. This results in a strong overestimation of T_2^* (32.7 ms and

26.9 ms for the joint and the single-echo reconstruction, respectively). Inspecting the laminar profiles of signal change upon activation in Fig. 5.24B,C shows that the joint reconstruction results in profiles devoid of TE_{GRE}-related signal variations as opposed to the individually reconstructed data. Moreover, the signal change amplitudes in Fig. 5.24B seem to be an average of those profiles shown in Fig. 5.24C.

The source of this deviation is not entirely clear, but the presented results strongly indicate that the shared information between echoes used in the joint reconstruction resulted in contrast leakage between echoes, the strongest to be seen at the shortest and longest echo time (Fig. 5.24A). This leakage also explains the similarity between echoes shown in Fig. 5.24B as the joint reconstruction partly removes signal differences between echoes which may result in an effect as if all signal change stems from a single average echo. This problem may be reduced by using a leak-block technique similar to that used in slice-GRAPPA reconstructions of SMS data[304] but it can be expected that this technique negate the attempted image quality improvements made by a joint reconstruction. A promising alternative is the recently introduced subspace reconstruction used in highly accelerated acquisitions[305,306].

Although these results suggest that a joint reconstruction was not an option for the purpose of the study described in chapter 5, it may be an attractive acceleration candidate if a *single averaged* echo is of interest. For instance, using a bipolar readout and modern imaging gradients, the TE_{GRE} could be 1.75/3.02/4.29/5.56 ms. With a 4-fold acceleration along PE_y, a single echo reconstruction would lead to a volume TR of $TR_{vol} \approx 18.4$ s. A joint reconstruction using an 8-fold (effectively 2-fold) or a 16-fold (effectively 4-fold) acceleration would reduce the TR_{vol} to 10.3 s or 6.2 s, respectively. Note that other measures to reduce the TR_{vol}, e.g. partial Fourier or zooming, are not yet taken into account. Averaging the echoes to an effective TE_{GRE} of 3.66 ms would likely result into a profile similar to the red profile shown in Fig. 5.13E but with twice the image SNR.

The research leading to these results has received funding from the DFG grant 310872863 and the NWO VIDI grant 016-178-052. We thank Philipp Ehses (German Center for Neurodegenerative Diseases (DZNE), Bonn, Germany) for providing the reconstruction code and Irati Markuerkiaga for providing the vascular model.

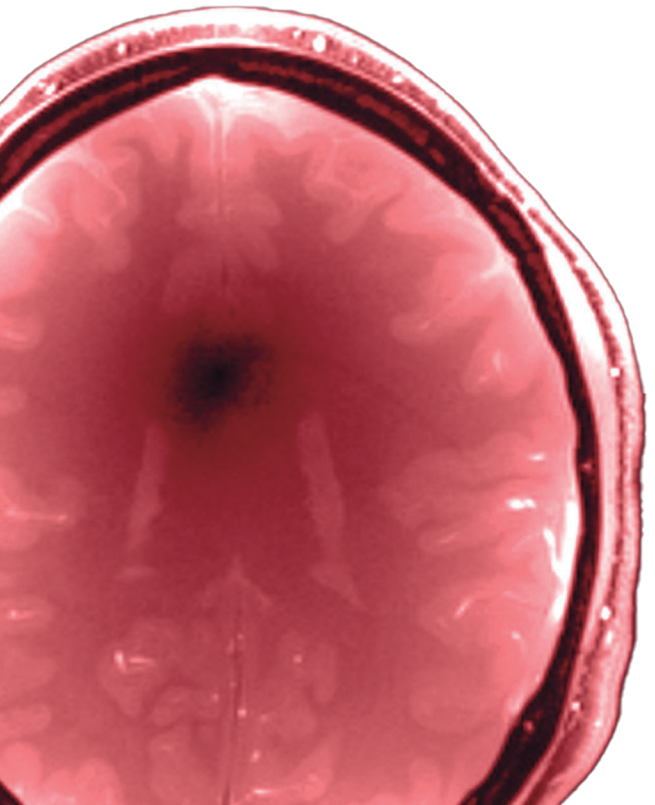

6

Magnetization Transfer weighted laminar fMRI with multi-echo 3D FLASH

Associated publication: **Pfaffenrot, V.** and Koopmans, P. J. "Magnetization Transfer weighted laminar fMRI with multi-echo FLASH". *Submitted to Neuroimage (in revision)*.

Abstract

Laminar functional magnetic resonance imaging (fMRI) using the gradient echo (GRE) blood oxygenation level dependent (BOLD) contrast is prone to signal changes arising from large unspecific venous vessels. Alternatives based on changes of cerebral blood volume (CBV) become more popular since it is expected that this hemodynamic response is dominant in microvasculature. One approach to sensitize the signal toward changes in CBV, and to simultaneously reduce unwanted extravascular (EV) BOLD blurring, is to selectively reduce gray matter (GM) signal via magnetization transfer (MT).

In this work, we use off-resonant MT-pulses with a 3D FLASH readout to perform MT-prepared (MT-prep) laminar fMRI of the primary visual cortex (V1) at multiple echo times at 7 T. With a GRE-BOLD contrast without additional MT-weighting as reference, we investigated the influence of the MT-preparation on the shape and the echo time dependency of laminar profiles. Through numerical simulations, we optimized the sequence parameters to maximize signal changes induced by changes in arterial CBV and to delineate the contributions of different compartments to the signal. We show that at 7 T, GM signals can be reduced by 30 %. Our laminar fMRI responses exhibit an increased signal change in the parenchyma at very short TE compared to a BOLD-only reference as a result of reduced EV signal intensity. By varying echo times, we could show that MT-prep results in less sensitivity toward unwanted signal changes based on changes in T_2^*. We conclude that off-resonant MT-prep combined with efficient short TE readouts is a promising method to reduce unwanted EV venous contributions in GRE-BOLD and/or to allow scanning at much shorter echo times without incurring a sensitivity penalty in laminar fMRI.

6.1 Introduction

Functional magnetic resonance imaging (fMRI) at sub-millimeter resolutions can probe neuronal activity at the level of cortical columns[239,240,308] and layers[243,244,246,247,309] opening the door toward the study of directionality of signal transductions between and within brain areas[148,310,311].

The majority of layer fMRI studies use the gradient echo (GRE) blood oxygenation dependent (BOLD) contrast due to its high sensitivity[128,130,136] and efficient sequence implementation with echo-planar imaging (EPI) readouts. However, the superior sensitivity stems from intravascular (IV) and extravascular (EV) field effects of micro- and macrovasculature. While the microvasculature is colocated with the neuronal source of activity, the latter, consisting of intracortical veins (ICV) perpendicular to the cortical surface and pial veins parallel to it[21], can blur local signal changes over multiple layers. This is due to ICVs draining blood from the capillary bed toward the pial surface causing IV and EV effects superficial to the site of actual activity. The effects are amplified when approaching the surface because ICVs increase in diameter from deep to superficial layers[21]. In addition, large pial veins at the cortical surface exhibit a strong, long ranging EV field effect onto the entire parenchyma even at deep layers[127,135].

As an alternative to GRE-BOLD, fMRI techniques based on an activity induced increase in CBV[144,146,312–314] become more popular since it is expected that this hemodynamic response is dominant in microvasculature [121,315] although it has been shown that macrovasculature also dilates when long stimuli are used[120,121]. CBV-weighted techniques rely on signal preparation to manipulate the ratio of blood and GM signal contributions. VASO[144,146] achieves this by selectively nulling blood signals, whereas magnetization transfer (MT) methods[123,316,317] opt to null GM signal instead. The latter could prove very interesting for high-resolution fMRI as MT preparation not only results in

sensitivity toward CBV changes, but also reduces EV BOLD blurring due to its GM signal suppression. MT contrast is created through the applications of strong radio frequency (RF) pulses[44,45]. With these, signal from tissue containing semi-solid macromolecules (like gray and white matter) is selectively attenuated while signal from blood is largely untouched. Upon activation, local CBV changes, mainly driven by dilation of arterioles and capillaries, would therefore result in a net positive signal change confined to the site of neuronal activity.

Recent work performed at 3 T shows increased signal change at short TE when applying an on-resonant MT prepulse[317] compared to non-MT GRE-BOLD, while earlier comparisons at 1.5 T showed a decrease in signal change with MT[318]. In this work, we were interested in a) the amount of achievable MT contrast and its effect on laminar fMRI at 7 T, b) how different influences of T_2^* affect the contrast and c) whether the aforementioned changes in the functional signal with MT stem from an increased sensitivity toward changes in CBV, visible in early echoes, in conjunction with reduced sensitivity to EV effects, visible in later echoes, compared to classical GRE-BOLD. To this end, we used an MT-prepared (MT-prep) 3D FLASH sequence to acquire laminar fMRI data of the primary visual cortex (V1) at multiple echo times at 7 T. Using a GRE-BOLD contrast without additional MT-weighting as a reference, we investigated the influence of the MT-preparation on the shape and the TE dependency of cortical depth-dependent activation profiles. Through numerical simulations, we optimized the sequence parameters to maximize signal changes induced by changes in arterial CBV and to delineate the contributions of different compartments to the signal. We expect fMRI with additional MT to have four main characteristics:

(a) The selective attenuation of tissue signal through MT introduces CBV-weighting of the fMRI signal. CBV changes are mostly driven by the dilation of arterioles and capillaries which are known to be well localized to the neuronal source of activity.

(b) In addition to the CBV-weighting character of MT, any tissue signal attenuation reduces EV signal changes which, in case of GRE type of sequences, are more pronounced around large venous vessels which are unwanted unspecific contributors to the fMRI contrast. Therefore, MT-weighting increases the sensitivity to more specific signal changes while at the same time reducing sensitivity to unspecific EV venous effects.

(c) It would be most favorable to selectively attenuate GM signal without directly suppressing blood signal to avoid contrast loss. However, if tissue suppression by MT alone is not sufficient one need to consider additional direct suppression and its effect on the functional contrast. The amount of direct suppression of the blood pool is dependent on its T_2[35]. Therefore, direct suppression will, on the one hand, mostly affect venous blood with its relatively short T_2 resulting in a weighting toward the arterial part of the CBV. However, transverse relaxation times of venous blood increase upon activity. Therefore, the direct suppression factor becomes a function of the functional activity. So, direct suppression is a double-edged sword: on the one hand it suppresses the intravascular signal of the large veins more than that of arteries, but on the other hand it introduces an intravascular T_2-weighted BOLD functional sensitivity in veins.

(d) It can be expected that signal changes induced by changes in CBV will be most pronounced at zero TE since a change in CBV will modify the bulk magnetization within a given voxel. With longer TE, these signal changes become mixed with T_2^* effects of the BOLD contrast.

6.2 Materials & methods

6.2.1 MR data acquisition

Data were acquired on a 7 T system (Terra 7 T, Siemens Healthcare, Erlangen, Germany) equipped with an 8-channel transmit, 32-channel receive head coil (NOVA Medical Inc.). Eight healthy subjects (four male, four female; 25.0 ± 4.4 years old, one subject scanned twice) were scanned after giving informed consent according to the guidelines of the local ethics committee. For each subject, B_0 shimming was performed locally on primary visual cortex using the vendor provided third order shimming capability. Transmitter amplitude was calibrated on V1 using B_1^+ maps acquired with the preSAT-TFL technique[319] in CP^{2+} transmit mode.

6.2.1.1 Structural scans

Whole brain T_1-weighted anatomical reference data were acquired with an MP2RAGE sequence[320] with fat navigators[321] at 0.75 mm isotropic resolution. Parameters were: sagittal orientation, 340 x 340 x 240 matrix size, TE/TR/TI1/TI2 = 1.81/6000/800/2750 ms, GRAPPA R = 3, total acquisition time = 14:56 min. The flip angles (FA) were FA1/FA2 = 4°/5°.

6.2.1.2 Functional scans

Functional data with and without MT-preparation were acquired using a segmented 3D multi-echo FLASH sequence with center-out phase encoding. The sequence parameters were chosen based on simulations (section 6.2.6) whose results are shown in section 6.3.1. In case of MT-prep, a 4 ms Gaussian RF pulse (697 Hz bandwidth) played out at -650 Hz off-resonance was used to generate the MT-contrast (see also sections 6.2.6 and 6.3.1). In one male subject, the pulse power was calibrated to achieve 100 % SAR in normal mode.

This resulted in a nominal MT-prep FA of 225° (10.9 μT peak B_1^+) which was held constant between subjects. SAR-mode was changed to first level if a higher reference amplitude was necessary. SAR never exceeded 65 % first level mode. For the BOLD reference, the MT pulse was turned off without changing the spoiler and segment repetition time (TR_{seg}). All functional scans were acquired in CP^{2+} mode to achieve a more homogeneous and power efficient excitation of V1 (see section 6.2.1.5, section 6.3.2 and Fig. 6.7).

A 252 x 252 x 32 matrix with an isotropic resolution of 0.75 mm was acquired at four equidistant echo times using a monopolar readout (1100 Hz/px bandwidth). The minimum and maximum TE was 1.86 ms and 9.12 ms, respectively. Echo spacing was 2.42 ms and TR was 11.6 ms. The excitation pulse was 1 ms long and the readout FA was 6° (see also section 6.2.6). Similar to previous work[238], we segmented the primary phase encode dimension (PE_y) 7-fold and undersampled it 3-fold resulting in a TR_{seg} of 179 ms at an MT-module duty cycle (i.e. time of the MT-module relative to TR_{seg}) of 9.3 %. The effective volume TR (TR_{vol}) was 40.1 s. To reach a steady state, 98 MT-prep dummy shots preceded each run. In addition, each MT-prep PE_y segment was preceded by two dummy lines to avoid variability due to signal instabilities in the first readouts. No RF spoiling was applied to avoid signal suppression of long T_1 species like blood. The FOV was positioned such that it symmetrically covered the calcarine sulcus.

6.2.1.3 Functional experiments

We used a classical flickering checkerboard block design as functional experiment. The functional session was split into four runs, two with and two without MT preparation, acquired in a pseudo-random order. Each run consisted of four baseline blocks during which the subject attended a red fixation cross on a gray background. Activity was induced with a radial full-field

checkerboard flickering at 8 Hz during four active blocks. The checkerboard started 6 s before an actual active volume to sample the BOLD response at its peak. Sixteen volumes were acquired per run of 13:19 min, with two volumes per block. Between runs, the participants had the opportunity to take a break within the scanner. To reduce the impact of frequency drifts, the frequency was reset before each run. MATLAB (The MathWorks, Natick, MA) and the Psychophysics Toolbox[268,269] (Version 3.0.15) were used to present the stimuli.

6.2.1.4 Data reconstruction

The functional data were reconstructed offline using custom-written MATLAB routines similar to previous work[238]. In short, GRAPPA[67] was calibrated on fully-sampled autocalibration (ACS) data. A slice- and echo-specific kernel with size 9 x 6 was used. The reconstructed single-coil images where combined using echo-specific coil-sensitivity profiles obtained with the SENSE1 algorithm as opposed to a sum-of-squares combination to avoid a raised noise floor[272]. All runs were put into the same intensity scale as the first BOLD run.

6.2.1.5 Additional measurements

To verify that the simulations as performed in section 6.2.6 (see section 2.1.5 for description of the theory) reflect the measurement situation, we performed validation experiments using different parameter combinations as summarized in tab. 6.1. The well-studied splenium corpus callosum (SCC)[48,322–324] was taken as the bound pool and cerebrospinal fluid (CSF) in ventricles I and II was taken as the free pool. Both regions had the same B_1 transmitter efficiency. Tissue parameters are given in tab. 6.2. Classically, the restricted pool T_1 has been assumed to be 1 s which has been questioned recently (Van Gelderen et

al.[48] and references within). We used the relationship between the observed T_1 and the restricted T_1 (eq. 2.22) to calculate $T_{1,r}$. To this end, we used $T_{1,obs}$ as obtained by Yarnykh et al.[325] with a very similar sequence as ours at 1.5 T and extrapolated it to 7 T[326]. Given the uncertainty of this approach, we also performed simulations with $T_{1,r}$ = 400 ms.

In addition to the main functional experiments, one subject was rescanned to assess the effects of inflow on the BOLD data. Within one session, BOLD experiments were performed using outer volume saturation pulses played out every TR with 40° FA. The TR and volume TR were 25.8 ms and 69.4 s, respectively, with otherwise parameters matched to the main experiment. As a control condition, a BOLD experiment without this suppression at identical TR was performed within the same session.

Another subject was scanned without functional stimulation with an MT pulse played out at -2 kHz. In this experiment, the magnetization transfer ratio (MTR) defined as

$$\mathrm{MTR} = 1 - \mathrm{MT_{ON}}/\mathrm{MT_{OFF}} \tag{6.1}$$

was compared using CP^+ and CP^{2+} transmit mode to investigate whether RF-shimming would result in improved tissue saturation in the occipital lobe.

Tab. 6.1 Sequence parameters used for the simulation verification experiments.

# measurement	1	2	3	4	5	6	7
T[a]/BW [ms/Hz]	9.3/300	9.3/300	25/100	25/100	25/100	25/100	25/100
FA [°]	319	319	1176	1201	917	1032	1032
δ[b][kHz]	1	-1	-1	-2	-2	-2	-2
TR_{seg} [ms]	385	385	385	385	223	223	223
α[c] [°]	7	7	5.8	5.8	4.8	4.8	4.8
TE [ms]	1.86	1.86	1.86	1.86	1.86	1.86	9.12

[a] MT-pulse duration
[b] off-resonance frequency
[c] readout flip angle

Tab. 6.2 Simulation parameters used for the verification.

Compartment	F [%]	k_f [1/s]	$M_{0,f}$	$T_{1,f}$ [s]	$T_{1,r}$ [s]	$T_{2,f}$ [ms]	$T_{2,r}$ [μs]	T_2^* [ms]
SCC	16[a]	3.3[a]	1	3.33[b]	0.3[c]/0.4	54[d]	10	18[d]
CSF	—	—	1.26[e]	4.5[g]	—	900[f]	—	130[d]

[a] [325]
[b] [48]
[c] estimated based on $T_{1,obs}$ = 670 ms at 1.5 T[325], extrapolated to 7 T via $T_1(7T) = T_1(1.5T)*(7/1.5)^{0.5}$[326] and used in eq.2.22 to calculate $T_{1,r}$
[d] estimated based on separate measurements
[e] taking proton density differences relative to SCC as reported in [327] into account
[f] [280]
[g] [281]

6.2.2 Data pre-processing

6.2.2.1 Structural scans

The MP2RAGE was denoised using freely available code (https://github.com/srikash/MP2RAGE-utils) and corrected for residual receive bias fields before being segmented using *spm_preproc* to create a brain mask. The masked brain was manually corrected in areas where the dura or the sagittal sinus were erroneously classified as tissue. FreeSurfer Version 6.0[273] with the *-cm* flag and with 50 iterations in *mris_inflate* was used to create GM/CSF boundaries.

6.2.2.2 Functional scans

BOLD and MT-prep functional data were separately pre-processed using MATLAB code based on SPM12 Version 7487 (Welcome Trust Centre for Neuroimaging, London). For one subject, one run was excluded from the analysis due to concentration loss at the end of the session. The remaining data were realigned within each run. To this end, an echo-averaged, biasfield-corrected image was calculated and segmented to create a brain mask. The mask served as weights within *spm_realign*, reducing the influence of subcutaneous fat onto motion estimates. Motion between runs was accounted for by realigning a biasfield-corrected volume average of the third TE of each run.

Registration to the structural image was performed in two steps within ITK-SNAP[225] Version 3.6.0 (www.itk-snap.org) First, registration of the aforementioned volume average was manually initialized. Second, the initialization was refined using the automatic registration tool of ITK-SNAP. To this end, the registration was run at the finest resolution using an affine transformation model. To guide the algorithm, a segmentation mask was drawn on the occipital lobe. The affine transformation takes small distortions

between functional and anatomical data owing to differences in readout direction and bandwidth into account. All transformation matrices were concatenated and a single resampling operation was applied.

6.2.3 Laminar profile extraction

In order to extract cortical profiles from the functional data, two ROIs, each targeting positive activation in the posterior calcarine sulcus of a hemisphere, were drawn on the inflated brain in FreeView Version 2.0. Only vertices corresponding to a reported cortical thickness between 2.3 mm and 3.5 mm within these ROIs were taken into account. Inside GM, 20 equidistant layers were sampled from the spatial functional data. In addition, to examine effects outside GM, sampling continued into WM and into CSF, for the same distance as inside GM resulting in a total of 60 spatial positions spanning three times the cortical thickness. To avoid influences of downstream effects of the sagittal sinus, profiles which sample through the sagittal sinus were excluded before averaging over vertices.

6.2.4 Data analysis

To account for between-run intensity offsets, all runs were globally scaled relative to the first one on the single subject level. Each run was high-pass filtered with a cutoff period of 4 x block duration, i.e. 320.8 s. For each cortical depth bin and volume, a mono-exponential decay function was fit to the data using MATLAB's Levenberg-Marquardt nonlinear least squares algorithm. With this, we obtained an extrapolated TE = 0 ms profile.

For each run, a GLM analysis was performed with a design matrix containing the stimulus design as the regressor of interest. Due to the long volume TR and the 6-second temporal shift of the stimulus paradigm with respect to the volume acquisition we did not convolve the task regressor with an HRF. We used a WM regressor using WM near V1 to capture unwanted signal

fluctuations like those associated with bulk motion. The design matrix was highpass-filtered with the same filter as the functional data and the first and the last volume of the design matrix of each run were removed to account for edge effects at the boundaries of each run's time series as a result of high-pass filtering[275]. The beta-weight corresponding to the task-induced signal change was averaged over runs and subjects.

For each subject, we quantified an MTR map (eq. 6.1) using non-biasfield corrected volumes averaged over the rest condition. This map was sampled (see previous section) to create a laminar MTR profile. These profiles were averaged over subjects.

6.2.5 Activation map estimation

For two subjects, activation maps were created to assess the general activity pattern visually. As our data with such high resolution were not intended nor suited for assessments at the individual voxel level (due to SNR), some smoothing was required for this visualization. To this end, the function *LN_GRADSMOOTH* from the LAYNII software distribution[274] version 1.6.0 archived in Zenodo was utilized to perform anatomically informed, three-step smoothing preventing averaging between different tissues. First, masks of large venous vessels were created by thresholding T_2^*-maps obtained for each run via fitting of the multi-echo data (see previous section). To determine the compartments, the MP2RAGE data, masked for venous vessels, and the average functional image were used. This way, WM, GM, CSF, and large pial veins were smoothed separately using an adaptive 3 mm smoothing kernel.

6.2.6 Simulations

We performed numerical simulations to estimate sequence parameters which maximize the sensitivity for measuring signal changes based on changes in

CBV while, at the same time, maximize GM signal suppression. To this end, we used the freely available MATLAB software package qMRLab[328] (http://qmrlab.org/) which incorporates the Bloch-McConnell equations (eq. 2.18-2.21). We modified the provided readout module to match our multi-echo sampling scheme. In conjunction to the MT-related part of the simulations, we used a simple four-compartment cortical vascular model[122,238,255] to account for cortical depth specific parameter variations. The simulated compartments were GM, venous blood, arterial blood and CSF. CSF was modeled to investigate EV effects of pial veins in this compartment. Tab. 6.3 shows the MT-specific simulation parameters where T_{2f} and T_2^* are averages over the cortical thickness.

Tab. 6.3 MT-related tissue parameters used in the laminar fMRI simulations.

Compartment	F [%]	k_f [1/s]	$M_{0,f}$	$T_{1,f}$ [s]	$T_{1,r}$ [s]	$T_{2,r}$ [μs]	$T_{2,f}$ [ms]		T_2^* [ms]	
							OFF	ON	OFF	ON
GM	7[a]	2.3[a]	1	3.33[b]	0.4	10	47.0[c]	48.2[c]	28.0[c]	29.0[c]
Venous blood	—	—	1.17[e]	2.1[f]	—	—	20.5[g]	29.7[g]	6.5[d]	8.6[c]
Arterial blood	—	—	1.17[e]	2.3[f]	—	—	68.1[c]	67.1[c]	14.6[c]	14.9[c]
CSF	—	—	1.26[e]	4.5[h]	—	—	900[i]	903[c]	130[d]	150[c]

[a] [324]
[b] [48]
[c] [255]
[d] estimated based on separate measurement
[e] taking proton density differences relative to GM as reported in [327] into account
[f] [329]
[g] [279]
[h] [281]
[i] [280]

In tab.6.4, these transverse relaxation times are subdivided into three cortical bins, referred to as deep, middle, and top reflecting cortical depth and, implicitly, vessel size dependent variations of $T_2^{(*)}$ and CBV (see Fig. 6.1). If not otherwise specified, the parameters were taken from simulation studies of Markuerkiaga et al.[255] and Uludag et al.[119]. The baseline blood volume distribution was taken from Duvernoy[21] and Lauwers et al.[106]. Cortical depth specific CBV changes upon activation were taken from Akbari et al.[122]. Changes in T_2^* in CSF were taken from Markuerkiaga[278] and Uludag et al.[119].

Tab. 6.4 Cortical depth-dependent tissue parameters.

Compartment	T_2 [ms]		T_2^* [ms]		Volume fraction [%]	
	OFF	ON	OFF	ON	OFF	ON
GM (deep)	48.1	48.7	29.5	30.45	97.98	97.62
GM (middle)	46.8	47.7	27.7	28.95	96.19	95.21
GM (top)	47.3	48.1	27.0	28.4	95.69	94.94
Ven. blood (deep)	20.5	29.7	6.5	8.6	1.39	1.59
Ven. blood (middle)	20.5	29.7	6.5	8.6	2.51	3.04
Ven. blood (top)	20.5	29.7	6.5	8.6	2.60	2.93
Art. blood (deep)	68.1	67.1	14.6	14.9	0.63	0.78
Art. blood (middle)	68.1	67.1	14.6	14.9	1.30	1.74
Art. blood (top)	68.1	67.1	14.6	14.9	1.71	2.13
CSF	900.0	903.0	130.0	150.0	95.05	94.89

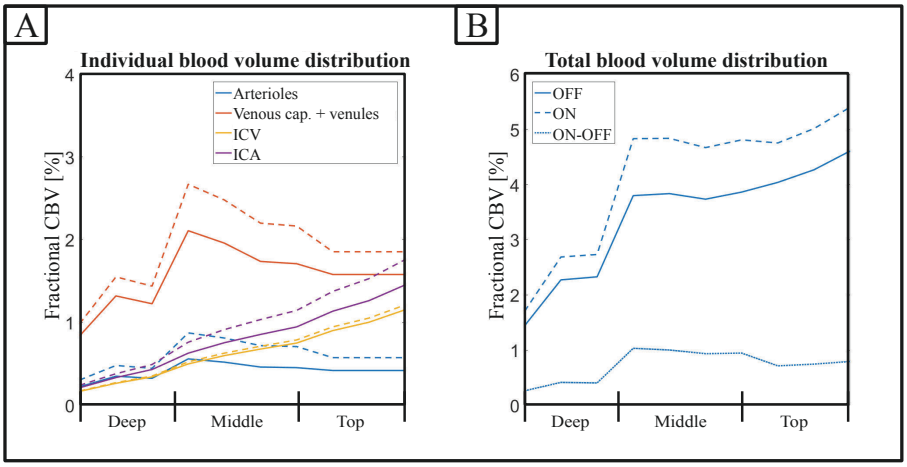

Fig. 6.1 Blood volume distribution as used in the simulations. (A) Individual blood volume of arterioles (blue lines), intracortical veins (yellow), intracortical arteries (purple) and venous capillaries together with venules (red) during rest (solid lines) and activity (dashed lines) for long stimuli. The bulk of CBV change upon activity stems from the capillaries, venules and arterioles. Due to the long stimuli, ICAs and ICVs dilate to a certain extend as well, although less than the microvasculature. (B) Total blood volume during rest, during activity and their difference.

The blood compartment was separated into laminar vasculature consisting of 21 % arterioles, 36 % capillaries and 43 % venules[105] and into intracortical macrovasculature consisting of intracortical arteries (ICA) and ascending veins (Fig. 6.1). The final MR signal was computed as

$$S = (1 - CBV)\, S_{Ex} + CBV S_{In} \tag{6.2}$$

with S_{Ex} and S_{in} being the extravascular and intravascular signal, respectively. CBV is the combined volume fraction of the vasculature within a specific bin. For long stimulus durations as used in this study, it has been shown that large venous vessels also dilate to a certain extend[120,121]. We linearly extrapolated the baseline blood volume of all vasculature to estimate pial CBV at rest.

Fractional CBV change for ICVs as taken from Akbari et al.[122] were linearly extrapolated to estimate a CBV change in the venous pial vasculature.

The functional signal change was calculated as $\Delta S = S_{ON} - S_{OFF}$. For the cortical bin close to the pial surface, a partial voluming effect was simulated by taking 50 % of signal change in CSF as part of the superficial bin. Moreover, a worst-case scenario regarding the EV effect of pial veins on the parenchyma was assumed, i.e. vessels of 200 μm diameter perpendicular to B_0 inducing a $\Delta T_2^{(*)}$ additional to the intravoxel change of dephasing in the top bin.

We simulated GM signal saturation and signal change of blood at TE = 0 ms, i.e. signal change induced by changes in CBV and T_2 (through T_2-weighting of the direct saturation effect), to optimize the off-resonance frequency δ, MT pulse duration T, readout segmentation factor and readout FA subject, with the constraint that the scan time should not increase by more than 10 % (i.e. MT-module duty cycle of less than 10 %). In addition, we used the model to try to predict cortical depth and TE dependent signal responses for both BOLD and MT-prep as well as the contributions from different compartments to the profiles.

6.3 Results

6.3.1 Simulations

Results of the model validation are shown in Fig. 6.2. Fig. 6.2A shows an example MT-weighted image depicting the SCC (green ROI) and the CSF (red ROI) for which simulations (tab. 6.2) of the measurement conditions as shown in tab. 6.1 were performed. Fig. 6.2B shows CSF signal relative to SCC signal for an MT-prep sequence (dashed lines) and for a classical GRE sequence (solid lines), i.e. identical parameters except for the MT-preparation.

The blues lines represent the measurement, red and yellow lines show the simulations for a $T_{1,r}$ of 300 ms and 400 ms, respectively. Overall, the results in Fig. 6.2B show that the measurements are well represented by the model for both MT-prep and classical GRE with $T_{1,r}$ = 400 ms. This indicates that the simulations reflect the measurements and can be used for further sequence optimization and measurement interpretation.

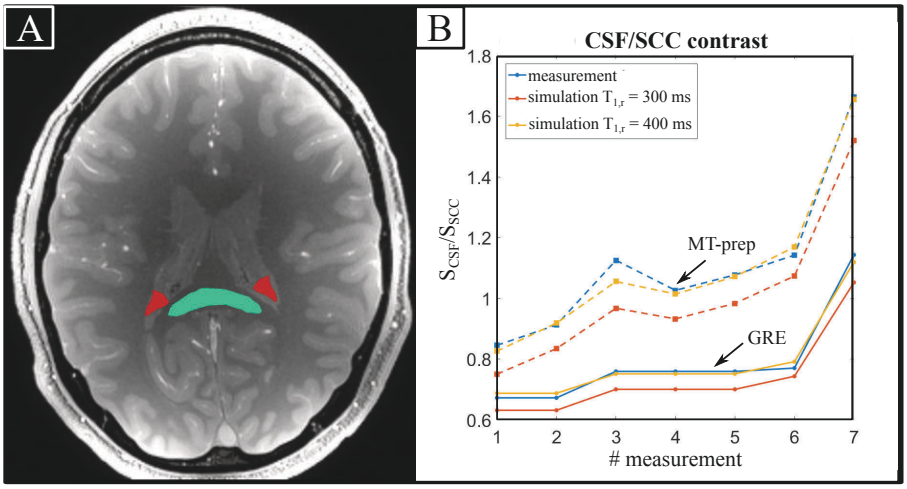

Fig. 6.2 Simulation validation. (A) MT-weighted image showing the SCC (green ROI) and the CSF (red ROI) used to obtain signal ratios. (B) Simulations and measurements of the signal ratio of CSF and SCC for a variety of sequence parameters for the sequence with (dashed lines) and without (solid lines) MT-preparation. The good agreement between measurement and simulation for both sequences with $T_{1,r}$ = 400 ms show that the simulation can be used for further sequence optimization and measurement interpretation.

Numerical optimization of the readout FA (α) and MT-prep off-resonance frequency (δ) is shown in Fig. 6.3 for a 4 ms MT pulse and TE = 0 ms. Signal change of arterial blood (Fig. 6.3A) is maximum at a FA of 6° and δ = -2 kHz. But, with these parameters and at the SAR limit, GM suppression (Fig. 6.3C) is only 12 %. Operating at frequencies closer to the water resonance frequency allows for higher bound pool suppression due to a stronger RF energy absorption as dictated by the Super-Lorentzian

lineshape[35]. However, direct suppression of the free pool increases with lower frequencies as well. The white dots in Fig. 6.3A-C indicate the chosen parameters (α = 6° and δ = -0.65 kHz) which represent a good compromise between bound and free pool signal suppression. In fact, the signal suppression for arterial blood, venous blood and GM at 6° FA as shown in Fig. 6.3D indicates the highest contrast between arterial blood and GM at -0.65 kHz.

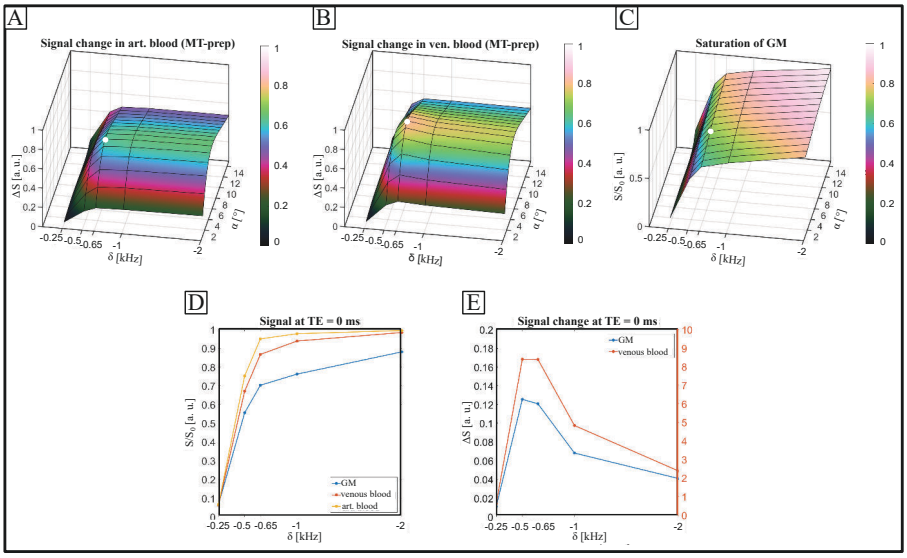

Fig. 6.3 Simulation of signal behavior with varying off-resonance frequency and readout flip angle. Functional signal change of arterial blood (A), venous blood (B) and GM signal saturation (C) as a function of readout FA α and MT-pulse off-resonance frequency δ at an MT pulse duration of 4 ms and 0 ms TE. At α = 6° and δ = -0.65 kHz (white dots) signal change of arterial blood is close to its maximum, signal change in venous blood is maximized and GM signal suppression is at around 30 %. (D) Signal saturation as a function of δ at α = 6° indicate the highest arterial blood to GM tissue contrast a -0.65 kHz. (E) Signal change of GM and venous blood at TE = 0 ms without taking baseline CBV and its change into account (i.e. only changes in T_2) show that both compartments exhibit a T_2-related signal change due to the T_2-weighting character of the MT-pulse played out at frequencies close to the water frequency. In case of GM, these EV changes are more confined to the capillary network. In case of venous blood the change is mostly within the capillaries and to a small extend also in ICVs as given by the differences in baseline blood volume between the two compartments.

Venous blood (Fig. 6.3B) exhibits, relative to arterial blood, a higher signal change due to stronger changes in CBV of small veins (tab. 6.4, Fig. 6.1). At lower off-resonance frequencies, signal change in venous blood increases up to a frequency of -0.65 kHz before decreasing again due to too strong signal saturation. Fig. 6.3E shows the T_2-related signal change in pure GM and venous blood voxels at TE = 0 ms. The changes seen in Fig. 6.3E are attributed to changes in T_2 upon activation due to the T_2-weighting character of the MT pulse played out at frequencies close to the water frequency. Taking together, with the chosen readout FA and off-resonance frequency, arterial blood is almost untouched, GM is suppressed by approximately 30 % and the arterial blood/GM contrast is maximized. GM and venous blood exhibit a non-CBV but T_2-related signal change at TE = 0 ms. In case of GM, this EV signal change is primarily associated with the capillary system[119]. Due to its relatively short T_2 and strong T_2-change upon activity (tab. 6.4, see also Fig. 2.20B), venous blood exhibits a strong IV signal change which will be mostly within the capillaries and to a small extend also in ICVs as given by their baseline blood volume contribution (seen in Fig. 6.1).

Fig. 6.4 shows simulations of arterial blood signal change (Fig. 6.4A) and GM signal suppression (Fig. 6.4B) as a function of δ and MT pulse duration T. The results indicate that the MT effect does not change significantly with different pulse durations as long as the SAR level being operated at does not change and strong on-resonant saturation due to broader bandwidths with shorter pulses is avoided. We chose a 4 ms MT pulse (white dots in Fig. 6.4) resulting in an MT module duty cycle of 9.3 % allowing time efficient data acquisition.

Numerical optimization of the readout segmentation factor, expressed as number of lines per segment, for δ = -0.65 kHz and TE = 0 ms is shown in Fig. 6.5A-C. Because a change in segmentation also changes the steady state, the readout FA must be additionally considered.

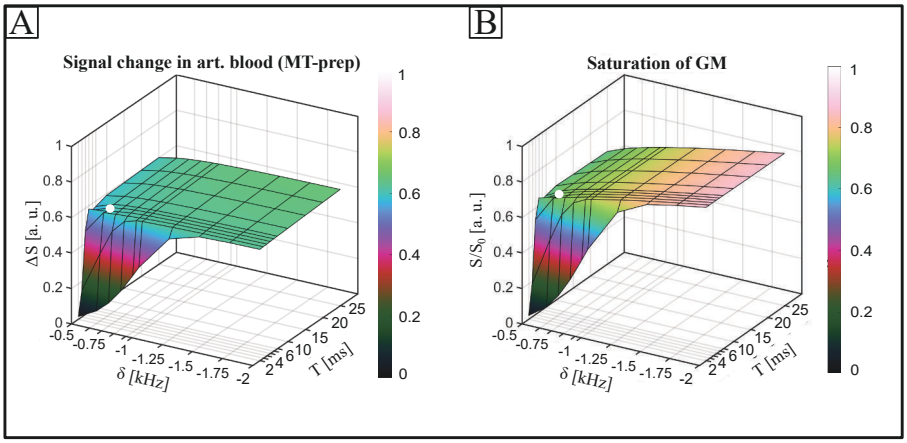

Fig. 6.4 Simulation of signal behavior with varying off-resonance frequency and MT pulse duration. (A) Functional signal change of arterial blood and (B) GM signal suppression simulated as a function of δ and MT pulse duration T at TE = 0 ms, α = 6° and SAR = 100 % in normal mode. The results indicate that the MT effect does not change significantly with different pulse durations as long as pulse power does not change and strong on-resonant saturation due to broader bandwidths with shorter pulses is avoided. With a 4 ms MT pulse (white dots), the duty cycle of the MT module is 9.3 % allowing time efficient data acquisition.

With 14 lines/segment (white dots), corresponding to 7-fold segmentation (TR_{seg} = 179 ms), the signal change in both blood compartments (Fig. 6.5A and B) is sampled at their plateaus. Fig. 6.5C indicates that when keeping readout FA constant, higher GM saturation can be achieved with higher segmentation factors (less lines per segment) even though RF power per pulse is reduced to stay within SAR constraints. In this scenario, the situation of a continuous wave experiment[45] is approached. Reducing the segmentation factor allows for more RF power per pulse which increases both the MT and the direct saturation effect as indicated by reduced GM signal and reduced blood signal change. If one were to decide to neglect time efficiency constraints, many good alternatives to the chosen parameter combinations are possible depending on whether a higher arterial blood signal change or a stronger GM signal suppression is preferred. For instance, keeping signal change in arterial

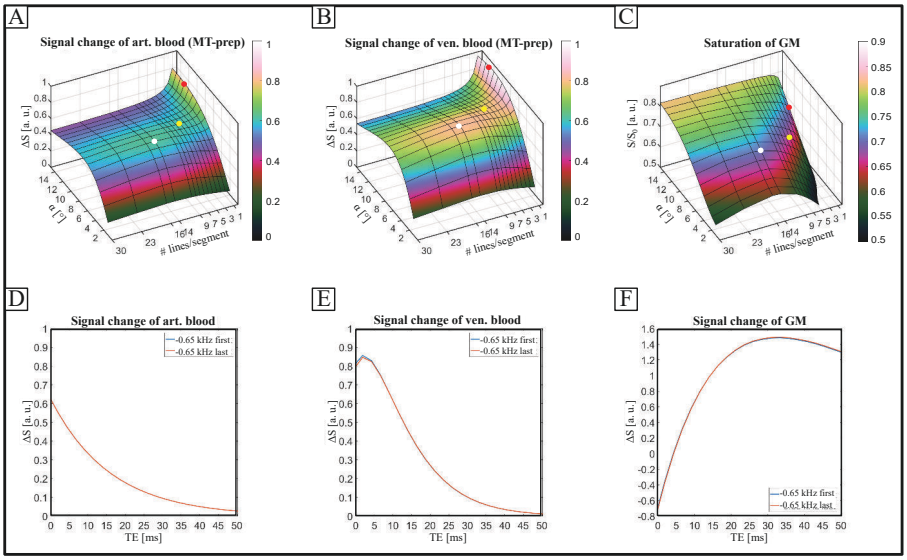

Fig. 6.5 Simulation of signal behavior with varying segmentation factor and readout flip angle. Signal change of arterial blood (A), venous blood (B) and GM signal saturation (C) as a function of α and segmentation factor expressed as number of lines per segment. With 14 lines/segment (white dots) corresponding to 7-fold segmentation as used in this study (TR_{seg} = 179 ms), both blood compartments are sampled at their plateaus and GM signal is suppressed by 30 %. Allowing for less time efficient acquisitions, arterial blood signal change and/or GM signal suppression can be increased e.g. with α = 8° and 5 lines/segment (TR_{seg} = 74.6 ms, yellow dots) GM signal suppression is 33.5 % (22.3 % MT-prep duty cycle) Alternatively, applying the MT-module every TR (TR = TR_{seg} = 28.2 ms) at a α = 12° (red dots) results in a GM suppression of 31.8 % and a 27 % higher signal change in arterial blood (58.9 % MT-prep duty cycle corresponding to a 2.1-fold slower acquisition). Signal change for arterial blood (D) venous blood (E) and GM (F) as a function of TE for the first and the last line in a segment of 14 lines show virtually identical curves for both time points indicating that the MT-contrast is preserved along readout.

blood approximately constant, a GM signal suppression of 33.5 % at α = 8° and 5 lines/segment (TR_{seg} = 74.6 ms, yellow dots) can be achieved but this results in a duty cycle of 22.3 % and thus an overall slower sequence. Alternatively, applying the MT-module every TR at a readout FA of 12° (red dots) results in a GM suppression of 31.8 % and a 27 % higher signal change in

arterial blood at the price of a 2.1-times slower acquisition. With 14 lines per segment, the question arises as to whether the MT contrast is sustained during readout. Fig. 6.5D-F shows the signal change for arterial blood, venous blood and GM as a function of TE for the first and the last line in a segment with an MT pulse played out at δ = -0.65 kHz. For all three compartments, signal change is virtually identical for both time points indicating that the MT contrast is preserved throughout the readout.

6.3.2 MT-prepared multi-echo imaging

Fig. 6.6 shows time-averaged images in the rest condition of one subject for BOLD (A-C) and MT-prep (D-F) and for the first and last gradient echo. All images were scaled identically.

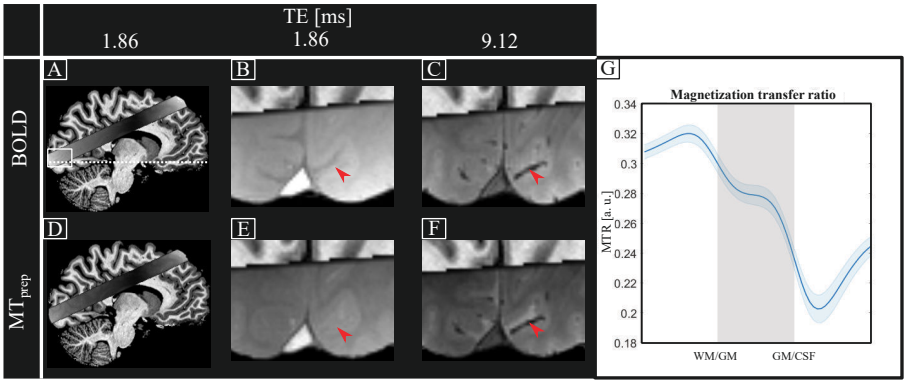

Fig. 6.6 MT-prepared multi-echo imaging. Time-averaged images in the rest condition of one subject for BOLD (A-C) and MT-prep (D-F) and for the first and last gradient echo. All images were scaled identically. In V1, a transverse slice (white, dashed lines inside white box in A) depicts attenuated WM and GM signals with MT-prep (E) relative to BOLD (B) with less affected blood signal as shown by the red arrows indicating a pial vein. The relatively bright blood signal in the sagittal sinus indicates an inflow effect. (G) MTR profile average over subjects (mean $\pm$ SE) show a reduction of signal saturation from WM to CSF with a plateau in mid-GM where the average saturation is 28 %. The reduction along the cortical thickness can be explained by different degrees of partial voluming and/or varying myelination.

A transverse view of the cross-section highlighted by the white dashed line in Fig. 6.6A is depicted for the first gradient echo (Fig. 6.6B,E) and the last echo (Fig. 6.6C,F). With MT-prep, WM and GM signals are attenuated, with a stronger signal attenuation of WM due to a stronger myelination. Notably, blood signal is less affected by MT as shown by red arrows in Fig. 6.6 marking a pial vein. In addition, the relatively bright blood signal in the sagittal sinus at the shortest TE indicates an inflow effect.

Fig. 6.6G shows the MTR profile averaged over subjects (shaded error region shows standard error of the mean). A systematic reduction of signal saturation from WM to CSF with a plateau in mid GM can be observed in line with a previous high-resolution study at 7 T[330]. The reduction can be explained by different degrees of partial voluming and by myelination varying along the cortical thickness as white matter tracts terminate at different depths leading to a myelination gradient. In center GM, the average saturation is 28 % slightly lower than the simulations predicted.

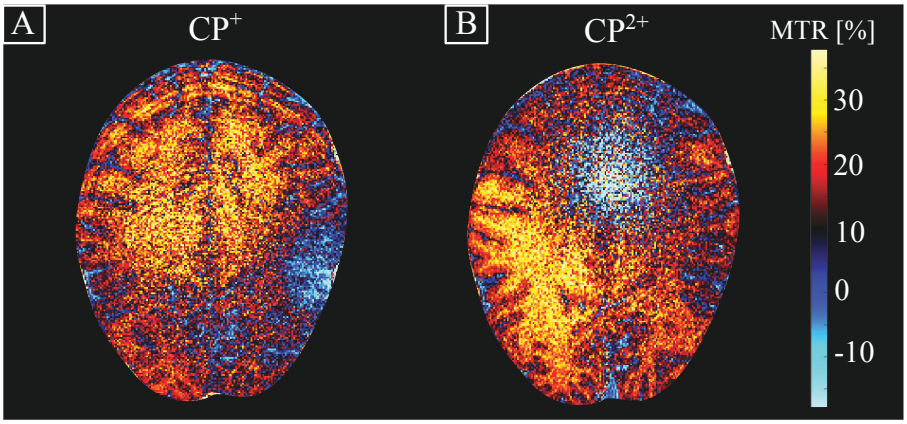

Fig. 6.7 Transmit mode comparison. A transverse slice of MTR maps calculated from fully-sampled images acquired in CP^{+} (A) and CP^{2+} transmit mode (B). The CP^{2+} mode clearly improves saturation intensity and homogeneity in the occipital lobe at virtually no cost in scan efficiency.

In Fig. 6.7, MTR maps calculated from fully-sampled images acquired in CP^{+} (A) and CP^{2+} mode (B) are shown. The CP^{2+} mode clearly improves saturation intensity and homogeneity in the occipital lobe at virtually no loss in scan efficiency because no additional RF-shim needs to be calculated.

6.3.3 Functional activation maps

Fig. 6.8 shows activation maps of two subjects for both BOLD and MT-prep and for all acquired echoes. Fig. 6.8A1,B1,A2,B2 shows the anatomical reference of V1 while C1,C2 shows a T_2^* map calculated from the multi-echo data highlighting large venous vessels (white arrows in C1,C2). The activation maps indicate that for the shortest TE, signal change within GM increases with MT-prep relative to BOLD (green arrows in D1,H1,D2,H2 highlight an example region). With longer TE, signal change due to changes in T_2^* becomes more prominent for both contrasts but MT-prep shows less sensitivity to these unspecific changes as highlighted by less blurred activity in the proximity of large venous vessels (white arrows in G1,K1,G2,K2).

6.3.4 Laminar profiles

We performed numerical simulations to model various vascular and non-vascular contributions to the shape of laminar profiles as shown in Fig. 6.9. Fig. 6.9A-C display the TE dependency of GM (solid lines), venous blood (dotted lines), arterial blood (dashed lines) and CSF (dotted-dashed lines) for BOLD (pink lines) and MT-prep (brown lines) at the deep, middle and top layer, respectively. The gray shaded area highlights the TEs corresponding to our measurements. For all three layers, arterial blood shows an initial positive signal change at TE = 0 ms due to an increased arterial CBV upon activation, being the strongest in the middle layer, before decaying with longer TE. With MT-prep, arterial IV signal change is virtually

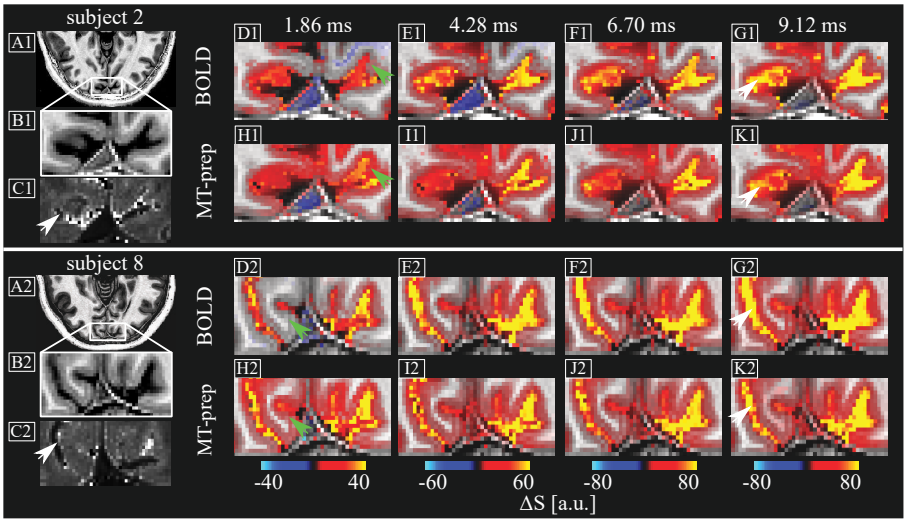

Fig. 6.8 Activation maps from smoothed data. (A1-C1,A2-C2) Anatomical references showing the T_1-weighted image of the second (A1) and eighth subject (A2), a zoomed portion of V1 (B1,B2) and a T_2^*-map from the same area (C1,C2). (D1-K2) Activation maps calculated from anisotropically smoothed data for all measured echoes. The maps acquired with MT-prep at the shortest TE exhibit a stronger signal change within GM relative to BOLD (green arrows). At longer TE, BOLD T_2^* effects become more prominent but MT-prep shows less sensitivity to these unspecific changes as shown by less blurred activity in the proximity of large venous vessels (white arrows in C1,G1,K1 and C2,G2,K2).

identical to BOLD as our MT pulse does not saturate arterial blood. Relative to arterial blood, the venous blood compartment exhibits a stronger signal change at TE = 0 ms due to higher baseline CBV and CBV change of capillaries and venules (see Fig. 6.1 and tab. 6.4). For TEs between 0 ms and approximately 5 ms, the venous IV signal change increases slightly due to changes in the very short T_2^* of venous blood before decaying again. Comparing MT-prep with BOLD, venous IV signal change is slightly increased at TEs near 0 ms for MT-prep, especially at middle and superficial layers, reflecting the weak T_2-weighting character of the MT pulse. Because of the CBV change upon activation (eq. 6.2), GM signal change starts

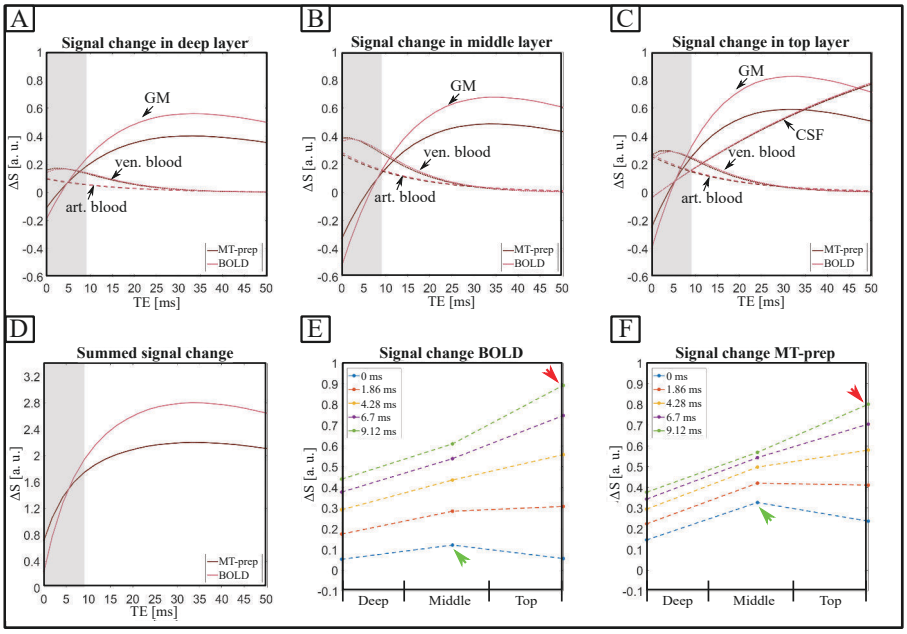

Fig. 6.9 Simulated TE dependency and laminar profiles. (A-C) Signal change as a function of TE for GM (solid lines), venous blood (dotted lines), arterial blood (dashed lines) and CSF (dotted-dashed lines) for BOLD (pink lines) and MT-prep (brown lines) at the deep (A), middle (B) and top layer (C), respectively. The gray shaded area highlights the TEs corresponding to the measurements. See main text for detailed explanations. Taking the sum of all compartments and layers (D) MT-prep has a higher signal change at short TE up to approximately 5.5 ms. At longer TEs, MT-prep exhibits a reduced sensitivity toward unspecific EV signal changes. Relative to the simulated BOLD profiles (E) profiles with MT-prep (F) show reduced contributions from EV signal changes especially at the pial surface (red arrows) and increased signal change in especially mid-GM (green arrows) at the zeroth and first TE.

negative and increases rapidly up to TE = T_2^* of GM. By reducing GM signal through MT, the magnitude of this negative signal change is reduced because less GM signal is available within any given voxel. At longer TE, MT-prep reduces the contribution of unwanted EV signal change in GM. Taking the sum of all compartments and layers, the sensitivity curves in Fig. 6.9D indicate that with MT-prep, a stronger signal change at short TE

is visible which, as explained in Fig. 6.9A-C, is driven by CBV changes of mostly venous microvasculature and small changes of IV T_2. Note that macrovascular changes of CBV[121] were taken into account (section 6.2.6, Fig. 6.1). At TEs of approximately 5.5 ms and longer, BOLD exhibits a stronger signal change, but this increased sensitivity stems from unspecific EV effects (see Fig. 6.9A-C), which are suppressed with MT-prep as seen in later echoes in Fig. 6.9D where the MT-prep signal change is a lot lower than in the BOLD-only case. By combining all compartments, we created artificial laminar profiles (Fig. 6.9E and F). The simulated MT-prep profiles exhibit a lower TE dependency reflecting less EV effects (as seen for instance at the pial surface highlighted with red arrows) and a stronger signal change at the zeroth and first echo, especially in mid-GM (green arrows), reflecting increased sensitivity toward changes of CBV.

Fig. 6.10A and B show the subject averaged profiles at rest. With MT-prep (Fig. 6.10B), baseline signal is reduced relative to the non-MT-prep reference but more in WM and GM as opposed to the pial compartment where blood and CSF is averaged with GM. The shaded areas correspond to the standard error of the mean over all subjects.

The profiles of functional signal change as shown in Fig. 6.10C,D exhibit an increase with longer TE, most prominently seen at the pial compartment (red arrows) where the signal change increases approximately linearly up to a TE of 6.7 ms before decreasing again. Within the parenchyma, signal changes increases with TE, and increases toward the pial surface indicating increased influence of T_2^*-effects around large venous vessels. Comparing MT-prep with BOLD, the profiles share similar features as the simulation (Fig. 6.9E,F) predict. The profiles obtained with MT-weighting (Fig. 6.10D) exhibit less TE dependent signal increase (lines closer together), best visible near the pial surface where the (partial volumed) gray matter is near the pial vessels (red arrows).

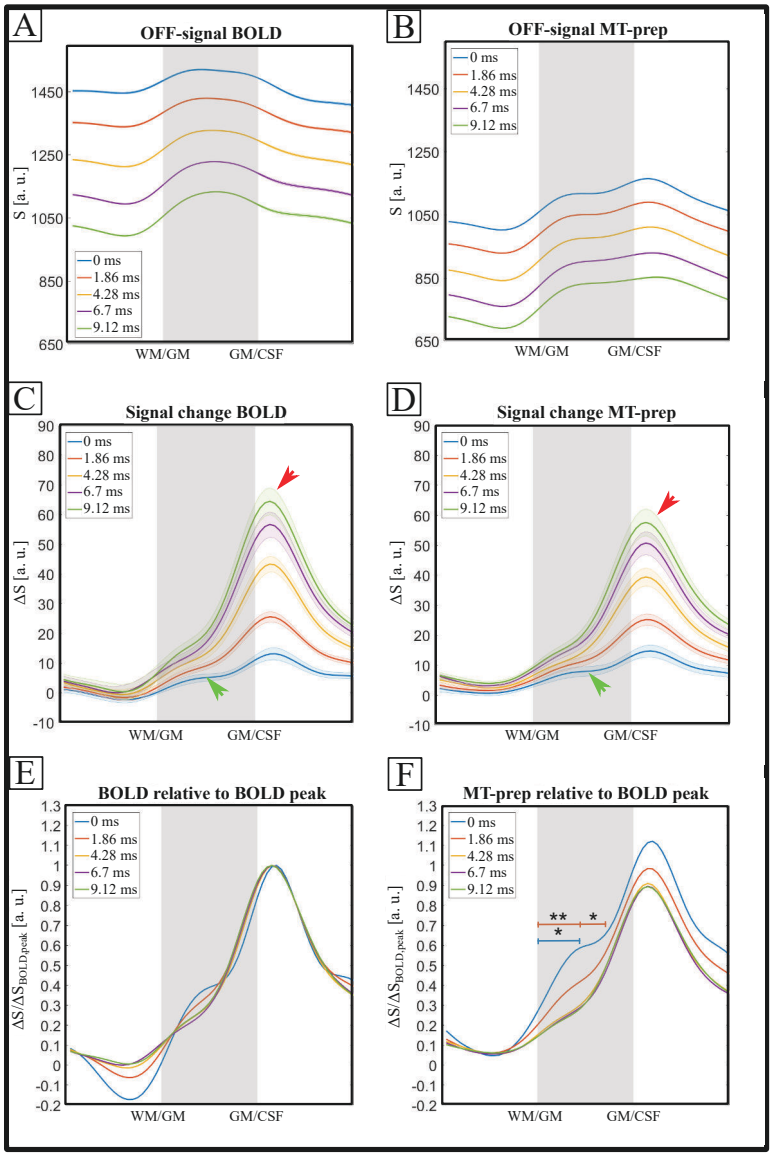

Fig. 6.10 Measured laminar profiles. (A-B) Average profiles (mean ± SE) at rest. With MT-prep (B), baseline signal is reduced relative to the non-MT-prep reference (A) but more in WM and GM as opposed to the pial compartment where blood and CSF is averaged with GM.

(C-D) The profiles of functional signal change increase with additional T_2^*-weighting, most prominently seen at the pial compartment (red arrows) but to a lesser extent with MT-prep. Within GM, the extrapolated profile at TE = 0 ms (blue curves) and the first measured echo (red curves) show a slightly stronger signal change (green arrows) with MT-prep (D) compared to BOLD (C). (E-F) By normalizing each echo relative to the peak of the BOLD profiles, BOLD (E) shows no significant difference between echoes. With MT-prep (F), the extrapolated and first measured profile show a significantly stronger signal change more confined to GM (Wilcoxon signed rank test: *p<0.05, **p<0.01. The blue and red bar indicate the part of the zeroth and first echo which is significantly different from the profile averaged over echo two to four). The GM-to-pial signal ratios for the zeroth and first echo are: 0.39 and 0.35 for BOLD relative to 0.53 and 0.44 for MT-prep. Panel F also shows that T_2^*-contrast starts to dominate the profiles at TE $>$ 4 ms.

The extrapolated profile at TE = 0 ms (blue curves in Fig. 6.10C,D) and the first measured echo show a slightly stronger signal change within GM (green arrows) with MT-prep compared to BOLD. This can be seen more clearly when normalizing each echo relative to the peak of the BOLD profiles (Fig. 6.10E,F). While with BOLD (Fig. 6.10E) all echoes exhibit almost identical profile shapes the extrapolated and the first echo of the MT-prep data (Fig. 6.10F) show a significantly stronger signal change compared to later echoes, particularly in the deep-middle layers (Wilcoxon signed rank test: *p<0.05, **p<0.01). This can be attributed to increased sensitivity to changes in CBV with MT-prep (see Fig. 6.9). Comparing signal changes of mid-GM relative to the pial surface signal as a crude measure of specificity, BOLD exhibits a GM-to-pial signal ratio of 0.39 and 0.35 for the zeroth and first echo, respectively. With MT-prep, the ratios are 0.53 and 0.44. At TE longer than 4 ms, no differences in the profile shape for MT-prep is observable (Fig. 6.10F) indicating that at those echo times, BOLD T_2^*-effects dominate the profiles.

The profiles in Fig. 6.10 all show a strong peak at the pial surface as is common in T_2^*-weighted laminar fMRI profiles. However, in particular for the non-MT BOLD experiment, this peak is unexpected at very short TE and at TE = 0 ms, as there has not been time yet for any T_2^* contrast to develop.

We hypothesized that this peak therefore could stem from inflow of unsaturated blood into the relatively narrow imaging slab. To support this theory, we performed an additional laminar fMRI BOLD experiment with outer volume saturation slabs (see section 6.2.1.5). We chose this BOLD variant as opposed to the MT-prep version as the former should be most devoid of any transverse relaxation related signal change at TE = 0 ms. Fig. 6.11A-C shows exemplar transverse slices in the case of no saturation for the first (A) and last echo (B) and in the case of saturation for the first echo (C). The sagittal sinus as an exemplary venous vessel (blue arrows) and a large artery (red arrows) are highlighted.

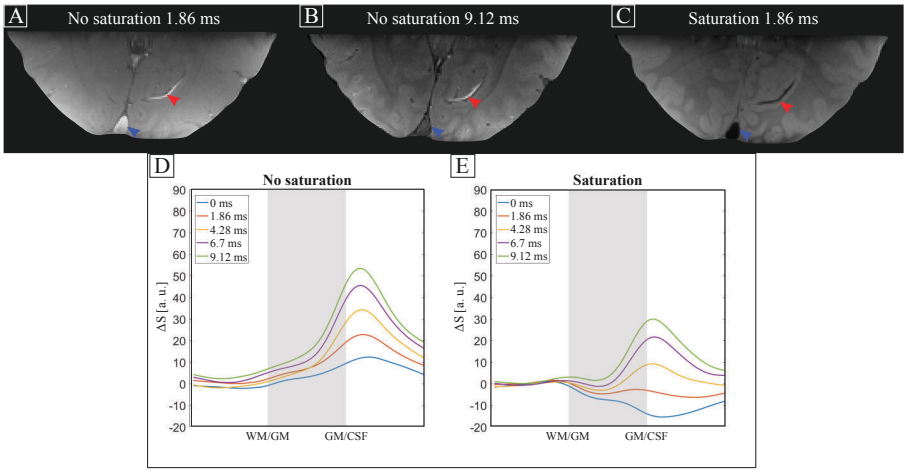

Fig. 6.11 Outer volume saturation experiment to assess influences of inflow effects. (A-C) Exemplar transverse slices without saturation for the first (A) and last echo (B) and with saturation for the first echo (C). The sagittal sinus as an exemplary venous vessel (blue arrows) and a large artery (red arrows) are highlighted. With saturation, venous and arterial blood are effectively nulled. Without saturation (D), the laminar profiles exhibit a similar shape and TE dependency as the profiles shown in Fig. 6.10C. With saturation (E), signal change is zero at the WM boundary and decreases toward the pial surface at 0 ms TE, caused by the increased inflow of saturated blood upon activation. With longer TE, additional positive EV BOLD effects contribute to the shape of the profiles. These results demonstrate that inflow of fresh blood unaffected by the imaging RF pulse causes the pial surface bias and peak at 0 ms TE.

With saturation, venous and arterial blood is nulled before entering the imaging slab (as well as leading to some MT contrast in WM and GM due to the saturation RF pulses). If no saturation is applied, the laminar profiles as shown in Fig. 6.11D exhibit a similar shape and TE dependency as the profiles shown in Fig. 6.10C. With saturation (Fig. 6.11E), we observe a VASO-like behavior: the nulled blood leads to a strong negative signal change at TE = 0 ms, and the magnitude of the signal change mimics the vascular density with the largest signal changes near the pial surface. At later TE, the negative change is counteracted by positive BOLD changes. These results support the notion that inflow of fresh blood unaffected by the imaging RF pulse causes the pial surface bias and peak at 0 ms TE in our BOLD and MT profiles. Whether this has any practical consequences is treated in the discussion section.

6.4 Discussion

In this study, we combined a multi-echo 3D FLASH sequence with off-resonance MT-preparation to sensitize the MR signal toward changes of CBV by reducing GM signal while preserving most of the blood signals. We assessed the CBV-weighting capacity of the sequence and systematically analyzed signal contributions from different vascular and non-vascular compartments in MT-prepared and classical BOLD via simulations and multi-echo laminar fMRI experiments. Our main findings can be summarized as follows:

(1) With the reduction of GM signal via MT, laminar fMRI experiments using the BOLD contrast are less sensitive to EV signal changes driven by unspecific venous vasculature.
(2) Simultaneously, at very short echo times, MT-prep is more sensitive to activity than BOLD.

The first finding is in line with an early MT-fMRI study at 1.5 T which showed that with the application of MT, functional signal change in GM is reduced[318]. Our results suggest that with the application of MT, this reduction of EV signal change improves the specificity of acquisitions based on the currently widely used GRE-BOLD contrast. The reduction is best seen at the pial surface (red arrows in Fig. 6.9E,F and Fig. 6.10C-D, white arrows in Fig. 6.8G1,K1,G2,K2) because the EV signal change scales with venous vessel diameter and vascular density both being the highest at the pial surface[21,119] contributing to the well-known superficial bias in laminar fMRI.

Our finding that MT-based fMRI is more sensitive than GRE-BOLD at short TE is in agreement with reports at 3 T in a recent study using on-resonant MT pulses[317]. The additional sensitivity gain can be explained by a redistribution of compartmental contributions to the total fMRI signal with MT-prep relative to BOLD: Upon activation, changes in CBV and $T_2^{(*)}$ can give rise to a measured signal change. Short-TE BOLD is not very sensitive to T_2^*-changes as the contrast has not developed yet, and as GM and blood signals are almost identical at short TE, not to CBV changes either. This can be seen in Fig. 6.6B, and in the blue curve in Fig. 6.9E (TE = 0 ms) which shows only a small positive signal change. With the application of MT, the sequence becomes sensitized toward CBV effects while still being insensitive toward unspecific EV effects, i.e. when CBV increases there is less negative signal change in GM (eq. 6.2) leading to a net positive signal change at short TE when summing over all compartments (Fig. 6.9, Fig. 6.10C-F). With additional T_2^*-weighting at longer TE, signal changes based on classical BOLD are superimposed onto the CBV-induced signal change and eventually dominate the shape of laminar profiles (Fig. 6.10F). In our measurements, this situation arises around a TE of approximately 4 ms.

Comparing the simulation results in Fig. 6.9 with the measurements in Fig. 6.10, the simulations agree well with our measurements, but do not capture two features of the measurement which we discuss in turn below:

(a) MT-prep shows a higher signal change in mid-GM than BOLD, but to a lesser extent than the simulations predict.

(b) The measurements exhibit a peak at the pial surface at TE = 0 ms for both MT-prep and BOLD which seems counterintuitive given no $T_2^{'}$-effects at 0 ms TE as shown by the simulations.

(a) It is well known in literature, that signal change based on CBV is more confined to GM[121,143,298,315]. Our measured activation maps (green arrows in Fig. 6.8D1,H1,D2,H2) as well as the laminar profiles (Fig. 6.10D,F) could confirm this. Our simulations indicate that most of the CBV change stems from the capillary network (Fig. 6.9A-C, Fig. 6.1) due to its high baseline blood volume and high contribution to the overall CBV change. It has been estimated that the contribution of small arterioles and capillaries to the total blood volume change would be up to 90 %[117]. However, with the application of MT, it can be expected that the contribution of the venous part of the capillaries is reduced given that saturated water within tissue exchanges with unsaturated water within the capillaries. As the consequence of an increase in blood volume and water exchange upon activation, IV signals of the venous part of the capillaries are diminished. In addition, although classical literature has reported low concentrations of macromolecules in blood[36,37], there is some evidence that blood exhibits strong Nuclear Overhauser Enhancement (NOE) which has been reported to arise from red blood cells independent of blood oxygenation[331]. NOE describes the magnetization saturation of highly mobile macromolecules within e.g. lipids[332]. The magnetization can be relayed via the backbone of the molecule before getting exchanged with water. This relayed NOE occurs upfield (negative frequencies) at a center frequency of -3.5 ppm[33] spanning approximately 1 to 2 ppm. The off-resonance frequency chosen in this study (-2.19 ppm $\pm$ 1.18 ppm) lies within the NOE frequency band of red blood cells therefore diminishing IV signal. For the sake of simplicity, the described two sources of IV signal reduction (increased

perfusion and NOE) were not included in the model. Therefore, our model slightly overestimates the contribution of especially venous capillaries to the overall fMRI signal. It must be noted however, that these two phenomena effectively weight the fMRI signal toward CBV changes of arterial blood which have been shown to be well localized to GM[121].
(b) The results from an outer-volume suppression (OVS) control measurement (Fig. 6.11) support the hypothesis that our results in Fig. 6.10 likely contain an inflow component leading to the unexpected positive signal change at TE = 0 ms in the GRE-BOLD experiment. In the OVS experiment, all blood outside the imaging slab was kept saturated throughout effectively resulting in a VASO-like measurement, in which the intra-vascular contribution is significantly reduced. It yielded profiles that differed considerably in comparison to our original GRE-BOLD data. At the shortest TE there was a negative signal change, which was subsequently canceled out by the positive T_2^*-based signal changes as TE increased.

The inflow contributions in Fig. 6.10 largely do not affect our comparison study. Our goal was to compare laminar profiles of GRE-BOLD with ones obtained with the same sequence preceded by MT-preparation modules, where we were interested in predicted specificity improvements. As our MT pulses only affect the arterial blood pool to a very minor degree (see Fig. 6.3), the comparison is largely unaffected by inflow (it causes a small underestimation of the improvements brought by MT). The laminar profiles admittedly do contain a common component we were not particularly interested in (driven by a CBF change) but this did not preclude us from interpreting MT-prep induced changes to the magnitude of the TE-dependent extravascular signal change, nor from interpreting CBV-related signal changes at TE = 0 ms.

In a practical neuroimaging fMRI setting using a slab-based sequence, it is important to consider the possible impact of inflow-related sensitivity biases at various cortical depths, as different functional paradigm-driven conditions

may correspond to different values of CBF. This bias may occur irrespective whether the measurement concerns a standard BOLD sequence or an MT-prep variant. In terms of laminar specificity, the inflow effect is relatively mild. The primary concern in GRE-BOLD with respect to specificity degradation are extravascular effects around large veins, and in particular around pial veins of which the magnetic fields (and their changes) affect the GM below the surface throughout the entire cortical depth[127,135]. The inflow effect does not have such an extravascular nature with the possible exception of perfusion effects but as these would be colocated with capillaries, specificity would be preserved. In fact, this mechanism has recently been capitalized on for measuring blood volume and perfusion changes in laminar fMRI[316]. Inflow does come with one mechanism for laminar resolution loss however: flow changes in vessels perpendicular to the cortical surface (i.e. diving arteries and ascending veins). These can result in a signal change profile contribution that is similar to the classical GRE-BOLD monotonic slope toward the surface. However, it is expected to be very small[119], due to the lack of extravascular contributions around these perpendicular vessels at short TE. In this scenario, the venous compartment would not significantly contribute due to its very short T_2^*. Nevertheless, a whole-brain solution would be preferable, for example by using a spiral-out EPI trajectory[333].

The amount of specificity improvement with MT-prep depends on the amount of GM signal reduction. Ideally, GM signal should be selectively nulled. This is not possible due to theoretical limitations brought about by T_1 relaxation and exchange rates, but in practice SAR and RF power limits are far more restrictive. This poses practical challenges especially at ultra-high fields where transmit B_1 inhomogeneity is more severe and SAR limits are reached faster. Both SAR and the desired bound pool saturation scale with RF pulse power (see section 2.1.5). To increase RF efficiency in V1, we used the CP^{2+} transmit mode as opposed to the classical birdcage mode as

a pragmatic optimization approach which allowed for a more homogeneous and power efficient bound pool suppression without any extra calibration. Recent work of numerical RF-shim optimization for MT[334] is a promising way to increase transmit efficiency and may be further improved to be more time efficient. Our simulation results in Fig. 6.5-6.6 show that MT-preparation can be implemented with minimal scan-time costs allowing efficient data acquisition. Furthermore, while a 10 % MT module duty cycle was set as the limit, other combinations of readout FA and segmentation factor (e.g. yellow dots in Fig. 6.5A-C) could be used if time efficiency is less of an issue.

While with frequencies closer to water resonance frequency MT-related saturation increases, direct saturation of free water increases as well. With the use of an off-resonance MT-pulse, the amount of superimposed direct saturation effects can be controlled (Fig. 6.3). Moreover, the off-resonant pulses can be played out at negative frequencies which result in more saturation than using positive offsets (as shown by e.g. Olsson et al.[335]) due to an asymmetry in the absorption line[336,337]. With the chosen frequency of -0.65 kHz some direct effects are present (Fig. 6.4E) next to the aforementioned NOE effects. The amount of attenuation varies with the width of the direct suppression lineshape which is dependent on T_2[33]. In the case of GM, T_2-weighting is more confined to EV field effects of capillaries which are exploited in sequences based on the SE-BOLD contrast[290,338–340]. In the case of blood, the situation is more complicated. Direct saturation will, on the one hand, mostly affect venous blood with its relatively short T_2 resulting in a weighting bias toward the arterial part of the CBV. On the other hand, transverse relaxation times of venous blood increase upon activity (absorption line becomes narrower). Hence, upon activation, the direct saturation of venous blood decreases leading to an additional signal increase mechanism next to the CBV increase itself. Therefore, care should be taken to not interpret the signal change as being caused by CBV alone. However, our simulations show that the bulk of the signal change

is caused by a change in blood volume (Fig. 6.3,Fig. 6.8A-C at TE = 0 ms) suggesting that a weak direct suppression of the blood pool may be advantageous to reduce venous sensitivity. The T_2-weighting character can also explain the higher peak at TE = 0 ms for MT-prep relative to BOLD as shown in Fig. 6.10F. The peak itself can be seen to stem from the aforementioned inflow effect. With MT-prep, the blood experiences a T_2-weighting which give rise to the increase in IV signal change, also seen at the mentioned pial surface. Nevertheless, the majority of signal change increase at TE = 0 ms with MT-prep lies within GM as seen by the GM-to-pial signal ratios.

The contrast provided by the transfer of saturated magnetization from the bound to the free pool is driven by many parameters, one if which is the pool size ratio F being strongly correlated with the degree of myelination[324,330]. This myelination varies across the cortical thickness of V1[341] being the highest at the WM/GM boundary and decreases steeply at the pial boundary. The MTR-profile as shown in Fig. 6.6G is in line with previous reported profiles[330] although partial voluming needs to be considered at the boundaries. The MTR-profile show an average saturation of 28 % for mid-GM slightly lower than the simulations predict. The uncertainties in the model parameters might be a possible explanation.

Given the SAR limits at 7 T, a 28-30 % GM signal reduction is relatively small. Alternative methods could include using on-resonance MT pulses that result in MT contrast and more direct suppression. As argued above, by combining these two saturation mechanisms, on-resonant MT pulses could possibly be tuned such that they produce a combined CBV- and T_2-weighting. Executing off-resonance MT at a more SAR-favorable field strength like 3 T is also attractive as a much larger GM suppression factor could be achieved. Nonetheless, our data provide strong evidence that the off-resonance 7 T method could be used as a straightforward tool to reduce unwanted GM dephasing by large veins in GRE-BOLD and/or allow scanning at much shorter

TEs without incurring a sensitivity penalty. Please note that through the use of shorter TEs there is an additional reduction in EV dephasing sensitivity, separate from the reduced GM signal due to MT suppression itself.

6.5 Concluding remarks

We showed that using off-resonant RF pulses in a multi-echo 3D FLASH sequence, GM signals can be reduced by 30 % at 7 T. Capitalizing on reduced EV signal intensity, laminar fMRI responses exhibit an increased signal change in the parenchyma at very short TE compared to a BOLD-only reference. We performed numerical simulations indicating that with MT-prep, this increased parenchymal signal change stems from increased sensitivity toward changes in CBV. By varying echo times, we could show that MT-preparation results in less sensitivity toward signal changes based on changes in T_2^*. At TEs of 4 ms and longer, BOLD T_2^*-effects contribute significantly to the shape of our MT-prep laminar activation profiles diminishing the specificity benefits.

Because off-resonant MT-prep can be easily implemented to reduce unwanted GM dephasing by large veins in GRE-BOLD and/or allow scanning at much shorter echo times without incurring a sensitivity penalty, we expect the off-resonance MT method in combination with efficient short TE readouts like center-out spirals to be a promising acquisition technique for high-resolution fMRI.

The authors thank David Norris for his helpful comments in preparation of this manuscript. The research leading to these results has received funding from the Deutsche Forschungsgemeinschaft (DFG, German Research Foundation) grant number 310872863. The 7-Tesla MRI system at the Erwin L. Hahn Institute was funded by DFG grant number 432657511.

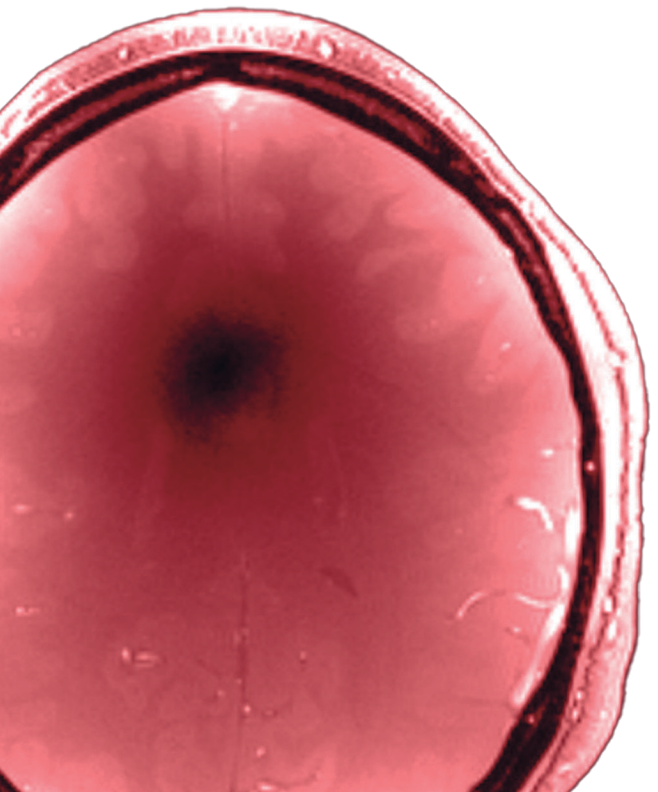

7

Summary and discussion

The field of human laminar fMRI is a relatively young discipline, yet continuously growing since approximately 2015. So far, the vast majority of laminar fMRI focus on isolated areas (Fig. 7.1A), one being the visual system. This is, for one thing, due to the high level of already existing knowledge obtained from animal work allowing to test and verify laminar fMRI contrast mechanisms and hypotheses. Beyond that, most of the visual system resides in the occopital lobe rendering it a relatively easy area of interest as it can be covered with a small imaging FOV.

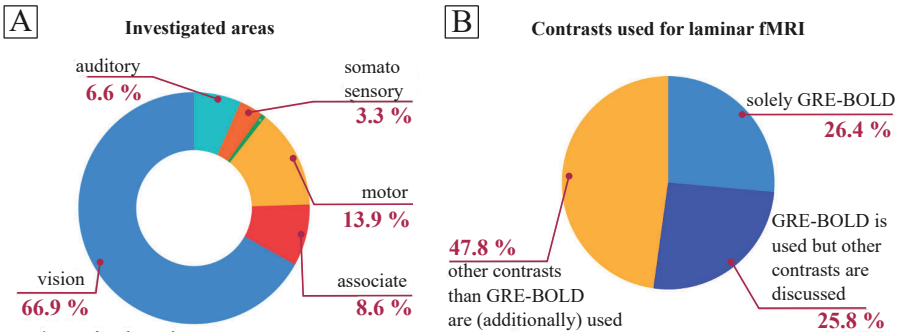

Fig. 7.1 Investigated areas and used contrasts in current laminar fMRI. Statistics from a collection of 187 laminar fMRI papers showing (A) the investigated brain areas and (B) the used contrasts. The vast majority focus on the visual system and most studies use GRE-BOLD (adapted from [342]).

However, many neuronal systems are more widely distributed throughout the brain. Covering these multiple, potentially widely spaced ROIs in one FOV at high spatial *and* temporal resolution is challenging as the sampling process in MRI is sequential rather than parallel. This currently limits laminar fMRI at high spatio-temporal resolution to small FOVs.

One objective of this thesis was to explore an approach to solve the problem of large FOVs and high spatio-temporal resolutions. This requires two prerequisites to be fulfilled: First, SNR and functional contrast-to-noise ratio

(fCNR), i.e. signal change driven by neuronal activity relative to the noise, must be high enough to compensate the loss in SNR due to high spatial resolution and typically high bandwidths. A straightforward way to fulfill this demand, at least partly, is to image at high main magnetic fields of 7 T and higher. Second, the used RF hardware should sufficiently cover all ROIs to capitalize on the higher provided baseline SNR at UHF.

These two prerequisites are not easy to fulfill together. Due to the RF inhomogeneity problem at UHF, RF pulses are applied with local transmit coils as opposed to large body coils typically used at field strengths of 1.5 T and 3 T. The FOV of commercially available RF head coils at 7 T are intrinsically limited and typically cover only the neocortex with optimal transmit and receive sensitivity. Therefore, in **Chapter 3**, we investigated the performance of an 8Tx/15Rx transceiver RF head coil for high coverage MRI with focus on fMRI of the cerebellum. Next to the larger FOV compared to an 1Tx/32Rx coil, the eight transmit channels allowed to shape the RF transmission field to excite all ROIs (cerebellum and motor cortex) with a homogeneous flip angle.

In the context of laminar fMRI of a few ROIs representing a network, sampling the rest of the brain can be considered wasteful as most of the brain signal will not be of interest. The benefits of being able to shape the transmission field to allow for homogeneous excitation of the whole brain at UHF can also be used to tailor the excitation profile to only cover specific ROIs. Initial results of the concept of zoomed multi-FOV imaging were presented in **Chapter 4** indicating that this approach allows to acquire widely spaced ROIs with equal or better signal quality compared to a full FOV reference.

The second objective of this thesis was to investigate and improve the intrinsic resolution of laminar fMRI, i.e. the resolution given by the MR contrast itself. The majority of laminar fMRI studies to date use the GRE-BOLD contrast (Fig. 7.1B) because it exhibits the highest sensitivity and can be com-

bined with time efficient EPI readouts. However, as explained in **Chapter 2**, GRE-BOLD is mainly sensitive to large unspecific venous vasculature. Therefore, the usefulness of GRE-BOLD versus alternative functional contrasts for laminar fMRI is an ongoing source of high debate in the field and alternative contrasts are discussed and used.

One proposed alternative is SE-BOLD which, as explained in section 2.4, is less sensitive to large draining and superficial veins. However, time-efficient implementation of this contrast often requires EPI readouts which are inherently T_2^*-weighted, hence re-introducing unwanted signal changes in and around large vessels. To investigate if pure T_2-weighting is feasible and how a T_2-weighted signal (by extrapolating to $TE_{GRE} = 0$ ms) is affected by different degrees of additional $T_2^{'}$-weighting imposed by different readout lengths, we used a T_2-prepared mutli-echo FLASH sequence in **Chapter 5** and analyzed the signal characteristics of this sequence via numerical simulations and high-resolution fMRI experiments.

Next to SE-BOLD, a variety of non-BOLD fMRI contrasts have been proposed and successfully used to overcome the specificity issue of GRE-BOLD. One contrast is based on changes in CBV and the most popular method exploiting those is VASO at present. Alternatively, fMRI can also be sensitized to changes in CBV by suppressing the GM signal through magnetization transfer effects. The resulting CBV sensitivity comes with the additional benefit of reduced sensitivity to extravascular BOLD, which unavoidably emerges during long EPI readouts. In **Chapter 6**, we characterized this MT-fMRI contrast in the context of laminar fMRI using a similar strategy as in chapter 5: The MT-contrast was achieved by preparing the signal using an MT-weighting module. Subsequent readout at different GRE echo times allowed to extrapolate to a condition without T_2^*-contamination and to assess the influence of different amounts of T_2^*-weighting on the shape of laminar fMRI profiles.

7.1 Chapter 3: Large FOV multi-transmit RF hardware for whole brain MRI at 7 T

In chapter 3, we were interested in imaging the cerebrum as well as the cerebellum and more caudal regions together in one FOV at UHF while the focus was on fMRI of the cerebellum. This small structure greatly benefits from the increased baseline SNR and improved susceptibility contrast at 7 T. However, the cerebellum is typically not very well covered with the commercially available 1Tx/32Rx RF coil from Nova Medical Inc., probably the most used coil for structural and functional MRI of the brain at 7 T[343]. Therefore, we seeked for an alternative, addressing the problems of small FOV and transmission field inhomogeneity at the same time in a pragmatic manner. The presented 8Tx/15Rx RF coil combination setup, consisting of an 8Tx/Rx transceiver and and 7-channel receive only array, is a cost-efficient hardware to switch the focus from imaging the neocortex to more caudal regions while simultaneously keeping the neocortex within the same FOV.

While the receive only array boosts SNR in the cerebellum, it is the ability of the 8Tx/Rx transceiver to shape the transmit field which greatly improved fMRI of the cerebellum. As both transmit and receive sensitivity contribute to the overall signal (eq. 2.47), both quantities need to be considered and optimized transmit sensitivity can compensate for missing sensitivity on the receiving end. This was demonstrated in the motor cortex where it was not expected that the 8Tx/15Rx coil would provide much signal given the low receive channel count. In fact, with standard CP^+ mode, sensitivity was poor (c.f. Fig. 3.10B,E,H), also because the birdcage mode of the 8Tx/Rx coil was sub-optimal (c.f. Fig. 3.7F and Fig. 4.6G-I). The optimization for a homogeneous excitation of the motor cortex with the Ernst angle was able to regain some sensitivity.

The approach of region-specific B_1^+ shimming can be further refined or even replaced by more sophisticated homogenization approaches like the design of spokes pulses[164–166]. However, session-specific pulse design can be considered less "plug-and-play" than the quick calculation of RF shims. In this regard, a promising candidate to improve the usability of pTx for B_1^+ homogenization are universal pulses (UP)[232] calculated only once for a given RF coil and used in any subsequent scan without the need for additional calibration scans and further pulse calculation. In fact, non-selective UP for a selection of sequences were recently released under the PASTEUR package[344] for the latest generation of 7 T systems and it can be expected that extensions to slice/slab-selective excitation will follow soon.

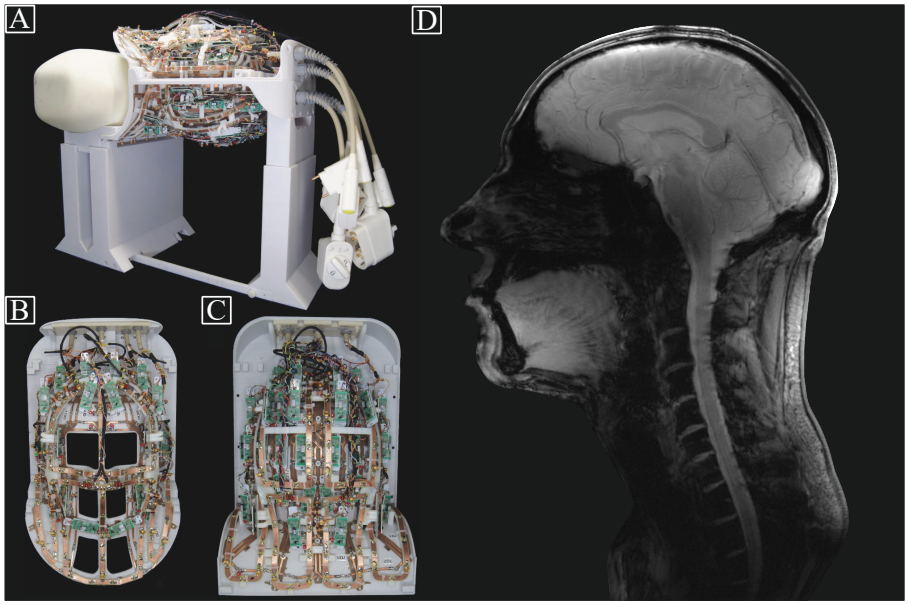

Fig. 7.2 High channel-density Rx/Tx RF hardware. (A-C) Side (A), top (B) and bottom (C) view of a 16Tx/64Rx head-neck RF coil. (D) Exemplary GRE image (0.3 x 0.3 x 2 mm resolution) demonstrating the achievable FOV (Figure courtesy of Markus May).

Clearly, more dedicated RF hardware covering the whole head and neck with a high number of RF receive and transmit channels is necessary. While an 8Tx/32Rx RF coil, commercially available for pTx systems, provide a better coverage in z-direction than its 1Tx/32Rx pendant, it does not utilize what current state-of-the-art 7 T MRI systems can offer in terms of transmit and receive channel numbers. On current 7 T systems, up to 64 receive and 16 transmit channels can be used and recent RF head-neck coil designs capitalizing on this high channel count (Fig. 7.2A-C) show promising perspectives of what FOV coverage can be expected in the future (Fig. 7.2D).

7.2 Chapter 4: Zoomed multi-FOV imaging

While the previous chapter dealt with large FOV RF hardware as a prerequisite for laminar fMRI of long-range connections, a solution to the incompatibility of high coverage and high spatio-temporal resolution needed to be found. The approach presented in chapter 4 is based on the working hypothesis that only selected areas participate in a given network. Hence, the selective excitation of only the areas of interest, a technique referred to as zoomed imaging, can greatly improve the spatio-temporal resolution. While zooming can also be achieved with single transmit systems, capitalizing on the pTx capability of multi-transmit RF hardware at 7 T allows to accelerate the 2D RF pulses, reducing TR and the susceptibility to off-resonance and T_2^* effects.

The hypothetical network chosen in chapter 4 could be related to the question of how attention (modulated with a working memory task which is known to activate GM around the SFS[345]) affects the affective processing of painful events within the insula[346]. These two areas could in principle be covered with one small FOV (effectively a FOV combining the two anterior beams in Fig. 4.7D,F). In this situation, however, acceleration along the left/right PE encoding direction would result in aliasing with unwanted signal

from medial parts. In addition, as soon as another ROI perpendicular to the plane spanned by the other ROIs contributes to the network, the FOV must be enlarged. Therefore, we included V1 as part of the network to illustrate the situation where almost complete brain coverage with conventional excitation would be required to cover all ROIs.

The results in chapter 4 show that when opting for similar temporal efficiency, a zoomed GRE 3D-EPI sequence can cover all ROIs while a non-zoomed EPI could not cover the insula. Moreoever, signal quality of the zoomed images was equal or better compared to the reference. It was shown that this was not due to a reduced g-noise penalty in the zoomed case as the acceleration factors in both compared sequences were chosen to result in approximately the same effective total acceleration factor of four. Instead, the image quality improvement stemmed from an improved transmit field homogeneously exciting the ROIs with the Ernst angle.

Comparing the conventional GRAPPA reconstruction with VCC-GRAPPA, the presented results indicate that a high-resolution 3D-EPI with partial Fourier acceleration does not benefit from a phase constrained reconstruction, in line with previous work[228]. However, the conditioning of the PC reconstruction can in principle be improved by tailoring the phase pattern imprinted by the 2D RF pulse such that, together with the intrinsic object phase, sets of aliased voxels are out of phase. These theoretical results have some implications: First, Hermitian symmetry of k-space must be guaranteed which is often perturbed in long EPI readouts at UHF. Second, partial Fourier should be kept to a minimum because PC reconstructions rely on the omitted k-space part. However, this recommendation also holds in general for laminar fMRI as the application of partial Fourier degrades the nominal resolution (but see also Koopmans and Pfaffenrot[61] for a PF method that prevents resolution loss). Third, the RF coil and object phase must be known which requires an additional prescan with identical phase as the main scan. However, the prescan can have the same (typically low) resolution

as the B_1^+ maps. Finally, the performance of PC reconstruction strongly depends on the intrinsic object phase which can exhibit a high degree of spatially dependent variation in GRE-EPI sequences depending on TE and B_0 inhomogeneity.

These mentioned points may indicate that other sequences than GRE-EPI might benefit more from PC reconstructions. In fact, the sequences presented in chapter 5 and 6 are highly synergetic with the zoomed multi-FOV approach. As they are based on the relative slow FLASH readout, they strongly benefit from the additional acceleration capability provided by zooming. Furthermore, Hermitian symmetry is to a large extend preserved in FLASH and both T_2-prep and MT-prep are intended to be performed at as short as possible TE to reduce confounding T_2^* effects (see the next two sections). At very short TE, object phase variations are small over most of the volume (Fig. 7.3). Therefore, it can be expected that phase optimization for PC reconstruction would result in smooth and easy to apply RF phase patterns resulting in low g-factors (Fig. 7.4).

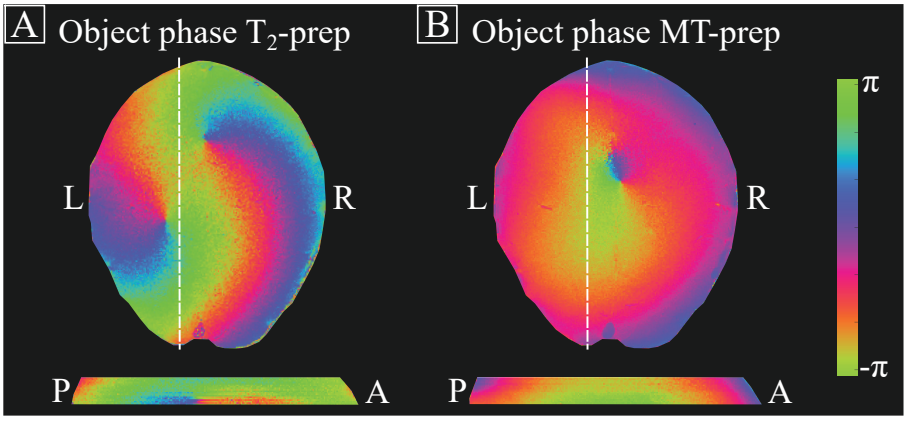

Fig. 7.3 T_2-prep and MT-prep object phases of a single subject. (A) Transverse (top) and sagittal (bottom, white dashed line in top view) slices of the T_2-prep object phase (TE_{prep} = 50 ms and TE_{GRE} = 2.25 ms) taken from fully sampled ACS data (0.75 mm isotropic resolution). The phase variation may be the result of the adiabatic refocussing pulses. (B) MT-prep object phase (TE = 1.86 ms).

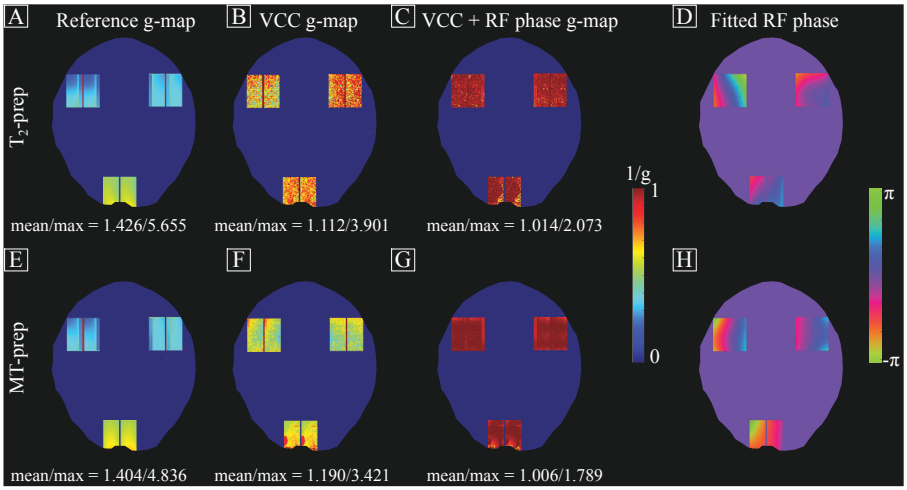

Fig. 7.4 Phase constrained reconstruction of zoomed T_2-prep and MT-prep FLASH. (A-C,E-G) 1/g-maps simulated using the receive sensitivity profiles of the 1Tx/32Rx NOVA coil and a 12-fold acceleration along the LR PE direction in case of zoomed T_2-prep (A-C) and MT-prep (E-G) acquisitions similar to that performed in chapter 4. The acceleration factor was chosen such that aliasing occurs between but also within the small ROIs. Without VCC, T_2-prep and MT-prep show relatively high g-factors in the anterior ROIs (A,E). Without phase optimization, both sequences already greatly benefit from a VCC reconstruction (B,F). Note that in this case, T_2-prep benefits more as its intrinsic object phase varies more than in MT-prep (c.f. Fig. 7.3). Phase optimization leads to smooth RF target phase patterns (D,H) and close to optimal g-factors (C,G).

7.3 Chapter 5: T_2-prepared non-EPI fMRI for enhanced neuronal specificity

In chapter 5 we were interested in improving the *intrinsic* spatial resolution of laminar fMRI by investigating whether a T_2-prepared sequence was capable of acquiring purely T_2-weighted signals and to what extend these signals would be affected by different degrees of superimposed $T_2^{'}$-weighting. To this end, we used a T_2-prepared multi-echo center-out 3D FLASH sequence with monopolar readouts in a laminar fMRI experiment of the primary visual cor-

tex as this is one of the most extensively studied areas in animals and humans. To interpret our measured data, we build upon the work of Markuerkiaga et al.[255] and used a multi-compartment, static model of the vasculature of V1.

Using the multi-echo data, we extrapolated to laminar profiles at TE_{GRE} = 0 ms, the first reported T_2-weighted laminar profiles devoid of $T_2^{'}$ contamination which are well confined to GM. Compared to these, the non-zero TE profiles indicate that already at very short GRE echo times, unwanted extravascular effects corrupt the spatial fidelity of T_2-weighted profiles. Although venous EV dephasing is present and seen throughout all layers of the cortex, the results also show that the bulk of profile corruption stems from CSF partial voluming into superficial layers which can in principle be addressed using engineering (i.e. developing higher resolution protocols) as opposed to being a fundamental biophysical issue that cannot be overcome this way. Hence, chapter 5 shows good prospects for T_2-weighted sequences with higher spatial resolutions.

However, achieving higher resolutions is challenging with SE-BOLD as it is intrinsically less time-efficient compared to GRE-BOLD due to longer GM and venous blood T_2 relaxation times. Our results show that it is in principle possible to obtain T_2-weighted laminar profiles slightly faster by reducing the SE TE to values below GM T_2, but this will come at the price of lower GM sensitivity and overall lower specificity as IV effects will start to contribute to the signal. Hence, for optimal contrast, the results suggest that TE should be close to GM T_2. Because of the intrinsically lower time efficiency, obtaining high spatio-temporal resolution and high coverage is more challenging with SE-BOLD type of sequences. The zoomed approach in chapter 4 could alleviate this problem. To illustrate using the example of the T_2-prep sequence: Targeting similar ROIs as in chapter 4, a 32-fold (8 x 4) total acceleration (effective 8-fold) factor could be achieved with 4.6 ms long 2D RF pulses (4.6 ms can be achieved through 3-fold undersampling of trans-

mit k-space). With parameters of a recently used whole brain protocol for VASO[347] (0.85 x 0.85 x 0.87 mm resolution, alternating TR_{vol} = 5.1/5.2 s), 226 x 226 x 112 matrix size, 192 x 192 x 97.4 mm FOV, left/right readout, echo times of TE_{prep}/TE_{GRE} = 50/1.58 ms and an TR of 8.26 ms, the volume TR can be reduced from 29.68 s to 7.42 s. Although the TR is not yet in the range of neuroscientifically desirable TRs, it should be noted that this estimated gain in acceleration capability through zooming does not take optimized phase patterns into account. Hence, it can be expected that the final volume TR can be further reduced. Alternatively to a PC reconstruction, EPOCS[61] partial Fourier reconstruction along PE_z can be used with a 5/8 or even 9/16 PF factor which would reduce the TR to 4.64 s or 4.17 s. These TR are similar to the reference protocol and the relevant areas are covered with optimal T_2 and minimal $T_2^{'}$ contrast with the upside of no EPI-related issues like distortions, drop-outs and Nyquist ghosts. Of course, multi-FOV zooming is not restricted to T_2-prep and it can be expected that other sequences can benefit from it as well.

In the T_2-prep sequence, we used a center-out encoding scheme to sample the k-space center directly after the T_2-preparation. However, we quickly realized that T_1 relaxation during the long readout reduced the desired T_2 contrast and introduced signals unaffected by the T_2-prep module, i.e. T_2^*-weighted signals. To overcome this problem, we segmented the readout and repeated the T_2-prep module which implied the design of power efficient adiabatic pulses. By capitalizing on the low B_0 variation in the occipital lobe (estimated to be $\pm$ 100 Hz based on pilot B_0 maps), the adiabatic pulses can be quite narrowband allowing for low pulse powers. To extend the sequence to wider coverage, stronger B_0 inhomogeneity at more critical air/tissue interfaces needs to be considered which poses new pulse design constraints. Universal pulses can alleviate this issue as they are broadband by design, as recently shown[348]. Although not improving the time efficiency, the applied

RF power would be reduced as the T_2-prep module would then only include one UP pulse as opposed to two adiabatic 180° pulses needed for phase profile compensation.

7.4 Chapter 6: MT-prepared fMRI for improved specificity of GRE-BOLD

It is evident from Fig. 7.1B that most of the laminar fMRI studies use the GRE-BOLD contrast as its sensitivity and temporal efficiency is unrivaled. While the T_2-prep sequence can be thought of as a very specific microscope which can be used when temporal efficiency is not critical, most of the neuroscience questions demand volume TRs of approximately 2 to 3 seconds. Hence, it is desirable to improve the specificity of GRE-BOLD without a too strong penalty in temporal efficiency.

The recently proposed ABC contrast[317] aims to increase spatial specificity and the range of possible TEs in GRE-BOLD at 3 T by utilizing on-resonant magnetization transfer pulses to decrease GM signal. As explained in section 2.4.4.2, the GM signal reduction effectively weights the signal toward changes of CBV which are mostly driven by the dilation of arterioles and capillaries. Therefore, it was expected that with MT weighting, GRE-BOLD signals at very short TE become more sensitive toward changes in microvascular volume, known to be more confined to GM. At the same time, GM signal attenuation was expected to decrease the sensitivity of GRE-BOLD toward EV venous effects which are more pronounced around large vessels. However, it was unclear how much GM signal reduction could be achieved with MT at 7 T given the higher SAR constraints. In addition, it was imperative to investigate how different amounts of T_2^* dephasing would influence the MT contrast. Therefore, we followed a similar strategy as in the previous chapter and designed and numerically optimized an MT-prepared multi-echo center-out 3D FLASH sequence to investigated the influence of the MT-preparation

on the shape and the TE dependency of laminar profiles obtained from V1. We used off-resonant MT pulses as they can be designed with flexible and well controlled degrees of direct saturation.

The results show that V1 GM signal can be reduced by about 30 % at 7 T and that MT has indeed the expected effects. At short TE, it outperforms GRE-BOLD in terms of sensitivity toward signal changes of specific vasculature. At long TE, it reduces the sensitivity toward EV signal changes which are primarily driven by macrovasculature. However, the size of the effects is relatively small. The main factors which limited higher degrees of *selective* GM saturation are that at UHF both pulse power and SAR are more limiting and that power is more restricted on current pTx systems. One reason is that for practical SAR supervision on pTx systems, simulated SAR matrices, which size can reach orders of 10^6, must be compressed. This comes with the trade-off between the number of matrix entries and an overestimation of the actual SAR. The amount of overestimation and hence the size of the introduced safety factors to account for that depend on the specific compression algorithm and recent work[349,350] shows promising prospects for more efficient SAR management on current pTx systems.

In our work, we used the CP^{2+} excitation mode to benefit from a higher power efficiency in the occipital lobe. To improve the homogeneity of MT-related signal reduction, Leitão et al.[334] recently designed an RF-shimming framework for off-resonant pTx MT pulses, opting for homogeneous root-mean squared B_1^+ over the whole brain by varying the magnitudes and phases between multiple MT sub-pulses of the same form. Initial simulations[1] using this concept of pulse design for saturation homogeneity (PUSH) indicate that the MT effect in GM can be homogenized and increased at the same time over a large FOV (Fig. 7.5). Trading homogeneity by shifting the optimiza-

[1] At this point, the author would like to thank David Leitão for providing the optimization code and for valuable discussions on the PUSH concept.

tion to maximize MT effects may provide further improvements in GM signal reduction and therefore in MT-weighted GRE-BOLD specificity.

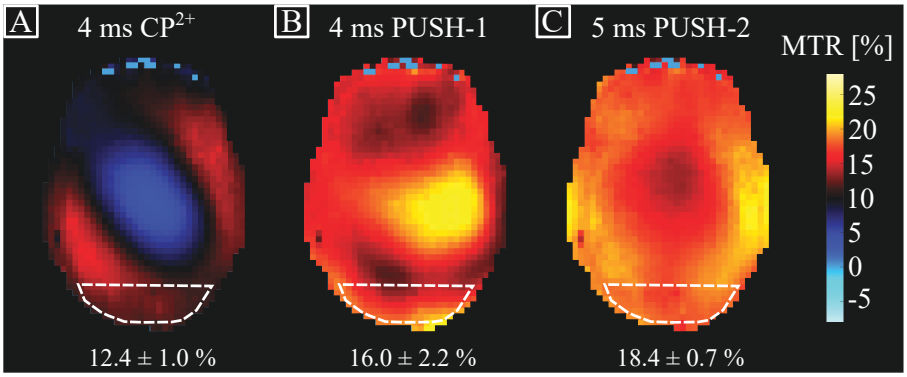

Fig. 7.5 MTR comparison between CP^{2+} mode and PUSH pulses played out at -2 kHz off-resonance frequency. (A) MTR map simulated for GM using a 4 ms MT pulse played out in CP^{2+} mode showing similar GM attenuation as obtained in chapter 6 (c.f. Fig. 6.3C and 6.7B). The mean ± std MTR within the white dashed ROI targeting the occipital lobe is shown below each panel. (B) Opting for a homogeneous MTR over the entire brain, a 4 ms PUSH-1 pulse, i.e. magnitude and phase of one pulse are varied, equivalent to RF-shimming, improves the amount of achievable MTR. (C) With a slightly longer PUSH-2 pulse (two sub-pulses each 2.5 ms long, 11.6 % MT-prep duty cycle compared to 9.3 % with a single 4 ms MT-pulse) increases MT homogeneity but also the amount of achieved MTR. Note that the pulses are not optimized for maximum MT.

The results in chapter 6 show that MT-weighting can relatively easily be implemented as a time-efficient pre-pulse in any desired GRE-BOLD fMRI sequence but it will most likely unveil its true potential in more time-efficient non-Cartesian readouts like center-out spirals. Although not as easy to implement as Cartesian sampling due to increased sensitivities to B_0 inhomogeneities, gradient imperfections and eddy currents, recent studies using field probes[351,352] or measured gradient impulse response functions (GIRF)[333] show promising results. In combination with MT preparation, the necessarily long TE for BOLD could be circumvented and temporal

efficiency as well as SNR and image quality could be further increased. When combining the spiral readout with zooming, all measures to improve the readout trajectory could also benefit the transmit k-space trajectory, potentially allowing for shorter pulse durations.

7.5 Uncovered topics and concluding remarks

The chapters presented in this thesis deal with the acquisition of human laminar fMRI data where the focus was laid on improving the spatio-temporal as well as the intrinsic resolution aiming to reduce the amount of similarity of signal changes between layers, i.e. increasing the specificity. Although not the focus of this thesis, it is important to note that the data analysis plays a similarly important role in laminar fMRI. Strong efforts have been made to improve existing analysis pipelines[353] and to develop new strategies[274] tailored for the special needs of sub-millimeter resolution data where the aim is to preserve the full resolution given by the acquisition, i.e. to reduce the amount of blurring imposed on the data through the post-processing/analysis[135,233,295]. Other approaches try to even improve specificity by means of reducing the impact of similarity between layers, i.e. masking out large vessels[244,245] or using regression techniques[354,355].

To optimize the contrast and to interpret the experimental results, a static model of the vasculature of V1[255] was used in chapter 5 and chapter 6. Having such models at our disposal is imperative because they not only allow the researcher to better understand the relationship between hemodynamics and the final measured (non)-BOLD signal but they also hold the promise to remove the vascular bias in GRE-BOLD by solving an inversion problem[356]. The increasing amount of data allows the field of laminar fMRI to continuously refine and develop realistic models[115,119,357–359], helping to understand wanted and remove unwanted contributions to the laminar fMRI signal.

Other approaches to dealing with the poor intrinsic resolution of GRE-BOLD include the design of the functional paradigm itself. By manipulating top-down modulations in the absence of bottom-up stimuli[245,248,360] or at constant stimuli[242], or by carefully using concurrent bottom-up and top-down modulations[361], feed-forward and feed-back signal responses can be obtained from GRE-BOLD data.

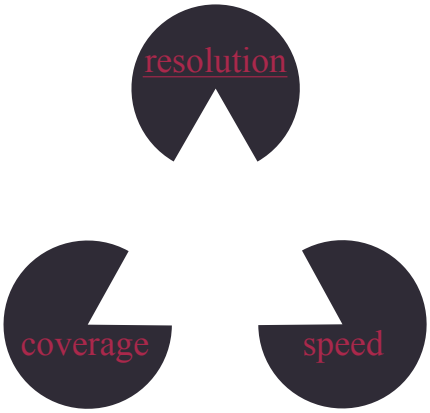

Fig. 7.6 The parameter space in laminar fMRI: A trade-off. In laminar fMRI, resolution, coverage and speed need to be traded for one another and one can typically only achieve two at the same time (adapted from [148]).

In conclusion, this thesis addresses fundamental problems in laminar fMRI: high spatio-temporal resolution and large coverage need to be constantly traded for one another (Fig. 7.6). Pushing one of these parameters comes at the cost of sacrificing the other and currently, only two of these three can be obtained with laminar fMRI. Furthermore, special focus was laid on understanding and improving the intrinsic resolution provided by the used fMRI contrast mechanism in order to obtain signals as confined as possible to the locus of activity. This thesis is considered as one piece in an intriguing puzzle, and together with other methodical improvements, laminar fMRI where long-range connections are simultaneously investigated at high spatio-temporal resolution could come a step closer to reality.

Bibliography

[1] Ogawa, S., Lee, T. M., Kay, A. R., and Tank, D. W. “Brain magnetic resonance imaging with contrast dependent on blood oxygenation”. In: *PNAS* 87 (1990), pp. 9868–9872.

[2] Ogawa, S., Tank, D. W., Menon, R., Ellermann, J. M., Kim, S.-G., Merkle, H., and Uğurbil, K. “Intrinsic signal changes accompanying sensory stimulation: functional brain mapping with magnetic resonance imaging”. In: *PNAS* 89 (1992), pp. 5951–5955.

[3] Bridge, H. “Mapping the visual brain: how and why”. In: *Eye (Lond).* 25 (2011), pp. 291–296.

[4] Pleger, B. and Villringer, A. “The human somatosensory system: From perception to decision making”. In: *Prog. Neurobiol.* 103 (2013), pp. 76–97.

[5] Olsson, A., Knapska, E., and Lindström, B. “The neural and computational systems of social learning”. In: *Nat. Rev. Neurosci.* 21 (2020), pp. 197–212.

[6] Lissek, S., Glaubitz, B., Uengoer, M., and Tegenthoff, M. “Hippocampal activation during extinction learning predicts occurrence of the renewal effect in extinction recall”. In: *NeuroImage* 81 (2013), pp. 131–143.

[7] Chai, W. J., Hamadi, A. I. A., and Abdullah, J. M. “Working Memory From the Psychological and Neurosciences Perspectives: A Review”. In: *Front. Psychol.* 9 (2018), pp. 1–116.

[8] Redcay, E. and Chillbach, L. “Using second-person neuroscience to elucidate the mechanisms of social interaction”. In: *Nat. Rev. Neurosci.* 20 (2019), pp. 495–505.

[9] Churchland, P. S. and Sejnowski, T. J. *The computational brain*. Cambridge: MIT Press, 1992.

[10] Snell, R. S. *Clinical Neuroanatomy*. Philadelphia: Lippincott Williams & Wilkins, 2010.

[11] Chen, S.-J., Liao, D.-L., Chen, C.-H., Wang, T.-Y., and Chen, K.-C. “Construction and Analysis of Protein-Protein Interaction Network of Heroin Use Disorder”. In: *Nature Sci. Rep.* 9 (2019).

[12] Osten, P. and Margrie, T. W. “Mapping brain circuitry with a light microscope”. In: *Nat. Methods.* 10 (2013), pp. 515–523.

[13] Brodmann, K. *Vergleichende Lokalisationslehre der Grosshirnrinde in ihren Prinzipien dargestellt auf Grund des Zellenbaues*. J.A. Barth, 1909.

[14] Fellemann, D. J. and Van Essen, D. C. “Distributed Hierarchical Processing in the Primate Cerebral Cortex”. In: *Cereb. Cortex* 1 (1991), pp. 1–47.

[15] Bastos, A. M., Usrey, W. M., Adams, R. A., Mangun, G. R., Fries, P., and Friston, K. J. “Canonical microcircuits for predictive coding”. In: *Neuron* 76 (2012), pp. 695–711.

[16] Douglas, R. J., Martin, K. A., and Whitteridge, D. “A canonical mircocircuit for neocortex”. In: *Neural Comput.* 1 (1989), pp. 480–488.

[17] Weber, B., Keller, A. L., Reichold, J., and Logothethis, N. K. “The microvascular system of the striate and extrastriate visual cortex of the macaque”. In: *Cereb. Cortex* 18 (2008), pp. 2318–2330.

[18] Duvernoy, H.M., Cattin, F., and Risold, P.-Y. *The Human Hippocampus*. Berlin, Heidelberg: Springer, 2013.

[19] Schmolesky, M. *The Primary Visual Cortex*. `https://www.ncbi.nlm.nih.gov/books/NBK11524/`(visited 2022-01-23). Salt Lake City (UT): University of Utah Health Sciences Center, 2007.

[20] Self, M. W., van Kerkoerle, T., Supér, H., and Roelfsema, P. R. "Distinct Roles of the Cortical Layers of Area V1 in Figure-Ground Segregation". In: *Curr. Biol.* 23 (2013), pp. 2121–2129.

[21] Duvernoy, H. M. "Cortical Blood Vessels of the Human Brain". In: *Brain Res. Bull.* 7 (1981), pp. 519–579.

[22] Keeler, J. *Understanding NMR Spectroscopy*. 2nd ed. New York: John Wiley & Sons Inc, 2010.

[23] Hanson, L. G. "Is Quantum Mechanics necessary for understanding Magnetic Resonance?" In: *Concepts Magn. Reson. A: Bridg. Educ. Res.* 32 (2008), pp. 329–340.

[24] Hobbie, R. K. and Roth, B. J. *Intermediate Physics for Medicine and Biology*. 5th ed. Springer Science + Business Media, 2015.

[25] Haacke, E. M., Brown, R. W., Thompson, M. R., and Vankatesan, R. *Magnetic Resonance Imaging: Physical Principles and Sequence Design*. New York: John Wiley & Sons Inc, 1999.

[26] Bernstein, M. A., King, K. F., and Zhou, Z. J. *Handbook of MRI pulse sequences*. 1st ed. Elsevier AcademicPress, 2004.

[27] Bloch, F. "Nuclear Induction". In: *Phys. Rev.* 70 (1946), pp. 460–474.

[28] Rabi, I. I. "On the Process of Space Quantization". In: *Phys. Rev.* 49 (1935), pp. 324–328.

[29] Bloch, F., Hansen, W. W., and Packard, M. “The Nuclear Induction Experiment”. In: *Phys. Rev.* 70 (1946), pp. 474–485.

[30] Solomon, I. “Relaxation Processes in a System of Two Spins”. In: *Phys. Rev.* 99 (1955), pp. 559–565.

[31] Crémillieux, Y., Ding, S., and Dunn, J. F. “High-Resolution in Vivo Measurements of Transverse Relaxation Times in Rats at 7 Tesla”. In: *Magn. Reson. Med.* 39 (1998), pp. 285–290.

[32] Michaeli, S., Garwood, M., Zhu, X.-H., DelaBarre, L., Andersen, P., Adriany, G., Merkle, H., Uğurbil, K., and Chen, W. “Proton T_2 Relaxation Study of Water, N-acetylaspartate,and Creatine in Human Brain Using Hahn and Carr-Purcell Spin Echoes at 4T and 7T”. In: *Magn. Reson. Med.* 47 (2002), pp. 629–633.

[33] van Zijl, P. C. M., Lam, W. W., Xu, J., Knutsson, L., and Stanisz, G. J. “Magnetization Transfer Contrast and Chemical Exchange Saturation Transfer MRI. Features and analysis of the field-dependent saturation spectrum”. In: *NeuroImage* 168 (2018), pp. 222–241.

[34] Sled, J. G. “Modelling and interpretation of magnetization transfer imaging in the brain”. In: *NeuroImage* 182 (2018), pp. 128–135.

[35] Morrison, C. and Henkelman, R. M. “A Model for Magnetization Transfer in Tissues”. In: *Magn. Reson. Med.* 33 (1995), pp. 475–482.

[36] Wolff, S. D. and Balaban, R. S. “Magnetization transfer contrast (MTC) and tissue water proton relaxation in vivo”. In: *Magn. Reson. Med.* 10 (1989), pp. 135–144.

[37] Balaban, R. S., Chesnick, S., Hedges, K., Samaha, F., and Heineman, F. W. “Magnetization Transfer Contrast in MR Imaging of the Heart”. In: *Radiology* 180 (1991), pp. 671–675.

[38] Cabana, J.-F. et al. “Quantitative magnetization transfer imaging made easy with qMT*Lab*: Software for data simulation, analysis, and visualization”. In: *Concepts Magn. Reson. A: Bridg. Educ. Res.* 44A (2016), pp. 263–277.

[39] de Boer, R. W. “Magnetization transfer contrast Part 1: MR physics”. In: *Medicamundi* 40 (1995), pp. 64–573.

[40] Kubach, M. R. “Quantification of the Longitudinal Relaxation Time for in vivo MRI-Influence of Magnetisation Transfer”. PhD thesis. RWTH Aachen, 2012.

[41] Henkelman, R. M., Huang, X., Xiang, Q.-S., Stanisz, G. J., Swanson, S. D., and Bronskill, M. J. “Quantitative interpretation of magnetization transfer”. In: *Magn. Reson. Med.* 29 (1993), pp. 759–766.

[42] Sled, J. G. and Pike, G. B. “Quantitative Interpretation of Magnetization Transfer in Spoiled Gradient Echo MRI Sequences”. In: *J. Magn. Reson.* 145 (2000), pp. 24–36.

[43] Sled, J. G. and Pike, G. B. “Quantitative imaging of magnetization transfer exchange and relaxation properties in vivo using MRI”. In: *Magn. Reson. Med.* 46 (2001), pp. 923–931.

[44] Hua, J. and Hurst, G. C. “Analysis of on- and off-resonance magnetization transfer techniques”. In: *J. Magn. Reson. Imaging* 5 (1995), pp. 113–120.

[45] Graham, S. J. and Henkelman, R. M. “Understanding Pulsed Magnetization Transfer”. In: *J. Magn. Reson. Imaging* 7 (1997), pp. 903–912.

[46] Davies, N. P., Summers, I. R., and Vennart, W. “Optimum Setting of Binomial Pulses for Magnetization Transfer Contrast”. In: *J. Magn. Reson. Imaging* 11 (2000), pp. 539–548.

[47] McConnell, H. M. “Reaction rates by nuclear magnetic resonance”. In: *J. Chem. Phys.* 28 (1958), pp. 430–431.

[48] Van Gelderen, P., Jiang, X., and Duyn, J. H. “Rapid measurement of brain macromolecular proton fraction with transient saturation transfer MRI”. In: *Magn. Reson. Med.* 77 (2017), pp. 2174–2185.

[49] Poser, A. B. “Techniques for BOLD and blood volume weighted fMRI”. PhD thesis. Radboud University Nijmegen, 2009.

[50] Hahn, E. L. “Spin Echoes”. In: *Phys. Rev.* 80 (2017), pp. 580–594.

[51] Jähne, B. *Digitale Bildverarbeitung*. 6th ed. Springer Science + Business Media, 2005.

[52] Shannon, C. E. “Communication in the presence of noise”. In: *Proc. of the IRE* 37 (1949), pp. 10–21.

[53] Zur, Y., Wood, M. L., and Neuringer, L. J. “Spoiling of transverse magnetization in steady-state sequences”. In: *Magn. Reson. Med.* 21 (1991), pp. 251–263.

[54] Haase, A., Frahm, J., Matthaei, D., Hänicke, W., and Merboldt, K.-D. “FLASH Imaging. Rapid NMR Imaging Using Low Flip-Angle Pulses”. In: *J. Magn. Reson.* 67 (1986), pp. 258–266.

[55] Mansfield, P. “Multi-planar imaging formation using NMR spin echoes”. In: *J. Phys. C: Solid State Phys.* 10 (1977), pp. L55–L58.

[56] Cho, Z. H. and Ro, Y. M. “Reduction of susceptibility artifact in gradient-echo imaging”. In: *Magn. Reson. Med.* 23 (1992), pp. 193–200.

[57] Margosian, P., Schmitt, F., and Purdy, D. “Faster MR imaging: imaging with half the data”. In: *Health Care Instrum.* 1 (1986), p. 195.

[58] Noll, D. C., Nishimura, D. G., and Macovski, A. “Homodyne detection in magnetic resonance imaging”. In: *IEEE Trans. Med. Imaging* 10 (1991), pp. 154–163.

[59] Cuppan, J. and van Est, A. “Reducing MR imaging time by one-sided reconstruction”. In: *Magn. Reson. Imaging* 5 (1987), pp. 526–527.

[60] Haacke, E. M., Lindskogj, E. D., and Lin, W. “A fast, iretative, partial-Fourier technique capable of local phase recovery”. In: *J. Magn. Reson.* 92 (1991), pp. 126–145.

[61] Koopmans, P. J. and Pfaffenrot, V. “Enhanced POCS reconstruction for partial Fourier imaging in multi-echo and time-series acquisitions”. In: *Magn. Reson. Med.* 85 (2021), pp. 140–151.

[62] Roemer, P. B., Edelstein, W. A., Hayes, C.E., Souza, S.P., and Mueller, O. M. “The NMR phased array”. In: *Magn. Reson. Med.* 16 (1990), pp. 192–225.

[63] Hamilton, J., Franson, D., and Seiberlich, N. “Recent advances in parallel imaging for MRI”. In: *Prog. Nucl. Magn. Reson. Spectrosc.* 101 (2017), pp. 71–95.

[64] Poser, B. A. and Setsompop, K. “Pulse sequences and parallel imaging for high spatiotemporal resolution MRI at ultra-high fields”. In: *NeuroImage* 168 (2018), pp. 101–118.

[65] Pruessmann, K. P., Weiger, M., Scheidegger, M. B., and Boesiger, P. “SENSE: Sensitivity Encoding for Fast MRI”. In: *Magn. Reson. Med.* 42 (1999), pp. 952–962.

[66] Sodickson, D. K. and Manning, W. J. “Simultaneous Acquisition of Spatial Harmonics (SMASH): Fast Imaging with Radiofrequency Coil Arrays”. In: *Magn. Reson. Med.* 38 (1997), pp. 591–603.

[67] Griswold, M. A., Jakob, P. M., Heidemann, R. M., Nittka, M., Jellus, V., Wang, J., Kiefer, B., and Haase, A. “Generalized Autocalibrating Partially Parallel Acquisitions (GRAPPA)”. In: *Magn. Reson. Med.* 47 (2002), pp. 1202–1210.

[68] Deshmane, A., Gulani, V., Griswold, M. A., and Seiberlich, N. “Parallel MR Imaging”. In: *Magn. Reson. Imaging* 36 (2012), pp. 55–72.

[69] Blaimer, M., Breuer, F., Mueller, M., Heidemann, M., griswold, M. A., and Jakob, P. M. “SMASH, SENSE, PILS, GRAPPA How to Choose the Optimal Method”. In: *Top. Magn. Reson. Imaging* 15 (2004), pp. 223–236.

[70] Breuer, F. A., Kannengiesser, A. R., Blaimer, M., Seiberlich, N., Jakob, P. M., and Griswold, M. A. “General Formulation for Quantitative G-factor Calculation in GRAPPA Reconstructions”. In: *Magn. Reson. Med.* 62 (2009), pp. 739–746.

[71] Pruessmann, K. P. “Parallel Imaging at High Field Strength Synergies and Joint Potential”. In: *Top. Magn. Reson. Imaging* 15 (2004), pp. 237–244.

[72] Wiesinger, F., Van de Moortele, P. -F., Adriany, G., De Zanche, N., Uğurbil, K., and Pruessmann, K. P. “Parallel Imaging Performance as a Function of Field Strength — An Experimental Investigation Using Electrodynamic Scaling”. In: *Magn. Reson. Med.* 52 (2004), pp. 953–964.

[73] Robitaille, P.-M. and Berliner, L. J. *Ultra High Field Magnetic Resonance Imaging*. Biological Magnetic Resonance 26. Springer Science + Business Media, 2006.

[74] Glover, G. H., Hayes, C. E., Pelc, N. J., Edelstein, W. A., Mueller, O. M., Hart, H. R., Hardy, C. J., O'Donnell, M., and Barber, W. D. "Comparison of Linear and Circular Polarization for Magnetic Resonance Imaging". In: *J. Magn. Reson.* 64 (1985), pp. 255–270.

[75] Hoult, D. I. and Richards, R. E. "The signal-to-noise ratio of the nulear magnetic resonance experiment". In: *J. Magn. Reson.* 24 (1976), pp. 71–85.

[76] Hoult, D. I. "The Principle of Reciprocity in Signal Strength Calculations - A Mathematical Guide". In: *Concepts Magn. Reson.* 12 (2000), pp. 173–187.

[77] Insko, E. K., Elliott, M. A., Schotland, J. C., and Leigh, J.S. "Generalized Reciprocity". In: *J. Magn. Reson.* 131 (1998), pp. 111–117.

[78] Yang, Q. X., Wang, J., Zhang, X., Collins, C. M., Smith, M. B., Liu, H., Zhu, X.-H., Vaughan, J. T., Uğurbil, K., and Chen, W. "Analysis of Wave Behavior in Lossy Dielectric Samples at High Field". In: *Magn. Reson. Med.* 47 (2002), pp. 982–989.

[79] Van de Moortele, P.-F., Akgun, C., Adriany, G., Moeller, S., Ritter, J., Collins, C. M., Smith, M. B., Vaughan, J. T., and Uğurbil, K. "B_1 Destructive Interferences and Spatial Phase Patterns at 7 T with a Head Transceiver Array Coil". In: *Magn. Reson. Med.* 54 (2005), pp. 1503–1518.

[80] Hayes, C. E., Edelstein, W. A., Schenk, J. F., Mueller, O. M., and Eash, M. "An efficient, highly homogeneous radiofrequency coil for whole-body NMR imaging at 1.5 T". In: *J. Magn. Reson.* 63 (1985), pp. 622–628.

[81] Fiedler, T. M., Ladd, M. E., and Bitz, A. K. "SAR Simulations & Safety". In: *NeuroImage* 168 (2018), pp. 33–58.

[82] Katscher, U., Rohrs, J., and Bornert, P. “Basic considerations on the impact of the coil array on the performance of Transmit SENSE”. In: *Magn. Reson. Mater. Phys. Biol. Med.* 18 (2005), pp. 81–88.

[83] Hoult, D. I. and Lauterbur, P. C. “The Sensitivity of the Zeugmatographic Experiment Involving Human Samples”. In: *J. Magn. Reson.* 34 (1979), pp. 425–433.

[84] Vaughan, J. T. et al. “7T vs. 4T: RF Power, Homogeneity, and Signal-to-Noise Comparison in Head Images”. In: *Magn. Reson. Med.* 46 (2001), pp. 24–30.

[85] Padormo, F., Beqiri, A., Hajnal, J. V., and Malik, S. J. “Parallel transmission for ultrahigh-field imaging”. In: *NMR Biomed.* 29 (2016), pp. 1145–1161.

[86] Deniz, C. M. “Parallel transmission for Ultrahigh Field MRI”. In: *Top. Magn. Reson. Imaging* 28 (2019), pp. 159–171.

[87] Pohmann, R. and Scheffler, K. “A theoretical and experimental comparison of different techniques for B_1 mapping at very high fields”. In: *NMR Biomed.* 26 (2013), pp. 265–275.

[88] Brunheim, S., Gratz, M., Johst, S., Bitz, A. K., Fiedler, T. M., Ladd, M. E., Quick, H. H., and Orzada, S. “Fast and accurate multi-channel B_1^+ mapping based on the TIAMO technique for 7T UHF body MRI”. In: *Magn. Reson. Med.* 79 (2018), pp. 2652–2664.

[89] Nehrke, K. and Börnert, P. “DREAM-a novel approach for robust, ultrafast, multislice B_1 mapping”. In: *Magn. Reson. Med.* 68 (2012), pp. 1517–1526.

[90] Tse, D. H. Y., Poole, M. S., Magill, A. W., Felder, J., Brenner, D., and Shah, N. J. “Encoding methods for B_1^+ mapping in parallel transmit

systems at ultra high field". In: *J. Magn. Reson.* 245 (2014), pp. 125–132.

[91] Ladd, M. E. "High Versus Low Static Magnetic Fields in MRI". In: *Comprehensive Biomedical Physics* 3 (2014), pp. 55–68.

[92] Mao, W., Smith, M. B., and Collins, C. M. "Exploring the Limits of RF Shimming for High-Field MRI of the Human Head". In: *Magn. Reson. Med.* 56 (2006), pp. 918–922.

[93] Pauly, J., Nishimura, D., and Macovski, A. "A k-space analysis of small-tip-angle excitation". In: *J. Magn. Reson.* 81 (1989), pp. 43–56.

[94] Grissom, W., Yip, C.-y., Zhang, Z., Stenger, A., Fessler, J. A., and Noll, D. C. "Spatial Domain Method for the Design of RF Pulses in Multicoil Parallel Excitation". In: *Magn. Reson. Med.* 56 (2006), pp. 620–629.

[95] Setsompop, K., Wald, L. L., Alagappan, V., Gagoski, B. A., and Adalsteinsson, E. "Magnitude Least Squares Optimization for Parallel Radio Frequency Excitation Design Demonstrated at 7 Tesla With Eight Channels". In: *Magn. Reson. Med.* 59 (2008), pp. 908–915.

[96] Saekho, S., Yip, C.-y., Noll, D. C., Boada, F. E., and Stenger, V. A. "Fast-k_Z Three-Dimensional Tailored Radiofrequency Pulse for Reduced B_1 Inhomogeneity". In: *Magn. Reson. Med.* 55 (2006), pp. 719–724.

[97] Cloos, M. A., Boulant, N., Luong, M., Ferrand, G., Giacomini, E., Le Bahin, D., and Amadon, A. "k_T-Points: Short Three-Dimensional Tailored RF Pulses for Flip-Angle Homogenization Over an Extended Volume". In: *Magn. Reson. Med.* 67 (2012), pp. 72–80.

[98] Katscher, U., Börnert, P., Leussler, C., and van den Brink, J. S. "Transmit SENSE". In: *Magn. Reson. Med.* 49 (2003), pp. 144–150.

[99] Zhu, Y. “Parallel Excitation With an Array of Transmit Coils”. In: *Magn. Reson. Med.* 51 (2004), pp. 775–784.

[100] Tannús, A. and Garwood, M. “Improved Performance of Frequency-Swept Pulses Using Offset-Independent Adiabaticity”. In: *J. Magn. Reson.* 120 (1996), pp. 133–137.

[101] Norris, D. G. “Adiabatic radiofrequency pulse forms in biomedical nuclear magnetic resonance”. In: *Concepts Magn. Reson.* 142 (2002), pp. 89–101.

[102] Tannús, A. and Garwood, M. “Adiabatic pulses”. In: *JNMR Biomed.* 10 (1997), pp. 423–434.

[103] Conolly, S., Glover, G., Nishimura, D., and Macovski, A. “A reduced power selective adiabatic spin-echo pulse sequence”. In: *Magn. Reson. Med.* 18 (1991), pp. 28–38.

[104] Watts, M. E., Pocock, R., and Claudianos, C. “Brain Energy and Oxygen Metabolism: Emerging Role in Normal Function and Disease”. In: *Front. Mol. Neurosci.* 11 (2018).

[105] Boas, D. A., Jones, S. R., Devor, A., Huppert, T. J., and Dale, A. M. “A vascular anatomical network model of the spatio-temporal response to brain activation”. In: *NeuroImage* 40 (2008), pp. 1116–1129.

[106] Lauwers, F., Cassot, F., Lauwers-Cances, V., Puwanarajah, P., and Duvernoy, H. “Morphometry of the human cerebral cortex microcirculation: General characteristics and space-related profiles”. In: *NeuroImage* 39 (2008), pp. 936–948.

[107] Tsai, P. S., Kaufhold, J. P., Blinder, P., Friedman, B., Drew, P. J., Karten, H. J., Lyden, P. D., and Kleinfeld, D. “Correlations of Neuronal and Microvascular Densities in Murine Cortex Revealed by Di-

rect Counting and Colocalization of Nuclei and Vessels". In: *J. Neurosci.* 29 (2008), pp. 14553–14570.

[108] Uludağ, K. and Blinder, P. "Linking brain vascular physiology to hemodynamic response in ultra-high field MRI". In: *NeuroImage* 168 (2018), pp. 279–295.

[109] Lecoq, J., Parpaleix, A., Roussakis, E., Ducros, M., Houssen, Y. G., Vinogradov, S. A., and Charpak, S. "Simultaneous two-photon imaging of oxygen and blood flow in deep cerebral vessels". In: *Nat. Med.* 17 (2011), pp. 893–898.

[110] Havlicek, M., Roebroeck, A., Friston, K., Gardumi, A., Ivanov, D., and Uludağ, K. "Physiologically informed dynamic causal modeling of fMRI data". In: *NeuroImage* 122 (2015), pp. 355–372.

[111] Phillips, A. A., Chan, F. H. N., Zheng, M. M. Z., Krassioukov, A. V., and Ainslie, P. N. "Neurovascular coupling in humans: Physiology, methodological advances and clinical implications". In: *J. Cereb. Blood Flow Metab.* 36 (2016), pp. 647–666.

[112] Huneau, C., Benali, H., and Chabriat, H. "Investigating Human Neurovascular Coupling Using Functional Neuroimaging: A Critical Review of Dynamic Models". In: *Front. Neurosci.* 9 (2015).

[113] Norris, D. G. "Principles of magnetic resonance assessment of brain function". In: *J. Magn. Reson. Imaging* 23 (2006), pp. 794–807.

[114] Buxton, R. B., Wong, R. C., and Frank, L. R. "Dynamics of Blood Flow and Oxygenation Changes During Brain Activation: The Balloon Model". In: *Magn. Reson. Med.* 39 (1998), pp. 855–864.

[115] Havlicek, M. and Uludağ, K. "A dynamical model of the laminar BOLD response". In: *NeuroImage* 204 (2020).

[116] Hall, C. N., Reynell, C., Gesslein, B., Hamilton, N.B., Mishra, A., Sutherland, B. A., O'Farrell, F. M., Buchan, A. M., Lauritzen, M., and Attwell, D. "Capillary pericytes regulate cerebral blood flow in health and disease". In: *Nature* 508 (2014), pp. 55–60.

[117] Krieer, S. N., Streicher, M. N., Trampel, R., and Turner, R. "Cerebral blood volume changes during brain activation". In: *J. Cereb. Blood Flow Metab.* 32 (2012), pp. 1618–1631.

[118] van Zijl, P. C. M., Eleff, S. M., Ulatowski, J. A., Oja, J. M. E., Uluğ, A. M., Traystman, R.J., and Kauppinen, R. A. "Quantitative assessment of blood flow, blood volume and blood oxygenation effects in functional magnetic resonance imaging". In: *Nat. Med.* 4 (1998), pp. 159–167.

[119] Uludağ, K., Müller-Bierl, B., and Uğurbil, K. "An integrative model for neuronal activity-induced signal changes for gradient and spin echo functional imaging". In: *NeuroImage* 48 (2009), pp. 150–165.

[120] Drew, P. J., Shih, A. Q., and Kleinfeld, D. "Fluctuating and sensory-induced vasodynamics in rodent cortex extend arteriole capacity". In: *PNAS* 108 (2011), pp. 8473–8478.

[121] Kim, T. and Kim, S.-G. "Temporal dynamics and spatial specificity of arterial and venous blood volume changes during visual stimulation: Implication for BOLD quantification". In: *J. Cereb. Blood Flow Metab.* 31 (2011), pp. 1211–1222.

[122] Akbari, A., Bollmann, S., Ali, T. S., and Barth, M. "Modelling the depth-dependent VASO and BOLD responses in human primary visual cortex". In: *bioRxiv* (2021).

[123] Kim, T. and Kim, S.-G. "Quantitative MRI of Cerebral Arterial Blood Volume". In: *Open Neuroimaging J.* 5 (2011), pp. 136–145.

[124] Gagnon, L. et al. “Quantifying the Microvascular Origin of BOLD-fMRI from First Principles with Two-Photon Microscopy and an Oxygen-Sensitive Nanoprobe”. In: *J. Neurosci.* 38 (2015), pp. 3663–3675.

[125] Pauling, L. and Coryell, C. D. “The magnetic properties and structure of hemoglobin, oxyhemoglobin and carbonmonoxyhemoglobin”. In: *PNAS* 22 (1936), pp. 210–216.

[126] Ogawa, S., Menon, R. S., Tank, D. W., Kim, S.-G., Merkle, H., Ellermann, J. M., and Uğurbil, K. “Functional brain mapping by blood oxygenation level-dependent contrast magnetic-resonance-imaging - a comparison of signal characteristics with a biophysical model”. In: *Biophys. J.* 64 (1993), pp. 803–812.

[127] Viessmann, O., Scheffler, K., Bianciardi, M., Wald, L. L., and Polimeni, J. R. “Dependence of resting-state fMRI fluctuation amplitudes on cerebral cortical orientation relative to the direction of B_0 and anatomical axes”. In: *NeuroImage* 196 (2019), pp. 337–350.

[128] Koopmans, P. J. and Yacoub, E. “Strategies and prospects for cortical depth dependent T_2 and T_2^* weighted BOLD fMRI studies”. In: *NeuroImage* 197 (2019), pp. 668–676.

[129] Báez-Yánez, M. G., Ehses, P., Mirkes, C., Tsai, P. S., Kleinfeld, D., and Scheffler, K. “The impact of vessel size, orientation and intravascular contribution on the neurovascular fingerprint of BOLD bSSFP fMRI”. In: *NeuroImage* 163 (2017), pp. 13–23.

[130] Boxermann, J. L., Hamberg, L. M., Rosen, B. R., and Weisskoff, R. M. “MR contrast due to intravascular magnetic susceptibility perturbations”. In: *Magn. Reson. Med.* (1995).

[131] Yablonskiy, D. A. and Haacke, E. M. “Theory of NMR signal behavior in magnetically inhomogeneous tissues: The static dephasing regime”. In: *Magn. Reson. Med.* 32 (1994), pp. 749–763.

[132] Elster, A. D. *Questions and Answers in MRI: BOLD and Brain Activity*. Last checked: 18.02.2022. URL: `https://mriquestions.com/does-boldbrain-activity.html`.

[133] Sirotin, Y. B., Hillman, E. M. C., Bordier, C., and Das, A. “Spatiotemporal precision and hemodynamic mechanism of optical point spreads in alert primates”. In: *PNAS* 106 (2009), pp. 18390–18395.

[134] van Zijl, P. C. M., Hua, J., and Lu, H. “The BOLD post-stimulus undershoot, one of the most debated issues in fMRI”. In: *NeuroImage* 62 (2012), pp. 1092–1102.

[135] Bause, J., Polimeni, J. R., Stelzer, K., In, M. H., Ehses, P., Kreamer-Fernandez, P., Aghaeifar, A., Lacosse, E., Pohmann, R., and Scheffler, K. “Impact of prospective motion correction, distortion correction methods and large vein bias on the spatial accuracy of cortical laminar fMRI at 9.4 Tesla”. In: *NeuroImage* 208 (2020).

[136] Weisskoff, R., Zuo, C. S., Boxerman, J. L., and Rosen, B. R. “Microscopic susceptibility variation and transverse relaxation: Theory and experiment”. In: *Magn. Reson. Med.* 31 (1994), pp. 601–610.

[137] Bandettini, P. A., Wong, E. C., Jesmanowicz, A., Hinks, R. S., and Hyde, J. S. “Spin-echo and gradient-echo epi of human brain activation using bold contrast: A comparative study at 1.5 T”. In: *NMR Biomed.* 7 (1994), pp. 12–20.

[138] Goense, J. B. M. and Logothetis, N. K. “Laminar specificity in monkey V1 using high-resolution SE-fMRI”. In: *Magn. Reson. Imaging* 24 (2006), pp. 381–392.

[139] Feinberg, D. A. and Oshio, K. “Phase Errors in Multi-Shot Echo Planar Imaging”. In: *Magn. Reson. Med.* 32 (1994), pp. 535–539.

[140] Hennel, F. “Multiple-shot echo-planar imaging”. In: *Concepts Magn. Reson.* 9 (1997), pp. 43–58.

[141] Oshio, K. and Feinberg, D. A. “GRASE (Gradient-and Spin-Echo) imaging: A novel fast MRI technique”. In: *Magn. Reson. Med.* 20 (1991), pp. 344–349.

[142] Feinberg, D. A., Harel, N., Ramanna, S., Uğurbil, K., and Yacoub, E. “Sub-millimeter single-shot 3D GRASE with inner volume selection for T2 weighted fMRI applications at 7 tesla”. In: *Proc. Int. Soc. Magn. Reson. Med. 16* (2008), #2373.

[143] Huber, L., Uludağ, K., and Moeller, H. E. “Non-BOLD contrast for laminar fMRI in humans: CBF, CBV, and $CMRO_2$”. In: *NeuroImage* 197 (2019), pp. 742–760.

[144] Lu, H., Golay, X., Pekar, J. J., and van Zijl, P. M. C. “Functional magnetic resonance imaging based on changes in vascular space occupancy”. In: *Magn. Reson. Med.* 50 (2003), pp. 263–274.

[145] Lu, H., Hua, H., and van Zijl, P. M. C. “Noninvasive functional imaging of cerebral blood volume with vascular-space-occupancy (VASO) MRI”. In: *NMR Biomed.* 26 (2013), pp. 932–948.

[146] Huber, L., Ivanov, D., Krieger, S. N., Mildner, R., Poser, B. A., Möller, H. E., and Turner, R. “Slab-selective, BOLD-corrected VASO at 7 Tesla provides measures of cerebral blood volume reactivity with high signal-to-noise ratio”. In: *Magn. Reson. Med.* 72 (2014), pp. 137–148.

[147] Huber, L. et al. “Beyond the limits of layer-dependent CBV fMRI in humans: strategies towards whole brain coverage, sub-second TR, and

very high 0.5mm (iso) resolutions". In: *Proc. Int. Soc. Magn. Reson. Med. 28* (2020), #3864.

[148] Huber, L. et al. "Layer-dependent functional connectivity methods". In: *Prog. Neurobiol.* 207 (2021).

[149] Pfaffenrot, V., Brunheim, S., Rietsch, S. H. G., Koopmans, P. J., Ernst, T. M., Kraff, O., Orzada, S., and Quick, H. H. "An 8/15-channel Tx/Rx head neck RF coil combination with region-specific B_1^+ shimming for whole brain MRI focused on the cerebellum at 7 Tesla". In: *Magn. Reson. Med.* 80 (2018), pp. 1252–1265.

[150] Manni, E. and Petrosini, L. "A century of cerebellar somatotopy". In: *Nat. Rev. Neurosci.* 5 (2004), pp. 241–249.

[151] Habas, C. "Functional imaging and the cerebellum: recent developments and challenges". In: *Cerebellum* 11 (2012), pp. 311–313.

[152] Ackermann, H., Wildgruber, D., Daum, I., and Grodd, W. "Does the cerebellum contribute to cognitive aspects of speech production? A functional magnetic resonance imaging (fMRI) study in humans". In: *Neurosci. Lett.* 24 (1998), pp. 187–190.

[153] Stoodley, C. J. and Schmahmann, J. D. "Functional topography in the human cerebellum: a meta-analysis of neuroimaging studies". In: *NeuroImage* 44 (2009), pp. 489–501.

[154] Thürling, M. et al. "Cerebellar cortex and cerebellar nuclei are concomitantly activated during eyeblink conditioning: a 7T fMRI study in humans". In: *J. Neurosci.* 21 (2015), pp. 1228–1239.

[155] Utz, A., Thürling, M., Ernst, T. M., Hermann, A., Stark, R., Wolf, O. T., Timmann, D., and Merz, C. J. "Cerebellar vermis contributes to the extinction of conditioned fear". In: *Neurosci. Lett.* 604 (2015), pp. 173–177.

[156] Spitzer, R., Kroenke, K., Williams, J.B.W., and Löwe, B. “A brief measure for assessing generalized anxiety disorder-the GAD-7”. In: *Arch. Intern. Med.* 166 (2006), pp. 1092–1097.

[157] Norris, D. G. “High Field Human Imaging”. In: *J. Magn. Reson. Imaging* 18 (2003), pp. 519–529.

[158] Olman, C. A., Harel, N., Feinberg, D. A., He, S., Zhang, P., Uğurbil, K., and Yacoub, E. “High Field Human Imaging”. In: *Plos One* 7 (2012).

[159] Marques, J. P., van der Zwaag, W., Granziera, C., Krueger, G., and Gruetter, R. “Cerebellar cortical layers: in vivo visualization with structural high-field-strength MR imaging”. In: *Radiology* 254 (2010).

[160] van der Zwaag, W., Kusters, R., Magill, A., Gruetter, R., Martuzzi, R., Blanke, O., and Marques, J. P. “Digit somatotopy in the human cerebellum: a 7 T fMRI study”. In: *NeuroImage* 67 (2013).

[161] Adriany, G. et al. “Transmit and receive transmission line arrays for 7 Tesla parallel imaging”. In: *Magn. Reson. Med.* 53 (2005).

[162] Curtis, A. T., Gilbert, K. M., Klassen, L. M., Gati, J. S., and Menon, R. S. “Slice-by-slice B_1^+ shimming at 7 T”. In: *Magn. Reson. Med.* 68 (2012).

[163] Wu, X., Schmitter, S., Auerbach, E. J., Uğurbil, K., and Van de Moortele, P.-F. “A generalized slab-wise framework for parallel transmit multiband RF pulse design”. In: *Magn. Reson. Med.* 75 (2016).

[164] Setsompop, K., Wald, L. L., Alagappan, V, Gagoski, B., Hebrank, F., Fontius, U., Schmitt, F., and Adalsteinsson, E. “Parallel RF transmission with eight channels at 3 Tesla”. In: *Magn. Reson. Med.* 56 (2006).

[165] Gras, V., Vignaud, A., Amadon, A., Mauconduit, F., Le Bahin, D., and Boulant, N. “In vivo demonstration of whole-brain multislice multispoke parallel transmit radiofrequency pulse design in the small and large flip angle regimes at 7 Tesla”. In: *Magn. Reson. Med.* 78 (2017).

[166] Tse, D. S. Y., Wiggins, C. J., and Poser, B. A. “High-resolution gradient recalled echo imaging at 9.4T using 16-channel parallel transmit simultaneous multislice spokes excitation with slice-by-slice flip angle homogenization”. In: *Magn. Reson. Med.* 78 (2017).

[167] Human anatomy: volume III head, neck and brain. *A. Halim*. Delhi, India: I.K. International Publishing House, 2008.

[168] Ojemann, J. G., Akburdak, E., Snyder, A. Z., McKinstry, R. C., Raichle, M. E., and Conturo, T. E. “Anatomic localization and quantitative analysis of gradient refocused echo-planar fMRI susceptibility artifacts”. In: *NeuroImage* 6 (1997).

[169] Marques, J. P., Gruetter, R., and van der Zwaag, W. “In vivo structural imaging of the cerebellum, the contribution of ultra-high fields”. In: *Cerebellum* 11 (2012).

[170] Diedrichsen, J., Verstynen, T., Schlerf, J., and Wiestler, T. “Advances in functional imaging of the human cerebellum”. In: *Curr. Opin. Neurol* 23 (2010).

[171] Van de Moortele, P.-F., Auerbach, E. J., Olman, C. A., Yacoub, E., Uğurbil, K., and Moeller, S. “T_1 weighted brain images at 7 Tesla unbiased for proton density T_2^* contrast and RF coil receive B_1 sensitivity with simultaneous vessel visualizarion”. In: *NeuroImage* 46 (2009).

[172] Hurley, A. C., Al-Radaideh, A., Bai, L., Aickelin, U., Coxon, R., Glover, P., and Gowland, P. A. “Tailored RF pulse for magnetization inversion at ultrahigh field”. In: *Magn. Reson. Med.* 63 (2010).

[173] Wrede, K. H., Johst, S., Dammann, P., Umutlu, L., Schlamann, M. U., Sandalcioglu, I. E., Sure, U., Ladd, M. E., and Maderwald, S. “Caudal image contrast inversion in MPRAGE at 7 Tesla: problem and solution”. In: *Acad. Radiol.* 19 (2012).

[174] O’Brian, K. R., Magill, A. W., Delacoste, J., Marques, J. P., Kober, T., Fautz, H.-P., Lazeyras, F., and Krueger, G. “Dielectric pads and low-B-1^{+} adiabatic pulses: Complementary techniques to optimize structural T_1w whole-brain MP2RAGE scans at 7 tesla”. In: *J. Magn. Reson. Imaging* 40 (2014).

[175] Orzada, S., Kraff, O., Schäfer, L. C., Brote, I., Bahr, A., Bolz, T., Maderwald, S., Ladd, M. E., and Bitz, A. K. “8-Channel Transmit/receive Head Coil for 7 T Human Imaging Using Intrinsically Decoupled Strip Line Elements with Meanders”. In: *Proc. Int. Soc. Magn. Reson. Med. 17* (2009), #3010.

[176] Rietsch, S. H. G., Kraff, O., Orzada, S., Lazik, A., and Quick, H. H. “Cost-efficient 7ch Rx shoulder array for 7T UHF MRI featuring external switchbox detuning”. In: *Proc. Int. Soc. Magn. Reson. Med. 24* (2016), #2142.

[177] Brunheim, S., Johst, S., Pfaffenrot, V., Quick, H. H., and Poser, B. A. “Variable slice thickness (VAST) EPI for the reduction of susceptibility artifacts in whole-brain GE-EPI at 7 Tesla”. In: *Magn. Reson. Mater. Phys.* 30 (2017), pp. 591–607.

[178] Teeuwisse, W. M., Brink, W. M., and Webb, A. G. “Quantitative assessment of the effects of high-permittivity pads in 7 Tesla MRI of the brain”. In: *Magn. Reson. Med.* 67 (2012), pp. 1285–1293.

[179] Bitz, A. K. et al. “An 8-channel add-on RF shimming system for whole-body 7 Tesla MRI including real-time SAR monitoring”. In: *Proc. Int. Soc. Magn. Reson. Med. 17* (2009), #4767.

[180] Eichfelder, G. and Gebhardt, M. “Local specific absorption rate control for parallel transmission by virtual observation points”. In: *Magn. Reson. Med.* 66 (2011), pp. 1468–1476.

[181] Christ, A. et al. “The Virtual Family–development of surface-based anatomical models of two adults and two children for dosimetric simulations”. In: *Phys. Med. Biol.* 55 (2010), N23–N38.

[182] Orzada, S., Maderwald, S., Poser, B. A., Bitz, A. K., Quick, H. H., and Ladd, M. E. “RF excitation using time interleaved acquisition of modes (TIAMO) to address B_1 inhomogeneity in high-field MRI”. In: *Magn. Reson. Med.* 64 (2010), pp. 327–333.

[183] Schmitter, S., Wu, X., Adriany, G., Auerbach, E. J., Uğurbil, K., and Van de Moortele, P.-F. “Cerebral TOF angiography at 7T: impact of B_1^+ shimming with a 16-channel transceiver array”. In: *Magn. Reson. Med.* 71 (2014), pp. 966–977.

[184] Tang, L., Hue, Y. K., and Ibrahim, T. S. “Studies of RF shimming techniques with minimization of RF power deposition and their associated temperature changes”. In: *Concepts Magn. Reson. Part B Magn. Reson. Eng.* 39 (2011), pp. 11–25.

[185] Metzger, G. J., Auerbach, E. J., Akgun, C., Simonson, J., Bi, X., Uğurbil, K., and Van de Moortele, P.-F. “Dynamically applied B_1^+ shimming solutions for non-contrast enhanced renal angiography at 7.0 Tesla”. In: *Magn. Reson. Med.* 69 (2013), pp. 114–126.

[186] Ibrahim, T.S. “Ultrahigh-field MRI whole-slice and localized RF field excitations using the same RF transmit array”. In: *IEEE Trans. Med. Imag.* 25 (2006), pp. 1341–1347.

[187] Kim, J., Krishnamurthy, N., Santini, T., Zhao, Y., Zhao, T., Ty Bae, K., and Ibrahim, T. S. “Experimental and numerical analysis of B_1^+ field and SAR with a new transmit array design for 7T breast MRI”. In: *J. Magn. Reson.* 269 (2016), pp. 55–64.

[188] Buckner, R. L., Krienen, F. M., Castellanos, A., Diaz, J. C., and Yeo, B. T. T. “The organization of the human cerebellum estimated by intrinsic functional connectivity”. In: *J. Neurophysiol.* 106 (2011), pp. 2322–2345.

[189] Diedrichsen, J., Balster, J.H., Falvell, J., Cussans, E., and Ramnani, N. “A probabilistic MR atlas of the human cerebellum”. In: *NeuroImage* 46 (2009), pp. 39–46.

[190] Rorden, C., Karnath, H. O., and Bonilha, L. “Improved lesion-symptom mapping”. In: *J. Cognitive. Neurosci* 19 (2007), pp. 1081–1088.

[191] Diedrichsen, J. and Shadmehr, R. “Detecting and adjusting for artifacts in fMRI time series data”. In: *NeuroImage* 27 (2005), pp. 624–634.

[192] Grootoonk, S., Hutton, C., Ashburner, J., Howseman, A. M., Josephs, O., Rees, G., Friston, K. J., and Turner, R. “Characterization and correction of interpolation effects in the realignment of fMRI time series”. In: *NeuroImage* 11 (2000), pp. 49–57.

[193] Stefanescu, M. R., Thürling, M., Maderwald, S., Wiestler, T., Ladd, M. E., Diedrichsen, J., and Timmann, D. “A 7T fMRI study of cerebellar activation in sequential finger movement tasks”. In: *Exp. Brain. Res.* 228 (2013), pp. 243–254.

[194] Thirion, B., Pinel, P., Mériaux, S., Roche, A., Dehaene, S., and Poline, J.-B. “Analysis of a large fMRI cohort: statistical and methodological issues for group analyses”. In: *NeuroImage* 35 (2007), pp. 105–120.

[195] Eklund, A., Nichols, T. E., and Knutsson, H. “Cluster failure: why fMRI inferences for spatial extent have inflated false-positive rates”. In: *PNAS* 113 (2016), pp. 7900–7905.

[196] Nichols, T. E. and Holmes, A. P. “Nonparametric permutation tests for functional neuroimaging: a primer with examples”. In: *Hum. Brain Mapp.* 15 (2001), pp. 1–25.

[197] Poser, B. A., Koopmans, P. J., Witzel, T., Wald, L. L., and Barth, M. “Three dimensional echo-planar imaging at 7 Tesla”. In: *NeuroImage* 51 (2010), pp. 261–266.

[198] Setsompop, K. et al. “Slice-Selective RF pulses for In-vivo B_1^+ Inhomogeneity Mitigation at 7 Tesla using Parallel RF Excitation with a 16-Element Coil”. In: *Magn. Reson. Med.* 60 (2008), pp. 1422–1432.

[199] Stefanescu, M. R., Dohnalek, M., Maderwald, S., Thürling, M., Minnerop, M., Beck, A., Schlamann, M., Diedrichsen, J., Ladd, M. E., and Timmann, D. “Structural and functional MRI abnormalities of cerebellar cortex and nuclei in SCA3, SCA6 and Friedreich’s ataxia”. In: *Brain* 138 (2015), pp. 1182–1197.

[200] Draganova, R., Pfaffenrot, V., Steiner, K. M., Göricke, S. L., Elangovan, N., Timmann, D., and Konczak, J. “Neurostructural changes and declining sensorimotor function due to cerebellarcortical degeneration”. In: *J. Neurophysiol.* 125 (2021), pp. 1735–1745.

[201] Triantafyllou, C., Hoge, R. D., Krueger, G., Wiggins, C. J., Potthast, A., Wiggins, G. C., and Wald, L. L. “Comparison of physiological

noise at 1.5 T, 3 T and 7 T and optimization of fMRI acquisition parameters". In: *NeuroImage* 26 (2005), pp. 243–250.

[202] Gonzales-Castillo, J., Roopchansingh, V., Bandettini, P. A., and Bodurka, J. "Physiological noise effects on the flip angle selection in BOLD fMRI". In: *NeuroImage* 54 (2011), pp. 2764–2778.

[203] Feinberg, D. A., Moeller, S., Smith, S. M., Auerbach, E., Ramanna, S., Glasser, M. F., Miller, K. L., Uğurbil, K., and Yacoub, E. "Multiplexed Echo Planar Imaging for Sub-Second Whole Brain FMRI and Fast Diffusion Imaging". In: *Plos One* 5 (2010).

[204] Guerin, B., Setsompop, K., Ye, H., Poser, B. A., Stenger, A. V., and Wald, L. L. "Design of parallel transmission pulses for simultaneous multislice with explicit control for peak power and local absorption rate". In: *Magn. Reson. Med.* 73 (2015), pp. 1946–1953.

[205] Guerin, B., Stockmann, J. P., Mehran, B., Torrado-Carvajal, A., Stenger, A. V., and Wald, L. L. "Robust time-shifted spoke pulse design in the presence of large B_0 variations with simultaneous reduction of through-plane dephasing, B_1^+ effects, and the specific absorption rate using parallel transmission". In: *Magn. Reson. Med.* 76 (2016), pp. 540–554.

[206] Davids, M., Guerin, B., Wald, L. L., and Schad, L. R. "B0-robust slice selective excitation for ultra-high field with flip-angle mitigation using parallel transmission". In: *Proc. Int. Soc. Magn. Reson. Med. 24* (2016), #1015.

[207] Pfeuffer, J., Van De Moortele, P.-F., Yacoub, E., Shmuel, A., Adriany, G., Andersen, P., Merkle, H., Garwood, M., Uğurbil, K., and Hu, X. "Zoomed Functional Imaging in the Human Brain at 7 Tesla with Simultaneous High Spatial and High Temporal Resolution". In: *NeuroImage* 17 (2002), pp. 272–286.

[208] Heidemann, R., Ivanov, D., Trampel, R., Fasano, F., Meyer, H., Pfeuffer, J., and Turner, R. "Isotropic submillimeter fMRI in the human brain at 7 T: Combining reduced field-of-view imaging and partially parallel acquisitions". In: *Magn. Reson. Med.* 68 (2012), pp. 1506–1516.

[209] Duong, T. Q., Yacoub, E., Adriany, G., Hu, X., Uğurbil, K., and Kim, S.-G. "Microvascular BOLD contribution at 4 and 7 T in the human brain: Gradient-echo and spin-echo fMRI with suppression of blood effects". In: *Magn. Reson. Med.* 16 (2003), pp. 1062–1067.

[210] Feinberg, D. A., Hoenninger, J. C., Crooks, L. E., Kaufman, L., Watts, J. C., and Arakaw, M. "Inner volume MR imaging: technical concepts and their application". In: *Radiology* 156 (1985), pp. 743–747.

[211] Poser, B. A., Kaas, A. L., Wiggins, C. J., Uludağ, K., and Tse, D. H. Y. "Dual region-selective spiral pTX excitation for digit mapping fMRI in motor cortex and cerebellum". In: *Proc. Int. Soc. Magn. Reson. Med. 25* (2017), #0588.

[212] Mooiweer, R., Sbrizzi, A., Raaijmakers, A. J. E., van den Berg, C. A. T., Luijten, P. R., and Hoogduin, H. "Combining a Reduced Field of Excitation With SENSE-Based Parallel Imaging for Maximum Imaging Efficiency". In: *Magn. Reson. Med.* 78 (2017), pp. 88–96.

[213] van der Zwaag, W., Reynaud, O., Narsude, M., Gillichan, D., and Marques, J. P. "High spatio-temporal resolution in functional MRI with 3D echo planar imaging using cylindrical excitation and a CAIPIRINHA undersampling pattern". In: *Magn. Reson. Med.* 79 (2018), pp. 2589–2596.

[214] Samsonov, A. A., Kholmovski, E. G., Parker, D. L., and Johnson, C. R. “POCSENSE: POCS-based reconstruction for sensitivity encoded magnetic resonance imaging”. In: *Magn. Reson. Med.* 52 (2004), pp. 1397–1406.

[215] Bydder, M. and Robson, M. D. “Partial Fourier partially parallel imaging”. In: *Magn. Reson. Med.* 53 (2005), pp. 1393–1401.

[216] Blaimer, M., Heim, M., Neumann, D., Jakob, P. M., Kannengiesser, S., and Breuer, F. A. “Comparison of Phase-Constrained Parallel MRI Approaches: Analogies and Differences”. In: *Magn. Reson. Med.* 75 (2016), pp. 1086–1099.

[217] Blaimer, M., Gutberlet, M., Kellman, P., Breuer, F. A., Köstler, H., and Griswold, M. A. “Virtual Coil Concept for Improved Parallel MRI Employing Conjugate Symmetric Signals”. In: *Magn. Reson. Med.* 61 (2009), pp. 93–102.

[218] Blaimer, M., Breuer, F. A., Seiberlich, N., Mueller, M. F., Heidemann, R. M., Jellus, V., Wiggins, G., Wald, L. L., Griswold, M. A., and Jakob, P. M. “Accelerated volumetric MRI with a SENSE/GRAPPA combination”. In: *Magn. Reson. Med.* 24 (2006), pp. 444–450.

[219] Setsompop, K., Gagoski, B. A., Polimeni, J. R., Witzel, T., Wedeen, V. J., and Wald, L. L. “Blipped-controlled aliasing in parallel imaging for simultaneous multislice echo planar imaging with reduced g-factor penalty”. In: *Magn. Reson. Med.* 67 (2012), pp. 1210–1224.

[220] Breuer, F. A., Blaimer, M., Mueller, M. F., Seiberlich, N., Heidemann, R. M., Griswold, M. A., and Jakob, P. M. “Controlled Aliasing in Volumetric Parallel Imaging (2D CAIPIRINHA)”. In: *Magn. Reson. Med.* 55 (2006), pp. 549–556.

[221] Zahneisen, B., Ernst, T., and Poser, B. A. “SENSE and Simultaneous Multislice Imaging”. In: *Magn. Reson. Med.* 74 (2015), pp. 1356–1362.

[222] Schneider, J. T., Blaimer, M., and Ullmann, P. “Tailoring the image background phase by spatially selective excitation for improved parallel imaging reconstruction performance”. In: *Proc. Int. Soc. Magn. Reson. Med. 20* (20012), #516.

[223] Kettinger, A. O., Kannengiesser, S. A. R., Breuer, F. A., Vidnyanszky, Z., and Blaimer, M. “Controlling the Object Phase for g-Factor Reduction in Phase-Constrained Parallel MRI Using Spatially Selective RF Pulses”. In: *Magn. Reson. Med.* 79 (2018), pp. 2113–2125.

[224] Pipe, J. G. and Zwart, N. R. “Spiral Trajectory Design: A Flexible Numerical Algorithm and Base Analytical Equations”. In: *Magn. Reson. Med.* 71 (2014), pp. 278–285.

[225] Yushkevich, P. A., Piven, J., Hazlett, H. C., Smith, R. G., Ho, S., Gee, J. C., and Gerig, G. “User-guided 3D active contour segmentation of anatomical structures: Significantly improved efficiency and reliability”. In: *NeuroImage* 31 (2006), pp. 1116–1128.

[226] Sbrizzi, A., Hoogduin, H., Lagendijk, J. J., Luijten, P., Sleijpen, G. L. G., and van den Berg, C. A. T. “Time Efficient Design of Multi dimensional RF Pulses: Application of a Multi shift CGLS Algorithm”. In: *Magn. Reson. Med.* 66 (2011), pp. 879–885.

[227] Blaimer, M., Jakob, P. M., and Breuer, F. A. “Regularization Method for Phase-Constrained Parallel MRI”. In: *Magn. Reson. Med.* 72 (2014), pp. 166–171.

[228] Kettinger, A. O., Setsompop, K., Kannengiesser, S. A. R., Breuer, F. A., Vidnyanszky, Z., and Blaimer, M. “Full utilization of conjugate symmetry: combining virtual conjugate coil reconstruction with partial Fourier imaging for g-factor reduction in accelerated MRI”. In: *Magn. Reson. Med.* 82 (2019), pp. 1073–1090.

[229] Robson, A. M., Grant, A. K., Madhuranthakam, A. J., Lattanzi, R., Sodickson, D. K., and McKinzie, C. A. “Comprehensive Quantification of Signal-to-Noise Ratio and g-Factor for Image-Based and k-Space-Based Parallel Imaging Reconstructions”. In: *Magn. Reson. Med.* 60 (2008), pp. 895–907.

[230] Uecker, M., Lai, P., Murphy, M. J., Virtue, P., Elad, M., Pauly, J. M., Vasanawala, S. S., and Lustig, M. “ESPIRiT—An Eigenvalue Approach to Autocalibrating Parallel MRI: Where SENSE Meets GRAPPA”. In: *Magn. Reson. Med.* 71 (2014), pp. 990–1001.

[231] Tse, D. H. Y., Wiggins, C. J., and Poser, B. A. “Estimating and Eliminating the Excitation Errors in Bipolar Gradient Composite Excitations Caused by Radiofrequency-Gradient Delay: Example of Bipolar Spokes Pulses in Parallel Transmission”. In: *Magn. Reson. Med.* 78 (2018), pp. 1883–1890.

[232] Gras, V., Vignaud, A., Amadon, A., Le Bahin, D., and Boulant, N. “Universal pulses: A new concept for calibration-free parallel transmission”. In: *Magn. Reson. Med.* 77 (2017), pp. 635–643.

[233] Polimeni, J. R., Renvall, V., Zaretskaya, N., and Fischl, B. “Analysis strategies for high-resolution UHF-fMRI data”. In: *NeuroImage* 168 (2018), pp. 296–320.

[234] Finn, E. S., Huber, L., Jangraw, D. C., Molfese, P. J., and Bandettini, P. A. “Layer-dependent activity in human prefrontal cortex during working memory”. In: *Nat. Neurosci.* 22 (2019), pp. 1687–1695.

[235] Davids, M., Schad, L. R., Wald, L. L., and Guérin, B. "Fast Three-Dimensional Inner Volume Excitations Using Parallel Transmission and Optimized k-Space Trajectories". In: *Magn. Reson. Med.* 76 (2016), pp. 1170–1182.

[236] Malik, S. J. and Hajnal, J. V. "Phase Relaxed Localized Excitation Pulses for Inner Volume Fast Spin Echo Imaging". In: *Magn. Reson. Med.* 76 (2016), pp. 848–861.

[237] Rietsch, S. H. G. et al. "A 32-channel transmit/receive radiofrequency head coil for 7T UHF MR". In: *Proc. Int. Soc. Magn. Reson. Med. 27* (2019), #1486.

[238] Pfaffenrot, V., Voelker, M. N., Kashyap, S., and Koopmans, P. J. "Laminar fMRI using T_2-prepared multi-echo FLASH". In: *NeuroImage* 236 (2021).

[239] Kim, D., Duong, S. Q., and Kim, S. "High-resolution mapping of iso-orientation column by fMRI". In: *Nat. Neurosci.* 3 (2000), pp. 1–6.

[240] Yacoub, E., Shmuel, A., Logothetis, N., and Uğurbil, K. "Robust detection of ocular dominance columns in humans using Hahn Spin Echo BOLD functional MRI at 7 Tesla". In: *NeuroImage* 37 (2007), pp. 1161–1177.

[241] Yacoub, E. and Harel, N. "High-field fMRI unveils orientation columns in humans". In: *PNAS* 105 (2008), pp. 10607–10612.

[242] De Martino, F., Moerel, M., Uğurbil, K., Goebel, R., Yacoub, E., and Formisano, E. "Frequency preference and attention effects across cortical depths in the human primary auditory cortex". In: *PNAS* 112 (2015), pp. 16036–16041.

[243] Huber, L., Handwerker, D. A., Goense, D.C., Poser, B. A., and Bandettini, P. A. “High-Resolution CBV-fMRI Allows Mapping of Laminar Activity and Connectivity of Cortical Input and Output in Human M1”. In: *Neuron* 96 (2017), pp. 1253–1263.

[244] Koopmans, P. J., Barth, M., and Norris, D. G. “Layer-Specific BOLD Activation in Human V1”. In: *Hum. Brain. Mapp.* 31 (2017), pp. 1297–1304.

[245] Muckli, L., De Martino, F., Vizioli, L., Goebel, R., and Yacoub, E. “Contextual Feedback to Superficial Layers of V1”. In: *Curr. Biol.* 25 (2015), pp. 2690–2695.

[246] Polimeni, J. R., Fischl, B., Greve, D. N., and Wald, L. L. “Laminar analysis of 7T BOLD using an imposed spatial activation pattern in human V1”. In: *NeuroImage* 52 (2010), pp. 1334–1346.

[247] Siero, J .C. W., Petridou, N., Hoogduin, H., Luijten, P. R., and Ramsey, N. F. “Cortical depth-dependent temporal dynamics of the BOLD response in the human brain”. In: *J. Cereb. Blood Flow Metab.* 31 (2011), pp. 1999–2008.

[248] Kok, P., Bains, L. J., Van Mourik, T., Norris, D. G., and De Lange, F. P. “Selective Activation of the Deep Layers of the Human Primary Visual Cortex by Top-Down Feedback”. In: *Curr. Biol.* 26 (2011), pp. 371–376.

[249] Lawrence, S. J. D., Formisano, E., Muckli, L., and De Lange, F. P. “Laminar fMRI: Applications for cognitive neuroscience”. In: *NeuroImage* 197 (2017), pp. 785–791.

[250] Stephan, K. E., Petzscher, F. H., Kasper, L., Bayer, J., Wellstein, K. V., Stefanics, G., Pruessmann, K. P., and Heinzle, J. “Laminar

fMRI and computational theories of brain function". In: *NeuroImage* 197 (2019), pp. 699–706.

[251] Grgac, K., Li, W., Huang, A., Qin, Q., and van Zijl, P. C. M. "Transverse water relaxation in whole blood and erythrocytes at 3T, 7T, 9.4T, 11.7T and 16.4T; determination of intracellular hemoglobin and extracellular albumin relaxivities". In: *Magn. Reson. Med.* 38 (2017), pp. 234–249.

[252] Khajehim, M. and Nasiraei Moghaddam, A. "Investigating the spatial specificity of S2-SSFP fMRI: A Monte Carlo simulation approach". In: *Magn. Reson. Imaging* 37 (2017), pp. 282–289.

[253] Turner, R. "How much codex can a vein drain? Downstream dilution of activation-related cerebral blood oxygenation changes". In: *NeuroImage* 16 (2002), pp. 1062–1067.

[254] Menon, R. S., Ogawa, S., Tank, D. W., and Uğurbil, K. "4 Tesla gradient recalled echo characteristics of photic stimulation-induced signal changes in the human primary visual cortex". In: *Magn. Reson. Med.* 30 (1993), pp. 380–386.

[255] Markuerkiaga, I., Barth, M., and Norris, D. G. "A cortical vascular model for examining the specificity of the laminar BOLD signal". In: *NeuroImage* 132 (2016), pp. 491–498.

[256] Pflugfelder, D., Vahedipour, K., Uludağ, K., Shah, N. J., and Stöcker, T. "On the numerically predicted spatial BOLD fMRI specificity for spin echo sequences". In: *Magn. Reson. Med.* 29 (2011), pp. 1195–1204.

[257] Budde, J., Shajan, G., Zeitsev, M., Scheffler, K., and Pohmann, R. "Functional MRI in human subjects with gradient-echo and spin-echo EPI at 9.4 T". In: *Magn. Reson. Med.* 71 (2014), pp. 209–218.

[258] Harmer, J., Sanchez-Panchuelo, R. M., Bowtell, R., and Fancis, S. T. “Spatial location and strength of BOLD activation in high-spatial-resolution fMRI of the motor cortex: A comparison of spin echo and gradient echo fMRI at 7T”. In: *NMR Biomed.* 25 (2012), pp. 717–725.

[259] Koopmans, P. J., Barth, M., Orzada, S., and Norris, D. G. “Multi-echo fMRI of the cortical laminae in humans at 7 T”. In: *NeuroImage* 56 (2011), pp. 1276–1285.

[260] Yacoub, E., Van De Moortele, P.-F., Shmuel, A., and Uğurbil, K. “Signal and noise characteristics of Hahn SE and GE BOLD fMRI at 7 T in humans”. In: *NeuroImage* 24 (2005), pp. 738–750.

[261] Hua, J., Qin, Q., Van Zijl, P. C. M., Pekar, J. J., and Jones, C. K. “Whole-brain three-dimensional T2-weighted BOLD functional magnetic resonance imaging at 7 Tesla”. In: *Magn. Reson. Med.* 72 (2006), pp. 1530–1540.

[262] Kupče, Ē. and Freeman, R. “Adiabatic Pulses for Wideband Inversion and Broadband Decoupling”. In: *J. Magn. Reson. Ser. A* 115 (1995), pp. 273–276.

[263] Bendall, M. R. and Pegg, D. T. “Uniform sample excitation with surface coils for in vivo spectroscopy by adiabatic rapid half passage”. In: *J. Magn. Reson.* 67 (1986), pp. 376–381.

[264] O’Dell, D. “The WURST kind of pulses in solid-state NMR”. In: *Solid State Nucl. Magn. Reson.* 55 (2013), pp. 28–41.

[265] Coristine, A. J., Heeswijk, R. B., and Van Stuber, M. “Fat Signal Suppression for Coronary MRA at 3T Using a Water-Selective Adiabatic T_2-Preparation Technique”. In: *Magn. Reson. Med.* 769 (2014), pp. 763–769.

[266] Patel, M. R., Klufas, R. A., Alberico, R. A., and Edelman, R. R. "Half-fourier acquisition single-shot turbo spin-echo (HASTE) MR: Comparison with fast spin-echo MR in diseases of the brain". In: *Am. J. Neuroradiol.* 18 (1997), pp. 1635–1640.

[267] Madelin, G., Oesingmann, N., and M.Inglese. "Double inversion recovery MRI with fat suppression at 7 Tesla: Initial experience". In: *J.Neuroimaging* 20 (2010), pp. 87–92.

[268] Brainard, D. H. "The Psychophysics Toolbox". In: *Spat.Vis.* (1997).

[269] Pelli, D. G. "The VideoToolbox software for visual psychophysics: Transforming numbers into movies". In: *Spat. Vis.* (1997).

[270] Majumdar, S. and Gore, J. C. "Studies of diffusion in random fields produced by variations in susceptibility". In: *J. Magn. Reson.* 78 (1988), pp. 41–55.

[271] Bartha, R., Micheali, S., Merkle, H., Adriany, G., Andersen, P., Chen, W., Uğurbil, K., and Garwood, M. "In vivo $1H_2O$ $T_2^{\dagger}$ measurement in the human occipital lobe at 4T and 7T by Carr-Purcell MRI: Detection of microscopic susceptibility contrast". In: *Magn. Reson. Med.* 47 (1988), pp. 742–750.

[272] Sotiropoulos, S. N. et al. "Effects of image reconstruction on fiber orientation mapping from multichannel diffusion MRI: Reducing the noise floor using SENSE". In: *Magn. Reson. Med.* 70 (2013), pp. 1682–1689.

[273] Fischl, B. "FreeSurfer". In: *NeuroImage* 62 (2012), pp. 774–781.

[274] Huber, L. et al. "LayNii: A software suite for layer-fMRI". In: *NeuroImage* 237 (2021).

[275] Stoewer, S., Goense, J., Keliris, G. A., Bartels, A., Logothetis, N. K., Duncan, J., and Sigala, N. “An analysis approach for high-field fMRI data from awake non-human primates”. In: *PloS One* 7 (2012).

[276] Kiselev, V. G. and Posse, S. “Analytical model of susceptibility-induced MR signal dephasing: Effect of diffusion in a microvascular network”. In: *Magn. Reson. Med.* 41 (1999), pp. 499–509.

[277] Lu, H. and Van Zijl, P. C. M. “Experimental measurement of extravascular parenchymal BOLD effects and tissue oxygen extraction fractions using multi-echo VASO fMRI at 1.5 and 3.0 T”. In: *Magn. Reson. Med.* 53 (2005), pp. 808–816.

[278] Markuerkiaga, I. “On the laminar specificity of BOLD-based cortical activation profiles”. PhD thesis. Radboud University Nijmegen, 2019.

[279] Krishnamurthy, L. C., Liu, P., Xu, F., Uh, J., Dimitrov, I., and Lu, H. “Dependence of blood T_2 on oxygenation at 7 T: In vitro calibration and in vivo application”. In: *Magn. Reson. Med.* 71 (2014), pp. 2035–2042.

[280] Spijkerman, J. M., Petersen, E. T., Hendrikse, J., Luijten, P., and Zwanenburg, J. J. M. “T_2 mapping of cerebrospinal fluid: 3 T versus 7 T”. In: *Magn. Reson. Mater. Phys. Biol. Med.* 31 (2018), pp. 415–424.

[281] Ronney, W. D., Johnson, G., Li, X., Cohen, E.R., Kim, S.-G., Uğurbil, K., and Springer Jr., C. S. “Magnetic Field and Tissue Dependencies of Human Brain Longitudinal ^1H_2O”. In: *Magn. Reson. Med.* 57 (2007), pp. 308–318.

[282] Ernst, R. R. and Anderson, W. A. “Application of fourier transform spectroscopy to magnetic resonance”. In: *Rev. Sci. Instrum.* 37 (1966), pp. 93–102.

[283] Wyss, M., Kirchner, T., Ringenbach, A., Pruessmann, K., and Henning, A. “Relaxation Parameter Mapping Adapted for 7T and Validation against Optimized Single Voxel MRS”. In: *Proc. Int. Soc. Magn. Reson. Med.* 26 (2013), p. 47.

[284] Koopmans, P. J., Manniesing, R., Niessen, W. J., Viergever, M. A., and Barth, M. “MR venography of the human brain using susceptibility weighted imaging at very high field strength”. In: *Magn. Reson. Mater. Physics, Biol. Med.* 21 (2008), pp. 149–158.

[285] Ivanov, D. et al. “In vivo estimation of the transverse relaxation time dependence of blood on oxygenations at 7 Tesla”. In: *Proc. Int. Soc. Magn. Reson. Med.* 21 (2013), p. 21.

[286] Silvennoinen, M. J., Clingman, C. S., Golay, X., Kauppinen, R. A., and Van Zijl, P. C. M. “Comparison of the dependence of blood R_2 and R_2^* on oxygen saturation at 1.5 and 4.7 Tesla”. In: *Magn. Reson. Med.* 49 (2003), pp. 47–60.

[287] Lee, S. P., Silva, A. C., Uğurbil, K., and Kim, S.-G. “Diffusion-weighted spin-echo fMRI at 9.4 T: Microvascular/tissue contribution to BOLD signal changes”. In: *Magn. Reson. Med.* 42 (1999), pp. 919–928.

[288] Lin, A. L., Qin, Q., Zhao, X., and Duong, T. Q. “Blood longitudinal (T_1) and transverse (T_2) relaxation time constants at 11.7 Tesla”. In: *Magn. Reson. Mater. Physics, Biol. Med.* 25 (2012), pp. 245–249.

[289] Li, T. Q., van Gelderen, P., Merkle, H., Talagala, L., Koretsky, A. P., and Duyn, J. “Extensive heterogeneity in white matter intensity in high-resolution T_2^*-weighted MRI of the human brain at 7.0 T”. In: *NeuroImage* 32 (2006), pp. 1032–1040.

[290] Yacoub, E., Duong, T. Q., Van De Moortele, P.-F., Lindquist, M., Adiany, G., Kim, S., and Hu, X. “Spin-Echo fMRI in Humans Using High Spatial Resolutions and High Magnetic Fields”. In: *Magn. Reson. Med.* 49 (2003), pp. 655–664.

[291] Pérez-Rodas, M., Pohmann, R., Scheffler, K., and Heule, R. “Intravascular BOLD signal characterization of balanced SSFP experiments in human blood at high to ultrahigh fields”. In: *Magn. Reson. Med.* 85 (2021), pp. 2055–2068.

[292] Helenius, J., Soinne, L., Perkiö, J., Salonen, O., Kangasmäki, A., Kaste, M., Carano, R. A. D., Aronen, H. J., and Tatlisumak, T. “Diffusion-weighted MR imaging in normal human brains in various age groups”. In: *Am. J. Neuroradiol.* 23 (2002), pp. 194–199.

[293] Le Bahin, D. and Johansen-Berg, H. “Diffusion MRI at 25: Exploring brain tissue structure and function”. In: *NeuroImage* 61 (2012), pp. 324–341.

[294] Fracasso, A., Luiten, P. R., Dumoulin, S. O., and Petridou, N. “Laminar imaging of positive and negative BOLD in human visual cortex at 7 T”. In: *NeuroImage* 164 (2018), pp. 100–111.

[295] Kashyap, S., Ivanov, D., Havlicek, M., Sengupta, S., Poser, B. A., and Uludağ, K. “Resolving laminar activation in human V1 using ultra-high spatial resolution fMRI at 7T”. In: *Nature Sci. Rep.* 8 (2018), pp. 1–11.

[296] Mugler, J. P., Epstein, F. H., and Brookeman, J. R. “Shaping the Signal Response during the Approach to Steady State in Three-Dimensional Magnetization-Prepared Rapid Gradient-Echo Imaging Using Variable Flip Angles”. In: *Magn. Reson. Med* 28 (1992), pp. 165–185.

[297] Gai, N. D., Talagala, S. L., and Butman, J. A. “Whole-brain cerebral blood flow mapping using 3D echo planar imaging and pulsed arterial tagging”. In: *J. Magn. Reson. Imaging* 33 (2011), pp. 287–295.

[298] Huber, L., Ivanov, D., Handwerker, D. A., Marrett, S., Guidi, M., Uludağ, K., Bandettini, P. A., and Poser, B. A. “Techniques for blood volume fMRI with VASO: From low-resolution mapping towards sub-millimeter layer-dependent applications”. In: *NeuroImage* 164 (2018), pp. 131–143.

[299] Bilgic, B., Kim, T. H., Liao, C., Manhard, M. K., Wald, L. L., Haldar, J. P., and Setsompop, K. “Improving parallel imaging by jointly reconstructing multi-contrast data”. In: *Magn. Reson. Med.* 80 (2018), pp. 619–632.

[300] Breuer, F. A., Kellman, P., Griswold, M. A., and Jakob, P. M. “Dynamic Autocalibrated Parallel Imaging Using Temporal GRAPPA (TGRAPPA)”. In: *Magn. Reson. Med.* 53 (2005), pp. 981–985.

[301] Beckmann, C. F. and Smith, S. M. “Probabilistic independent component analysis for functional magnetic resonance imaging”. In: *IEEE Trans. Med. Imaging* 230 (2004), pp. 137–152.

[302] Salimi-Khorshidi, G., Douaud, G., Beckmann, C. F., Glasser, M. F., Griffanti, L., and Smith, S. M. “Automatic denoising of functional MRI data: Combining independent component analysis and hierarchical fusion of classifiers”. In: *NeuroImage* 90 (2014), pp. 449–468.

[303] Gonzalez-Gastillo, J., Panwar, P., Buchanan, L. C., Handwerker, C. Caballero-Gaudes D. A., Jangraw, D. C., Zachariou, V., Inati, S., Roopchansingh, V., Derbyshire, J. A., and Bandettini, P. A. “Evaluation of multi-echo ICA denoising for task based fMRI

studies: Block designs, rapid event-related designs, and cardiac-gated fMRI". In: *NeuroImage* 141 (2016), pp. 452–468.

[304] Cauley, S. F., Polimeni, J. R., Bhat, H., Wald, L. L., and Setsompop, K. "Interslice Leakage Artifact Reduction Technique for Simultaneous Multislice Acquisitions". In: *Magn. Reson. Med.* 72 (2014), pp. 93–102.

[305] Dong, Z., Wang, F., Reese, T.G., Bilgic, B., and Setsompop, K. "Echo planar time-resolved imaging with subspace reconstruction and optimized spatiotemporal encoding". In: *Magn. Reson. Med.* 84 (2020), pp. 2442–2455.

[306] Wang, F., Dong, Z., Wald, L. L., Polimeni, J. R., and Setsompop, K. "Simultaneous pure T_2 and varying T_2-weighted BOLD fMRI using Echo Planar Time-resolved Imaging for mapping cortical-depth dependent responses". In: *NeuroImage* 245 (2021).

[308] Huber, L. et al. "Sub-millimeter fMRI reveals multiple topographical digit representations that form action maps in human motor cortex". In: *NeuroImage* 208 (2020).

[309] Kashyap, S., Ivanov, D., Havlicek, M., Huber, L., Poser, B. A., and Uludağ, K. "Sub-millimetre resolution laminar fMRI using Arterial Spin Labelling in humans at 7 T". In: *PloS One* 16 (2021), pp. 1–23.

[310] Scheeringa, R., Bonnefond, M., Van Mourik, T., Jensen, O., Norris, D. G., and Koopmans, P. J. "Relating neural oscillations to laminar fMRI connectivity". In: *bioRxiv* (2020).

[311] Wu, P. Y., Chu, Y. H., Lin, J. F. L., Kuo, W. J., and Lin, F. H. "Feature-dependent intrinsic functional connectivity across cortical depths in the human auditory cortex". In: *Nature Sci. Rep.* 8 (2018), pp. 1–14.

[312] Hua, J., Donahue, M. J., Zhao, J. M., Grgac, K., Huang, A. J., Zhou, K., and van Zijl, P. C. M. "Magnetization transfer enhanced Vascular-space-occupancy (MT-VASO) functional MRI". In: *Magn. Reson. Med.* 61 (2009), pp. 944–951.

[313] Hua, J., Jones, C. K., Qin, Q., and Van Zijl, P. C. M. "Implementation of Vascular-space-occupancy (VASO) MRI at 7 Tesla". In: *Magn. Reson. Med.* 69 (2013), pp. 1003–1013.

[314] Stefanovic, B. and Pike, G. B. "Venous refocusing for volume estimation: VERVE functional magnetic resonance imaging". In: *Magn. Reson. Med.* 53 (2005), pp. 339–347.

[315] Jin, T. and Kim, S. G. "Cortical layer-dependent dynamic blood oxygenation, cerebral blood flow and cerebral blood volume responses during visual stimulation". In: *NeuroImage* 43 (2008), pp. 1–9.

[316] Chai, Y., Li, L., Huber, L., Poser, B. A., and Bandettini, P. A. "Integrated VASO and perfusion contrast: A new tool for laminar functional MRI". In: *NeuroImage* 207 (2020).

[317] Schulz, J., Fazal, Z., Metere, R., Marques, J. P., and Norris, D. G. "Arterial blood contrast (ABC) enabled by magnetization transfer (MT): A novel MRI technique for enhancing the measurement of brain activation changes". In: *bioRxiv* (2020).

[318] Zhang, R., Cox, R. W., and Hyde, J. S. "The effect of magnetization transfer on functional MRI signals". In: *Magn. Reson. Med.* 38 (1997), pp. 187–192.

[319] Chung, S., Kim, D., Breton, E., and Axel, L. "Rapid B_1^+ mapping using a preconditioning RF pulse with TurboFLASH readout MRI". In: *Magn. Reson. Med.* 64 (2010), pp. 439–446.

[320] Kober, J. P. Marques andT., Krueger, G., van der Zwaag, W., Van de Moortele, P. F., and Gruetter, R. “MP2RAGE, a self bias-field corrected sequence for improved segmentation and T_1-mapping at high field”. In: *NeuroImage* 49 (2010), pp. 1271–1281.

[321] Gallichan, D., Marques, J. P., and Gruetter, R. “Retrospective correction of involuntary microscopic head movement using highly accelerated fat image navigators (3D FatNavs) at 7T”. In: *Magn. Reson. Med.* 75 (2016), pp. 1030–1039.

[322] Dortch, R. D., Moore, J., Li, K., Jankiewicz, M., Gochberg, D. F., Hirtle, J. A., Gore, J. C., and Smith, S. A. “Quantitative magnetization transfer imaging of human brain at 7T”. In: *NeuroImage* 64 (2013), pp. 640–649.

[323] Garcia, M., Gloor, M., Wetzel, S. G., Radue, E. W., Scheffler, K., and Bieri, O. “Characterization of normal appearing brain structures using high-resolution quantitative magnetization transfer steady-state free precession imaging”. In: *NeuroImage* 52 (2010), pp. 532–537.

[324] Sled, J. G., Levesque, I., Santos, A. C., Francis, S. J., Narayanan, S., Brass, S. D., Arnold, D. L., and Pike, G. B. “Regional Variations in Normal Brain Shown by Quantitative Magnetization Transfer Imaging”. In: *Magn. Reson. Med.* 51 (2004), pp. 299–303.

[325] Yarnykh, V. L. and Yuan, C. “Cross-relaxation imaging reveals detailed anatomy of white matter fiber tracts in the human brain”. In: *NeuroImage* 23 (2004), pp. 409–424.

[326] Korb, J. P. and Bryant, R. G. “Magnetic field dependence of proton spin-lattice relaxation times”. In: *Magn. Reson. Med.* 48 (2002), pp. 21–26.

[327] Mezer, A., Rokem, A., Berman, S., Hastie, T., and Wandell, B. A. "Evaluating quantitative proton-density-mapping methods". In: *Hum. Brain Mapp.* 37 (2016), pp. 3623–3635.

[328] Karakuzu, A. et al. "qMRLab: Quantitative MRI analysis, under one umbrella". In: *J. Open Source Softw.* 5 (2020).

[329] Rane, S. D. and Gore, J. C. "Measurement of T1 of human arterial and venous blood at 7T". In: *Magn. Reson. Imaging* 31 (2013), pp. 477–479.

[330] Mougin, O. E., Cemence, M., Peters, A., Pitiot, A., and Gowland, P. "High-resolution imaging of magnetisation transfer and nuclear Overhauser effect in the human visual cortex at 7 T". In: *NMR Biomed.* 26 (2013), pp. 1508–1517.

[331] Shah, S. M., Mougin, O. E., Carradus, A. J., Geades, N., Dury, R., Morley, W., and Gowland, P. A. "The z-spectrum from human blood at 7 T". In: *NeuroImage* 167 (2018), pp. 31–40.

[332] Jin, T., Wang, P., Zong, X., and Kim, S. G. "MR imaging of the amide-proton transfer effect and the pH-insensitive nuclear overhauser effect at 9.4 T". In: *Magn. Reson. Med.* 69 (2013), pp. 760–770.

[333] Graedel, N. N., Kasper, L., Engel, M., Nussbaum, J., Wilm, B. J., Pruessmann, K. P., and Vannsjo, S. J. "Feasibility of spiral fMRI based on an LTI gradient model". In: *NeuroImage* 245 (2021).

[334] Leitão, D. et al. "Parallel transmit pulse design for saturation homogeneity (PUSH) for magnetization transfer imaging at 7T". In: *Magn. Reson. Med.* (2022), pp. 1–15.

[335] Olsson, H., Andersen, M., Wirestam, R., and Helms, G. "Mapping magnetization transfer saturation (MTsat) in human brain at 7T:

Protocol optimization under specific absorption rate constraints". In: *Magn. Reson. Med.* 86 (2021), pp. 2562–2576.

[336] Hua, J., Jones, C. J., Blakeley, J., Smith, S. A., Van Zijl, P. M. C., and Zhou, J. "Quantitative description of the asymmetry in magnetization transfer effects around the water resonance in the human brain". In: *Magn. Reson. Med.* 58 (2007), pp. 786–783.

[337] Pekar, J., Jezzard, P., Roberts, D. A., Leigh, J. S., Frank, J. A., and McLaughlin, A.G. "Perfusion imaging with compensation for asymmetric magnetization transfer effects". In: *Magn. Reson. Med.* 35 (1996), pp. 70–79.

[338] De Martino, F., Zimmermann, J., Muckli, L., Uğurbil, K., Yacoub, E., and Goebel, R. "Cortical Depth Dependent Functional Responses in Humans at 7T: Improved Specificity with 3D GRASE". In: *PloS One* 8 (2013), pp. 30–32.

[339] Kemper, V. G., De Martino, F., Vu, A. T., Poser, B. A., Feinberg, D. A., Goebel, R., and Yacoub, E. "Sub-millimeter T_2 weighted fMRI at 7 T: Comparison of 3D-GRASE and 2D SE-EPI". In: *Front. Neurosci.* 9 (2015), pp. 1–14.

[340] Scheffler, K., Engelmann, J., and Heule, R. "BOLD sensitivity and vessel size specificity along CPMG and GRASE echo trains". In: *Magn. Reson. Med.* 86 (2021), pp. 2076–2083.

[341] Annese, J., Pitiot, A., Dinov, I. D., and Toga, A. W. "A myelo-architectonic method for the structural classification of cortical areas". In: *NeuroImage* 21 (2004), pp. 15–26.

[342] Huber, Laurentius. *layer fMRI blog. Category: layer-fMRI papers*. Last checked: 14.03.2022. URL: `https://layerfmri.com/category/layer-fmri-papers/`.

[343] Kraff, O. and Quick, H. H. “Radiofrequency Coils for 7 Tesla MRI”. In: *Top. Magn. Reson. Imaging* 28 (2019), pp. 145–158.

[344] Massire, A., Mauconduit, F., Gras, V., Lapert, M., Naudin, M., Guillevin, R., Vignaud, A., and Boulant, N. “PASTEUR: Package of Anatomical Sequences Using Parallel Transmission Universal Pulses Now Available for MAGNETOM Terra”. In: *MAGNETOM Flash* 80 (2022), pp. 2–13.

[345] Nee, D. E., Brown, J. W., Askren, M. K., Berman, M. G., Demiralp, E., Krawitz, A., and Jonides, J. “A Meta-Analysis of Executive Components of Working Memory”. In: *Cereb. Cortex* 23 (2013), pp. 264–282.

[346] Shirvalkar, P., Veuthey, T. L., Dawes, H. E., and Chang, E. F. “Closed-Loop Deep Brain Stimulation for Refractory Chronic Pain”. In: *Front. Comput. Neurosci.* 12 (2018).

[347] Koiso, K., Dresbach, S., Wiggins, C. J., Gulban, O. F., Miyawaki, Y., Poser, B. A., and Huber, R. “Towards whole-brain layer-fMRI connectivity: methodological advancements for functional layer connectomics”. In: *ISMRM Workshop on Ultra-High Field MR* (2022).

[348] Gras, V., Pracht, E. D., Mauconduit, F., Le Bahin, D., Stöcker, T., and Boulant, N. “Robust nonadiabatic T_2 preparation using universal parallel-transmit k_T-point pulses for 3D FLAIR imaging at 7 T”. In: *Magn. Reson. Med.* 81 (2019), pp. 3202–3208.

[349] Orzada, S., Fiedler, T. M., Bitz, A. K., Ladd, M. E., and Quick, H. H. “Local SAR compression with overestimation control to reduce maximum relative SAR overestimation and improve multi-channel RF array performance”. In: *Magn. Reson. Mater. Phys. Biol. Med.* 34 (2021), pp. 153–163.

[350] Orzada, S., Fiedler, T. M., Quick, H. H., and Ladd, M. E. “Post-processing algorithms for specific absorption rate compression”. In: *Magn. Reson. Med.* 86 (2021), pp. 2853–2861.

[351] Engel, M., Kasper, L., Wilm, B., Dietrich, B., Vionnet, L., Hennel, F., Reber, J., and Pruessmann, K. P. “T-Hex: Tilted hexagonal grids for rapid 3D imaging”. In: *Magn. Reson. Med.* 85 (2021), pp. 2507–2523.

[352] Kasper, L. et al. “Advances in spiral fMRI: A high-resolution study with single-shot acquisition”. In: *NeuroImage* 246 (2022).

[353] van Mourik, T., Snoek, L., Knapen, T., and Norris, D. G. “Porcupine: A visual pipeline tool for neuroimaging analysis”. In: *PLoS Comput. Biol* (2018).

[354] Stanley, O. W., Kuurstra, A. B., Klassen, L. M., Menon, R. S., and Gati, J. S. “Effects of phase regression on high-resolution functional MRI of the primary visual cortex”. In: *NeuroImage* 227 (2021).

[355] Huang, P., Correia, M. M., Rua, C., Rodgers, C. T., Henson, R. N., and Carlin, J. D. “Correcting for Superficial Bias in 7T Gradient Echo fMRI”. In: *Front. Neurosci.* 15 (2021).

[356] Markuerkiaga, I., Marques, J. P., Gallagher, T. E., and Norris, D. G. “Estimation of laminar BOLD activation profiles using deconvolution with a physiological point spread function”. In: *J. Neurosci. Methods* 353 (2021).

[357] Uludağ, K. and Havlicek, M. “Determining laminar neuronal activity from BOLD fMRI using a generative model”. In: *Prog. Neurobiol.* 207 (2021).

[358] Heinzle, J., Koopmans, P. J., den Ouden, H. E., Raman, S., and Stephan, K. E. “A hemodynamic model for layered BOLD signals”. In: *NeuroImage* 125 (2016), pp. 556–570.

[359] Corbitt, P. T., Ulloa, A., and Horwitz, B. “Simulating laminar neuroimaging data for a visual delayed match-to-sample task”. In: *NeuroImage* 173 (2018), pp. 199–222.

[360] Lawrence, S. J. D., van Mourik, T., Kok, P., Koopmans, P. J., Norris, D. G., and de Lange, F. P. “Laminar organization of working memory signals in human visual cortex”. In: *Curr. Biol.* 28 (2018), pp. 3435–3440.

[361] Lawrence, S. J. D., Norris, D. G., and de Lange, F. P. “Dissociable laminar profiles of concurrent bottom-up and top-down modulation in the human visual cortex”. In: *Elife* 8 (2019).

Samenvatting

Laminar functional magnetic resonance imaging (fMRI) is een relatief jonge en nog steeds groeiende discipline voor het niet-invasief bestuderen van de werking van de menselijke hersenen. Laminaire fMRI is de sleutel tot het onthullen van de richting van de informatiestroom tussen verschillende regio's van de hersenen, en die richtingsgevoeligheid beidt unieke nieuwe kansen met betrekking tot de studie van hersen netwerken. Echter, tot op heden is laminaire fMRI met hoge spatio-temporele resolutie beperkt tot kleine blikvelden (field-of-views; FOVs) wat lastig is aangezien de netwerken informatie van gebieden intergreren die op grote afstand van elkaar liggen. Daarom is het hoofddoel van dit proefschrift het aanpakken van fundamentele problemen van laminaire fMRI: De verwerving van zuivere laminaire signalen van meerdere, ver van elkaar verwijderde gebieden van de menselijke hersenen.

Het feit dat veel hersengebieden in wijdverspreide netwerken zijn georganiseerd, vormt een uitdaging bij de acquisitie van hoge resolutie, d.w.z. sub-millimeter, laminaire data. Aan de criteria van een grote FOV en, simultaan, hoge spatio-temporele resoluties kan niet gemakkelijk worden voldaan omdat het beeldverwervingsproces bij MRI sequentieel is in plaats van parallel. Daarom was de eerste doelstelling van dit proefschrift het verkrijgen van een hoge spatio-temporele resolutie en een grote hersendekking tegelijkertijd. Daartoe moet worden voldaan aan de eisen van een hoge signaal-ruisverhouding (SNR) en radiofrequente (RF) spoelen met een grote FOV. Aan de eerste eis kan worden voldaan door te scannen in een ultrahoog veld (UHF) van 7 T, maar commerciële lokale zendspoelen die bij 7 T worden gebruikt vertonen, als gevolg van het RF inhomogeniteitsprobleem bij UHF,

gebrekkige dekking. Daarom werd in **hoofdstuk 3** de prestatie onderzocht van een 8-kanaals transmit (Tx) 15-kanaals receive (Rx) RF hoofdspoel voor MRI met hoge dekking, met de nadruk op fMRI van het cerebellum.

In de context van laminaire fMRI van een paar doelgebieden (ROI's) die een netwerk vertegenwoordigen, kan het meten van de rest van de hersenen worden beschouwd als verspilde moeite. De voordelen van het kunnen vormen van het transmissieveld om homogene excitatie van de gehele hersenen op UHF mogelijk te maken, zoals gedaan in hoofdstuk 3, kan ook worden gebruikt om het excitatieprofiel op maat te maken om alleen specifieke ROI's te bestrijken. In **hoofdstuk 4** werd een methode gepresenteerd die, in plaats van beeldvorming van de gehele FOV, alleen exciteert in de gebieden die van belang zijn met behulp van op maat gemaakte 2D RF pulsen. Deze ingezoomde multi-FOV beeldvorming vermindert de belasting op de beeldacquisitie en maakt een hogere versnelling mogelijk, wat leidt tot meer tijd-efficiënte acquisities van lange-afstand verbindingen zonder in te boeten op spatiële resolutie.

De tweede doelstelling van dit proefschrift was het verkrijgen van een hoge intrinsieke resolutie, d.w.z. de resolutie die door het MR-contrast zelf wordt gegeven. Het is bekend dat het meest gebruikte gradiënt-echo (GRE) bloedzuurstofniveau-afhankelijk (BOLD) contrast lijdt aan een voorkeursbehandeling qua gevoeligheid voor signaalveranderingen van grote aspecifieke aders. Daarom, zelfs met een nominaal hoge ruimtelijke resolutie, verhindert de intrinsieke vervaging in GRE-BOLD door de overgerepresenteerde grote bloedvaten, de verwerving van ruimtelijk verschillende laminaire signalen. Een voorgesteld alternatief is SE-BOLD dat minder gevoelig is voor grote drainerende en oppervlakkige aders. Een tijdsefficiënte implementatie van dit contrast vereist echter vaak EPI-uitlezingen die inherent T_2^*-gewogen zijn, waardoor opnieuw ongewenste signaalveranderingen in en rond grote vaten opnieuw worden geïntroduceerd.

Om te onderzoeken of zuivere T_2-weging haalbaar is en hoe een T_2-gewogen signaal wordt beïnvloed door verschillende gradaties van extra T_2'-weging opgelegd door verschillende uitleeslengtes, werd een T_2-gewogen multi-echo 3D FLASH sequentie gebruikt in **hoofdstuk 5**. De signaalkarakteristieken van deze sequentie werden geanalyseerd via numerieke simulaties en hoge-resolutie fMRI experimenten.

Naast SE-BOLD zijn er verschillende niet-BOLD fMRI contrasten voorgesteld en met succes gebruikt om het specificiteitsprobleem van GRE-BOLD te ondervangen. Eén van deze contrasten is gebaseerd op veranderingen in het cerebrale bloedvolume (CBV). Functionele MRI kan gevoelig gemaakt worden voor veranderingen in CBV, onder andere door het grijze massa (GM) signaal te onderdrukken via magnetisatie overdracht (MT) effecten. De resulterende CBV gevoeligheid heeft als bijkomend voordeel dat het een verminderde gevoeligheid voor extravasculair BOLD heeft, dat onvermijdelijk naar voren komt tijdens lange EPI uitlezingen. In **hoofdstuk 6** hebben we dit MT-fMRI contrast gekarakteriseerd in de context van laminaire fMRI met behulp van een vergelijkbare strategie als in hoofdstuk 5: Het MT-contrast werd bereikt door het signaal voor te bereiden met behulp van een MT-weging module. De daaropvolgende uitlezing bij verschillende GRE echotijden maakte het mogelijk om te extrapoleren naar een conditie zonder T_2^*-contaminatie en om de invloed van verschillende hoeveelheden T_2^*-weging op de vorm van laminaire fMRI-profielen te beoordelen. De resultaten van hoofdstuk 5 en 6 laten zien dat de contrasten een meer specifieke acquisitie van laminaire data mogelijk maken, maar ze vereisen ook een hogere versnelling van het beeldvormingsproces. Dit kan worden bereikt met de methode gepresenteerd in hoofdstuk 4 en er wordt aangetoond dat de methoden en contrastmechanismen die in dit proefschrift zijn onderzocht in hoge mate synergetisch zijn.

Zusammenfassung

Das Gebiet der laminaren funktionellen Magnetresonanztomographie (fMRT) ist eine relativ junge, aber stetig wachsende Disziplin zur nicht-invasiven Untersuchung der Funktion des menschlichen Gehirns. Die laminare fMRT hält den Schlüssel zur Aufdeckung der Richtung des Informationsflusses zwischen verschiedenen Hirnregionen und eröffnet eine neue Dimension der Untersuchung von Gehirnnetzwerken. Bislang ist die laminare fMRT mit hoher räumlicher und zeitlicher Auflösung jedoch auf kleine Sichtfelder (field-of-views; FOV) beschränkt. Daher besteht der Hauptzweck dieser Arbeit darin, sich mit grundlegenden Problemen der laminaren fMRT zu befassen: Die Erfassung von sauberen laminaren Signalen aus mehreren, weit voneinander entfernten Bereichen des menschlichen Gehirns.

Die Tatsache, dass viele Hirnareale in weit verzweigten Netzwerken organisiert sind, stellt eine Herausforderung für die Erfassung von hochaufgelösten, d.h. sub-millimeter, laminaren Daten dar. Die Erfüllung der Kriterien eines großen FOV und hoher räumlich-zeitlicher Auflösungen ist nicht einfach, da der Bildaufnahmeprozess in der MRT eher sequentiell als parallel erfolgt. Daher bestand das erste Ziel dieser Arbeit darin, eine hohe räumlich-zeitliche Auflösung und eine zeitgleich große Gehirnabdeckung zu erreichen. Zu diesem Zweck müssen die Anforderungen eines hohen Signal-zu-Rausch Verhältnisses (SNR) und Hochfrequenzspulen (HF) mit großem FOV erfüllt werden. Das Scannen bei einem ultrahohen Feld (UHF) von 7 T erfüllt die erste Anforderung, aber kommerzielle lokale Sendespulen, die bei 7 T verwendet werden, weisen aufgrund des Problems der HF-Inhomogenität bei UHF einen Mangel an Abdeckung auf. Daher wurde in **Kapitel 3** die Leistung einer 8-Kanal Sende- (Tx) und

15-Kanal Empfangs- (Rx) HF-Kopfspule für die MRT mit hoher Abdeckung untersucht, wobei der Schwerpunkt auf der fMRT des Kleinhirns lag.

Im Zusammenhang mit der laminaren fMRT einiger Regionen von Interesse (ROIs), die ein Netzwerk repräsentieren, kann es als Verschwendung angesehen werden, den Rest des Gehirns aufzunehmen. Die Vorteile, die sich aus der Möglichkeit ergeben, das Übertragungsfeld so zu gestalten, dass eine homogene Anregung des gesamten Gehirns bei UHF möglich ist (wie in Kapitel 3 durchgeführt), können auch genutzt werden, um das Anregungsprofil so zu gestalten, dass nur bestimmte ROIs erfasst werden. In **Kapitel 4** wurde eine Methode vorgestellt, bei der nicht das gesamte FOV abgebildet wird, sondern nur die interessierenden Bereiche mit maßgeschneiderten 2D-HF-Pulsen angeregt werden. Diese gezoomte Multi-FOV-Bildgebung reduziert die Last auf der Bildakquise und ermöglicht eine höhere Beschleunigung, was zu einer zeiteffizienteren Aufnahme von weit auseinanderliegenden Hirnregionen bei hoher räumlicher Auflösung führt.

Das zweite Ziel dieser Arbeit war es, eine hohe intrinsische Auflösung zu erreichen, d. h. die Auflösung, die durch den MR Kontrast selbst gegeben ist. Der am weitesten verbreitete Blutsauerstoffniveau-abhängige Gradientenechokontrast (GRE-BOLD) leidet bekanntermaßen unter einer Empfindlichkeitsverzerrung in Richtung Signaländerungen von großen unspezifischen Venen. Selbst bei einer nominell hohen räumlichen Auflösung verhindert daher die intrinsische GRE-BOLD Unschärfe die Erfassung räumlich getrennter laminarer Signale. Eine vorgeschlagene Alternative ist spin echo (SE)-BOLD, das weniger empfindlich auf große drainierende und oberflächliche Venen reagiert. Die zeiteffiziente Implementierung dieses Kontrasts erfordert jedoch häufig EPI-Auslesemethoden, die von Natur aus T_2^*-gewichtet sind, was wiederum zu unerwünschten Signaländerungen in und um große Gefäße führt. Um zu untersuchen, ob eine reine T_2-Gewichtung durchführbar ist und wie ein T_2-gewichtetes Signal durch verschiedene Grade zusätzlicher $T_2^{'}$-Gewichtung,

hervorgerufen durch unterschiedliche Ausleselängen, beeinflusst wird, wurde in **Kapitel 5** eine T_2-präparierte Mutli-Echo 3D FLASH Sequenz verwendet. Die Signaleigenschaften dieser Sequenz wurden durch numerische Simulationen und hochauflösende fMRT-Experimente analysiert.

Neben SE-BOLD wurde eine Vielzahl von nicht-BOLD fMRT-Kontrasten vorgeschlagen und erfolgreich eingesetzt, um das Spezifitätsproblem von GRE-BOLD zu überwinden. Ein Kontrast basiert auf Veränderungen des zerebralen Blutvolumens (CBV). Die funktionelle MRT kann für Veränderungen des CBV sensibilisiert werden, indem das Signal der grauen Substanz (GM) durch Magnetisierungstransfereffekte (MT) unterdrückt wird. Die daraus resultierende CBV-Sensitivität hat den zusätzlichen Vorteil, dass die Empfindlichkeit gegenüber extravaskulärem BOLD, das bei langen EPI-Auslesen unvermeidlich auftritt, reduziert wird. In **Kapitel 6** haben wir diesen MT-fMRT-Kontrast im Kontext der laminaren fMRT mit einer ähnlichen Strategie wie in Kapitel 5 charakterisiert: Der MT-Kontrast wurde durch Präparierung des Signals mit einem MT-Gewichtungsmodul erreicht. Das anschließende Auslesen bei verschiedenen GRE-Echozeiten ermöglichte die Extrapolation auf einen Zustand ohne T_2^*-Kontamination und die Beurteilung des Einflusses verschiedener T_2^*-Gewichtungen auf die Form laminarer fMRT-Profile. Die Ergebnisse von Kapitel 5 und 6 zeigen, dass die Kontraste eine spezifischere Erfassung laminarer Daten ermöglichen, aber auch eine höhere Beschleunigung des Bildgebungsprozesses erfordern. Dies kann mit der in Kapitel 4 vorgestellten Methode erreicht werden, und es wird gezeigt, dass die in dieser Arbeit untersuchten Methoden und Kontrastmechanismen in hohem Maße synergetisch sind.

Acknowledgments

Just as science in general thrives on exchange and collaboration, this work was only possible through the support and guidance of many kind people. I would like to express my heartfelt thanks to all of them!

First and foremost, **Peter**, I think if there is such a thing as a perfect supervisor, you come pretty close. Thank you for being such a patient and instructive supervisor throughout, and for allowing me to bug you with my questions and problems at the most impossible times (I've had to free up the memory space taken up by our many voicemails by now). Thank you for your immensely vast wealth of knowledge, for sharing it with me and for giving me the freedoms to find my own way. Although we are in the same boat, it is not given that the supervisor understands a young fathers' time management issues, but you did it perfectly and for that, I like to thank you. I would also like to thank you for the short but very nice time in Nijmegen and your hospitality (and your exceptionally good taste in beer). Hopefully we can go bouldering together again someday, even though I'll probably have to train a bit more until then to even get close to your level. Although you have left ELH to embrace the matrix, I sincerely hope that we will continue to be in touch and who knows, maybe I will join the dark side of the force as well some day. I am sure that your new PhD students will definitely be lucky to have you as a supervisor because you know how its done. Thank you.

David, thank you for your support, your extraordinary wealth of wisdom, your always open ear, your curiosity, and your humor. Thank you for including me as part of your group and I am looking forward to continue working with you and picking the low-hanging fruits together.

Many thanks to **Tom Scheenen**, **Wietske van der Zwaag**, and **Benedikt Poser** for agreeing to be in my manuscript committee.

I am grateful to **Harald** who was kind enough to not reject my application as a master student despite the bad photo. Thank you for letting me start my journey at the Erwin Hahn Institute with you and for your support and responsiveness since then.

Many thanks to **Oliver**, for your friendly manner and that I always have the opportunity to drop by your office (and often did). Thanks for always making sure that the cross is in the right place in the project proposal and for keeping us safe from any plagues from the dirty coffee machine. Thanks for the nice beer afternoons and I am very happy to know you as our RF safety expert at the ELH.

Stefan, thank you for managing our institute, for walking around the building looking for the missing water in the system, for discussing issues and their solutions and for the cool chats in the hallway and kitchen. My back also wants to thank you for asking me so many times to lift that heavy plate in the kitchen.

Marcus, even though you just started at the ELH, it feels like you have always been part of the team. Thank you for being such a nice person and colleague and for pimping our RF lab.

A big thanks to Linux magician **Marcel** for running so many things behind the curtain and for being responsive even after working times. I think that joining team Linux was a good idea and I am thankful for all your help.

Jenni, thank you for all the nice conversations, professional and personal, and for sharing IDEA solutions and hassles. I hope you will continue to stay with the ELH.

I thank **Annika**, who helped me out so often and who I could fry so many times in the scanner. I think by now I have more datesets from you than from myself. Thank you for your kind personality and I wish you all the best for your medical studies.

Thomas, thank you for your kind and open manner, and for being so good on the phone at explaining how to fiddle with the fMRI rack to get it working again. Also thank you for your experience with cerebellar (f)MRI. Man, what a challenging area but you keep on going strong.

Steffi, thank you for all the entertaining conversations we had about Japanese culture and books. You are a really cool person and I look forward to stopping by your office again.

Franziska, thank you so much for your amazing talent of managing an institute like the ELH, for quickly helping in many different aspects of bureaucracy and for being so responsive.

Sascha, I don't want to miss out the chance to thank you for your support during my start at the ELH. Thank you for your patience, your humor and your kind personality. I hope you have a great time at the DZNE.

Max, I really enjoyed all the tea afternoons we spend together at the ELH talking about the latest problems with the pTx system. Thank you for your funny manner and for organizing the Christmas parties so often.

A big thank you goes out the the entire **Donders MR group**, past and present, for all the interesting seminars that keep reminding me that MRI is not just about high-resolution fMRI. Thank you guys and I look forward to working with you and learning from you.

Sri, although our time in Maastricht was short, it was essential to this work and to me. You really saved me when you organized all the scan sessions and spent a good part of your already scarce time helping a stranger. I am grateful you did and I hope that one day our paths will cross for a longer time. In the meantime, I wish you all the best for your time in Canada.

Danke, **Pascal**, dass du so viel Zeit und Mühe in das Design des Covers dieser Arbeit gesteckt hast.

Eric, Konstantin, Martin, Niklas, Yannick, Jungs, obwohl uns die Zeit in verschiedene Richtungen getrieben hat und der Alltag sein übriges dazu tut, so bin ich doch dankbar dafür, zu wissen, dass ich in euch Freunde gefunden habe. Die Studienzeit wäre ohne euch nicht dieselbe gewesen und ich verbinde viele schöne Erinnerungen mit jedem von euch. Ich hoffe, dass wir es schaffen uns öfter zu treffen und sei es nur online beim Malen unerkennbarer Bilder.

Nico, was soll ich sagen? Es hat wohl doch alles mit diesem MRT Praktikum angefangen. Jetzt bin ich auch Teil des Teams PhD und ich will dir dafür danken. Danke, dass wir uns in der ganzen Zeit gegenseitig den Rücken und die Leber stärken konnten. Danke, dass ich dir ab und an mein Leid klagen konnte und danke, dass du mich immer wieder aufgebaut hast. Aber vor Allem danke ich dir dafür, dass du mein bester Freund bist.

Karl, Maria, danke, für eure liebevolle Hingabe als Großeltern und für die Freiräume, die ihr mir geschaffen habt. Ohne euch wäre diese Arbeit nicht so geworden, wie sie jetzt ist. Vielen Dank, dass ihr neben eurem unermesslichen seelischen Beistand auch wöchentlich für unser leibliches Wohl sorgt und somit den Laden am Laufen haltet. Danke, dass ihr uns so oft euer Auto geliehen habt, ohne wären die Scans in Maastricht niemals möglich gewesen. Aber vor Allem möchte ich euch dafür danken, dass ihr mich als Teil eurer Familie aufgenommen habt.

Mein Dank gilt natürlich auch **Gregor** und **Lukas**, die sich mit mir geärgert haben, wenn mal was nicht lief, und die sich mit mir gefreut haben, wenn es dann doch geklappt hat. Danke, dass ihr so seid, wie ihr seid und dafür, dass man mit euch echt viel Spaß haben kann.

Papa, Rita, Ira, wir hatten es nicht immer leicht und doch haben wir es geschafft, zusammenzuhalten. Ich wäre heute nicht dort, wo ich jetzt bin, wenn nicht du, Papa, dich für unsere Famile zerrissen hättest. Ich danke dir für deine Aufopferung, für dein Wissen, für deine Stärke und für deine Liebe. Danke, dass du immer für mich da warst und ich weiß, dass du es auch weiterhin sein wirst. Ich kann mich glücklich schätzen, dein Sohn zu sein. Danke Ira, dass mein Vater in dir sein Glück gefunden hat und ihr gemeinsam das Leben meistert. Ich bin froh, dass du Teil unserer Familie geworden bist und Leonie in dir eine fürsorgliche Mutter hat. Rita, ich kann gar nicht in Worte fassen, wie dankbar ich dir für alles bin, was du für mich getan hast, damals und heute noch. Obwohl uns das Leben auf unterschiedliche Pfade geführt hat, so weiß ich doch, was ich an dir habe und dafür möchte ich dir von Herzen danken.

Mama, ich wünschte, du könntest das hier lesen. Es würde mich so glücklich machen, dich stolz zu sehen. Obwohl meine Erinnerung an dich langsam verblasst, so verblasst doch nicht meine Liebe zu dir. Danke, dass ich dein Sohn sein darf.

Meine geliebte **Wiebke**, hurra, es ist vollbracht! Ich weiß nicht, ob die Danksagung in einer Doktorarbeit ausreicht, um meinen Dank dir gegenüber auszudrücken. All das hier wäre ohne dich niemals möglich gewesen. Du bringst in allen Bereichen meines Lebens das Beste in mir zum Vorschein. Danke, für deine Geduld und für deine Fürsorge. Danke, dafür, dass meine Schusseligkeit dir (meistens) nichts ausmacht. Dafür, dass du meine allabendliche Fachsimpelei erträgst. Dafür, dass du mir immer den Rücken stärkst und dafür, dass ich in dir einen Menschen gefunden habe, der immer an meiner Seite ist. Ich bin unermesslich froh, dass es dich gibt.

Jakob, ich freue mich schon darauf, wenn du alt genug bist, das hier zu lesen. Wenn es etwas gibt, was ich richtig gemacht habe, dann bist du es. Ich glaube, ich habe seit dem du auf der Welt bist, noch nie so viel gelacht. Danke, dass du mein Leben auf so vielen Ebenen bereicherst und ich bin unglaublich froh und stolz, dich als meinen Sohn aufwachsen zu sehen.

Danke euch allen!

Viktor Pfaffenrot
Essen
October 5, 2022

Curriculum Vitae

Viktor Pfaffenrot was born in Pavlodar, Kazakhstan the 6th of Juli 1990. He grew up in Remscheid (near cologne), with his parents Viktor and Valentina and his sister Margarita. After finishing secondary education in 2010, he worked at the Neurological and Internal Functional Diagnostics department of the Evangelische Stiftung Tannenhof in Remscheid to complete his community service. During this time, he came into contact with technological aspects of medicine which let to the decision to pursue a Bachelor of Science degree in Medical Physics at the Heinrich-Heine University (HHU) in Duesseldorf from 2011 to 2015. During his Bachelor's, he found interest in MRI and carried out his Bachelor's thesis in the Institute for Diagnostic and Interventional Radiology under the supervision of Prof. Hans-Jörg Wittsack and Dr. Georg Oeltzschner, measuring the T_1-relaxation time of the neurotransmitter GABA in vivo using MR spectroscopy at 3 T. Upon graduation, he continued with a Master of Science degree in Medical Physics at the HHU. He wrote his Master's thesis in 2017 at the Erwin L. Hahn Institute for MRI in 2017 under the supervision of Prof. Harald Quick and Sascha Brunheim, where he evaluated an RF coil combination for fMRI of the human cerebellum at 7 T. In 2017, he started a PhD under the supervision of Prof. David Norris and Dr. Peter Koopmans at the ELH working on methods and contrast mechanisms to acquire clean laminar fMRI signals from widely spaced brain regions. Following his PhD, he continues as a post-doctoral fellow at the ELH in the group of Prof. David Norris where he studies methods for laminar fMRI of the human hippocampus.

List of publications

Articles

Pfaffenrot, V. and Koopmans, P. J. ”Magnetization Transfer weighted laminar fMRI with multi-echo FLASH”. *Submitted to Neuroimage (in revision)*

Deistung, A., Jäschke, D., Draganova, R., **Pfaffenrot, V.**, Hulst, T., Steiner, K. M., Thieme, A., Giordano, I. A., Klockgether, T., Tunc, S., Münchau, A., Minnerop, M., Göricke, S. L., Reichenbach, J. R., and Timmann, D. “Quantitative susceptibility mapping reveals alter ations of dentate nuclei in common types of degenerative cerebellar ataxias”. In: *Brain commun.* 4 (2022), pp. 1–18

Draganova, R., **Pfaffenrot, V.**, Steiner, K. M., Göricke, S. L., Elangovan, N., Timmann, D., and Konczak, J. “Neurostructural changes and declining sensorimotor function due to cerebellarcortical degeneration”. In: *J. Neurophysiol.* 125 (2021), pp. 1735–1745

Pfaffenrot, V., Voelker, M. N., Kashyap, S., and Koopmans, P. J. “Laminar fMRI using T_2-prepared multi-echo FLASH”. in: *NeuroImage* 236 (2021)

Koopmans, P. J. and **Pfaffenrot, V.** “Enhanced POCS reconstruction for partial Fourier imaging in multi-echo and time-series acquisitions”. In: *Magn. Reson. Med.* 85 (2021), pp. 140–151

Pfaffenrot, V., Brunheim, S., Rietsch, S. H. G., Koopmans, P. J., Ernst, T. M., Kraff, O., Orzada, S., and Quick, H. H. “An 8/15-channel Tx/Rx head neck RF coil combination with region-specific B_1^+ shimming for whole brain MRI focused on the cerebellum at 7 Tesla”. In: *Magn. Reson. Med.* 80 (2018), pp. 1252–1265

Brunheim, S., Johst, S., **Pfaffenrot, V.**, Quick, H. H., and Poser, B. A. “Variable slice thickness (VAST) EPI for the reduction of susceptibility artifacts in whole-brain GE-EPI at 7 Tesla”. In: *Magn. Reson. Mater. Phys.* 30 (2017), pp. 591–607

Rietsch, S. H. G., **Pfaffenrot, V.**, Bitz, A. K., Orzada, S., Brunheim, S., Lazik-Palm, A., Theysohn, J. M., Ladd, M. E., Quick, H. H., and Kraff, O. “An 8-channel transceiver 7-channel receive RF coil setup for high SNR ultrahigh-field MRI of the shoulder at 7T”. in: *Med. Phys.* 44 (2017), pp. 6195–6208

Conference talks

Pfaffenrot, V., Brunheim, S., Rietsch, S. H. G., Ernst, T. M., Kraff, O., Orzada, S., and Quick, H. H. “An 8/15-Channel Tx/Rx Head Neck RF coil Combination with Semi-Dynamic B_1 Shimming for Improved fMRI of the Cerebellum at 7 T”. in: *Proc. Int. Soc. Magn. Reson. Med. 25* (2017), #1127

Conference posters

Pfaffenrot, V. and Koopmans, P. J. “Laminar fMRI with MT-prepared multi-echo 3D FLASH”. in: *Proc. Int. Soc. Magn. Reson. Med. 31* (2022), #4809

Rietsch, S. H. G., Orzada, S., Brunheim, S., Bitz, A. K., Voelker, M. N., **Pfaffenrot, V.**, Gratz, M., Leinweber, D., Weine, J., Handtke, S., Kraff, O., Ladd, M. E., Koopmans, P., and Quick, H. H. “A 32-channel transmit/receive radiofrequency head coil for 7T UHF MR”. in: *Proc. Int. Soc. Magn. Reson. Med. 27* (2019), #1486

Pfaffenrot, V. and Koopmans, P. J. “Laminar fMRI with T_2-prepared multiecho FLASH”. in: *Proc. Int. Soc. Magn. Reson. Med. 27* (2019), #3763

Güllmar, D., **Pfaffenrot, V.**, Draganova, R., Feng, X., Reichenbach, J. R., Timmann, D., and Deistung, A. “cBEaST: Cerebellar Brain Extraction based on Nonlocal Segmentation Technique – A comparison with state-of-the-art methods”. In: *Proc. Int. Soc. Magn. Reson. Med. 25* (2017), #0771

Research data management

Ethics

This thesis is based on the results of human studies, which were conducted in accordance with the principles of the Declaration of Helsinki. The Ethical Committee of the faculty of Medicine at the University of Duisburg-Essen, Essen, Germany, approved the conduct of theses studies (Number 16-7214-BO). This research is primarily funded by the Deutsche Forschungsgemeinschaft (DFG, German Research Foundation). Detailed funding sources are given in the footnote at the end of each chapter.

Findable, Accessible

For chapters 3, 4, 5 and 6, research data have been archived on two external hard drives stored at the Erwin L. Hahn Institute for Magnetic Resonance Imaging (ELH) and accessible to the institute's administrative director, the PhD supervisor and the author of this thesis.

For chapters 3 and 4, written informed consent was obtained only for publishing the data in scientific articles and/or scientific conferences, hence the data for these chapters cannot be made accessible. For chapters 5 and 6, anonymized data are made accessible according to the DFG Guidelines for Safeguarding Good Research Practice (DOI:10.5281/zenodo.6472827) and can be obtained from the institute's administrative director or the PhD supervisor.

For all chapters, the written informed consent is archived in the ELH for 15 years after termination of the studies.

Interoperable, Reusable

MRI data are stored in the .nifti file format. On the archive hard drive, folders containing the data of chapter 5 and 6 also contain a subfolder with the used analysis scripts and a readme file describing the used data organizational structure. For each chapter, the Materials & Methods section includes the used software and version numbers.

Privacy

The privacy of the participants in this thesis has been warranted using individual subject codes. A pseudonymization key linked this code with the personal data. The key was stored at the ELH and was only accessible by the author of this thesis. The keys of chapter 3, 4 and 5 were destroyed within one month after finalization of these projects. The key of chapter 6 is still stored as the article of chapter 6 is still under review. The key will be destroyed one month after finalization. MRI data of chapter 5 and 6 are defaced and shared according to the DFG Guidelines for Safeguarding Good Research Practice.